

IMAGING OF STEEP REFLECTORS IN ANISOTROPIC MEDIA
BY WAVEFIELD EXTRAPOLATION

A DISSERTATION
SUBMITTED TO THE DEPARTMENT OF GEOPHYSICS
AND THE COMMITTEE ON GRADUATE STUDIES
OF STANFORD UNIVERSITY
IN PARTIAL FULFILLMENT OF THE REQUIREMENTS
FOR THE DEGREE OF
DOCTOR OF PHILOSOPHY

Guojian Shan
August 2008

© Copyright by Guojian Shan 2008
All Rights Reserved

I certify that I have read this dissertation and that, in my opinion, it is fully adequate in scope and quality as a dissertation for the degree of Doctor of Philosophy.

(Biondo L. Biondi) Principal Adviser

I certify that I have read this dissertation and that, in my opinion, it is fully adequate in scope and quality as a dissertation for the degree of Doctor of Philosophy.

(Jon F. Claerbout)

I certify that I have read this dissertation and that, in my opinion, it is fully adequate in scope and quality as a dissertation for the degree of Doctor of Philosophy.

(Howard Zebker)

Approved for the University Committee on Graduate Studies.

Abstract

Seismic migration based on isotropic downward continuation is an effective technique for imaging complex subsurface geologic structure. However, this approach has difficulty in imaging steep reflectors, such as faults and salt flanks, that are often important in hydrocarbon exploration. Waves illuminating steep reflectors usually have nearly horizontal or overturned raypaths. This thesis addresses two major challenges in propagating these types of waves using isotropic downward continuation methods. First, when anisotropy is present in the subsurface, the errors associated with propagating near-horizontal waves under the isotropic assumption become severe. Second, downward continuation methods using the one-way wave equation have difficulty propagating near-horizontal or overturned waves. In theory, both issues can be resolved by using anisotropic reverse-time migration, which uses the two-way wave-equation, but such schemes are significantly more computationally expensive.

I present a new one-way wave-equation based method that efficiently images steep reflectors in anisotropic media. First, I incorporate anisotropy in wave propagation by developing a new one-way wavefield extrapolation scheme, optimized finite-difference, for anisotropic media. The scheme is designed by fitting the dispersion relation with a rational function using the weighted least-squares methods, and it propagates waves accurately and efficiently in anisotropic media. Synthetic data examples show that with anisotropy taken into account, reflectors are positioned correctly with this scheme.

Second, I develop a new migration algorithm, plane-wave migration in tilted coordinates. The recorded surface data are transformed by slant stacking to a collection of

plane-wave source datasets with all possible take-off angles. Each plane-wave source dataset is migrated independently in a tilted coordinate system with the tilting angle determined by the take-off angle of the plane-wave source. For waves illuminating steep reflectors, the propagation direction is close to the extrapolation direction, thus they are accurately propagated by plane-wave migration in tilted coordinates. For steep reflectors in tilted coordinates, the subsurface offset direction is close to the dip direction of reflectors, thus plane-wave migration in tilted coordinates generates robust angle-domain common-image gathers for steep reflectors. I apply plane-wave migration in tilted coordinates to synthetic and 3D field datasets. Results show that steep salt flanks and faults are well imaged.

Acknowledgments

It was a long journey to get this dissertation done. I would like to take this opportunity to express my sincere appreciation to all who have helped me to reach this point.

My gratitude goes to Professors Biondo Biondi and Jon Claerbout for the generous support, constructive ideas, warm encouragement and freedom on research. Thanks to them for offering me an outstanding research environment. Thanks to my committee member Professor Howard Zebker for the discussion and suggestions. I would like to thank Professor Guanquan Zhang in Chinese academy of science. It was he who brought me to exploration geophysics ten years ago. I also enjoy the discussion with him by phone during these years. I would like to thank Professor Ken Lerner in Colorado school of mines for his suggestions and editing my thesis carefully. His editing makes this thesis in a much better shape. I also thank him for teaching me how to express my idea clearly. Thanks to Bob Clapp for helping me work on the 3D field data. I would like to thank Dennis Michael in the Stanford Center for Computational Earth and Environmental Science. He maintains the clusters in CEES so well that I finished my 3D field data example smoothly. I would also like to acknowledge the sponsors of SEP for financial support and providing datasets for this thesis.

Thanks also to our administrator, Diane Lau. She deals with all the details and keeps everything running in order in SEP.

Thanks to all my fellow students in SEP for the friendship and sharing ideas. Among them: Bill Curry, Alejandro Valenciano, Jesse Lomask, Jeff Shragge, Daniel

Rosales, Morgan Brown, Antoine Guitton, Paul Sava, Marie Clapp, Weitian Chen, Thomas Tisserant, Nick Vlad, Brad Artman, Gabriel Alvarez, Yaxun Tang, Ben Witten, Madhav Vyas, Pierrer Jousselin, Claudio Cardoso, Gboyega Ayeni, Roland Gunther, Sjoerd Ridder, Xukai Shen, Adam Halpert, Abdullah Al Theyab and Mohammad Maysami. I enjoy seminars, coffee breaks, and Friday beers with you guys. Because all of you, my experience in SEP becomes wonderful and enjoyable. Having spent some time on clusters, I know how much effort that computer administrators in SEP put on computers. Thanks to Bob Clapp, Bill Curry and Alejandro Valenciano for keeping our computer system running. Thanks to Jeff Shragge for reading an early thesis draft and suggesting useful improvements.

Thanks to my friends, Daoliu Wang, Faqi Liu, Hongbo Zhou and Yu Zhang for the help and encouragement during these years.

Finally, none of this would have been possible without the love, support and patience of my parents, my parents-in-law, and especially my wife, Yulin Xuan, to whom I owe everything.

Contents

Abstract	v
Acknowledgments	vii
1 Introduction	1
2 Wavefield extrapolation in anisotropic media	11
3 Plane-wave migration in tilted coordinates: theory	53
4 Plane-wave migration in tilted coordinates: examples	107
5 Angle-domain CIGs for steep reflectors	131
6 Conclusion	157
A 3D CIGs in tilted coordinates	159

List of Tables

List of Figures

1.1	Comparison of waves illuminating horizontal (a) and steep (b) reflectors. The angle θ is the opening angle, α is the dip angle of the reflector, S is the source location, and R is the receiver location. Waves illuminating a horizontal reflector usually travel in a direction that is less than 40° from the vertical, while those illuminating steep reflectors have a portion of wave path that is almost horizontal.	3
1.2	Steep reflectors are not well imaged with imaging methods based on the isotropic downward continuation.	4
1.3	Comparison of wavefronts propagated from a point source at $x = 0$, $z = 0$ in isotropic and VTI media: the solid line is the wavefront propagated in an isotropic medium; the dashed line is the wavefront propagated in a VTI medium with $\varepsilon = 0.2$ and $\delta = 0.2$; and dotted line is the wavefront propagated in a VTI medium with $\varepsilon = 0.2$ and $\delta = -0.2$. The vertical velocity of the medium is 2000 m/s in all three cases, and the travelttime from the point source to the wavefronts is 1 s.	5

2.1 Dispersion relation comparison: curve “True” is the true dispersion relation; curve “Taylor-weak-2” is the second-order approximate dispersion relation obtained by Taylor-series and Padé expansion analysis based on weak anisotropy assumption; curve “Taylor-2” is the second-order approximate dispersion relation obtained by Taylor-series and Padé expansion analysis for equation 2.10; curve “Optimization-2” is the second-order approximate dispersion relation obtained by weighted least-square optimization; curve “Optimization-4” is the fourth-order approximate dispersion relation by weighted least-square optimization. 20

2.2 Relative dispersion error comparison: curve “Taylor-weak-2” is the relative dispersion error of the second-order approximation by conventional Taylor- and Padé-expansion analysis based on weak anisotropy assumption; curve “Taylor-2” is the relative dispersion error of the second-order approximation by conventional Taylor- and Padé-expansion analysis for equation 2.10; curve “Optimization-2” is the relative dispersion error of the second-order approximation by optimization; curve “Optimization-4” is the relative dispersion error of the fourth-order approximation by optimization. If we accept one percent relative dispersion error, the second-order approximation by Taylor-series and Padé-expansion analysis based on weak anisotropy assumption is accurate to 30° , the second-order approximation by Taylor-series and Padé-expansion analysis using dispersion relation equation 2.10 is accurate to 38° , the second-order approximation by optimization is accurate to 60° and the fourth-order one is accurate to 80° 22

2.3 Impulse responses at $t = 1$ s for a VTI medium with the parameters $v_{p0} = 2000$ m/s, $\varepsilon = 0.4$ and $\delta = 0.2$: (a) the second-order approximation by optimization; (b) the fourth-order approximation by optimization. The solid line is the theoretical impulse response calculated by using the group velocity as a function of the group angle of the medium. 26

2.4	Impulse responses at $t = 1$ s for a VTI medium with the parameters $v_{p0} = 2000$ m/s, $\varepsilon = 0$ and $\delta = -0.2$: (a) the second-order approximation by optimization; (b) the fourth-order approximation by optimization. The solid line is the theoretical impulse response calculated by using the group velocity as a function of the group angle of the medium.	27
2.5	Impulse responses at $t = 1$ s for a VTI medium with the parameters $v_{p0} = 2000$ m/s, $\varepsilon = 0.2$ and $\delta = -0.2$: (a) the second-order approximation by optimization; (b) the fourth-order approximation by optimization. The solid line is the theoretical impulse response calculated by using the group velocity as a function of the group angle of the medium.	28
2.6	The vertical velocity and anisotropy parameters for the synthetic data: (a) vertical velocity; (b) anisotropy parameter ε ; (c) anisotropy parameter δ .	29
2.7	Implicit FD migrations for the synthetic dataset: (a) the second-order approximation by optimization; (b) the fourth-order approximation by optimization.	30
2.8	FFD migrations for the synthetic data: (a) using minimal nonzero anisotropy parameters as the reference ones; (b) using zero as the reference anisotropy parameters.	36
2.9	Dispersion relation for tilted TI media with a tilting angle of 30° : (a) $\varepsilon = 0.2$ and $\delta = 0.2$; (b) $\varepsilon = 0.2$ and $\delta = 0.1$; (c) $\varepsilon = 0.2$ and $\delta = 0$; (d) $\varepsilon = 0.2$ and $\delta = -0.1$; (e) $\varepsilon = 0.2$ and $\delta = -0.2$; (f) $\varepsilon = 0.2$ and $\delta = -0.3$.	40
2.10	Comparison of the true and approximate dispersion relations for a TTI medium with $\varepsilon = 0.4$, $\delta = 0.2$ and $\varphi = 30^\circ$: the solid line is the true dispersion relation for TTI media; the dashed line is the approximate dispersion relation for the finite-difference scheme. The dispersion relation for the finite-difference scheme is very close to the true one.	41

2.11	Relative dispersion-relation error of the finite-difference approximation for a TTI medium with $\varepsilon = 0.4$, $\delta = 0.2$ and $\varphi = 30^\circ$	41
2.12	Impulse response of a tilted TI medium with $v_{p0} = 2000$ m/s, $\varepsilon = 0.4$, $\delta = 0.2$ and $\phi = 30^\circ$ calculated by 4th-order FD. The solid line is the theoretical impulse response calculated using the group velocity as a function of the group angle.	45
2.13	Impulse response of a tilted TI medium with $v_{p0} = 2000$ m/s, $\varepsilon = 0.2$, $\delta = 0.1$ and $\phi = 30^\circ$ calculated by 4th-order FD. The solid line is the theoretical impulse response calculated using the group velocity as a function of the group angle.	45
2.14	Impulse response of a tilted TI medium with $v_{p0} = 2000$ m/s, $\varepsilon = 0.2$, $\delta = 0.1$ and $\phi = 30^\circ$ calculated by 4th-order FD. The solid line is the theoretical impulse response calculated using the group velocity as a function of the group angle.	46
2.15	Impulse response of a tilted TI medium with $v_{p0} = 2000$ m/s, $\varepsilon = 0.2$, $\delta = 0.0$ and $\phi = 30^\circ$ calculated by 4th-order FD. The solid line is the theoretical impulse response calculated using the group velocity as a function of the group angle.	46
2.16	Impulse response of a tilted TI medium with $v_{p0} = 2000$ m/s, $\varepsilon = 0.0$, $\delta = -0.2$ and $\phi = 30^\circ$ obtained by 4th-order FD. The solid line is the theoretical impulse response calculated using the group velocity as a function of the group angle.	47
2.17	Impulse response of a tilted TI medium with $v_{p0} = 2000$ m/s, $\varepsilon = 0.2$, $\delta = -0.2$ and $\phi = 30^\circ$ obtained by 4th-order FD. The solid line is the theoretical impulse response calculated using the group velocity as a function of the group angle.	47

2.18	Impulse response of a tilted TI medium with $v_{p0} = 2000$ m/s, $\varepsilon = 0.0$, $\delta = -0.2$ and $\phi = 30^\circ$ obtained by 6th-order FD. The solid line is the theoretical impulse response calculated using the group velocity as a function of the group angle.	48
2.19	Impulse response of a tilted TI medium with $v_{p0} = 2000$ m/s, $\varepsilon = 0.2$, $\delta = -0.2$ and $\phi = 30^\circ$ obtained by 6th-order FD. The solid line is the theoretical impulse response calculated using the group velocity as a function of the group angle.	48
2.20	Thrust model for the synthetic data imaged in Figure 2.21.	49
2.21	Image comparisons: (a) image obtained by isotropic migration; (b) image obtained by anisotropic migration for VTI media; (c) image obtained by anisotropic migration for TTI media.	51
3.1	The accuracy of one-way wavefield extrapolation operator determines the propagation direction of waves that it can handle. If the extrapolation operator is accurate to ψ , the shadow area in panel (a) represents the directions of waves that it can handle for source wavefield and the shadow area in panel (b) represents the directions of waves that it can handle for receiver wavefield.	58
3.2	The waves illuminating steep reflectors: (a) high-angle waves; (b) over-turned waves. The source location is S and the receiver location is R . Angles φ_1 , φ_2 and φ_3 are the difference between the propagation direction and extrapolation direction at “A”, “B” and “C”, respectively. If the accuracy angle ψ in Figure 3.1 is smaller than φ_1 , φ_2 and φ_3 , the events in panels (a) and (b) cannot be accurately imaged.	59

3.3	Two-dimensional coordinate system rotation. The coordinates (x, z) are conventional vertical Cartesian coordinates, and (x', z') are tilted coordinates. The notation s_x represents the source location and $r_{xi}, i = 1, 2, \dots, 5$, represent receiver locations. The source and receivers are on regular grids in vertical Cartesian coordinates.	63
3.4	Source and receivers in a grid defined in a tilted coordinate system. Coordinates (x, z) are conventional vertical Cartesian coordinates, and (x', z') are tilted coordinates. Notation s_x represents the source location and $r_{xi}, i = 1, 2, \dots, 5$, represent receiver locations. In tilted coordinates, these locations are on a slanted surface and do not fall on regular grid points. The wavefield values recorded at these locations are interpolated onto regular grid points around the slanted surface. For example, the wavefield on r_{x3} is interpolated onto the grids a, b, c, and d.	64
3.5	A velocity model revised from Sigsbee 2A. The sedimentary part of the model is extended to allow the overturned waves from the overhanging salt flanks to be received at the surface. The rays represent the overturned waves from the overhanging salt flank.	65
3.6	The velocity model and overturned waves in a tilted coordinate system. The overturned waves in vertical Cartesian coordinates do not overturn in the tilted coordinate system.	66
3.7	VTI media in vertical Cartesian coordinates become tilted TI media in tilted coordinates. (a) A thin-layer VTI medium, its symmetry axis, and tilted coordinates shown in vertical Cartesian coordinates. (b) The VTI medium in tilted coordinates. The horizontal layers become dipping layers; thus the medium becomes a tilted TI medium in the new coordinates.	67

3.8	Point source (a) and plane-wave sources (b) in tilted coordinates. Waves from a point source propagate radially, and the waves represented by the dash line rays in panel (a) cannot be propagated accurately when we rotate the coordinates counter-clockwise. In contrast, the propagation directions of the plane-wave source are similar at different spacial points along the surface $z = 0$, so generally they can be extrapolated accurately in a tilted coordinate system.	68
3.9	Plane-wave sources and their associated tilted coordinates. The tilting direction for the coordinates corresponding to the plane-wave source depends on its take-off angle. Depicted are three typical plane-wave sources with zero, negative, and positive ray parameter, respectively. For $p_{s_x} = 0$, I use conventional Cartesian coordinates. For $p_{s_x} > 0$, I rotate coordinates counter-clockwise, and for $p < 0$, I rotate coordinates clockwise.	69
3.10	Reciprocity improves plane-wave migration in tilted coordinates. The source location is at s , and the receiver location is at r . For this event, the source ray does not overturn, but the receiver ray does. If we were to run plane-wave migration in tilted coordinates only the original one-side offset data, we would use the coordinates (x_s, z_s) for both source and receiver waves. The direction of (x_s, z_s) is determined by the initial source ray direction at the surface. In this coordinate system, the source waves can be handled well but the overturned receiver wave cannot. If we were to run the same migration only for the data generated by reciprocity, we would use the coordinates (x_r, z_r) for both source and receiver wavefield extrapolation. The direction of (x_r, z_r) is determined by the receiver ray direction at the surface. In this coordinate system, both the source and receiver waves can be handled with accuracy.	71

3.11	The exploding reflector dataset from the revised Sigsbee 2A model. The overturned energy are recorded from -20 to 5km at $t = 10$ to 25s . The energy recorded earlier than 10s is muted before migration to verify the imaging of overturned waves.	74
3.12	Migrated image of the overturned waves: migration in tilted coordinates (a) and reverse-time migration (b).	74
3.13	Impulse-response comparison among (a) two-way wave equation migration, (b) one-way wave equation migration in vertical Cartesian coordinates, and (c) plane-wave migration in tilted coordinates.	75
3.14	The velocity model of BP velocity benchmark.	76
3.15	Detail of velocity model for the left salt body.	77
3.16	Image of the left salt body obtained by plane-wave migration in tilted coordinates.	78
3.17	Image of the left salt body obtained by plane-wave migration in vertical Cartesian coordinates.	79
3.18	Detail of velocity model for the right salt body.	81
3.19	Image of the right salt body obtained by plane-wave migration in tilted coordinates.	82
3.20	Image of the right salt body obtained by plane-wave migration in vertical Cartesian coordinates.	83
3.21	The parameters of the VTI model: density (a), qP-wave vertical velocity v_{p_0} (b), and anisotropy parameter ε . The anisotropy parameter δ is zero.	84
3.22	Rays show that the steep salt flank is mainly illuminated by overturned energy.	85

3.23	The resulting image obtained by isotropic plane-wave migration in tilted coordinates.	86
3.24	The resulting image obtained by anisotropic plane-wave migration in vertical Cartesian coordinates.	87
3.25	The resulting image obtained by anisotropic plane-wave migration in tilted coordinates.	87
3.26	The density model overlaid with the image obtained by anisotropic plane-wave migration in tilted coordinates.	88
3.27	A snapshot of the source wavefield generated using equation 3.18: (a) dense shot gathers with a 25 m shot interval and (b) sparse shot gathers with a 300 m shot interval.	89
3.28	Shot-profile migration of the dataset with 3 single-trace shots.	92
3.29	Migration of a single ray-parameter section ($p_{s_x} = 0$): (a) phase-encoded source, (b) plane-wave source.	93
3.30	Images of 65 ray parameters: (a) plane-wave source, (b) phase-encoded source.	94
3.31	Images of 13 ray parameters: (a) plane-wave source, (b) phase-encoded source.	95
3.32	Image of the 2004 BP velocity benchmark with a shot interval of 500 m: (a) plane-wave source, (b) phase-encoded source.	97
3.33	Single phase-encoded source image of a dataset with three single trace shots: (a) ray parameter $p_{s_x} = -0.0003$ s/m, tilted coordinates with tilting angle $\theta = -35^\circ$; (b) ray parameter $p_{s_x} = 0$ s/m, vertical Cartesian coordinates; and (c) ray parameter $p_{s_x} = 0.0003$ s/m, tilted coordinates with tilting angle $\theta = 35^\circ$	100

3.34	Image of a dataset with three single trace shots: (a) shot-profile migration in tilted coordinates with tilting angle $\theta = -35^\circ$; (b) shot-profile migration in vertical Cartesian coordinates; (c) shot-profile migration in tilted coordinates with tilting angle $\theta = -35^\circ$	101
3.35	Phase-encoded source migration in tilted coordinates for the dataset with 3 single-trace shots: (a) 3 phase-encoded sources with $\Delta p = 0.0003$ s/m and (b) 65 phase-encoded sources with $\Delta p = 0.000015$. . .	102
3.36	Image of BP velocity benchmark with shot interval of 500 m: (a) phase-encoded source migration in vertical Cartesian coordinates, (b) phase-encoded source migration in tilted coordinates, and (c) reverse-time migration.	104
4.1	A plane-wave source, its azimuth ϕ , take-off angle θ , and propagation-direction vector $\mathbf{q} = (q_x, q_y, q_z)$	113
4.2	Rotation about the axis z by ϕ	114
4.3	Rotation about the axis y_1 by θ	114
4.4	A plane-wave source and its coordinates for imaging the salt body. The original vertical Cartesian coordinate system is (x, y, z) , and (x_2, y_2, z_2) is the new tilted coordinate system. The dashed lines with arrows are the source and receiver rays of the plane-wave source. The extrapolation direction, the z_2 axis, in the tilted coordinate system, is close to the propagation direction of the plane-wave source.	115
4.5	The dots represent all possible plane-wave sources. The circles are contours related to their take-off angles; the smallest circle represents plane-wave sources with a take-off angle of 15° . The radial lines show the contours of azimuth angles. All possible plane-wave sources are divided into small cells. The plane-wave sources in any given cell have a similar take-off and azimuth angle and share a coordinate system defined by the central point in the cell.	116

4.6	Vertical velocity model of the field dataset. The salt body is not complex, but its flanks are steep.	119
4.7	The anisotropy parameter ε of the field dataset. The energy illuminating the salt flanks travels through the anisotropic sediments.	120
4.8	The anisotropy parameter δ	120
4.9	The vertical velocity model used for migration. The salt body is filled with the sediment velocity.	121
4.10	The image obtained by 3D plane-wave migration in tilted coordinates using the velocity with sediment flooding.	122
4.11	The image obtained by 3D plane-wave migration in vertical Cartesian coordinates using the velocity with sediment flooding.	123
4.12	A depth slice of the images: (a) 3D plane-wave migration in tilted coordinates; (b) 3D plane-wave migration in vertical Cartesian coordinates.	124
4.13	An inline section of the images: (a) 3D plane-wave migration in tilted coordinates; (b) 3D plane-wave migration in vertical Cartesian coordinates.	125
4.14	An inline section of the images: (a) 3D plane-wave migration in tilted coordinates; (b) 3D plane-wave migration in vertical Cartesian coordinates.	126
4.15	A cross-line section of the images: (a) 3D plane-wave migration in tilted coordinates; (b) 3D plane-wave migration in vertical Cartesian coordinates.	127
4.16	A cross-line section of the images: (a) 3D plane-wave migration in tilted coordinates; (b) 3D plane-wave migration in vertical Cartesian coordinates.	128

5.1	Horizontal subsurface offset for a horizontal reflector (a) and steep reflector (b). S and R are end points of source and receiver rays, respectively. Angle θ is the opening angle and α is the dip of the steep reflector. Given an opening angle θ , the steep reflector needs a much larger subsurface offset than the horizontal reflector to construct the angle gather.	134
5.2	Geometry of geologic offset and a general-direction offset.	138
5.3	Angle-domain CIGs with the true velocity: (a) horizontal reflector; (b) dipping reflector; (c) vertical reflector.	140
5.4	Angle-domain CIGs with too low migration velocity: (a) horizontal reflector; (b) dipping reflector; (c) vertical reflector.	141
5.5	Geometric relation linking the shift in normal direction, Δn , the horizontal shift, Δx and the vertical shift, Δz	143
5.6	Velocity model of the BP velocity Benchmark.	144
5.7	Image obtained by plane-wave migration in tilted coordinates. Both a steep salt flank and nearly horizontal sediments are present in this area.	145
5.8	Horizontal offset-domain CIGs obtained by reverse-time migration with the true velocity. (a) For relatively horizontal sediments, the energy focuses well at zero offset; (b) For steep salt flanks, the energy leaks to far offsets and the frequency is low.	146
5.9	Vertical offset-domain CIGs obtained by reverse-time migration with the true velocity. For the steep salt flank at $x = 33.2$ km, the energy focuses well at zero offset. For the nearly horizontal sediments at $x = 24.5$ km, the energy leaks to far offsets.	147

5.10	Angle-domain CIGs from horizontal offset CIGs obtained by reverse-time migration with the true velocity. (a) For the nearly horizontal sediments at $x = 23$ km, the gathers are flat except for multiples. (b) For the steep salt flank at 33.2 km, the gathers are smeared because of the horizontal-offset stretch.	147
5.11	Angle-domain CIGs from vertical offset CIGs obtained by reverse-time migration with the true velocity. The CIGs of the sediments at $x = 24.5$ km are smeared, and the CIGs for the salt flank are at the same horizontal location for all angles.	148
5.12	Angle-domain CIGs from horizontal offset CIGs obtained by reverse-time migration with the velocity underestimated by 3 percent. (a) For the nearly horizontal sediments at $x = 23$ km, the gathers show reasonable curvature. (b) For the steep salt flank at $x = 33.2$ km, the gather is a little smeared. The moveout is not reasonable, given the 3 percent velocity error.	148
5.13	Angle-domain CIGs from vertical offset CIGs obtained by reverse-time migration with the velocity underestimated by 3 percent. The gather of the salt flank at $x = 33$ km shows reasonable moveout. The gathers of the sediments at $x = 30.5$ km look smeared.	149
5.14	Angle-domain CIG cube obtained by reverse-time migration with the true velocity.	150
5.15	Angle-domain CIG cube obtained by plane-wave migration in tilted coordinates with the true velocity.	150
5.16	Stack images from angle-domain CIGs with the true velocity: (a) reverse-time migration; (b) plane-wave migration in tilted coordinates.	151

5.17	Angle-domain CIGs with the velocity underestimated by 3 percent:	
	(a) Vertical view of angle-domain CIGs obtained by reverse-time migration at $x = 32.6$ km.	
	(b) Vertical view of angle-domain CIGs obtained by plane-wave migration in tilted coordinates at $x = 32.6$ km.	
	(c) Normal-direction view of angle-domain CIGs obtained by reverse-time migration at $x = 32.6$ km, $z = 4.4$ km.	
	(d) Normal-direction view of angle-domain CIGs obtained by plane-wave migration in tilted coordinates at $x = 32.6$ km, $z = 4.4$ km.	153
5.18	Dip-dependent RMO for velocity ratio parameters ρ ranging from 0.93 to 1 for an image point on the salt flank. The vertical axis is the direction normal to the apparent dip, and the horizontal axis is the opening angle. The apparent dip is about 70°	154
5.19	Semblance for an image point on a steep reflector with an apparent dip of 70°	155

Chapter 1

Introduction

During the past decade, *seismic imaging* based on wave equations has become practical in oil industry. One of the most important steps of seismic imaging is to simulate the source and receiver wave propagation in the subsurface. It would be ideal if we could simulate the physical processes of wave propagation using computers in exactly the same way that they occur in the Earth. Simplifying assumptions, however, are always required because of limited computing power and a limited ability to estimate parameters of the Earth from the recorded surface data. These assumptions are either about the model of the Earth or about the physical process of wave propagation. Two assumptions usually made in today's wave-equation seismic imaging are that the Earth is isotropic and that waves propagate only downward from the source and upward to the receiver. These assumptions lead to problems in imaging of steep reflectors such as salt flanks and faults. The goal of this thesis is to obtain the accurate image of steep reflectors in anisotropic media using one-way wavefield extrapolation.

PROBLEM DESCRIPTION

It is crucial to know the accurate position of salt boundaries and faults in seismic exploration in complex areas such as the Gulf of Mexico. First, salt flanks and faults serve as potential seals for oil or gas reservoirs. Hydrocarbons migrate laterally and

vertically along porous and permeable sediments. A hydrocarbon reservoir trap forms where seals prevent the escape of hydrocarbon so that hydrocarbons accumulate. Faults potentially cause fault traps, and salt traps usually form where sedimentary beddings tilt during the uplifting of salt bodies. Also, the propagation velocities on the opposite sides of salt boundaries or faults are often highly different. Therefore, it is important to image salt boundaries and faults accurately for further velocity estimation.

Faults and salt flanks are often steep, and some salt flanks overhang. The ray paths of waves illuminating steep reflectors differ greatly from those illuminating near-horizontal reflectors. Figure 1.1 compares waves illuminating a horizontal reflector with those illuminating a steep reflector. The angle θ is the opening angle, α the dip of the reflector, S the source location, and R the receiver location. Near-horizontal reflectors are usually illuminated by waves that travel in a direction that is less than 40° from the vertical, while steep reflectors are illuminated by waves that partly propagate nearly horizontally or even overturn. *Downward continuation* (Claerbout, 1985), which is based on one-way wave propagation, extrapolates wavefields vertically and cannot accurately model waves that propagate nearly horizontally. It also filters out overturned waves, which travel downward over a portion of their path and upward over another portion. As a result, it is difficult to image steep reflectors by imaging methods based on downward continuation.

A medium is anisotropic if its properties change with the direction. Otherwise, the medium is isotropic. In seismic imaging, anisotropy usually means that the velocity of wave propagation changes with the propagation direction. Usually, reflections from reflectors with gentle dip are used for velocity estimation. Therefore, most waves used in velocity estimation travel in a direction that is less than 40° from the vertical. If anisotropy is present in the subsurface, the velocity in the near-horizontal direction differs greatly from that in the nearly vertical. For accurate imaging of steep reflectors with the velocity that is estimated using reflections from near-horizontal reflectors, it is important to include anisotropy in the wavefield extrapolation.

Figure 1.2 shows an image of reflectors in the subsurface overlaid with the model.

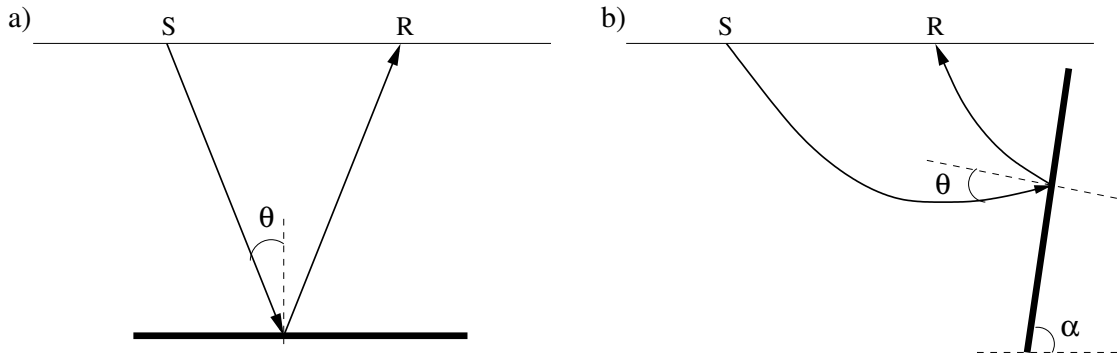


Figure 1.1: Comparison of waves illuminating horizontal (a) and steep (b) reflectors. The angle θ is the opening angle, α is the dip angle of the reflector, S is the source location, and R is the receiver location. Waves illuminating a horizontal reflector usually travel in a direction that is less than 40° from the vertical, while those illuminating steep reflectors have a portion of wave path that is almost horizontal. intro/. wavepath

The image is obtained by a imaging method based on the isotropic downward continuation. Although ignoring anisotropy in imaging does not cause serious problems for reflectors with mild dip, steep reflectors (such at “A” and “B”) are imaged at incorrect positions. Also, because downward continuation cannot propagate nearly horizontal waves accurately, the steep salt flank at “C” is lost.

ISOTROPIC OR ANISOTROPIC MEDIA

Although anisotropy was reported in exploration seismology in the 1930s (McCollum and Snell, 1932), it did not play a significant role in seismic imaging until the 1980s. Until now, the transverse isotropic (TI) model, which is rotationally symmetric about an axis, has been the one most commonly used in seismic imaging, even though anisotropy in the subsurface can be much more complicated. Because TI model is the simplest anisotropy model in theory and most practical for computation for seismic data, and it is a reasonable approximation for much of the sedimentary layers in the subsurface. The wave propagation in the transverse plane of a TI medium is isotropic. Postma (1955) and Helbig (1956) develop theory showing that a sequence of isotropic

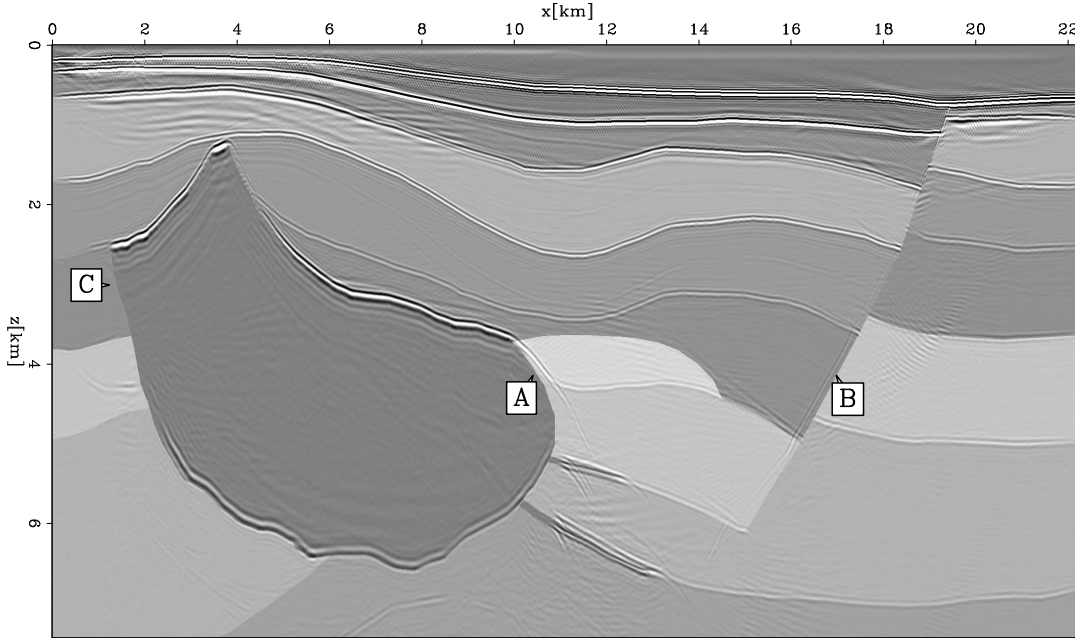


Figure 1.2: Steep reflectors are not well imaged with imaging methods based on the isotropic downward continuation. intro/. isonotilteps

layers on a scale much shorter than the wavelength leads to an anisotropic medium. If the symmetry axis of the medium is vertical, the medium is said to be vertical TI (VTI). A VTI medium is commonly formed because of thin bedding of finely spaced isotropic or VTI layers, such as deposits of shales. A VTI medium changes to a general tilted TI medium if layers become dipping.

For P-waves, a homogeneous TI medium is described by the direction of its symmetry axis, the velocity along its symmetry axis, v_{p0} , and two dimensionless anisotropy parameters, ε and δ , defined by Thomsen (1986):

$$\varepsilon = \frac{C_{11} - C_{33}}{2C_{33}}, \quad (1.1)$$

$$\delta = \frac{(C_{11} + C_{44})^2 - (C_{33} - C_{44})^2}{2C_{33}(C_{33} - C_{44})}, \quad (1.2)$$

where C_{ij} are the elastic moduli. Comparisons of wavefronts in Figure 1.3 show the

influence of the two anisotropy parameters, ε and δ , on wave propagation in VTI media. The wavefronts here are propagated from a point source at $x = 0, z = 0$ in a medium with a vertical velocity of 2000 m/s. The traveltime from the source to the wavefronts is $t = 1$ s. The solid line is the wavefront propagated in an isotropic medium; the dashed line is the wavefront propagated in a VTI medium with $\varepsilon = 0.2$ and $\delta = 0.2$; and the dotted line is the wavefront propagated in a VTI medium with $\varepsilon = 0.2$ and $\delta = -0.2$. Figure 1.3 shows that a negative δ makes the P-wave in the near-vertical direction travel slower than its isotropic counterpart, while a positive δ makes the P-wave in near-vertical direction travel faster. In contrast, the positive ε leads to advanced wavefronts in the near-horizontal direction.

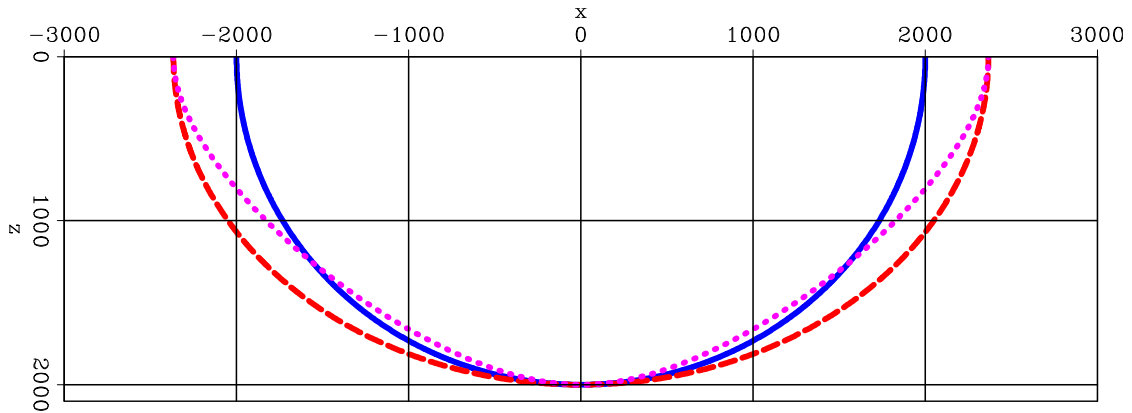


Figure 1.3: Comparison of wavefronts propagated from a point source at $x = 0, z = 0$ in isotropic and VTI media: the solid line is the wavefront propagated in an isotropic medium; the dashed line is the wavefront propagated in a VTI medium with $\varepsilon = 0.2$ and $\delta = 0.2$; and dotted line is the wavefront propagated in a VTI medium with $\varepsilon = 0.2$ and $\delta = -0.2$. The vertical velocity of the medium is 2000 m/s in all three cases, and the traveltime from the point source to the wavefronts is 1 s.

intro/. vtiwavefronts

Anisotropy can be incorporated in wave propagation by solving the elastic wave equation. It is computationally expensive, however, to solve an elastic wave equation, and, more important, it is almost impossible to obtain all the parameters required by the elastic wave equation from the recorded surface data alone. That is one of the reasons why the acoustic wave equation is predominantly used in seismic imaging, although it is well known that the Earth is not an acoustic medium. Simulating

the wave propagation in an anisotropic medium using the acoustic wave equation with the velocity independent of direction, however, leads to kinematic errors. That is why ignoring the anisotropy causes serious problems in imaging steep reflectors. Therefore, it is necessary to incorporate anisotropy into the acoustic wave equation to propagate waves accurately in anisotropic media.

ONE-WAY OR TWO-WAY WAVE PROPAGATION

Propagation of waves in all directions can be well simulated by solving the two-way wave equation. For an acoustic medium, the two-way wave equation is as follows:

$$\frac{1}{v^2} \frac{\partial^2}{\partial t^2} P = \left(\frac{\partial^2}{\partial x^2} + \frac{\partial^2}{\partial y^2} + \frac{\partial^2}{\partial z^2} \right) P, \quad (1.3)$$

where $P = P(x, y, z, t)$ is the wavefield field in the time-space domain, $v = v(x, y, z)$ is the velocity of the medium, x , y , and z are the spatial coordinates, and t is travelttime. Migrations based on the two-way wave equation are usually referred to as *reverse-time migration* (Whitmore, 1983; Baysal et al., 1983; McMechan, 1983; Biondi and Shan, 2002). In that process, the source wavefield is extrapolated forward along the t -axis, using an impulse in space at the source location as the initial condition. The receiver wavefield is extrapolated backward along the t -axis, using the recorded surface data as the boundary condition. The image of the subsurface is constructed by using cross-correlation to locate events where source and receiver wavefields are coincident in both spatial location and time (Claerbout, 1971).

Ever since Claerbout (1971) proposed propagating waves using the 15° equation, the one-way wave equation has been extensively used in seismic imaging. The one-way wave equation applied in seismic imaging is usually in Cartesian coordinates oriented in the vertical direction:

$$\frac{v}{\omega} \frac{\partial}{\partial z} P = \pm i \sqrt{1 + \left(\frac{v}{\omega} \frac{\partial}{\partial x} \right)^2 + \left(\frac{v}{\omega} \frac{\partial}{\partial y} \right)^2} P, \quad (1.4)$$

where $i = \sqrt{-1}$, ω is the circular frequency, $v = (x, y, z)$ is the velocity, and $P = P(x, y, z, \omega)$ is the wavefield in the frequency-space domain. Equation 1.4 is the down-going one-way equation for the negative sign on the right side and up-going for the positive sign. Migrations based on the one-way wave equation are referred to as *downward-continuation migration* (Claerbout, 1985). In this thesis, I call it *conventional* one-way wave-equation migration. There are two types of downward-continuation migration: shot-profile migration and source-receiver migration (Claerbout, 1985), which are equivalent to each other (Biondi, 2003; Shan and Zhang, 2003). Wavefields are usually extrapolated along the z -axis (vertical direction) in the frequency domain. The source wavefield is extrapolated by solving the down-going one-way wave equation, and the receiver wavefield is extrapolated by solving the up-going one-way wave equation. As with reverse-time migration, the image is constructed by identifying events in source and receiver wavefields that are coincident in both spatial location and time.

In contrast to the two-way wave equation, the one-way wave equation intrinsically has a preference for the propagation direction of waves. First, in downward continuation, only down-going waves are allowed to propagate in the source wavefield, and only up-going waves are allowed to propagate in the receiver wavefield. Overturned energy is filtered out during the wavefield extrapolation. Second, waves along the extrapolation direction of the one-way wave equation, which is the vertical direction in conventional one-way wave-equation migration, are propagated most accurately. Accuracy deteriorates as the direction of propagation departs increasingly from the vertical. For a homogeneous medium, the one-way wave equation can be solved by the phase-shift method (Gazdag, 1978) in the wavenumber domain, and it can accurately model waves propagating in directions that are as large as almost 90° from the vertical. But for a medium with strong lateral variation, approximation must be made for the square-root operator to solve equation 1.4 numerically. Many algorithms, such as the implicit finite-difference method (Claerbout, 1971; Lee and Suh, 1985), Fourier finite-difference method (Ristow and Ruhl, 1994; Biondi, 2002), general screen propagator (de Hoop, 1996; Huang and Wu, 1996), and explicit finite-difference method (Holberg, 1988; Blacquiere et al., 1989; Hale, 1991b,a), have been developed to solve

the one-way wave equation in laterally varying media, but for all of them, it is difficult to accurately propagate waves along nearly horizontal directions.

CONTRIBUTIONS

In this thesis, in order to image steep reflectors with good accuracy, I incorporate anisotropy into wave propagation, and make the extrapolation direction close to the propagation direction by plane-wave migration in tilted coordinates. The main contributions are the following:

- I develop new one-way wavefield extrapolation schemes for VTI media, optimized implicit finite-difference and Fourier finite-difference schemes, which allow efficiently and accurately propagating waves in laterally varying VTI media.
- I develop a new one-way wavefield extrapolation scheme for tilted TI media, optimized implicit finite-difference schemes, which allows accurately propagating waves in laterally varying tilted TI media.
- I develop a new migration algorithm, plane-wave migration in tilted coordinates. It uses one-way wavefield extrapolation, but it can handle near-horizontal and overturned waves, and image steep reflectors efficiently.
- I develop a new method to generate reliable angle-domain common-image gathers for steep reflectors. These gathers are useful for further velocity estimation.
- I derive a new residual-moveout scheme, which takes the dip of reflectors into account and estimates the curvature of angle-domain common-image gathers accurately.

THESIS OVERVIEW

There are four main chapters in this thesis. Chapter 2 is about the wavefield extrapolation in anisotropic media, chapters 3 and 4 are about plane-wave migration in tilted

coordinates, and chapter 5 is about angle-domain common-image gathers for steep reflectors.

Wavefield extrapolation in anisotropic media

In chapter 2, I design implicit finite-difference and Fourier finite-difference wavefield extrapolation operators for VTI and tilted TI media. I approximate the dispersion relation of TI media with a rational function, and estimate coefficients of the rational function by weighted least-squares optimization. I design implicit finite-difference and Fourier finite-difference schemes based on the estimated rational function. For a medium with lateral variation, the coefficients of finite-difference schemes laterally vary, and they are obtained by looking up values in a table computed before doing wavefield extrapolation. I show impulse responses and synthetic data examples. The wavefield-extrapolation operators developed in this chapter are used in migrations in chapters 3, 4 and 5.

Plane-wave migration in tilted coordinates: Theory and synthetic data examples

In chapter 3, I describe the basic idea of plane-wave migration in tilted coordinates in 2D. I convert the recorded surface data to plane-wave source data by slant-stacking processing, and migrate each plane-wave source dataset independently in tilted coordinate systems with the extrapolation direction determined by the source plane-wave direction at the surface. The extrapolation direction is close to the propagation direction in the tilted coordinates, allowing the nearly horizontal waves to be accurately propagated, and plane-wave migration in tilted coordinates to image steep reflectors accurately. I demonstrate the technique using impulse responses and synthetic data examples for both isotropic and anisotropic media.

Plane-wave migration in tilted coordinates: A 3-D field-data example

In chapter 4, I extend plane-wave migration in tilted coordinates to 3D. I present 3D plane-wave migration in tilted coordinates and conical wave migration in tilted coordinates. I discuss how to design the coordinate system for a plane-wave source in 3D, and how to implement plane-wave migration in tilted coordinates efficiently. I show a 3-D field-dataset example to demonstrate that 3D plane-wave migration in tilted coordinates is an effective tool for imaging steep salt flanks and faults in anisotropic media.

Angle-domain common-image gathers for steep reflectors

In chapter 5, I present a method for constructing reliable angle-domain common-image gathers (gathers showing reflectivity as a function of opening angle) for steep reflectors, and a residual moveout algorithm, called *dip-dependent residual moveout*, for steep reflectors. In the method, I generate subsurface offset-domain common-image gathers by plane-wave migration in tilted coordinates, and transform offset-domain common-image gathers to angle-domain common-image gathers by slant-stacking. The direction of the subsurface offset is close to the dip direction of the reflector, and the extrapolation direction is close the wave propagation direction, so this method is robust for both nearly horizontal and steep reflectors. Dip-dependent residual moveout accurately estimates the curvature of angle-domain common-image gathers of steep reflectors by shifting the image point along the normal direction of the reflector.

Chapter 2

Wavefield extrapolation in anisotropic media

INTRODUCTION

The Earth is heterogeneous and anisotropic, meaning that the propagation velocity of seismic waves depends not only on their spatial location, but also on their propagation direction. Much research has addressed heterogeneity in wavefield extrapolation (Claerbout, 1971; Holberg, 1988; Ristow and Ruhl, 1994; de Hoop, 1996; Huang and Wu, 1996), but fewer attempts have been made to incorporate anisotropy in wavefield extrapolation (Rousseau, 1997; Zhang et al., 2001a; Ristow, 1999). Anisotropy is usually neglected for most seismic processing; however, if anisotropy present in the subsurface is neglected in migration, reflectors are imaged at incorrect positions (Larner and Cohen, 1993), or even worse, defocused. Imaging in a general anisotropic medium is still a challenging problem. TI model, the simplest form of anisotropy, is a reasonable approximation for much of the Earth's subsurface. In this chapter, I derive one-way acoustic wave equations for VTI and general TI media, and show how to solve them by using implicit finite-difference (FD) and Fourier finite-difference (FFD) schemes, both of which I use for migrations in later chapters.

Compared to that of an isotropic medium, the dispersion relation of a TI medium is much more complicated, because the propagation velocity depends on the phase angle. As a result, generalized phase-shift methods (Rousseau, 1997; Ferguson and Margrave, 1998) or explicit convolution methods (Uzcategui, 1995; Zhang et al., 2001a,b; Baumstein and Anderson, 2003; Shan and Biondi, 2005; Ren et al., 2005) are usually used in anisotropic wavefield extrapolation, because the complex dispersion relation does not increase the complexity of these algorithms. Phase-shift with interpolation for TI media, however, requires a large number of reference wavefields, because there are several anisotropy parameters, in addition to the vertical velocity, and none might be correlated with others spatially. Explicit convolution methods do not guarantee stability even for homogeneous media and also require long convolution filters to achieve good accuracy. The additional anisotropy parameters also lead to much larger coefficient tables than are required for isotropic media. In general tilted TI media, the dispersion relation function in vertical Cartesian coordinates is not circular symmetric. For 3D media, the McClellan transformation (Hale, 1991a), which requires circular symmetry of the dispersion relation, therefore can not be applied. As a consequence, a 2D convolution operator must be applied on each grid point, which is prohibitively expensive to achieve reasonable accuracy.

The implicit FD method has been one of the most attractive migration methods for isotropic media. It can handle lateral variation naturally and is stable for most practical applications. To design implicit FD schemes, the dispersion relation is approximated with a rational function. Traditional FD methods, such as the 15° equation (Claerbout, 1971) and the 45° equation (Claerbout, 1985), obtain the coefficients of the rational function through analytical Padé expansion analysis or rational factorization. Lee and Suh (1985) numerically estimate coefficients of the rational function by least-square optimization to achieve a scheme accurate to 65° with the same cost as that of the 45° equation. Designing an implicit FD wavefield extrapolation scheme for TI media through analytical Padé expansion analysis is much more difficult because of the complex dispersion relation. Ristow (1999) designs an implicit FD scheme for VTI media based on Padé expansion analysis under the weak-anisotropy assumption and suggest an optimization procedure for general VTI media.

To improve accuracy, Liu et al. (2005) apply a phase-correction operator (Li, 1991) after using the FD operator.

The FFD method (Ristow and Ruhl, 1994), a combination of phase-shift and FD, is widely in the hydrocarbon exploration industry applied for isotropic media. FFD achieves good accuracy where the actual velocity is close to the reference velocity and handles lateral velocity variation using the FD correction. Ristow and Ruhl (1994) suggest that its coefficients can be derived through Taylor series analysis or by an optimization procedure. Zhang et al. (2005a); Fei and Liner (2006) develop FFD migration for VTI media based on Taylor series and Padé expansion analysis.

Here, I develop implicit FD and FFD wavefield-extrapolation schemes for TI media not by Taylor series and Padé expansion, but instead by numerical function fitting. I approximate the dispersion relation with a rational function and estimate its coefficients by weighted least-square optimization (Thorbecke et al., 2004). For laterally varying TI media, the coefficients of the rational function are pre-calculated and stored in a table before wavefield extrapolation. The coefficients for FD are found from the table by table look-up during the wavefield extrapolation.

I first show how to design implicit FD and FFD wavefield-extrapolation schemes for VTI media, and then discuss the implicit FD scheme for general tilted TI media.

IMPLICIT FD WAVEFIELD EXTRAPOLATION IN VTI MEDIA

Although the dispersion relation for VTI media is much more complicated than that for isotropic media, the procedure for designing the implicit FD scheme is almost the same. Therefore, I start this section with a review of implicit FD for isotropic media.

Implicit FD for isotropic media

The dispersion relation for isotropic media is as follows:

$$s_z^2 + s_r^2 = 1, \quad (2.1)$$

where $s_z = \frac{vk_z}{\omega}$, $s_r = \frac{v\sqrt{k_x^2+k_y^2}}{\omega}$, ω is the circular frequency, $v = v(x, y, z)$ is the velocity of the medium, k_x , k_y and k_z are wavenumbers corresponding to the x , y and z axes, respectively. By inverse Fourier transforming on equation 2.1, we can obtain the two-way acoustic equation 1.3. Given s_r , we can calculate s_z analytically from the following equation:

$$s_z = \pm\sqrt{1 - s_r^2}. \quad (2.2)$$

By inverse Fourier transforming on equation 2.2, we can obtain the up-going and down-going one-way wave equations 1.4. To derive FD schemes for one-way wave equations, we approximate the square-root operator on the right side of equation 2.2 with a rational function as follows:

$$\sqrt{1 - s_r^2} \approx 1.0 - \frac{\sum_{i=1}^n \alpha_i (s_r^2)^i}{1 - \sum_{i=1}^n \beta_i (s_r^2)^i}, \quad (2.3)$$

with $2n$ the order of the approximation. The coefficients α_i and β_i , $i = 1, \dots, n$ can be obtained by analytical Padé expansion or rational factorization. For instance, the second-order approximation ($n = 1$) is the classic 45° equation,

$$\sqrt{1 - s_r^2} \approx 1.0 - \frac{\frac{1}{2}s_r^2}{1 - \frac{1}{4}s_r^2}. \quad (2.4)$$

The coefficients of the rational function α_i and β_i , $i = 1, \dots, n$, can also be estimated by least-square optimization, which leads to more accurate FD schemes. For instance, the 65° equation has the same computational cost as the 45° equation but it is more accurate (Lee and Suh, 1985).

Dispersion relation of VTI media

A VTI medium has a vertical axis of rotational symmetry. The phase velocity depends on the vertical velocity of the medium and the angle between the propagation direction and the symmetry axis. In a VTI medium, the phase velocity of qP- and qSV-waves in Thomsen's notation can be expressed as follows (Tsvankin, 1996):

$$\frac{v^2(\theta)}{v_{p0}^2} = 1 + \varepsilon \sin^2 \theta - \frac{f}{2} \pm \frac{f}{2} \sqrt{\left(1 + \frac{2\varepsilon \sin^2 \theta}{f}\right)^2 - \frac{2(\varepsilon - \delta) \sin^2 2\theta}{f}}, \quad (2.5)$$

where θ is the phase angle of the wave, which is the angle between the propagation direction and the vertical axis; $f = 1 - (v_{s0}/v_{p0})^2$; v_{p0} and v_{s0} are the qP- and qSV-wave velocities in the vertical, respectively. In equation 2.5, $v(\theta)$ is qP-wave phase-velocity when the sign in front of the square root is positive, and is the qSV-wave phase velocity otherwise.

For plane-wave propagation, the phase angle, θ , and the wavenumbers, k_x , k_y and k_z , are linked by the relations,

$$\sin \theta = \frac{v(\theta)k_r}{\omega}, \quad \text{and} \quad \cos \theta = \frac{v(\theta)k_z}{\omega}, \quad (2.6)$$

where ω is the temporal frequency, and $k_r = \sqrt{k_x^2 + k_y^2}$. By squaring equation 2.5 and substituting equation 2.6 into 2.5, we can obtain the dispersion relation for VTI media,

$$d_4 s_z^4 + d_2 s_z^2 + d_0 = 0, \quad (2.7)$$

where $s_z = \frac{k_z v_{p0}}{\omega}$, and the coefficients d_0 , d_2 , and d_4 are,

$$\begin{aligned} d_0 &= (2 + 2\varepsilon - f)s_r^2 - 1 - [(1 - f)(1 + 2\varepsilon)]s_r^4, \\ d_2 &= [-2(1 - f)(1 + \varepsilon) - 2f(\varepsilon - \delta)]s_r^2 + (2 - f), \\ d_4 &= f - 1, \end{aligned}$$

with $s_r = \frac{k_r v_{p0}}{\omega}$. The dispersion relation for VTI media (equation 2.7) is a quartic equation with four roots: two represent up-going and down-going qP-waves and two

represent up-going and down-going qSV-waves. In this chapter, I discuss wavefield extrapolation only for qP-waves. Wavefield extrapolation for qSV-waves could face more complication associated with singularities in the dispersion relation.

Alkhalifah (1998) shows that the contribution of v_{s_0} to the phase velocity of qP-waves is very limited for practical applications. Assuming that the qSV-wave velocity is much smaller than the qP-wave velocity, we have $f \approx 1$ and the dispersion relation for qP-waves (equation 2.7) simplifies to

$$s_z^2 = \frac{1 - (1 + 2\varepsilon)s_r^2}{1 - 2(\varepsilon - \delta)s_r^2}. \quad (2.8)$$

From equation 2.8, by the inverse Fourier transform (replacing s_z^2 with $-v_{p_0}^2 \frac{\partial^2}{\partial z^2}$, and s_r^2 with $-v_{p_0}^2 \left(\frac{\partial^2}{\partial x^2} + \frac{\partial^2}{\partial y^2} \right)$), we can obtain the two-way acoustic wave equation for VTI media:

$$\left[\frac{\partial^4}{\partial z^2 \partial t^2} - 2(\varepsilon - \delta)v_{p_0}^2 \left(\frac{\partial^4}{\partial z^2 \partial x^2} + \frac{\partial^4}{\partial z^2 \partial y^2} \right) \right] P = \left[\frac{1}{v_{p_0}^2} \frac{\partial^4}{\partial t^4} - (1 + 2\varepsilon) \left(\frac{\partial^4}{\partial t^2 \partial x^2} + \frac{\partial^4}{\partial t^2 \partial y^2} \right) \right] P, \quad (2.9)$$

where $P = (x, y, z, t)$ is the wavefield in the space-time domain. As with isotropic media, we obtain up-going and down-going modes of the dispersion relation by solving s_z as a function of s_r from equation 2.8:

$$s_z(\varepsilon, \delta; s_r) = \pm \sqrt{\frac{1 - (1 + 2\varepsilon)s_r^2}{1 - 2(\varepsilon - \delta)s_r^2}}. \quad (2.10)$$

By the inverse Fourier transform (replacing s_z with $i \frac{v_{p_0}^2}{\omega} \frac{\partial}{\partial z}$, and s_r^2 with $-\frac{v_{p_0}^2}{\omega^2} \left(\frac{\partial^2}{\partial x^2} + \frac{\partial^2}{\partial y^2} \right)$), we can obtain up-going and down-going one-way acoustic wave equations for VTI media

$$\frac{\partial}{\partial z} P = \pm i \frac{\omega}{v_{p_0}} \sqrt{\frac{1 + (1 + 2\varepsilon) \frac{v_{p_0}^2}{\omega^2} \left(\frac{\partial^2}{\partial x^2} + \frac{\partial^2}{\partial y^2} \right)}{1 + 2(\varepsilon - \delta) \frac{v_{p_0}^2}{\omega^2} \left(\frac{\partial^2}{\partial x^2} + \frac{\partial^2}{\partial y^2} \right)}} P, \quad (2.11)$$

where $P = P(x, y, z, \omega)$ is the wavefield in the space-frequency domain.

Dispersion-relation approximation by function fitting

For a weak VTI medium (Thomsen, 1986), Ristow (1999) designs FD schemes based on the dispersion relation, $s_z^{weak}(\varepsilon, \delta, s_x)$, derived from the linearized phase velocity equation

$$\frac{v^2(\theta)}{v_{p0}^2} = 1 + 2\delta \sin^2 \theta \cos^2 \theta + 2\varepsilon \sin^4 \theta, \quad (2.12)$$

and equation 2.6. They approximate the dispersion relation s_z^{weak} with a rational function

$$s_z^{weak} \approx 1 - \sum_{i=1}^n \frac{a_i (s_r^2)^i}{1 - b_i (s_r^2)^i}, \quad (2.13)$$

and obtain coefficients, a_i and b_i , $i = 1, \dots, n$, analytically through Taylor-series and Padé-expansion analysis. For the second-order approximation ($n=1$), they suggest

$$a_1 = 0.5(1 + 2\delta), \quad (2.14)$$

$$b_1 = \frac{2(\varepsilon - \delta)}{1 + 2\delta} + 0.25(1 + 2\delta). \quad (2.15)$$

If $\varepsilon = 0$ and $\delta = 0$, equation 2.13 becomes the classic 45° equation for isotropic media. Notice that the coefficients α_1 and β_1 are functions of the anisotropy parameters ε and δ . Therefore, unlike in isotropic media, the FD coefficients α_1 and β_1 vary laterally in VTI media. For a general VTI medium, Ristow (1999) uses the phase-velocity equation 2.5, and suggest that coefficients a_i and b_i , $i = 1, \dots, n$, can be obtained by optimization. They also claim that the 6th-order FD scheme ($n=3$) by optimization is accurate to 70°.

I design FD schemes based on the dispersion relation 2.10, which is derived without weak anisotropy assumption. The square-root operator on the right side of equation 2.11 is a pseudo-differential operator. In order to design FD schemes for equation 2.11, I approximate the dispersion relation s_z with a rational function,

$$\bar{s}_z(\varepsilon, \delta; s_r) = 1 - \frac{\sum_{i=1}^n \alpha_i (s_r^2)^i}{1 - \sum_{i=1}^n \beta_i (s_r^2)^i}. \quad (2.16)$$

The coefficients of the rational function, α_i and β_i , $i = 1, \dots, n$, can be obtained by Taylor series and Padé expansion analysis. The Taylor series and Padé expansion for s_z as a function of s_r^2 are as follows:

$$s_z(\varepsilon, \delta; s_r) = 1 - \frac{2\delta + 1}{2}s_r^2 - \frac{1}{8}(2\delta + 1)(1 + 8\varepsilon - 6\delta)s_r^4 + \dots, \quad (2.17)$$

$$= 1 - \frac{0.5(2\delta + 1)s_r^2}{1 - (2(\varepsilon - \delta) + 0.25(1 + 2\delta))s_r^2} + \dots. \quad (2.18)$$

Therefore, for the second-order approximation ($n=1$), $\alpha_1 = 0.5(1 + 2\delta)$, $\beta_1 = 2(\varepsilon - \delta) + 0.25(1 + 2\delta)$. Compared to FD coefficients (equations 2.14 and 2.15) derived by Ristow (1999), coefficients α_1 and β_1 are derived without the weak anisotropy assumption.

The coefficients of the rational function can also be estimated by weighted least-square function fitting, which does not require analytical Taylor series and Padé expansion analysis for the dispersion relation. This is especially useful for an anisotropic medium because of its complex dispersion relation. I could use the dispersion relation equation 2.7, given the value of f in the subsurface. But I still use dispersion relation equation 2.10, since equation 2.10 is much simpler than equation 2.7 and kinematically they are almost the same.

To obtain the coefficients α_i and β_i , $i = 1 \dots n$, I set up the following optimization problem:

$$\min \int_0^{S_r} w(s_r) \left(s_z(\varepsilon, \delta; s_r) - 1 + \frac{\sum_{i=1}^n \alpha_i (s_r^2)^i}{1 - \sum_{i=1}^n \beta_i (s_r^2)^2} \right)^2 ds_r, \quad (2.19)$$

where $w(s_r)$ is a weight function, and S_r is determined by the maximal optimization angle ϕ :

$$\tan \phi = \frac{S_r}{\sqrt{\frac{1 - (1 + 2\varepsilon)S_r^2}{1 - 2(\varepsilon - \delta)S_r^2}}}. \quad (2.20)$$

Directly solving the optimization problem, 2.19, needs a non-linear least-square method.

But it can be changed to the following optimization problem,

$$\min \int_0^{S_r} w(s_r) \left[(s_z(\varepsilon, \delta; s_r) - 1) \left(1 - \sum_{i=0}^n \beta_i (s_r^2)^i \right) + \left(\sum_{i=0}^n \alpha_i (s_r^2)^i \right) \right]^2 ds_r, \quad (2.21)$$

which can be solved by an iterative linear least-square method or a direct method such as QR decomposition (Golub and Van Loan, 1996).

With the coefficients α_i and β_i , $i = 1, \dots, n$, estimated from equation 2.21, equation 2.16 can be further split into the low-order rational-function series (Ma, 1981),

$$\bar{s}_z = 1 - \sum_{i=1}^n \frac{a_i s_r^2}{1 - b_i s_r^2}, \quad (2.22)$$

where the coefficients a_i and b_i are calculated from α_i and β_i , $i = 1, \dots, n$.

Figure 2.1 compares the approximate and true dispersion relations for anisotropy parameters ε and δ given by 0.4 and 0.2, respectively. Curve “True” is the true dispersion relation calculated from equation 2.10. Curve “Taylor-weak-2” is the second-order ($n = 1$) approximate dispersion relation obtained by Taylor series and Padé expansion analysis based on weak anisotropy assumption, using the formulas $a_1 = 0.5(1 + 2\delta) = 0.7$ and $b_1 = \frac{2(\varepsilon - \delta)}{1 + 2\delta} + 0.25(1 + 2\delta) = 0.635714$. Curve “Taylor-2” is the second-order ($n = 1$) approximate dispersion relation obtained by Taylor series and Padé expansion analysis for equation 2.10, using the formulas $a_1 = 0.5(1 + 2\delta) = 0.7$ and $b_1 = 2(\varepsilon - \delta) + 0.25(1 + 2\delta) = 0.75$. Curve “Taylor-2” fits the true dispersion relation better than curve “Taylor-weak-2”. Curve “Optimization-2” is the second-order approximate dispersion relation obtained by weighted least-square optimization. The coefficients used for curve “Optimization-2” are $a_1 = 0.664820$ and $b_1 = 0.948380$. For the same order, curve “Optimization-2” fits the true dispersion relation much better than does curve “Taylor-2”. Curve “Optimization-4” is the fourth-order ($n = 2$) approximate dispersion relation obtained by weighted least-square optimization. The coefficients used for curve “Optimization-4” are $a_1 = 0.657870$, $b_1 = 0.857544$, $a_2 = 0.019111$, and $b_2 = 1.723828$. Curve “Optimization-4” fits the true dispersion relation well. The comparison between curves “Optimization-2” and

“Optimization-4” shows that the accuracy of the approximation increases with its order.

The relative dispersion error for the approximate dispersion relation 2.22 is defined as

$$\mu = \frac{\bar{s}_z - s_z}{s_z}. \quad (2.23)$$

Also, for each s_r , the phase angle θ satisfies

$$\tan \theta = \frac{s_r}{s_z}, \quad (2.24)$$

where s_z is given by equation 2.10. We can consider the relative dispersion error, μ , as a function of the phase angle θ . If we accept one percent relative dispersion error, the phase angle where the relative dispersion error exceeds one percent defines the accuracy of the approximation. Figure 2.2 shows the relative dispersion error as a function of the phase angle. As with Figure 2.1, the anisotropy parameters ε and δ are 0.4 and 0.2, respectively. Curve “Taylor-weak-2” is the relative dispersion error of the second-order approximation for the dispersion relation with weak anisotropy assumption using the Taylor-series and Padé expansion analysis. Curve “Taylor-2” is the relative dispersion error of the second-order approximation for the dispersion relation 2.10 using the Taylor-series and Padé expansion analysis. Curve “Optimization-2” is the relative dispersion error of the second-order approximation by least-square optimization. Curve “Optimization-4” is the relative dispersion error of the fourth-order approximation by least-square optimization. The anisotropy parameters used in this example do not satisfy the weak-anisotropy assumption, so it is not surprising that the second-order approximate dispersion relation based on weak anisotropy assumption by Taylor series and Padé expansion analysis is accurate to only 30° . The second-order approximate dispersion relation by optimization is accurate to 60° . The comparison shows that optimization greatly improves the accuracy of the approximate rational dispersion relation. The fourth-order approximate dispersion relation by optimization is accurate to 80° . This is similar to the dispersion error analysis for isotropic media by Lee and Suh (1985).

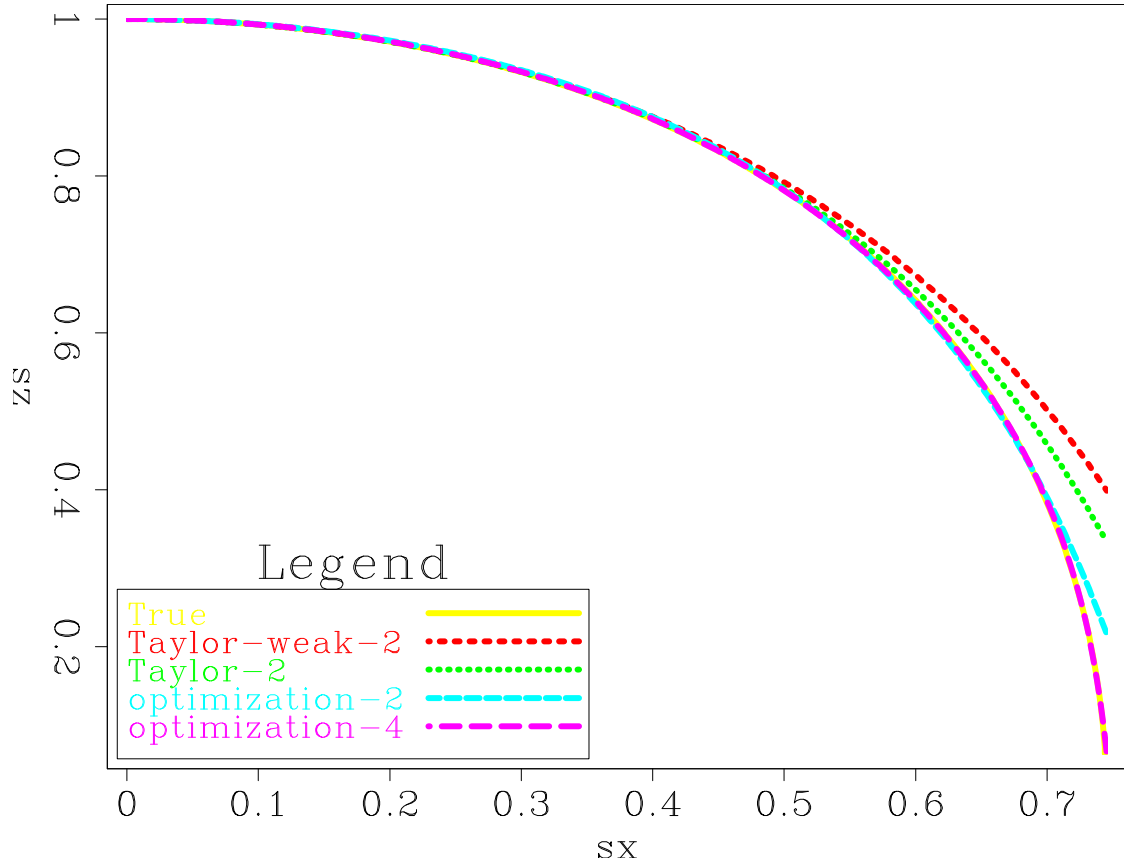


Figure 2.1: Dispersion relation comparison: curve “True” is the true dispersion relation; curve “Taylor-weak-2” is the second-order approximate dispersion relation obtained by Taylor-series and Padé expansion analysis based on weak anisotropy assumption; curve “Taylor-2” is the second-order approximate dispersion relation obtained by Taylor-series and Padé expansion analysis for equation 2.10; curve “Optimization-2” is the second-order approximate dispersion relation obtained by weighted least-square optimization; curve “Optimization-4” is the fourth-order approximate dispersion relation by weighted least-square optimization.

anifd/. vtidispersion

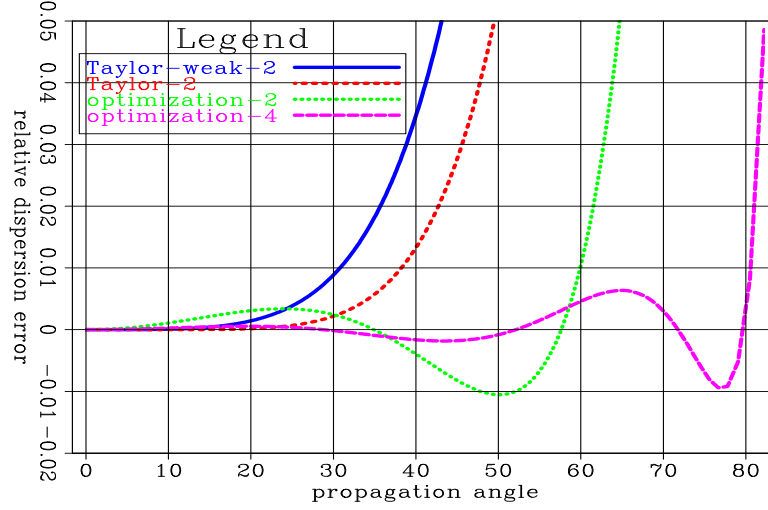


Figure 2.2: Relative dispersion error comparison: curve “Taylor-weak-2” is the relative dispersion error of the second-order approximation by conventional Taylor- and Padé-expansion analysis based on weak anisotropy assumption; curve “Taylor-2” is the relative dispersion error of the second-order approximation by conventional Taylor- and Padé-expansion analysis for equation 2.10; curve “Optimization-2” is the relative dispersion error of the second-order approximation by optimization; curve “Optimization-4” is the relative dispersion error of the fourth-order approximation by optimization. If we accept one percent relative dispersion error, the second-order approximation by Taylor-series and Padé-expansion analysis based on weak anisotropy assumption is accurate to 30° , the second-order approximation by Taylor-series and Padé-expansion analysis using dispersion relation equation 2.10 is accurate to 38° , the second-order approximation by optimization is accurate to 60° and the fourth-order one is accurate to 80° . anifd/. errvti

Table-driven implicit FD migration

By inverse Fourier transform, we can get the corresponding partial differential equation for equation 2.22:

$$\frac{\partial P}{\partial z} = i \frac{\omega}{v_{p0}} + i \frac{\omega}{v_{p0}} \sum_{i=1}^n \frac{a_i \frac{v_{p0}^2}{\omega^2} \left(\frac{\partial^2}{\partial x^2} + \frac{\partial^2}{\partial y^2} \right)}{1 + b_i \frac{v_{p0}^2}{\omega^2} \left(\frac{\partial^2}{\partial x^2} + \frac{\partial^2}{\partial y^2} \right)} P, \quad (2.25)$$

where $P = P(x, y, z, \omega)$ is the wavefield. Equation 2.25 can be solved by cascading. For example, for the second-order approximation ($n = 1$), equation (2.25) is changed to the following cascaded partial differential equations:

$$\frac{\partial}{\partial z} P = i \frac{\omega}{v_{p0}} P, \quad (2.26)$$

$$\frac{\partial}{\partial z} P = i \frac{\omega}{v_{p0}} \frac{a_1 \frac{v_{p0}^2}{\omega^2} (\frac{\partial^2}{\partial x^2} + \frac{\partial^2}{\partial y^2})}{1 + b_1 \frac{v_{p0}^2}{\omega^2} (\frac{\partial^2}{\partial x^2} + \frac{\partial^2}{\partial y^2})} P. \quad (2.27)$$

Equation 2.26 is the thin-lens term (Claerbout, 1985), which is solved by a phase-shift operator in the space domain. Equation 2.27 is solved by the FD method. For isotropic media, a_1 and b_1 are constant. In contrast, for VTI media, a_1 and b_1 are functions of the anisotropy parameters ε and δ , which vary laterally in a laterally varying media. It is too expensive to calculate a_1 and b_1 for each grid point during the wavefield extrapolation. I pre-compute a_1 and b_1 for a range of ε and δ and store them in a table, and then look up a_1 and b_1 in the table during wavefield extrapolation. After inserting a_1 and b_1 into equation 2.27, the FD scheme for VTI media is performed in the same way as that for isotropic media. Therefore, the computational cost of FD schemes for VTI media is the cost of the counterpart for isotropic media plus the cost of table looking-up, which is almost neglectable, compared to the total cost of FD schemes. Therefore, the cost of FD schemes of VTI media is almost the same as the counterpart in isotropic media.

For constant media, Fourier analysis shows the implicit FD operator developed from equation 2.27 is a unitary operator, therefore the FD scheme is stable. For media with strong lateral variation, the bulletproofing theory developed by Godfrey et al. (1979) and Brown (1979) can be applied and the FD scheme is stable.

For 3D propagation, as in isotropic media (Claerbout, 1985), equation 2.27 is split into x and y components as follows:

$$\frac{\partial}{\partial z} P = i \frac{\omega}{v_p} \left[\frac{a_1 \frac{v_p^2}{\omega^2} \frac{\partial^2}{\partial x^2}}{1 + b_1 \frac{v_p^2}{\omega^2} \frac{\partial^2}{\partial x^2}} + \frac{a_1 \frac{v_p^2}{\omega^2} \frac{\partial^2}{\partial y^2}}{1 + b_1 \frac{v_p^2}{\omega^2} \frac{\partial^2}{\partial y^2}} \right] P. \quad (2.28)$$

This two-way splitting causes numerical anisotropy, which can be remedied by a phase-correction filter (Li, 1991) in the frequency and wavenumber domain. For the second-order approximation ($n=1$), the phase-correction operator is

$$P = P e^{i\Delta z k_L}, \quad (2.29)$$

where

$$k_L = \frac{\omega}{v_p^r} \sqrt{\frac{1 - (1 + 2\varepsilon_r) \frac{k_r^2}{(\omega/v_p^r)^2}}{1 - 2(\varepsilon_r - \delta_r) \frac{k_r^2}{(\omega/v_p^r)^2}}} - \frac{\omega}{v_p^r} \left[1 - \frac{a_1^r \left(\frac{\omega}{v_p^r} k_x\right)^2}{1 - b_1^r \left(\frac{\omega}{v_p^r} k_x\right)^2} - \frac{a_1^r \left(\frac{\omega}{v_p^r} k_y\right)^2}{1 - b_1^r \left(\frac{\omega}{v_p^r} k_y\right)^2} \right], \quad (2.30)$$

where v_p^r is the reference vertical velocity, ε_r and δ_r are the reference anisotropy parameters, and a_1^r and b_1^r are the optimized FD coefficients corresponding to the anisotropy parameters ε_r and δ_r . The numerical anisotropy can also be reduced by multi-way splitting instead of two-way splitting (Ristow and Ruhl, 1997).

Impulse responses

Figures 2.3 to 2.5 show impulse responses of the implicit FD for homogeneous VTI media with typical anisotropy parameters. The vertical velocity, used to calculate all the impulse responses, is $v_{p0} = 2000$ m/s and the travel time is $t = 1$ s. I also use theoretical impulse responses (the solid lines in the figures) to calibrate the impulse responses of FD schemes. These theoretical impulse responses are calculated by using the group velocity as a function of group angle for VTI media suggested by Tsvankin (1996). The anisotropy parameters ε and δ used to generate Figure 2.3 are 0.4 and 0.2, respectively. Figure 2.3(a) is the impulse response of the second-order optimized FD scheme with coefficients $a_1 = 0.648202$ and $b_1 = 0.982790$. Figure 2.3(b) is the impulse response of fourth-order optimized FD scheme with coefficients $a_1 = 0.657870$, $b_1 = 0.857544$, $a_2 = 0.019111$ and $b_2 = 1.723828$. The anisotropy parameters ε and δ used to generate Figure 2.4 are 0 and -0.2 , respectively. Figure 2.4(a) shows the impulse response of the second-order optimized FD scheme with

coefficients $a_1 = 0.289754$ and $b_1 = 0.617360$. Figure 2.4(b) is the impulse response of the fourth-order optimized FD scheme with coefficients $a_1 = 0.281395$, $b_1 = 0.560497$, $a_2 = 0.015003$ and $b_2 = 0.948317$. The anisotropy parameters ε and δ used to generate Figure 2.5 are 0.2 and -0.2 , respectively. Figure 2.5(a) is the impulse response of the second-order optimized FD scheme with coefficients $a_1 = 0.287487$ and $b_1 = 1.026222$. Figure 2.5(b) is the impulse response of the fourth-order optimized FD scheme with coefficients $a_1 = 0.282201$, $b_1 = 0.959859$, $a_2 = 0.014668$ and $b_2 = 1.349724$.

Comparisons between the impulse responses and the theoretical curves show the optimized second-order approximation is accurate to about 60° , and the optimized fourth-order approximation is accurate to about 80° . The impulse responses verify the relative-dispersion-relation error analysis in Figure 2.2. Figures 2.3 through 2.5 show that FD schemes for VTI media with different anisotropy parameters have almost the same accuracy. Therefore, the accuracy of FD schemes for VTI media does not depend on the value of anisotropy parameters, ε and δ .

The heart-shape artifacts in all impulse responses are the evanescent waves of the FD wave equation (Claerbout, 1985). They can be attenuated by using a dip filter (Claerbout, 1985) or by fitting the dispersion relation with a rational function having complex coefficients (Yevick and Thomson, 2000).

Synthetic data example

Figure 2.6 shows the vertical velocity and anisotropy parameters for the synthetic dataset. Figure 2.6 (a) shows the vertical velocity of the medium. Figures 2.6 (b) and (c) depict the anisotropy parameters ε and δ of the medium, respectively. The overall structure is not very complicated other than having a salt body surrounded by anisotropic sedimentary layers and a fault plane. The salt flanks and the fault are relatively steep. Two low-velocity thin sediment targets can be seen immediately to right of the salt body. The 720 shots are acquired with a shot spacing of 31 m, and the maximum offset for each shot is 8 km.

Figure 2.7 shows images of the synthetic dataset. Figure 2.7(a) is the resulting

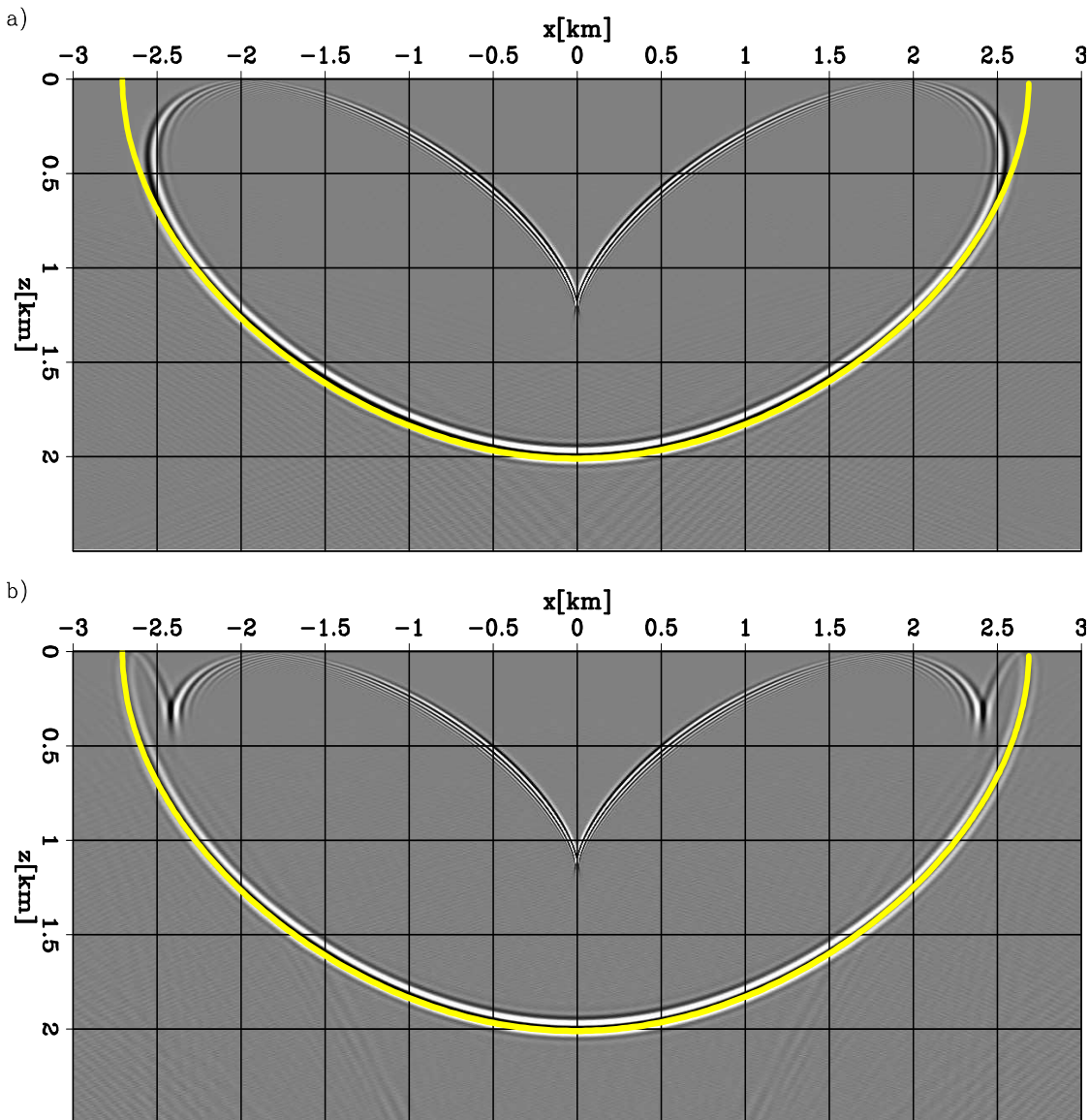


Figure 2.3: Impulse responses at $t = 1$ s for a VTI medium with the parameters $v_{p_0} = 2000$ m/s, $\varepsilon = 0.4$ and $\delta = 0.2$: (a) the second-order approximation by optimization; (b) the fourth-order approximation by optimization. The solid line is the theoretical impulse response calculated by using the group velocity as a function of the group angle of the medium. [anifd/. vti-impulse-e04d02](#)

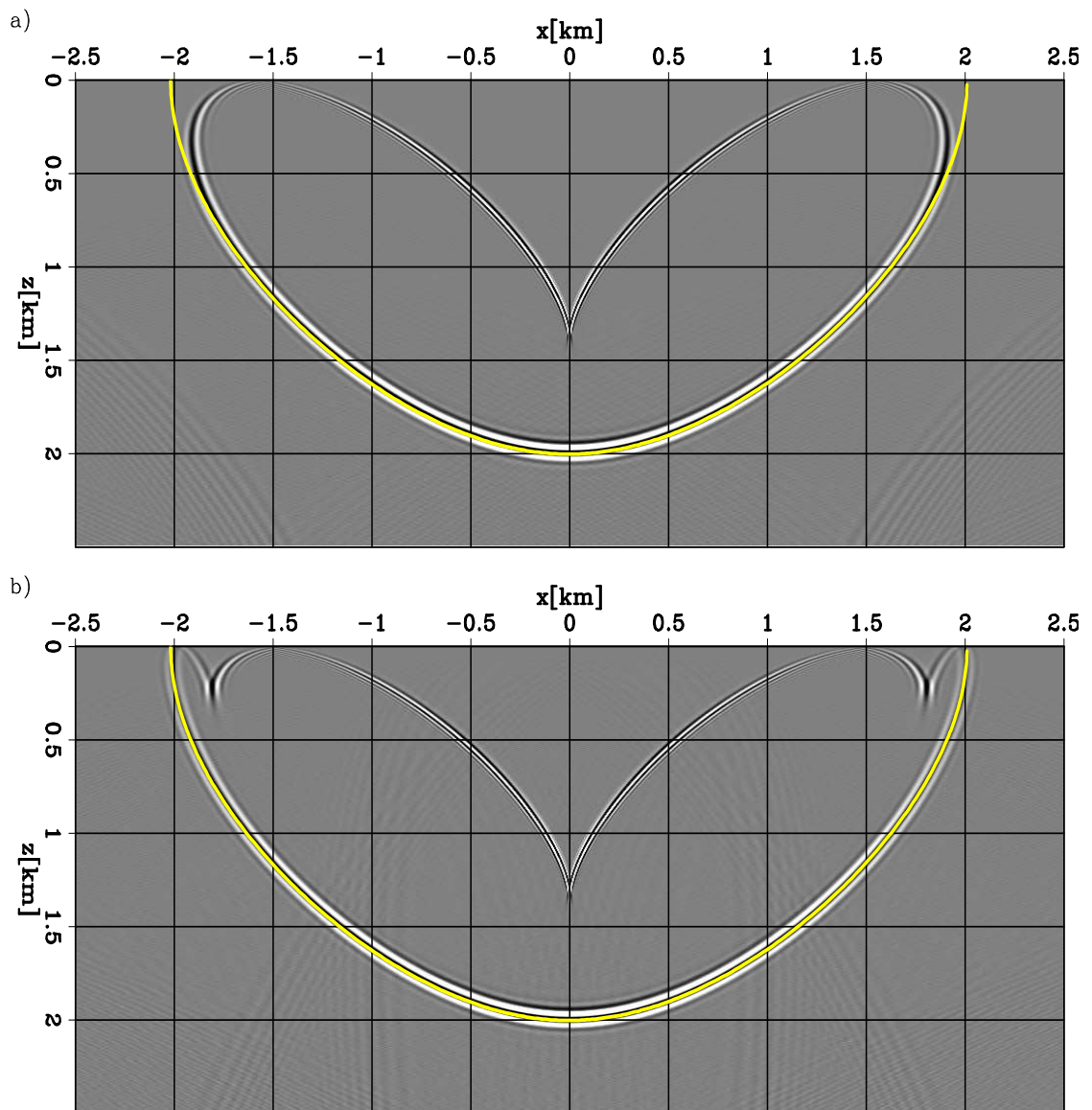


Figure 2.4: Impulse responses at $t = 1$ s for a VTI medium with the parameters $v_{p0} = 2000$ m/s, $\varepsilon = 0$ and $\delta = -0.2$: (a) the second-order approximation by optimization; (b) the fourth-order approximation by optimization. The solid line is the theoretical impulse response calculated by using the group velocity as a function of the group angle of the medium. `anifd/.vti-impulse-e0d-02`

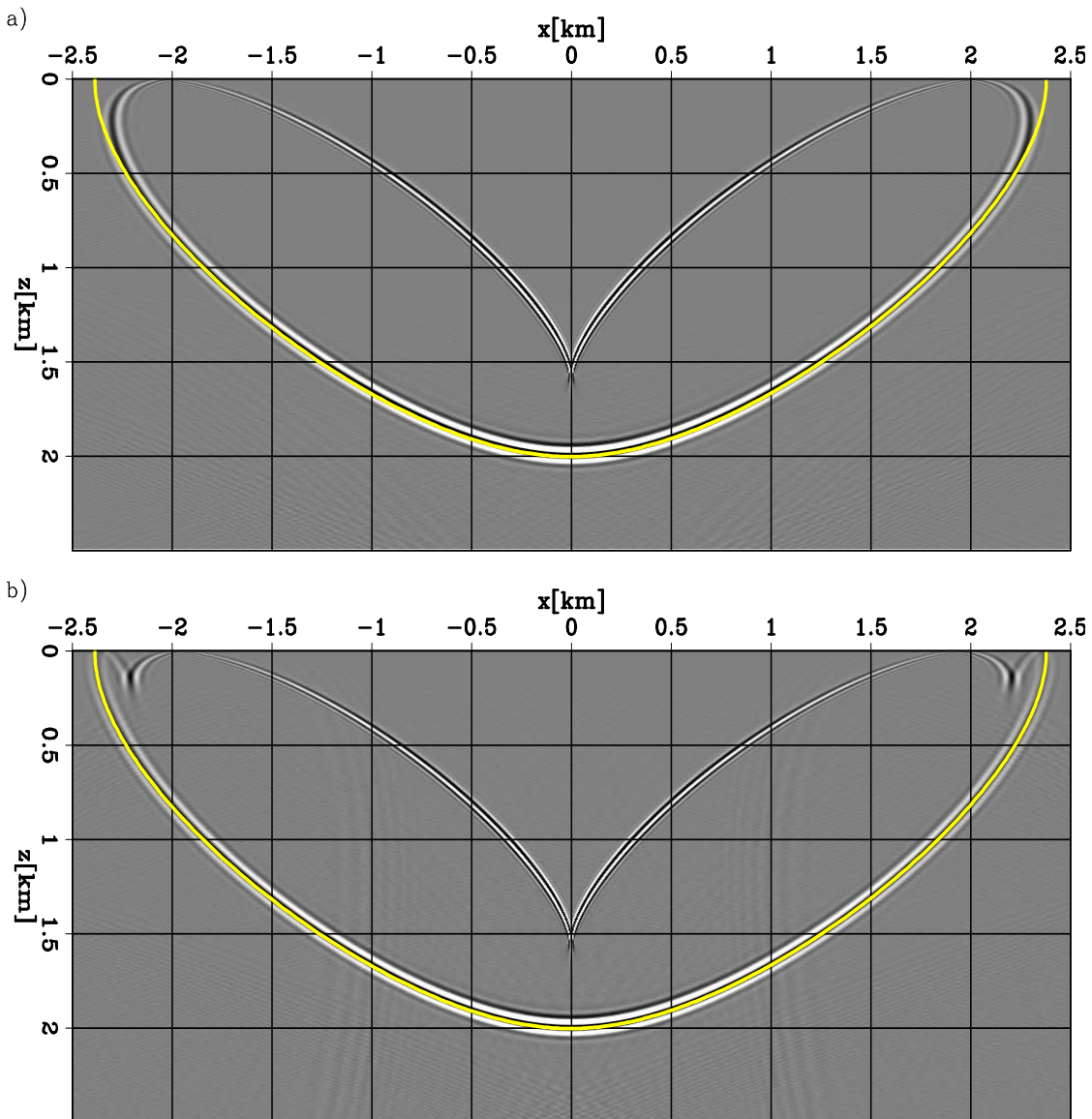


Figure 2.5: Impulse responses at $t = 1$ s for a VTI medium with the parameters $v_{p0} = 2000$ m/s, $\varepsilon = 0.2$ and $\delta = -0.2$: (a) the second-order approximation by optimization; (b) the fourth-order approximation by optimization. The solid line is the theoretical impulse response calculated by using the group velocity as a function of the group angle of the medium. `anifd/.vti-impulse-e02d-02`

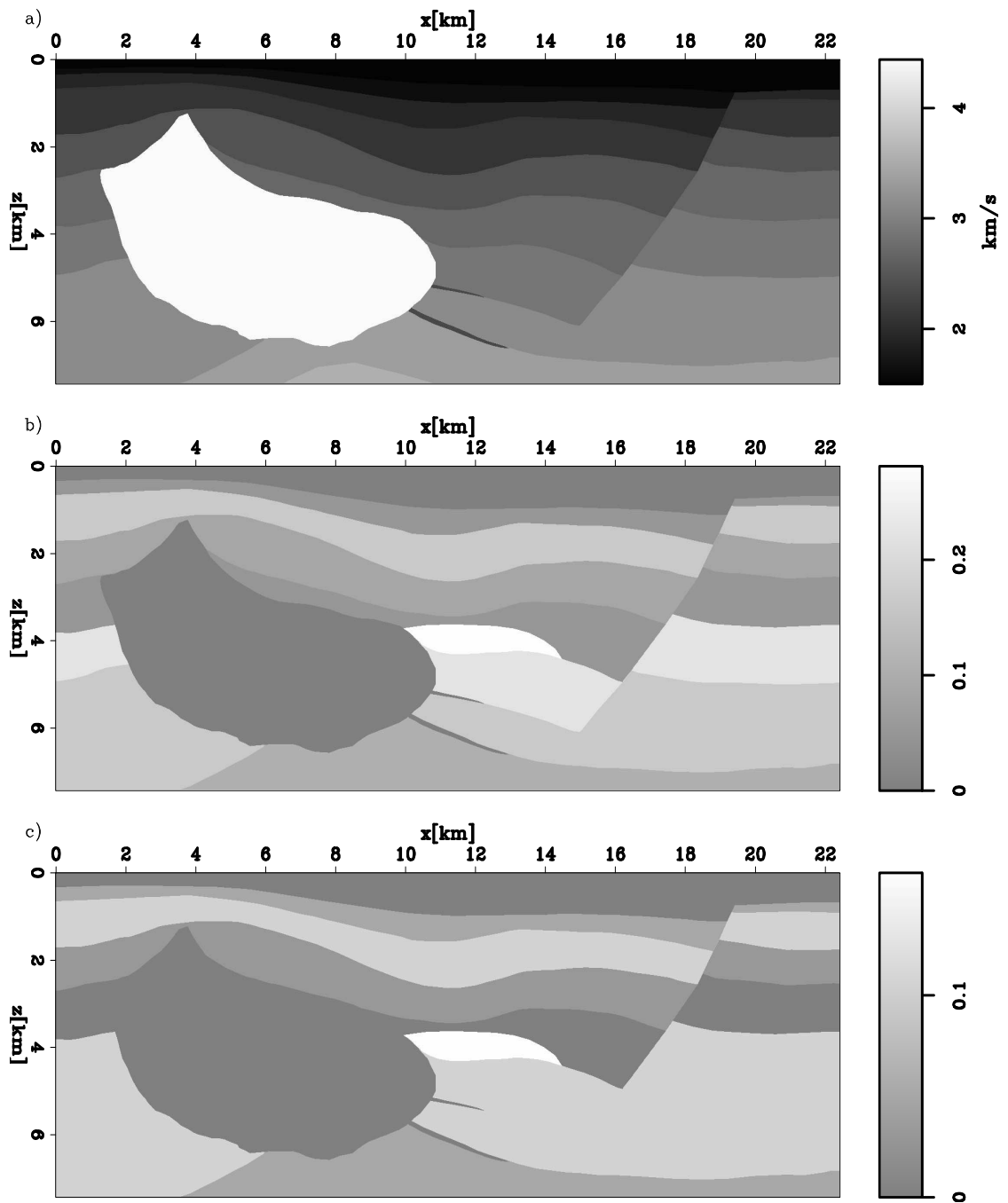


Figure 2.6: The vertical velocity and anisotropy parameters for the synthetic data: (a) vertical velocity; (b) anisotropy parameter ε ; (c) anisotropy parameter δ . `anifd/. model-hess`

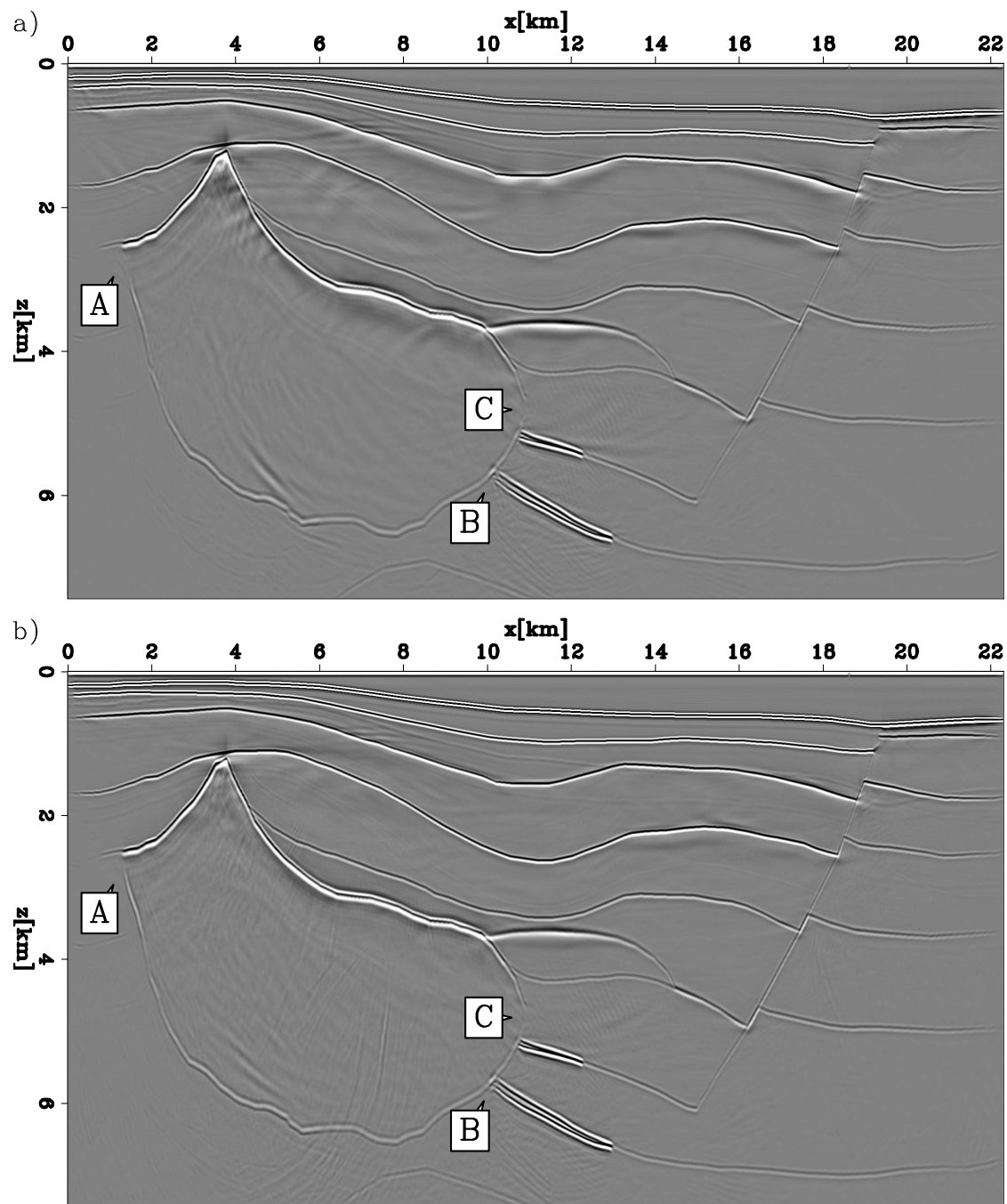


Figure 2.7: Implicit FD migrations for the synthetic dataset: (a) the second-order approximation by optimization; (b) the fourth-order approximation by optimization.

anifd/. image-hess-fd

image of a migration with the second-order optimized wavefield extrapolation and Figure 2.7(b) is the resulting image of a migration with the fourth-order optimized wavefield extrapolation. The steep fault and the majority of the salt flanks are well imaged in Figure 2.7(a). The salt flank at A, with dip beyond the accuracy of the wavefield extrapolation operator (60°), is not imaged. The top low-velocity sediment target is well imaged, but discontinuity exists at B in the bottom target. Images of both the salt flank at A and the sediment at B are improved in Figure 2.7(b). The salt flank at C is vertical. It is illuminated by prismatic energy that cannot be imaged by a conventional one-way wave equation migration.

FFD WAVEFIELD EXTRAPOLATION IN VTI MEDIA

FFD for isotropic media

In FFD for isotropic media, the lowest velocity value $c(z)$ at the depth z is taken to be the background velocity for a medium with actual velocity field $v(x, y, z)$. The difference between the wavefield extrapolation operators with the actual velocity and the reference velocity is

$$\Delta s_z(\rho; s_r) = \frac{v}{\omega} \Delta k_z = \frac{v}{\omega} (k_z - k_z^r) = \sqrt{1 - s_r^2} - \sqrt{\frac{1}{\rho^2} - s_r^2}, \quad (2.31)$$

where $\rho = \frac{c(z)}{v(x,z)}$, $s_r = \frac{vk_r}{\omega}$, $k_r = \sqrt{k_x^2 + k_y^2}$ and k_x, k_y, k_z are wavenumbers corresponding to x, y , and z , respectively. As with implicit FD, the difference of the migration operators, Δs_z , can be approximated by a rational function $\Delta \bar{s}_z$ as follows:

$$\Delta \bar{s}_z(\rho; s_r) = (1 - 1/\rho) - \sum_{i=1}^n \frac{a_i s_r^2}{1 - b_i s_r^2}. \quad (2.32)$$

As before, the coefficients a_i and b_i , $i = 1, \dots, n$, can be obtained by either analytical Taylor-series and Padé expansion analysis or numerical optimization. With the

estimated coefficients, the dispersion relation is approximated by

$$k_z \approx \frac{\omega}{c} \sqrt{1 - \frac{c^2}{\omega^2} k_r^2} + \left(\frac{\omega}{v} - \frac{\omega}{c} \right) - \frac{\omega}{v} \sum_{i=1}^n \frac{a_i s_r^2}{1 - b_i s_r^2}. \quad (2.33)$$

For the second-order approximation ($n = 1$), Ristow and Ruhl (1994) suggest $a_1 = 0.5(1 - \rho)$ and $b_1 = 0.25(\rho^2 + \rho + 1)$ through Taylor-series analysis. They also suggest that coefficient b_1 can be obtained by an optimization procedure.

By running the inverse Fourier transformation on equation 2.33, we can obtain the FFD scheme as follows:

$$\frac{\partial}{\partial z} P = i \left[\frac{\omega}{c} \sqrt{1 + \frac{c^2}{\omega^2} \left(\frac{\partial^2}{\partial x^2} + \frac{\partial^2}{\partial y^2} \right)} + \left(\frac{\omega}{v} - \frac{\omega}{c} \right) + \frac{\omega}{v} \sum_{j=1}^n \frac{a_j \frac{v^2}{\omega^2} \left(\frac{\partial^2}{\partial x^2} + \frac{\partial^2}{\partial y^2} \right)}{1 + b_j \frac{v}{\omega} \left(\frac{\partial^2}{\partial x^2} + \frac{\partial^2}{\partial y^2} \right)} \right] P, \quad (2.34)$$

where, again, $P = P(x, y, z, \omega)$ is the wavefield. Equation 2.34 can be solved by cascading, as before. On the right side of equation 2.34, the first term is performed in the frequency-wavenumber domain by phase-shift method and the other two terms are performed in the frequency-space domain by FD methods. FFD benefits from both phase-shift and FD migration methods. When the actual velocity is close to the reference one ($\rho \approx 1$), the phase-shift part dominates, and FFD achieves good accuracy. When the actual velocity is much larger than the reference one, the FD part dominates, so FFD is also effective for strong lateral velocity variation.

FFD for VTI media by optimization

As with isotropic media, I first calculate the difference of the migration operators with the actual and reference parameters of the medium. I approximate the difference with a rational function, estimate its coefficients with weighted least squares, and design the FD scheme based on the optimized rational function.

In a VTI medium with anisotropy parameter fields $\varepsilon(x, y, z)$ and $\delta(x, y, z)$ and a vertical velocity field $v_{p_0}(x, y, z)$, if we use the reference anisotropy parameter fields

$\varepsilon^r(z)$ and $\delta^r(z)$ and reference vertical velocity $c_{p_0}(z)$, the difference between the wavefield extrapolation operators with the actual and reference parameters is as follows:

$$\Delta s_z(\varepsilon, \delta, \varepsilon^r, \delta^r, \rho; s_r) = \frac{v_{p_0}}{\omega} (k_z - k_z^r) \quad (2.35)$$

$$= \sqrt{\frac{1 - (1 + 2\varepsilon)s_r^2}{1 - 2(\varepsilon - \delta)s_r^2}} - \sqrt{\frac{1/\rho^2 - (1 + 2\varepsilon^r)s_r^2}{1 - 2\rho^2(\varepsilon^r - \delta^r)s_r^2}}, \quad (2.36)$$

where $\rho = \frac{c_{p_0}(z)}{v_{p_0}(x,z)}$ and $s_r = \frac{v_{p_0}^2(k_x^2 + k_y^2)}{\omega}$. As with isotropic media, I approximate the operator difference, Δs_z , with a rational function, $\Delta \bar{s}_z$, as follows:

$$\Delta \bar{s}_z(\varepsilon, \delta, \varepsilon^r, \delta^r, \rho; s_r) = (1 - 1/\rho) - \frac{\sum_{i=1}^n \alpha_i (s_r^2)^i}{1 - \sum_{i=1}^n \beta_i (s_r^2)^i}. \quad (2.37)$$

The coefficients α_i and β_i are estimated by weighted least-squares optimization as follows:

$$\min \int_0^{S_r} w(s_r) \left[\Delta s_z(\varepsilon, \delta, \varepsilon^r, \delta^r, \rho; s_r) - (1 - 1/\rho) + \frac{\sum_{i=1}^n \alpha_i (s_r^2)^i}{1 - \sum_{i=1}^n \beta_i (s_r^2)^i} \right] ds_r, \quad (2.38)$$

where $w(s_r)$ is a weight function and S_r is determined by the maximal approximation angle in equation 2.20. As with equation 2.19, directly solving the optimization problem, 2.38, needs a non-linear least-square method. But it can be changed to an optimization problem as follows:

$$\min \int_0^{S_r} w(s_r) \left[(\Delta s_z(\varepsilon, \delta, \varepsilon^r, \delta^r, \rho; s_r) - (1 - 1/\rho)) \left(1 - \sum_{i=0}^n \beta_i (s_r^2)^i \right) + \left(\sum_{i=0}^n \alpha_i (s_r^2)^i \right) \right]^2 ds_r, \quad (2.39)$$

which can be solved by a linear least-square method. Equation 2.39 is similar to equation 2.21, except that the wavefield extrapolation operator $s_z(\varepsilon, \delta, s_r)$ in equation 2.21 is now the operator difference $\Delta s_z(\varepsilon, \delta, \varepsilon^r, \delta^r, \rho; s_r)$. The coefficients α_i and β_j are functions of $\rho, \varepsilon, \delta, \varepsilon^r$ and δ^r . As with the implicit FD method, the rational function in equation 2.37 can be further split into low-order rational functions as follows:

$$\Delta \bar{s}_z(\varepsilon, \delta, \varepsilon^r, \delta^r, \rho; s_r) = (1 - 1/\rho) - \sum_{i=1}^n \frac{a_i s_r^2}{1 - b_i s_r^2}, \quad (2.40)$$

where the coefficients a_i and b_i are calculated from α_i and β_i and are also functions of ρ , ε , δ , ε^r and δ^r . For the second-order approximation ($n = 1$), the dispersion relation function k_z is approximately

$$k_z \approx \frac{\omega}{c_{p0}} \sqrt{\frac{1 - (1 + 2\varepsilon^r) \left(\frac{c_{p0}k_r}{\omega}\right)^2}{1 - 2(\varepsilon^r - \delta^r) \left(\frac{c_{p0}k_r}{\omega}\right)^2}} + \left(\frac{\omega}{v_{p0}} - \frac{\omega}{c_{p0}}\right) - \frac{\omega}{v_{p0}} \frac{a_1 \left(\frac{v_{p0}k_r}{\omega}\right)^2}{1 - b_1 \left(\frac{v_{p0}k_r}{\omega}\right)^2}. \quad (2.41)$$

By inverse Fourier transform on equation 2.41, we obtain its corresponding partial differential equation. It can be solved by cascading as follows:

$$\frac{\partial P}{\partial z} = i \frac{\omega}{c_{p0}} \sqrt{\frac{1 - (1 + 2\varepsilon^r) \left(\frac{c_{p0}k_r}{\omega}\right)^2}{1 - 2(\varepsilon^r - \delta^r) \left(\frac{c_{p0}k_r}{\omega}\right)^2}} P, \quad (2.42)$$

$$\frac{\partial P}{\partial z} = i \left(\frac{\omega}{v_{p0}} - \frac{\omega}{c_{p0}}\right) P, \quad (2.43)$$

$$\frac{\partial P}{\partial z} = i \frac{\omega}{v_{p0}} \frac{a_1 \frac{v_{p0}^2}{\omega^2} \left(\frac{\partial^2}{\partial x^2} + \frac{\partial^2}{\partial y^2}\right)}{1 + b_1 \frac{v_{p0}^2}{\omega^2} \left(\frac{\partial^2}{\partial x^2} + \frac{\partial^2}{\partial y^2}\right)} P. \quad (2.44)$$

Equation 2.42 is solved in the frequency-wavenumber domain by the phase-shift method and equations 2.43 and 2.44 are solved in the frequency-space domain by the FD method.

As with isotropic media, I choose the lowest vertical velocity at the depth z as the reference velocity for that depth. We can choose nonzero minimal anisotropy parameters or use zero as the reference parameters. Using zero implies an isotropic phase-shift followed by a FD correction for both anisotropy and the lateral velocity variation. As with the implicit FD, we calculate the coefficients and store them in a table before wavefield extrapolation. If we choose nonzero minimal anisotropy parameters at each depth as the reference values, the coefficient table is a 5-D table, because the difference of the wavefield extrapolation operators Δs_z depends not only on ε , δ , ρ , but also on the reference parameters ε^r and δ^r . If we choose zero for the reference parameters, the coefficient table is only three-dimensional.

Biondi (2002) demonstrates that the bulletproofed (Godfrey et al., 1979; Brown, 1979) FFD scheme for isotropic media is unconditionally stable for arbitrary variations in the velocity of the medium no matter the reference velocity is lower or higher than the medium velocity. This is still true for the FFD scheme for VTI media since the it is almost the same as the FFD scheme for isotropic media except that its coefficients, a_i and b_i , $i = 1, \dots, n$, laterally vary.

Synthetic data example

The vertical velocity and anisotropy parameters for the example are those shown before in Figure 2.6. Figure 2.8 shows the images obtained by the second-order FFD method. Figure 2.8(a) is the resulting image using the nonzero minimal anisotropy parameter as the reference one, and Figure 2.8(b) is the resulting image using zero for the reference anisotropy parameters. The images for the two approaches are comparable. This suggests that using zero as the reference anisotropy parameters is acceptable, allowing a much reduced size of the coefficients table. Compared to the second-order implicit FD method (Figure 2.7(a)), the bottom thin low-velocity sediment layer (at B) immediately to the right of salt body is better imaged in Figures 2.8(a) and (b). It is not surprising that FFD does not improve the salt flank at A, because the minimal velocity, which is much lower than the salt velocity, is used as the reference, so the FD part dominates the operator.

IMPLICIT FD WAVEFIELD EXTRAPOLATION FOR TILTED TI MEDIA

Dispersion relation for tilted TI media

Rotating the symmetry axis from vertical to a tilted angle φ , we obtain the phase velocity as a function of the phase angle and anisotropy parameters for a tilted TI

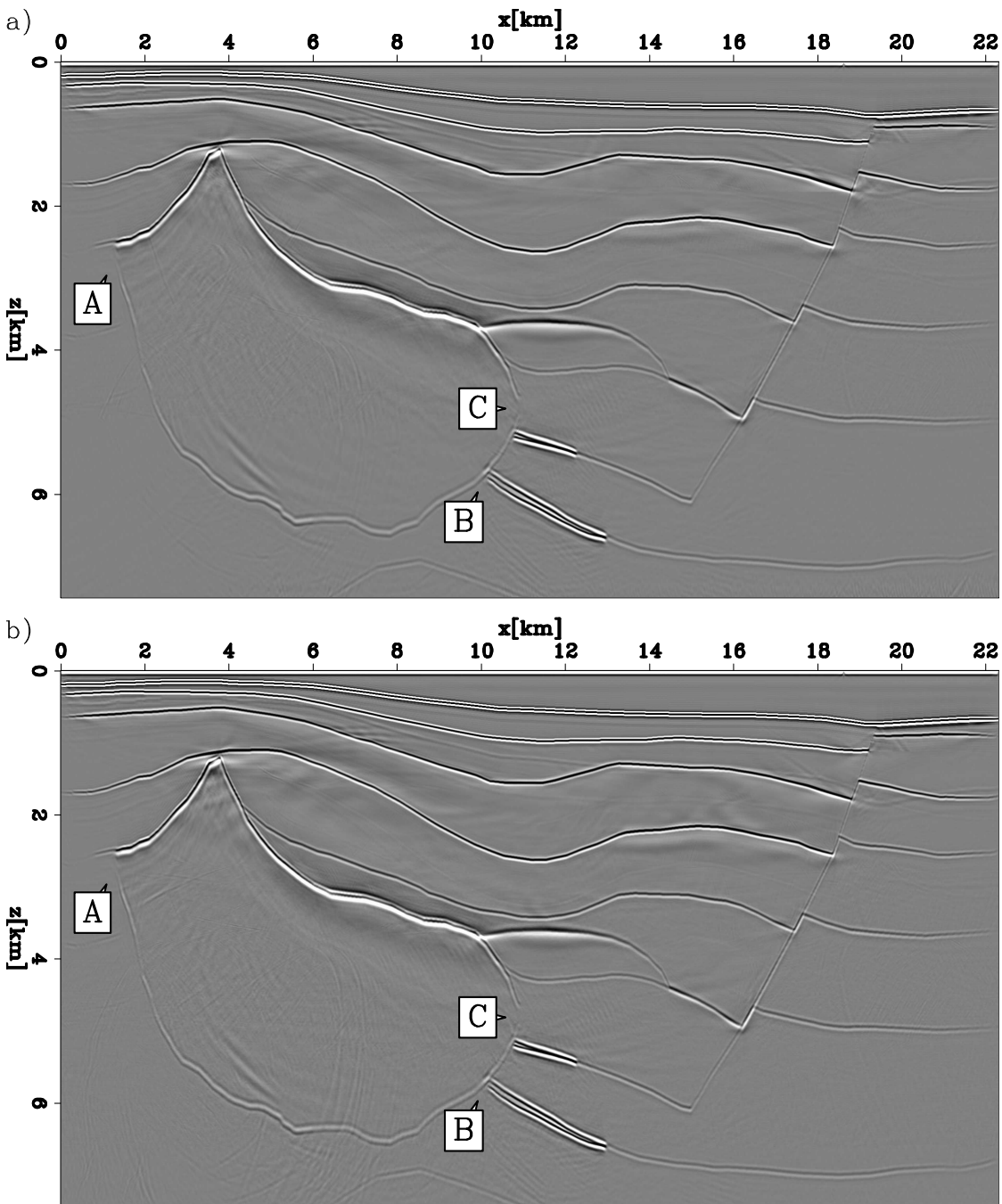


Figure 2.8: FFD migrations for the synthetic data: (a) using minimal nonzero anisotropy parameters as the reference ones; (b) using zero as the reference anisotropy parameters. `anifd/. image-hess-ffd`

medium with a tilting angle of φ :

$$\frac{v^2(\theta, \varphi)}{v_{p_0}^2} = 1 + \varepsilon \sin^2(\theta - \varphi) - \frac{f}{2} \pm \frac{f}{2} \sqrt{\left(1 + \frac{2\varepsilon \sin^2(\theta - \varphi)}{f}\right)^2 - \frac{2(\varepsilon - \delta) \sin^2 2(\theta - \varphi)}{f}}, \quad (2.45)$$

where θ is the phase angle, and $f = 1 - (v_{s_0}/v_{p_0})^2$. Here, in contrast to equation 2.5, ε and δ are defined for symmetry axes tilted by the angle φ from the vertical direction. Also v_{p_0} and v_{s_0} are the qP- and qSV- wave velocities along the symmetry axis, respectively.

For plane-wave propagation, the phase angle θ is linked to the wavenumbers k_x and k_z by the following relations:

$$\sin \theta = \frac{v(\theta, \varphi)k_x}{\omega}, \quad \text{and} \quad \cos \theta = \frac{v(\theta, \varphi)k_z}{\omega}, \quad (2.46)$$

where ω is the circular frequency. By squaring equation 2.45 and substituting equation 2.46 into 2.45, we can obtain the dispersion relation equation for the tilted TI medium:

$$d_4 s_z^4 + d_3 s_z^3 + d_2 s_z^2 + d_1 s_z + d_0 = 0, \quad (2.47)$$

where $s_z = \frac{k_z v_{p_0}}{\omega}$, and the coefficients d_0, d_1, d_2, d_3 , and d_4 are

$$\begin{aligned} d_0 &= (2 + 2\varepsilon \cos^2 \varphi - f)s_x^2 - 1 - \left[(1 - f)(1 + 2\varepsilon \cos^2 \varphi) + \frac{f}{2}(\varepsilon - \delta) \sin^2 2\varphi\right] s_x^4, \\ d_1 &= [2\varepsilon(1 - f) \sin 2\varphi - f(\varepsilon - \delta) \sin 4\varphi]s_x^3 - 2\varepsilon \sin 2\varphi s_x, \\ d_2 &= [f(\varepsilon - \delta) \sin^2 2\varphi - 2(1 - f)(1 + \varepsilon) - 2f(\varepsilon - \delta) \cos^2 2\varphi]s_x^2 + (2 + 2\varepsilon \sin^2 \varphi - f), \\ d_3 &= [f(\varepsilon - \delta) \sin 4\varphi + 2\varepsilon(1 - f) \sin 2\varphi]s_x, \\ d_4 &= f - 1 + 2\varepsilon(f - 1) \sin^2 \varphi - \frac{f}{2}(\varepsilon - \delta) \sin^2 2\varphi, \end{aligned}$$

with $s_x = \frac{k_x v_{p_0}}{\omega}$. Dispersion relation equation 2.47 is a quartic equation, which can be solved analytically (Abramowitz and Stegun, 1972) or numerically by Newton's Method (Stoer and Bulirsch, 1992). But unlike with VTI media, it is difficult to obtain an explicit analytical expression for s_z as a function of s_x for tilted TI media, even though we assume $f = 1$ in equation 2.45. An alternative approach, however, is

to solve the dispersion relation for VTI media (equation 2.7 or 2.10) analytically and obtain the dispersion relation for tilted TI media by rotating the solution (s_x, s_z) with the tilting angle φ numerically. I use the second method for calculating the dispersion relation of TI media for designing finite-difference schemes. Equation 2.47 has four roots, which are related to up-going and down-going qP- and qSV- waves, respectively. They are functions of tilting angle φ , anisotropy parameters ε and δ , and s_x . I discuss wavefield extrapolation operators only for qP-waves in this section. Wavefield extrapolation operators for qSV-waves could face added complication associated with singularities in the dispersion relation.

Figure 2.9 compares dispersion-relation curves for tilted TI media. The tilting angle and parameter ε used in panels are 30° and 0.2, respectively. The δ value used in panels (a) through (f) are 0.2, 0.1, 0, -0.1 , -0.2 and -0.3 , respectively. The dispersion relation changes from an elliptical-shaped curve (panel (a)) to somewhat diamond-shaped one (panel (c)) as the value of δ decreases from 0.2 (panel (a)) to -0.3 (panel (f)).

Dispersion relation approximation by function fitting

For an isotropic or VTI medium, s_z is an even function of s_x ; thus we approximate the dispersion relation with even components of rational functions, such as s_x^2 , s_x^4 . However, in equation 2.47, coefficients d_1 and d_3 are functions of s_x and s_x^3 , so the solution of equation 2.47, s_z , is not a symmetric function of s_x . As a consequence, in addition to even rational-function components, we need odd ones to approximate the dispersion relation for tilted TI media, such as s_x , s_x^3 . I approximate the dispersion relation $s_z(\varphi, \varepsilon, \delta; s_x)$ with the rational function \bar{s}_z ,

$$\bar{s}_z = s_{z0} - \frac{\sum_{j=1}^{2n} \alpha_j s_x^j}{1 - \sum_{i=1}^n \beta_i (s_x^2)^i}, \quad (2.48)$$

where n defines the order of the approximation, $s_z(\varphi, \varepsilon, \delta; s_x)$ is solved from equation 2.47, and $s_{z0} = s_z(\varphi, \varepsilon, \delta; s_x = 0)$. As with VTI media, the coefficients α_j , $j =$

$1, \dots, 2n$, and β_i , $i = 1, \dots, n$, are estimated by weighted least-square optimization. The optimization problem is set up as follows:

$$\min \int_{S_x^{min}}^{S_x^{max}} w(s_x) \left(s_z(\varphi, \varepsilon, \delta; s_x) - s_{z0} + \frac{\sum_{j=1}^{2n} \alpha_j s_x^j}{1 - \sum_{i=1}^n \beta_i (s_x^2)^i} \right)^2 ds_x, \quad (2.49)$$

where $w(s_x)$ is a weight function, and S_x^{min} and S_x^{max} are determined by the highest approximation angle in the negative direction θ^- and positive direction θ^+ as

$$\tan(\theta^-) = \frac{S_x^{min}}{s_z(\varphi, \varepsilon, \delta; S_x^{min})}, \quad (2.50)$$

$$\tan(\theta^+) = \frac{S_x^{max}}{s_z(\varphi, \varepsilon, \delta; S_x^{max})}, \quad (2.51)$$

where $s_z(\varphi, \varepsilon, \delta; S_x^{min})$ and $s_z(\varphi, \varepsilon, \delta; S_x^{max})$ are solved from equation 2.47, given S_x^{min} and S_x^{max} . Equations 2.50 and 2.51 are non-linear. They can be solved by Newton's Method or by just scanning S_x^{min} and S_x^{max} over a range. As with equation 2.19, directly solving the optimization problem 2.49 needs a non-linear least-square method. But again it can be changed to the following optimization problem,

$$\min \int_{S_x^{min}}^{S_x^{max}} w(s_x) \left[(s_z(\varphi, \varepsilon, \delta; s_x) - s_{z0}) \left(1 - \sum_{i=1}^n \beta_i (s_x^2)^i \right) + \sum_{j=1}^{2n} \alpha_j s_x^j \right]^2 ds_x, \quad (2.52)$$

which can be solved by a linear least-square method or QR decomposition.

Given the estimated coefficients α_i , $i = 1, \dots, 2n$, and β_j , $j = 1, \dots, n$, the rational function in equation 2.48 can be further split into low-order rational functions:

$$\bar{s}_z(s_x) = s_{z0} - \sum_{i=1}^n \frac{a_i s_x^2 + c_i s_x}{1 - b_i s_x^2}, \quad (2.53)$$

with the coefficients a_i , b_i and c_i , $i = 1, \dots, n$, calculated from α_j and β_i , $i = 1, \dots, n$, $j = 1, \dots, 2n$.

Figure 2.10 compares the true dispersion relation with the approximate one for a tilted TI medium with the parameters $\varepsilon = 0.4$, $\delta = 0.2$ and $\varphi = 30^\circ$. The solid

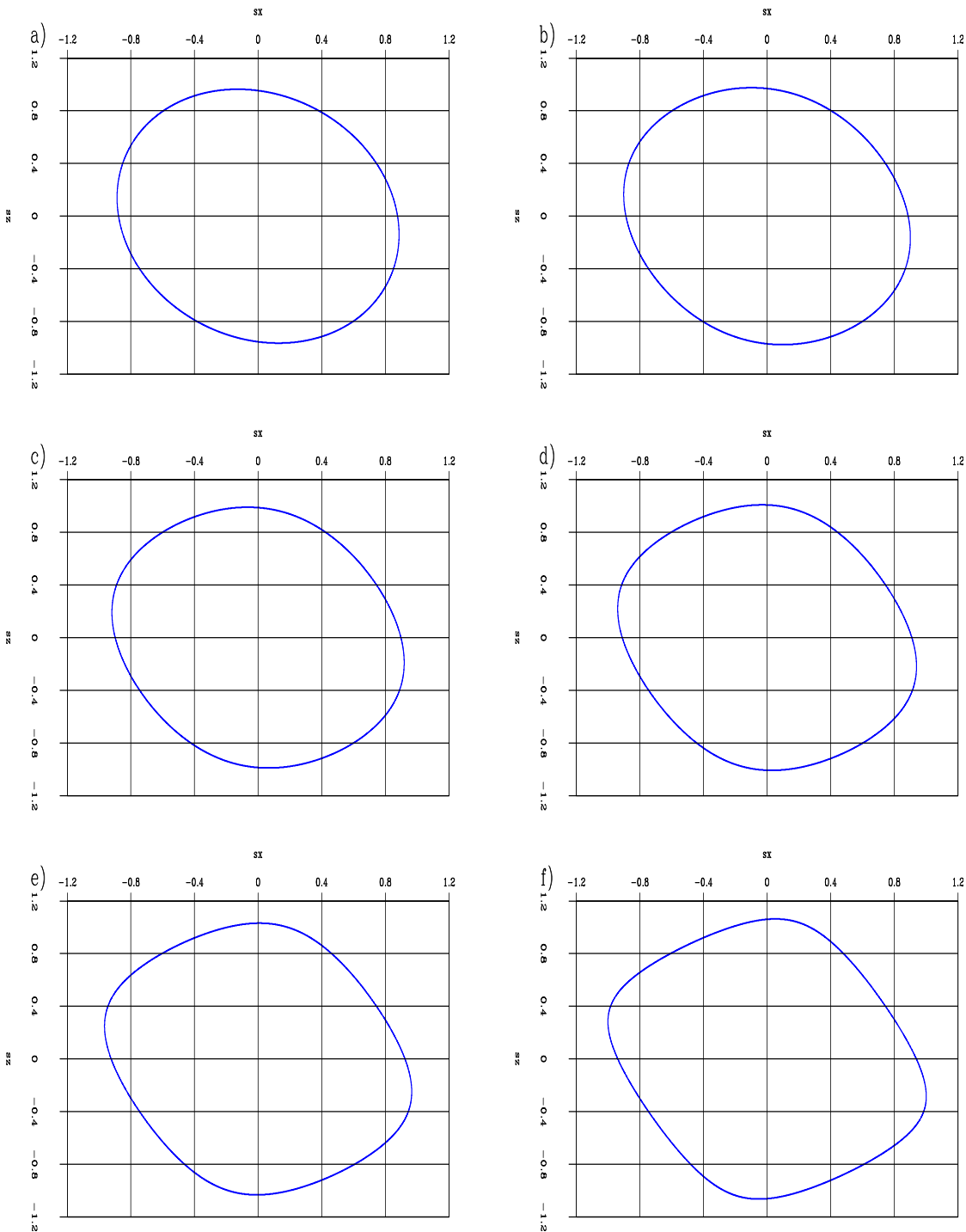


Figure 2.9: Dispersion relation for tilted TI media with a tilting angle of 30° : (a) $\epsilon = 0.2$ and $\delta = 0.2$; (b) $\epsilon = 0.2$ and $\delta = 0.1$; (c) $\epsilon = 0.2$ and $\delta = 0$; (d) $\epsilon = 0.2$ and $\delta = -0.1$; (e) $\epsilon = 0.2$ and $\delta = -0.2$; (f) $\epsilon = 0.2$ and $\delta = -0.3$. anifd/. tti-dis-curves

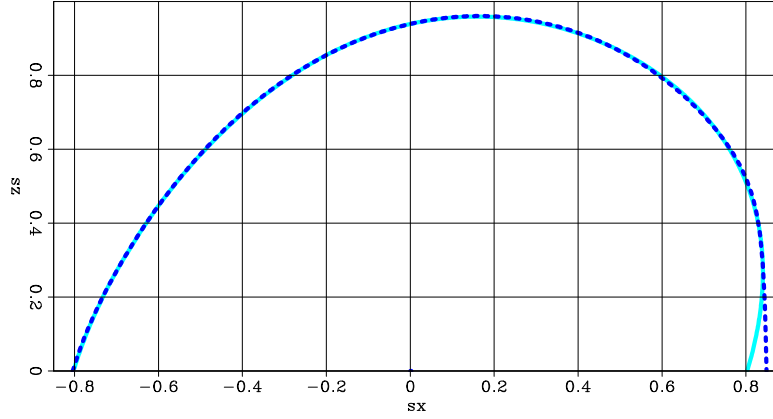


Figure 2.10: Comparison of the true and approximate dispersion relations for a TTI medium with $\varepsilon = 0.4$, $\delta = 0.2$ and $\varphi = 30^\circ$: the solid line is the true dispersion relation for TTI media; the dashed line is the approximate dispersion relation for the finite-difference scheme. The dispersion relation for the finite-difference scheme is very close to the true one. `anifd/. ttidispersion`

line is the true dispersion relation for the medium, and the dashed line is the fourth-order approximation ($n=2$). The coefficients for the approximate dispersion relation are $s_{z0} = 0.939116$, $a_1 = 0.774005$, $b_1 = 0.273686$, $c_1 = 0.259079$, $a_2 = 0.014030$, $b_2 = 1.360609$, and $c_2 = 0.000229$. The comparison shows that the approximate dispersion relation fits the true one well.

As with VTI media, the relative dispersion error for the approximate dispersion relation 2.53 is defined as

$$\mu = \frac{\bar{s}_z - s_z}{s_z}, \quad (2.54)$$

where s_z is the true one calculated from equation 2.47. Figure 2.11 shows the relative dispersion error for the fourth-order approximation ($n = 2$) and a tilted TI medium with the same parameters as those used in Figure 2.10.

As shown in Figure 2.9, negative δ (panels d, e, and f in Figure 2.9) makes the dispersion relation curve diamond-shaped. The tangent of the diamond-shaped curve increases rapidly around its vertices, which makes it difficult to fit the curve accurately with a rational function. As a result, given the same order, the accuracy of the

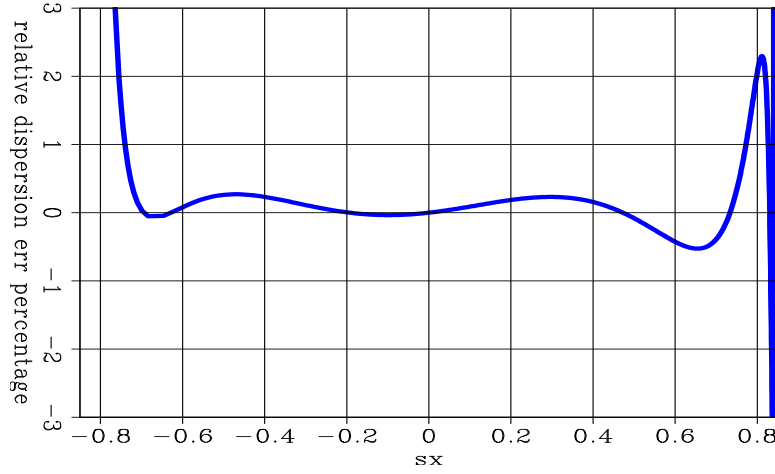


Figure 2.11: Relative dispersion-relation error of the finite-difference approximation for a TTI medium with $\varepsilon = 0.4$, $\delta = 0.2$ and $\varphi = 30^\circ$. `anifd/.errtti`

approximation for the dispersion relation is not as good when δ is negative as when it is positive.

Finite-difference scheme

By the inverse Fourier transform of equation 2.53, we obtain its corresponding partial differential equation in the frequency-space domain:

$$\frac{\partial P}{\partial z} = i \frac{\omega}{v_{p0}} \left(s_{z0} + \sum_{j=1}^n \frac{a_j \frac{v_{p0}^2}{\omega^2} \frac{\partial^2}{\partial x^2} + i c_j \frac{v_{p0}}{\omega} \frac{\partial}{\partial x}}{1 + b_j \frac{v_{p0}^2}{\omega^2} \frac{\partial^2}{\partial x^2}} \right) P, \quad (2.55)$$

where $P = (\omega, x, z)$ is the wavefield. As before, equation 2.55 can be solved by cascading. For instance, the second-order approximation case ($n = 1$) is solved by cascading:

$$\frac{\partial}{\partial z} P = i \frac{\omega}{v_{p0}} s_{z0} P, \quad (2.56)$$

$$\frac{\partial}{\partial z} P = i \frac{\omega}{v_{p0}} \left(\frac{-a_1 \frac{v_{p0}^2}{\omega^2} \frac{\partial^2}{\partial x^2} + i c_1 \frac{v_{p0}}{\omega} \frac{\partial}{\partial x}}{1 - b_1 \frac{v_{p0}^2}{\omega^2} \frac{\partial^2}{\partial x^2}} \right) P. \quad (2.57)$$

Equation 2.56 is the thin lens term, which can be solved by a phase-shift in the space domain. But notice, unlike in isotropic and VTI media, the phase-shift is weighted by the term s_{z0} . Equation 2.57 is solved by the finite-difference method. Let $P_j^k(\omega) = P(\omega, j\Delta x, k\Delta z)$, where Δx is sampling interval of the x and Δz is the step size of wavefield extrapolation. The partly discrete form of equation 2.57,

$$\frac{P^{k+1} - P^k}{\Delta z} = i \frac{\omega}{v_{p0}} \left(\frac{a_1 \frac{v_{p0}^2}{\omega^2} \frac{\partial^2}{\partial x^2} + i c_1 \frac{v_{p0}}{\omega} \frac{\partial}{\partial x}}{1 + b_1 \frac{v_{p0}^2}{\omega^2} \frac{\partial^2}{\partial x^2}} \right) \frac{P^{k+1} + P^k}{2}, \quad (2.58)$$

can be rewritten as

$$\left(1 + d_1 \frac{\partial^2}{\partial x^2} - c_1 \frac{\partial}{\partial x} \right) P^{k+1} = \left(1 + d_1^* \frac{\partial^2}{\partial x^2} + c_1 \frac{\partial}{\partial x} \right) P^k, \quad (2.59)$$

where $d_1 = b_1 \frac{v_{p0}^2}{\omega^2} - i \frac{a_1 \Delta z}{2} \frac{v_{p0}}{\omega}$, and d_1^* is complex conjugate of d_1 . I approximate $\frac{\partial^2}{\partial x^2}$ as follows:

$$\frac{\partial^2}{\partial x^2} \approx \frac{\delta_x^2}{\Delta x^2 (1 + \tau \delta_x^2)}, \quad (2.60)$$

where $\delta_x^2 P_j^k = P_{j+1}^k - 2P_j^k + P_{j-1}^k$ and τ is called 1/6 trick, which is not necessary 1/6 but can be estimated by optimization (Claerbout, 1985). I approximate $\frac{\partial}{\partial x}$ as follows:

$$\frac{\partial}{\partial x} \approx \frac{\delta_x^+ + \delta_x^-}{2\Delta x (1 + \tau \delta_x^2)}, \quad (2.61)$$

where $\delta_x^+ P_j^k = P_{j+1}^k - P_j^k$ and $\delta_x^- P_j^k = P_j^k - P_{j-1}^k$. For a medium with no lateral variation, Fourier analysis shows that the extrapolation operator from P^k to P^{k+1} in equation 2.59 is a unitary operator, so the stability of this equation is similar to that of the classic 45° equation (Claerbout, 1985) for isotropic media. The computational cost to solve equation 2.59 is almost the same as that of the finite-difference scheme for isotropic media.

As with VTI media, the FD scheme is solved by the table-driven method in laterally varying tilted TI media. In equation 2.55, the coefficients a_j , b_j , and c_j , $j = 1, \dots, n$, are functions of parameters ε , δ and φ . They are pre-calculated and

stored in a table before the wavefield extrapolation. During the extrapolation, given the anisotropy parameters ε , δ , and the tilting angle ϕ , we look up the coefficients from the table. Inserting the coefficients into equation 2.59, we solve it in the same way as for the 45° FD scheme for isotropic media. Therefore, as with VTI media, the cost of FD schemes for tilted TI media is almost the same as the counterpart in isotropic media.

Impulse responses

Figures 2.12 through 2.17 show impulse responses of the fourth-order FD scheme ($n = 2$) for tilted homogeneous TI media. The impulse location is at zero. The qP-wave velocity along the symmetry axis is 2000 m/s, the tilting angle, θ , is 30° and, the travel time of the impulse is 1 s for all impulse responses. The impulse responses of the FD scheme are calibrated by the theoretical curves (solid lines in figures), which are calculated by using group velocity as a function of group angle. Anisotropy parameters used in Figure 2.12 are $\varepsilon = 0.4$ and $\delta = 0.2$. The values for the anisotropy parameter δ in Figures 2.13, 2.14 and 2.15 are 0.2, 0.1 and 0, respectively. The value of ε used in these three figures is 0.2. For these more ellipse-shaped wavefronts (Figures 2.12, 2.13, 2.14 and 2.15), the fourth-order FD impulse responses match the theoretical curves well. The overturned energy is not correctly imaged because the one-way wave-equation is used.

Anisotropy parameter ε value used in Figures 2.16 and 2.17 are 0 and 0.2, respectively. The parameter δ used in both figures is -0.2 . The wavefronts in Figures 2.16 and 2.17 are more diamond-shaped because of negative δ . In contrast to ellipse-shaped wavefronts, however, the FD scheme for tilted TI media with negative δ is less accurate because of the large curvature in portions of the diamond-shaped dispersion-relation curve. The accuracy of the FD scheme is improved by increasing its order. Figures 2.18 and 2.19 are impulse responses of the sixth-order FD scheme ($n=3$). The medium parameters used in Figure 2.18 are the same as in Figure 2.16, and those used in Figure 2.19 are the same as in Figure 2.17. The impulse-responses of the

sixth-order FD scheme match the theoretical ones well.

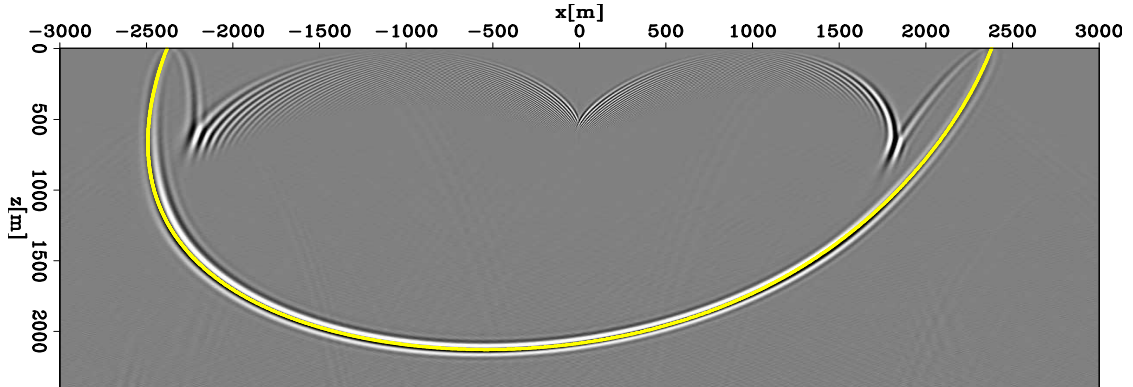


Figure 2.12: Impulse response of a tilted TI medium with $v_{p0} = 2000$ m/s, $\varepsilon = 0.4$, $\delta = 0.2$ and $\phi = 30^\circ$ calculated by 4th-order FD. The solid line is the theoretical impulse response calculated using the group velocity as a function of the group angle. `anifd/. tti-impulse-e04d02`

A thrust model

Figure 2.20 shows an anisotropic model with a dipping, anisotropic thrust sheet embedded in an isotropic background (Fei et al., 1998). This model represents the thrust shale layer usually seen in the Canadian Foothills. In the thrust sheet, the anisotropy parameters are $\varepsilon = 0.15$, $\delta = 0.081$, defined along symmetry axis, the normal to the thrust sheet. The qP-wave velocity along the symmetry axis is 2925 m/s. The thrust sheet has a varying symmetry axis, and the tilting angles of the four blocks of the thrust layer are 0° , 30° , 50° and 61° , respectively. The background velocity is 2740 m/s. There are 86 shots that are modeled by the elastic FD and recorded with a split-spread geometry. This model shows problems that arise when one migrates reflectors beneath an anisotropic dipping thrust sheet without taking its anisotropy into account.

The dataset is first migrated with the isotropic FD migration, neglecting the anisotropy of the thrust sheet. A pull-up of the flat reflector below the thrust sheet (at “A”) appears in the resulting image (Figure 2.21a). This happens because isotropic

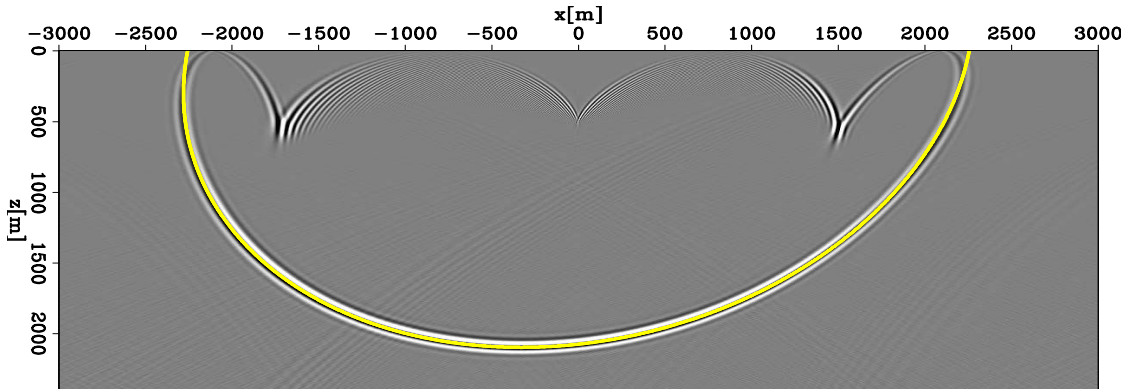


Figure 2.13: Impulse response of a tilted TI medium with $v_{p0} = 2000$ m/s, $\varepsilon = 0.2$, $\delta = 0.1$ and $\phi = 30^\circ$ calculated by 4th-order FD. The solid line is the theoretical impulse response calculated using the group velocity as a function of the group angle.
 anifd/. tti-impulse-e02d02

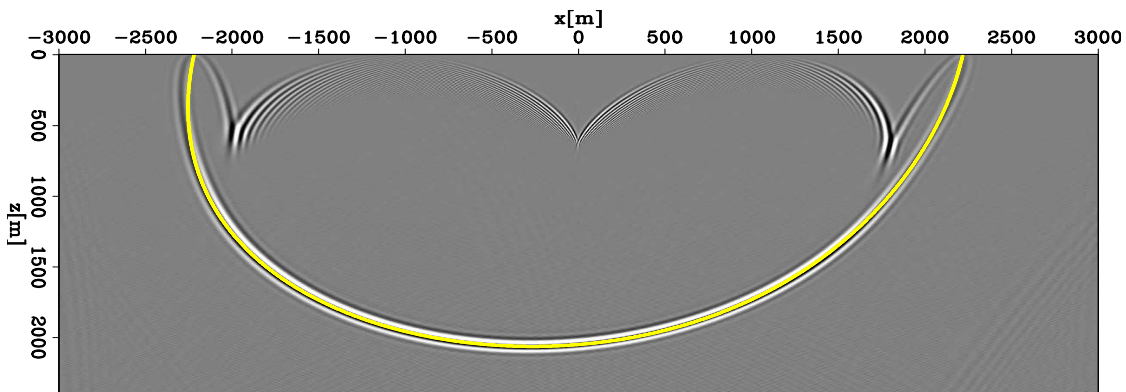


Figure 2.14: Impulse response of a tilted TI medium with $v_{p0} = 2000$ m/s, $\varepsilon = 0.2$, $\delta = 0.1$ and $\phi = 30^\circ$ calculated by 4th-order FD. The solid line is the theoretical impulse response calculated using the group velocity as a function of the group angle.
 anifd/. tti-impulse-e02d01

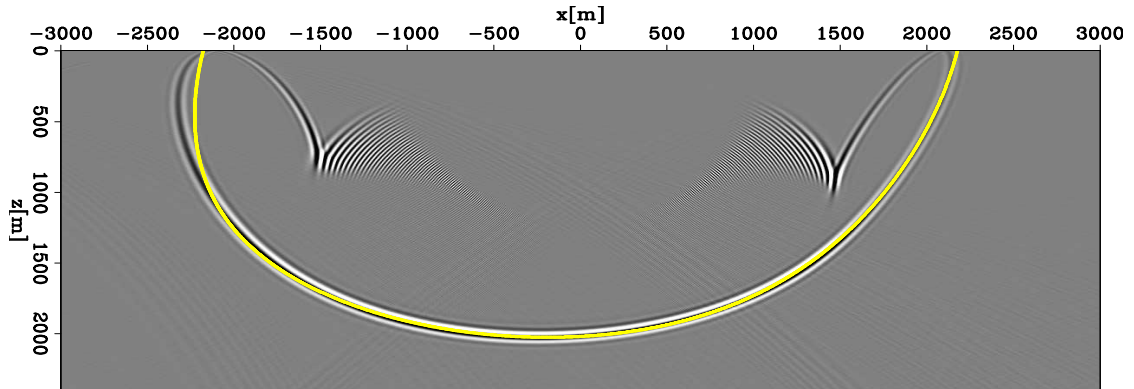


Figure 2.15: Impulse response of a tilted TI medium with $v_{p0} = 2000$ m/s, $\varepsilon = 0.2$, $\delta = 0.0$ and $\phi = 30^\circ$ calculated by 4th-order FD. The solid line is the theoretical impulse response calculated using the group velocity as a function of the group angle.
 anifd/. tti-impulse-e02d0

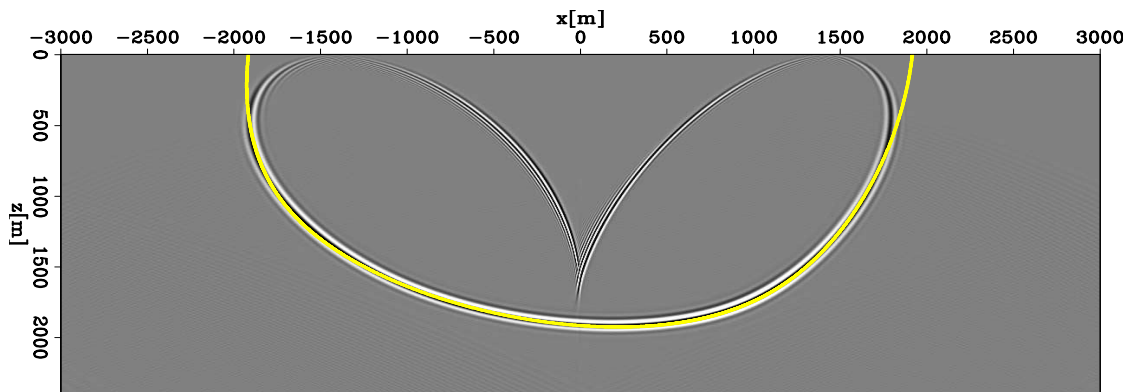


Figure 2.16: Impulse response of a tilted TI medium with $v_{p0} = 2000$ m/s, $\varepsilon = 0.0$, $\delta = -0.2$ and $\phi = 30^\circ$ obtained by 4th-order FD. The solid line is the theoretical impulse response calculated using the group velocity as a function of the group angle.
 anifd/. tti-impulse-e0d-02

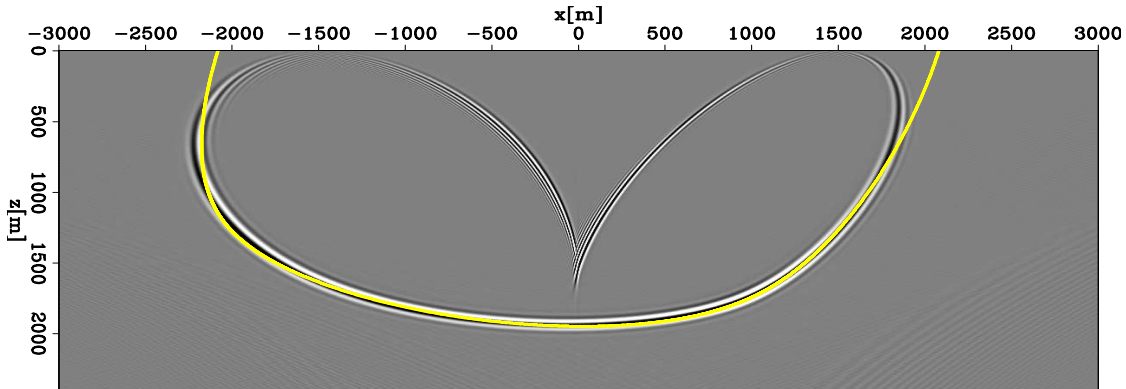


Figure 2.17: Impulse response of a tilted TI medium with $v_{p0} = 2000$ m/s, $\varepsilon = 0.2$, $\delta = -0.2$ and $\phi = 30^\circ$ obtained by 4th-order FD. The solid line is the theoretical impulse response calculated using the group velocity as a function of the group angle.
 anifd/. tti-impulse-e02d-02

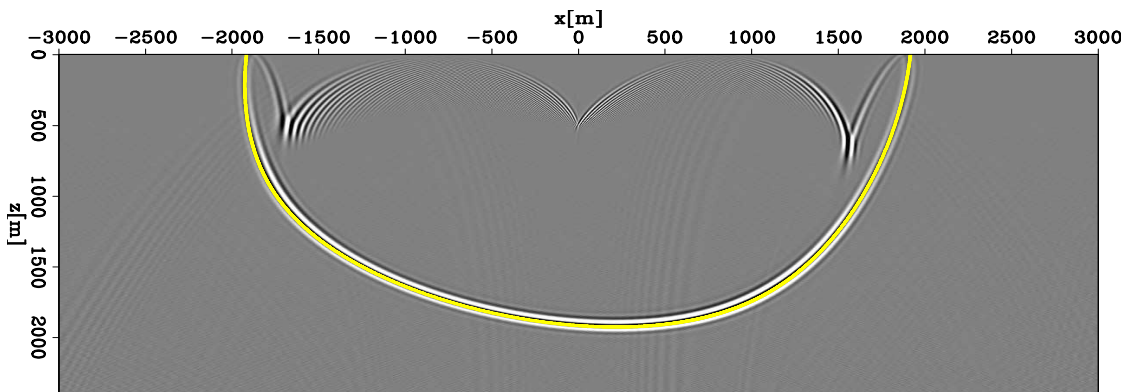


Figure 2.18: Impulse response of a tilted TI medium with $v_{p0} = 2000$ m/s, $\varepsilon = 0.0$, $\delta = -0.2$ and $\phi = 30^\circ$ obtained by 6th-order FD. The solid line is the theoretical impulse response calculated using the group velocity as a function of the group angle.
 anifd/. tti-impulse-e0d-02-6th

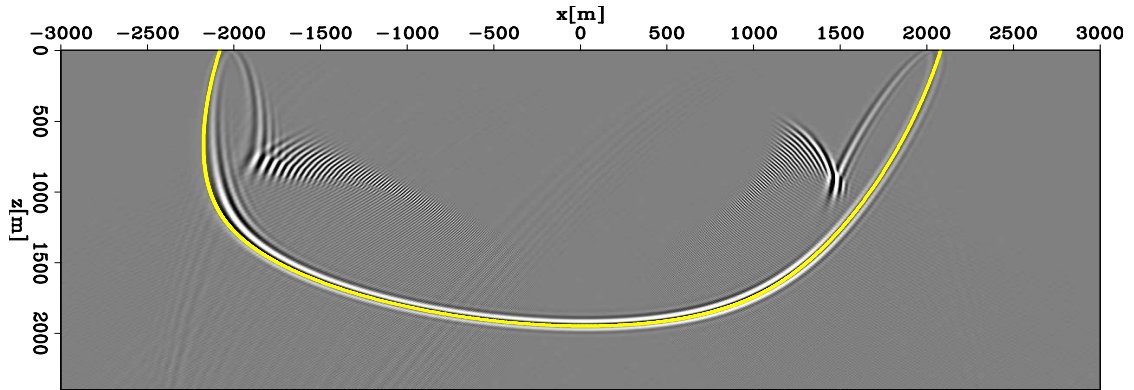


Figure 2.19: Impulse response of a tilted TI medium with $v_{p0} = 2000$ m/s, $\varepsilon = 0.2$, $\delta = -0.2$ and $\phi = 30^\circ$ obtained by 6th-order FD. The solid line is the theoretical impulse response calculated using the group velocity as a function of the group angle.
 anifd/. tti-impulse-e02d-02-6th

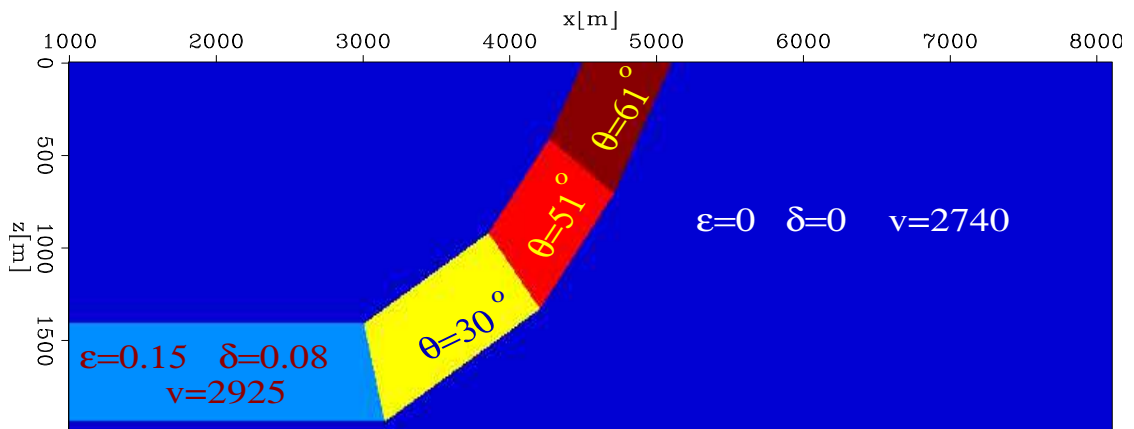


Figure 2.20: Thrust model for the synthetic data imaged in Figure 2.21.
 anifd/. thrustmodel

migration uses the velocity along the symmetry axis, which is lower than the true propagation velocity of the waves for most propagation directions, since the parameters ε and δ are positive in the thrust sheet. The dataset is also migrated with the VTI FD migration by disregarding the tilt of the anisotropy axis in thrust sheet. The resulting image (Figure 2.21b) shows a similar pull-up of the flat reflector. The image obtained by the tilted TI FD migration (Figure 2.21c) shows that the reflector below the thrust sheet is well imaged.

Notice that the bottom boundary of the 60° thrust sheet (at “B”) is better imaged in the isotropic migration (Figure 2.21(a)), than in the migration for VTI media (Figure 2.21(b)). The position of the bottom boundary of thrust sheet is almost correct in Figure 2.21a, although there are some defocusing artefacts. This is not surprising, because most of the energy illuminating the bottom boundary of the thrust propagates in a direction close to that of the symmetry axis of the medium, and the propagation velocity along these directions is almost correct if we regard the medium as isotropic. But the velocity in most directions is incorrect, the medium taken as VTI. Vertical transverse isotropy here is not a good approximation for the tilted TI medium.

CONCLUSION

I present an implicit finite-difference scheme for wavefield extrapolation for TI media. The scheme is designed by approximating the dispersion relation of TI media with a rational function and estimating its coefficients by weighted least-square optimization. For a TI medium with lateral variation, the FD coefficients are pre-computed and stored in a table. During the wavefield extrapolation, the coefficients are looked up from the table. The FD scheme for TI media has the same stability and almost same cost as the same routine for isotropic media. If the scheme is based on bulletproofing theory, it is stable. The FD scheme for VTI media also has similar accuracy to that of the same routine for isotropic media, but for tilted TI media the accuracy of the FD scheme depends on the δ value. FD schemes with the same order have

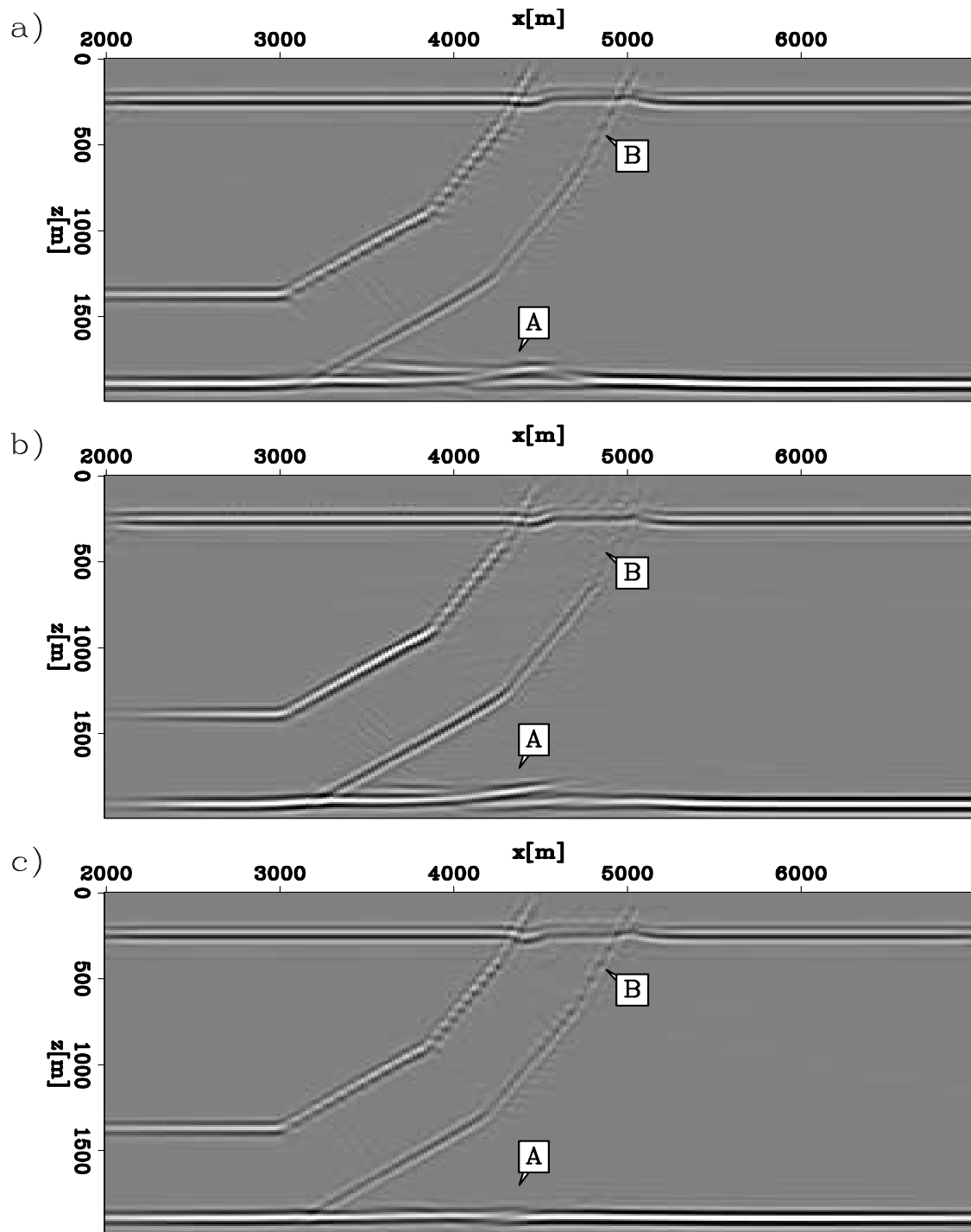


Figure 2.21: Image comparisons: (a) image obtained by isotropic migration; (b) image obtained by anisotropic migration for VTI media; (c) image obtained by anisotropic migration for TTI media. `anifd/. thrustimage`

better accuracy for positive- δ media than for negative- δ media. The synthetic data examples show that the FD scheme extrapolates the wavefield accurately in laterally varying TI media.

ACKNOWLEDGMENTS

I thank Amerada Hess for providing the VTI synthetic dataset and BP for providing the synthetic dataset for the tilted TI thrust model.

Chapter 3

Plane-wave migration in tilted coordinates: Theory and synthetic data examples

INTRODUCTION

Wave-equation migration, which is performed by recursive wavefield extrapolation, has been demonstrated to handle multi-pathing intrinsically and produce good images in areas of complex geology. Conventional downward-continuation methods extrapolate wavefields using a one-way wave equation in vertical Cartesian coordinates. For a medium without lateral variation, the phase-shift method (Gazdag, 1978) can be applied, and one-way wave equation can model waves propagating in directions up to 90° away from the extrapolation direction. But in a laterally varying medium, it is difficult to model waves propagating in directions far from the extrapolation direction using the one-way wave equation. Much effort has been made to improve the accuracy of the wavefield-extrapolation operator in laterally varying media. Examples include Fourier finite-difference (Ristow and Ruhl, 1994; Biondi, 2002), general screen propagator (de Hoop, 1996; Huang and Wu, 1996), and optimized finite difference (Lee

and Suh, 1985) with a phase correction (Li, 1991). Even if we could model waves accurately up to 90° using the one-way wave equation, overturned waves, which travel downward first and then curve upward, are filtered out during the wavefield extrapolation because of the assumption that the waves propagate vertically only downward for source wavefields and only upward for receiver wavefields. But overturned waves and waves propagating in a high-angle direction play a key role in imaging the steep reflectors. As a consequence, imaging steep reflectors, such as salt flanks and faults, remains a major problem in downward-continuation migration. In this chapter, I present a migration method based on wavefield extrapolation, plane-wave migration in tilted coordinates, which can image overturned waves and steeply dipping reflectors. I discuss plane-wave migration in tilted coordinates in 2D with synthetic data examples to introduce the concepts and demonstrate the ideas. In chapter 4, I show how to perform plane-wave migration in tilted coordinates for 3D anisotropic media and show migration results of a 3D field dataset.

The one-way wave equation favors its extrapolation direction. Waves traveling along the extrapolation direction are most accurately propagated. The extrapolation direction can be changed by coordinate transformation, such as tilted coordinates (Higginbotham et al., 1985; Etgen, 2002), the combination of downward continuation and horizontal continuation (Zhang and McMechan, 1997), and wavefield extrapolation in general coordinates such as ray coordinates (Nichols, 1994) and Riemannian coordinates (Sava and Fomel, 2005; Shragge, 2006). In tilted coordinates, the accuracy of the extrapolator determines the maximum angle between the propagation direction and the extrapolation direction. For a point source, waves travel in all directions from a point, so it is impossible for one tilted coordinate system to cover all these directions. For a plane-wave source, waves leave all spacial points of the surface in nearly the same direction, and most of them can be propagated accurately in a tilted coordinate system with a proper tilting direction. I therefore apply plane-wave source migration (Whitmore, 1995; Rietveld, 1995; Duquet et al., 2001; Liu et al., 2002; Zhang et al., 2005b) in tilted coordinates. Plane-wave migration has been demonstrated to be a useful tool in seismic imaging. By slant-stacking receiver gathers, the recorded surface data are synthesized into areal plane-wave-source

gathers, which are the data that would have been recorded if plane-wave sources had been excited at the surface. A plane-wave source is characterized by a ray parameter. Given the velocity at the surface, its take-off angle can be calculated from the ray parameter. Each areal plane-wave source gather is migrated independently as in shot-profile migration, and the image is formed by stacking the images of all possible plane-sources. Given a plane-wave source, I assign a tilted coordinate system whose tilting direction is determined by the take-off angle of the plane-wave source. In plane-wave migration in tilted coordinates, the extrapolation direction of most waves is generally close to their propagation direction; thus we can image steep reflectors correctly using a one-way wave equation. Plane-wave migration is potentially more efficient than shot-profile migration (Zhang et al., 2005b; Etgen, 2005). To image steep reflectors and overturned waves, a large migration aperture is required to cover the whole propagation path of source and receiver waves. In shot-profile migration, this requires large padding in space. In contrast, plane-wave migration uses the entire seismic survey as the migration aperture. It is well understood that one-way wave equation shot-profile migration is less computationally costly than reverse-time migration. Compared to conventional plane-wave migration, the cost of plane-wave migration in tilted coordinates is higher because of the interpolation required for the data and velocity model, but it is still much less than reverse-time migration.

In this chapter, I begin with a review of one-way wave-equation migration and plane-wave migration. Then I introduce how to extrapolate wavefields in a tilted coordinate system and discuss the implications of tilted coordinates for VTI media. Next I describe plane-wave migration in tilted coordinates. Finally I demonstrate the technique with synthetic data examples.

ONE-WAY WAVE EQUATION MIGRATION

The recorded surface seismic data are usually recorded as shot gathers. Each shot gather represents an impulsive point-source exploding experiment. A particularly

straight forward way to obtain the subsurface image of the earth is shot-profile migration, in which we obtain the partial image of each experiment by migrating each shot gather independently and construct the whole image of the subsurface by stacking all the partial images. There are two stages to migrating one shot gather using a typical shot-profile migration algorithm. First, source and receiver wavefields are extrapolated from the surface to all depths in the subsurface. Second, the image is constructed by cross-correlating the source and receiver wavefields.

Conventionally the propagation of waves in the subsurface is taken to be governed by a two-way wave equation, which in an isotropic medium, is given in two dimensions by

$$\frac{1}{v^2} \frac{\partial^2}{\partial t^2} P = \left(\frac{\partial^2}{\partial x^2} + \frac{\partial^2}{\partial z^2} \right) P, \quad (3.1)$$

where $P = P(x, z, t)$ is the pressure field and $v = v(x, z)$ is the velocity of the medium, x and z are the horizontal and vertical coordinates, and t is time. To reduce computational cost, we usually use the one-way instead of two-way wave equation,

$$\frac{\partial}{\partial z} S = -\frac{i\omega}{v} \sqrt{1 + \left(\frac{v}{\omega} \frac{\partial}{\partial x} \right)^2} S, \quad (3.2)$$

$$\frac{\partial}{\partial z} R = +\frac{i\omega}{v} \sqrt{1 + \left(\frac{v}{\omega} \frac{\partial}{\partial x} \right)^2} R, \quad (3.3)$$

for wavefield extrapolation, where ω is circular frequency, $S = S(s_x, x, z, \omega)$ is the source wavefield, $R = R(s_x, x, z, \omega)$ is the receiver wavefield, and s_x is the source location. Written in the form of equations 3.2 and 3.3, the vertical coordinate, z , defines the extrapolation direction. Taking account of the propagation direction of the source and receiver wavefields, we use the down-going one-way wave equation (equation 3.2) for the source wavefield and the up-going one-way wave equation (equation 3.3) for the receiver wavefield. Both of them are obtained by splitting the two-way acoustic equation 3.1 (Zhang, 1993). After the wavefield extrapolation, we have the source and receiver wavefields at all depths and I construct the image of the shot by

cross-correlating the source and receiver wavefields as follows:

$$I_{s_x} = \int S^*(s_x, x, z, \omega) R(s_x, x, z, \omega) d\omega, \quad (3.4)$$

where S^* is the complex conjugate of the source wavefield S . Finally the whole image is generated by stacking the images of all the shots as follows:

$$I = \int I_{s_x} ds_x. \quad (3.5)$$

If there is no lateral variation in the velocity field $v(x, z)$, equations 3.2 and 3.3 can be solved by the phase-shift method in the frequency-wavenumber domain with accuracy to 90° . Otherwise, as shown in chapter 2, some approximation for the square-root operator has to be made to solve equations 3.2 and 3.3 numerically. Most algorithms can well model waves that propagate almost vertically downward. For example, the classic 15° equation (Claerbout, 1971) can accurately propagate waves that are 15° from the vertical. However, they perform poorly for waves propagating almost horizontally in media with strongly lateral variation. Finite-difference methods handle lateral variation of the medium well, but they require much more costly computation to achieve little accuracy improvement for the high angle energy. Hybrid algorithms such as Fourier finite-difference take advantage of the strengths of both the finite-difference and phase-shift methods. When the lateral variation of the medium is mild, phase-shift term plays the dominant role and gives good accuracy. The finite-difference term becomes more important when the local velocity value is far from the reference velocity; of course ultimately it is difficult to propagate high-angle energy for reasonable cost. When there is strong lateral velocity variation, one-way wave equations are just not well suited to modeling waves traveling nearly orthogonal to the extrapolation direction.

The accuracy of a wavefield-extrapolation operator governs the maximum angle of the propagation direction from the vertical direction that it can accurately handle. Figure 3.1 illustrates the propagation direction of waves that a one-way wavefield-extrapolation operator, which is accurate to ψ ($\psi \leq 90^\circ$), can accurately propagate.

For source wavefields, the shadow area in Figure 3.1 (a) represents the propagation direction of waves that the wavefield-extrapolation operator can handle. For example, the wavefield-extrapolation operator can propagate waves along the direction “A”, while it cannot propagate waves along the directions “B” and “C”. Similarly, for receiver wavefields, the shadow area in Figure 3.1(b) represents the propagation direction of waves that the wavefield-extrapolation operator can handle. For example, the extrapolation operator can propagate waves along the direction “D”, while it cannot propagate waves along the directions “E” and “F”.

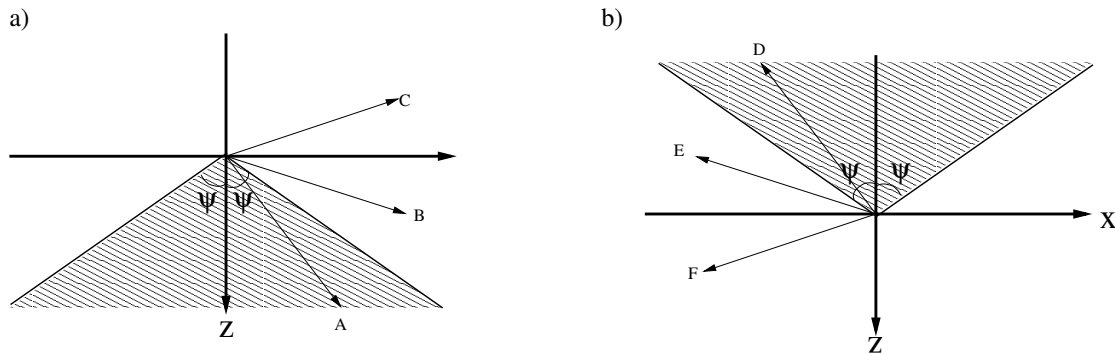
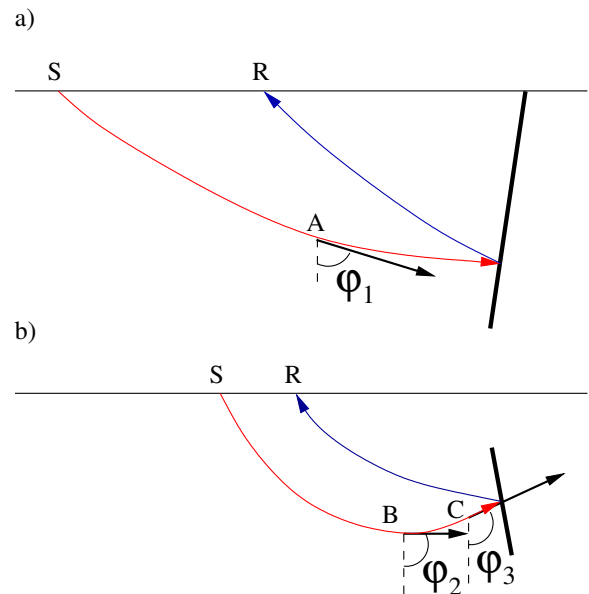


Figure 3.1: The accuracy of one-way wavefield extrapolation operator determines the propagation direction of waves that it can handle. If the extrapolation operator is accurate to ψ , the shadow area in panel (a) represents the directions of waves that it can handle for source wavefield and the shadow area in panel (b) represents the directions of waves that it can handle for receiver wavefield. plane2d/. oneway

Figure 3.2 illustrates the ray path of waves illuminating steep reflectors. Figure 3.2(a) shows waves illuminating steep reflectors has a portion of wave path that is nearly horizontal. Figure 3.2(b) shows waves illuminating steep reflectors overturn. Figure 3.2 also shows the propagation directions of waves at “A”, “B” and “C”. Angles φ_1 , φ_2 and φ_3 are the difference between the extrapolation direction and propagation direction of waves at “A”, “B” and “C”, respectively. A one-way wavefield-extrapolation operator could propagate the waves accurately at “A” and “B”, if it is sufficiently accurate ($\psi \geq \varphi_1$, $\psi \geq \varphi_2$), but it leads to a very expensive wavefield-extrapolation operator. Since ψ in Figure 3.1 is always smaller than 90° , a one-way wavefield-extrapolation operator can never propagate waves at

“C” in vertical Cartesian coordinates. Therefore, in vertical Cartesian coordinates, one-way wavefield extrapolation operators cannot propagate overturned waves. Actually, overturned energy is regarded as evanescent energy and filtered out in one-way wavefield extrapolation. Therefore, both the high-angle and overturned energy is not well handled in conventional one-way wave equation migration in vertical Cartesian coordinates. But as shown in Figure 3.2, high-angle and overturned energy is crucial for imaging steep reflectors. As a result, imaging of steep reflectors is still a problem in conventional one-way wave equation migration. These are the main two migration issues that I am attempting to resolve with plane-wave migration in tilted coordinates.

Figure 3.2: The waves illuminating steep reflectors: (a) high-angle waves; (b) overturned waves. The source location is S and the receiver location is R . Angles φ_1 , φ_2 and φ_3 are the difference between the propagation direction and extrapolation direction at “A”, “B” and “C”, respectively. If the accuracy angle ψ in Figure 3.1 is smaller than φ_1 , φ_2 and φ_3 , the events in panels (a) and (b) cannot be accurately imaged. `plane2d/. steep`



PLANE-WAVE SOURCE MIGRATION

Because of the linearity of wave equations, shot gathers can be combined into a new dataset representing a physical experiment that is not performed in reality. An important example is to combine shot gathers to synthesize plane-wave source gathers. A plane-wave source gather represents what would be recorded if a planar source originated on the surface, with geophones covering the entire survey area. It can also be regarded as an accurate phase-encoding of the shot gathers (Liu et al., 2002).

Plane-wave source gathers can be generated by performing slant-stacking over shots for each receiver. The process can be described as follows:

$$R_p(p_{s_x}, r_x, z = 0, \omega) = \int R(s_x, r_x, z = 0, \omega) e^{i\omega s_x p_{s_x}} ds_x, \quad (3.6)$$

where p_{s_x} is the ray parameter corresponding to s_x , and r_x is the receiver location at the surface. Its corresponding plane-wave source wavefield at the surface is

$$S_p(p_{s_x}, r_x, z = 0, \omega) = \int \delta(r_x - s_x) e^{i\omega s_x p_{s_x}} ds_x = e^{i\omega r_x p_{s_x}}. \quad (3.7)$$

Similar to the Fourier transformation, we can transform the plane-wave source gathers back to conventional receiver gathers by the inverse slant-stacking (Claerbout, 1985)

$$R(s_x, r_x, z = 0, \omega) = \int |\omega| R_p(p_{s_x}, r_x, z = 0, \omega) e^{-i\omega s_x p_{s_x}} dp_{s_x}. \quad (3.8)$$

In contrast to the inverse Fourier transformation, the kernel of the integral is weighted by the frequency $|\omega|$. This inverse transform is also called “rho filter” in Radon transform literature (Claerbout, 1985).

Similar to shot-profile migration, there are two steps to migrating a plane-wave source gather by typical plane-wave migration. First, the source wavefield S_p and receiver wavefield R_p are extrapolated independently to all depths in the subsurface, using one-way wave equations 3.2 and 3.3, respectively. Second, the image of a plane-wave source with a ray parameter p_{s_x} is constructed by cross-correlating the source and receiver wavefields weighted with the frequency ω :

$$I_{p_{s_x}}(x, z) = \int |\omega| S_p^*(p_{s_x}, x, z, \omega) R_p(p_{s_x}, x, z, \omega) d\omega, \quad (3.9)$$

where S_p^* is the complex conjugate of the source wavefield S_p . The whole image is constructed by stacking the images of all possible plane-wave sources:

$$I_p = \int \int I_{p_{s_x}}(x, z) dp_{s_x}. \quad (3.10)$$

Because both slant-stacking and migration are linear operations, in the continuous case, the image of the plane-wave migration I_p is equivalent to the image obtained by shot-profile migration (Liu et al., 2002; Zhang et al., 2005b). In the discrete form in practice, a sufficient number of p_{sx} values are needed to make the two images equivalent.

WAVEFIELD EXTRAPOLATION IN TILTED COORDINATES

The extrapolation direction plays a key role in one-way wave equation wavefield extrapolation, because the waves traveling along the extrapolation direction are propagated the most accurately. The extrapolation direction, however, has no physical meaning; it is only a direction artificially assigned in numerical algorithms. In conventional one-way wave equation migration, we use vertical Cartesian coordinates and extrapolate wavefields vertically. In 2D, the extrapolation direction can be changed by rotating the coordinates as follows:

$$\begin{pmatrix} x' \\ z' \end{pmatrix} = \begin{pmatrix} \cos \theta & \sin \theta \\ -\sin \theta & \cos \theta \end{pmatrix} \begin{pmatrix} x \\ z \end{pmatrix}. \quad (3.11)$$

We call the new coordinate system, (x', z') , a tilted Cartesian coordinate system (tilted coordinate system), and the angle θ the tilting angle for the coordinate system.

The acoustic wave equation 3.1 is invariant to coordinate rotations. Therefore, similar to the vertical Cartesian coordinates, the up-going and down-going one-way wave equations can be obtained by splitting the acoustic wave equation in the tilted coordinate system (x', z') :

$$\frac{\partial}{\partial z'} S = -\frac{i\omega}{v} \sqrt{1 + \left(\frac{v}{\omega} \frac{\partial}{\partial x'} \right)^2} S, \quad (3.12)$$

$$\frac{\partial}{\partial z'} R = +\frac{i\omega}{v} \sqrt{1 + \left(\frac{v}{\omega} \frac{\partial}{\partial x'} \right)^2} R. \quad (3.13)$$

The extrapolation direction of equations 3.12 and 3.13 parallels the z' axis, which is at the angle θ from the vertical direction. Figure 3.3 illustrates the coordinate transformation. Coordinates (x, z) are vertical Cartesian coordinates and (x', z') are tilted coordinates. The notation s_x represents the source location and $r_{x1}, r_{x2}, \dots, r_{x5}$, represent the corresponding receiver locations. The accuracy of the one-way extrapolators remains important for wavefield extrapolation in tilted coordinates. The more accurate extrapolator we design, the less sensitive the migration to the extrapolation direction. With an extrapolator that is not very accurate, such as 15° equation, if we rotate from one tilted coordinate system to another through a small angle, waves handled well in one coordinate system might not be handled well in the other one. In contrast, with an accurate extrapolator, waves can be handled in both tilted coordinate systems. Since one-way wave equations in tilted coordinates are exactly same as those in vertical Cartesian coordinates, all the schemes used to improve the accuracy in the conventional Cartesian coordinates developed in chapter 2 still work in tilted coordinates.

In order to extrapolate wavefields in a tilted coordinate system, it is required to interpolate the surface dataset, velocity model and image between the coordinate systems and migrate the dataset on a slanted surface in implementation. In Figure 3.3, source and receivers are on a regular grid at the surface $z = 0$ in the conventional Cartesian coordinates. Figure 3.4 shows the source and receivers in a grid in the tilted coordinates (x', z') . The source and receivers in the tilted coordinates are on the inclined surface given by

$$x' \cos \theta - z' \sin \theta = 0. \quad (3.14)$$

In tilted coordinates, source and receiver locations do not fall on regular grid nodes of the tilted coordinate system. To run wavefield extrapolation, the recorded dataset received at the receivers $r_{x1}, r_{x2}, \dots, r_{x5}$ must be interpolated onto the regularized grid points around the slanted surface define by equation 3.14 in the new coordinate system (x', z') . For instance, the value of the wavefield at r_{x3} is spread onto the grid points a,b,c, and d. The velocity must also be interpolated onto the regular

grid in the new coordinates. In tilted coordinates, the survey is taken along the slanted surface defined by equation 3.14. As I extrapolate the wavefield, I inject the recorded data on the slanted surface (along $z = 0$ or $x' \cos \theta - z' \sin \theta = 0$) into the downward continued field at each step. I begin the wavefield extrapolation from the plane $z' = 0$. For the i -th step extrapolation, when the depth level $z' = i\Delta z$ intersects the slanted recording surface, $x' \cos \theta - z' \sin \theta = 0$, the wavefield on the regular grid points around the slanted surface, which is spread from the recorded wavefield, is added to the wavefield extrapolated from its previous depth level. After the wavefields on the slanted surface being injected, the wavefield extrapolation is the same as the conventional one.

Figure 3.3: Two-dimensional coordinate system rotation. The coordinates (x, z) are conventional vertical Cartesian coordinates, and (x', z') are tilted coordinates. The notation s_x represents the source location and $r_{xi}, i = 1, 2, \dots, 5$, represent receiver locations. The source and receivers are on regular grids in vertical Cartesian coordinates.

plane2d/. tiltcoordinate1

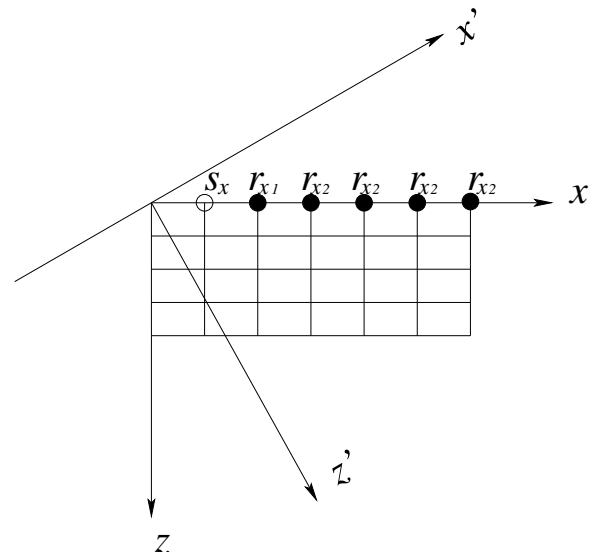
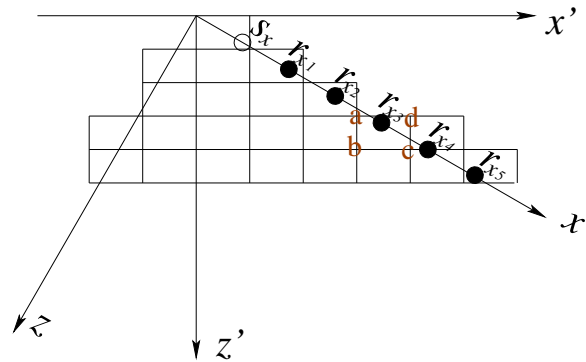


Figure 3.5 shows a model revised from the Sigsbee 2A (Sava, 2006). The sedimentary part of the model has been extended vertically and horizontally to allow recording the overturned waves at the surface from the overhanging salt flank. The rays depict portions of the overturned waves from the overhanging flanks on opposite sides of the salt. Figure 3.6 shows the model and rays in a tilted coordinate system with a tilting angle of 70° . Figure 3.5 and 3.6 illustrate that waves that overturn in vertical Cartesian coordinates do not overturn in a tilted coordinate system with a proper tilting direction.

Figure 3.4: Source and receivers in a grid defined in a tilted coordinate system. Coordinates (x, z) are conventional vertical Cartesian coordinates, and (x', z') are tilted coordinates. Notation s_x represents the source location and $r_{xi}, i = 1, 2, \dots, 5$, represent receiver locations. In tilted coordinates, these locations are on a slanted surface and do not fall on regular grid points. The wavefield values recorded at these locations are interpolated onto regular grid points around the slanted surface. For example, the wavefield on r_{x3} is interpolated onto the grids a, b, c, and d.



VERTICAL TRANSVERSELY ISOTROPIC (VTI) MEDIA IN TILTED COORDINATES

As defined in chapter 1, a medium is VTI if it has a vertical rotation symmetry axis in physical space. For wavefield extrapolation, as long as the symmetry axis of the medium parallels the extrapolation direction, a VTI wavefield extrapolation operator will be effective. For migration for VTI media in vertical Cartesian coordinates, both the symmetry axis of the medium and the extrapolation direction are vertical. Thus the symmetry axis parallels the extrapolation direction, and we use VTI wavefield extrapolation operator for migration. Figure 3.7 illustrates the behavior of a thin-layer VTI medium in tilted coordinates. Panel a shows that the VTI medium, tilted coordinates (x', z') , and symmetry axis in vertical Cartesian coordinates (x, z) . The symmetry axis parallels the extrapolation direction (z -axis). Panel b shows that in tilted coordinates, the thin layers become dipping, and the symmetry axis of the

medium does not parallel the extrapolation direction (z' -axis). Therefore, the medium becomes tilted TI in the new coordinates. A tilted TI wavefield-extrapolation scheme is then needed to run a migration when coordinates for a VTI medium are tilted. We can use either implicit finite-difference schemes for tilted TI media based on weighted least-square optimization developed in chapter 2 or explicit finite-difference schemes (Shan and Biondi, 2005).

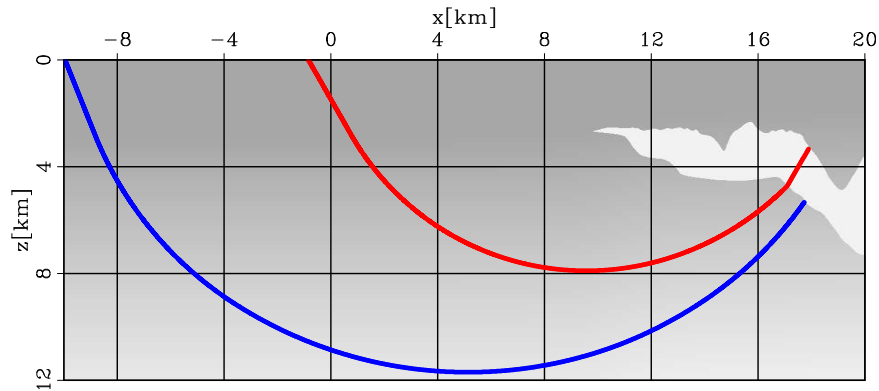


Figure 3.5: A velocity model revised from Sigsbee 2A. The sedimentary part of the model is extended to allow the overturned waves from the overhanging salt flanks to be received at the surface. The rays represent the overturned waves from the overhanging salt flank. `plane2d/. zigvelwithraycart`

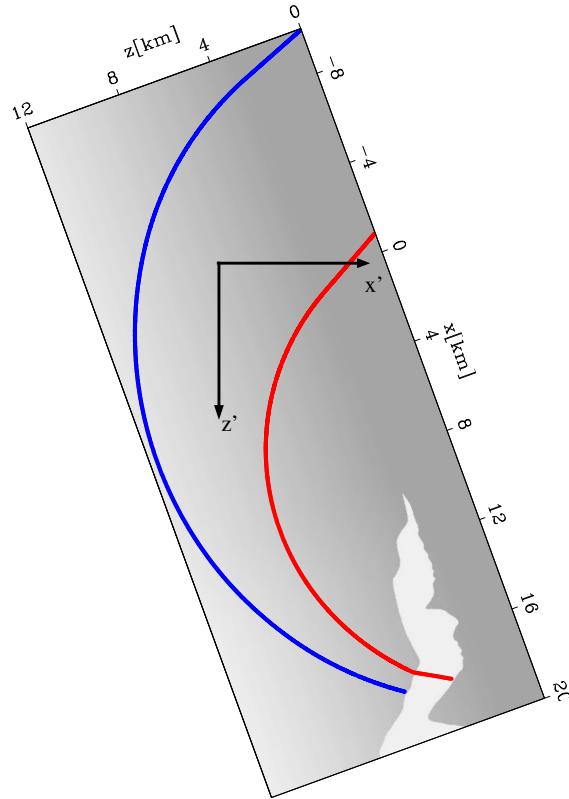
PLANE-WAVE MIGRATION IN TILTED COORDINATES

I introduced the concepts of plane-wave migration and migration in tilted coordinates in previous sections. Here, I discuss the combination of these two and provide a powerful method for migrating steep and overturned events. I first discuss why point-source migration in tilted coordinates would be ineffective. Then I describe how to design tilted coordinates for each plane-wave source, and finally I discuss how the use of reciprocity improves plane-wave migration in tilted coordinates.

Waves from a point source propagate radially, so waves start from the same spatial location and travel along all directions. Therefore, a tilted coordinate system offers no advantage; no matter what choice of tilting direction, no Cartesian coordinate

Figure 3.6: The velocity model and overturned waves in a tilted coordinate system. The overturned waves in vertical Cartesian coordinates do not overturn in the tilted coordinate system.

plane2d/. zigvelwithraytilt



system can cover all the propagation directions of a point source. Figure 3.8a shows rays illustrating waves from a point source in tilted coordinates. In Figure 3.8a, with the coordinates (x, z) rotated counter-clockwise, the high-angle energy traveling toward the right can be well propagated but that traveling toward the left (represented by dash lines), cannot be accurately propagated, even at small starting angle from vertical. The propagation directions of a plane-wave source at different horizontal spacial locations at the surface, however, are generally similar (Figure 3.8b). In plane-wave migration, I decompose the wavefield into plane-wave source gathers by slant-stacking with each plane-wave source gather characterized by a ray-parameter p_{s_x} . Given the velocity at the surface v_{z_0} , the propagation direction of the plane-wave source is defined by the vector (q_x, q_z) , where $q_x = p_{s_x} v_{z_0}$ and $q_z = \sqrt{1 - q_x^2}$. Therefore, the ray parameter p_{s_x} defines the propagation direction of the plane-wave source at the surface. The take-off angle of the plane-wave source, α , can be calculated

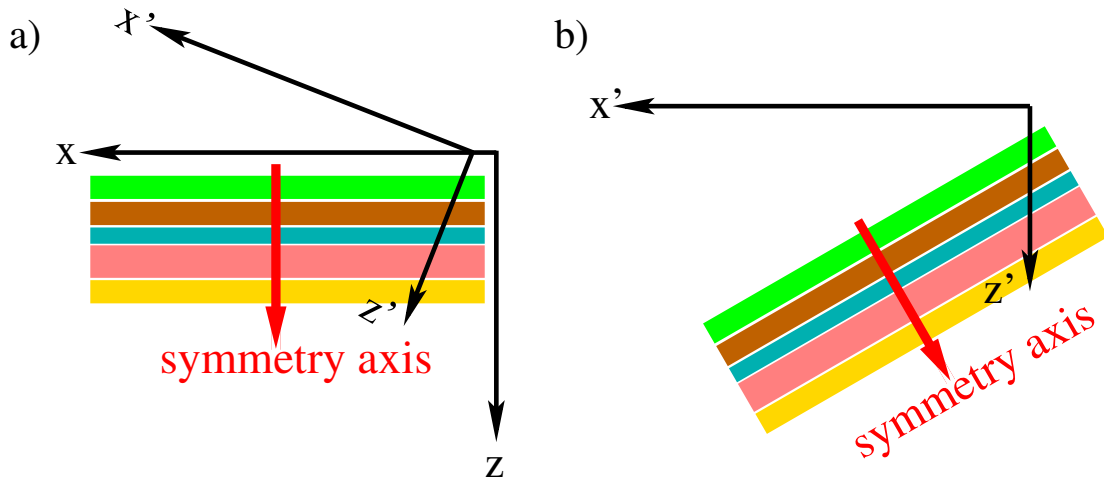


Figure 3.7: VTI media in vertical Cartesian coordinates become tilted TI media in tilted coordinates. (a) A thin-layer VTI medium, its symmetry axis, and tilted coordinates shown in vertical Cartesian coordinates. (b) The VTI medium in tilted coordinates. The horizontal layers become dipping layers; thus the medium becomes a tilted TI medium in the new coordinates. `plane2d/. vti-tilted`

as follows:

$$\alpha = \arccos q_z. \quad (3.15)$$

If we assume the velocity to be invariant at the surface, the initial propagation direction of the plane-wave source defined in equation 3.7 at the surface is same for all spacial points. This is true for marine datasets; for land datasets the starting direction of a plane-wave source is similar for all spacial points if the velocity at the surface does not vary strongly. Therefore, a tilted coordinate system can cover most propagation directions of a plane-wave source at different spacial points, although the propagation direction of plane-waves can change because of the velocity heterogeneities.

Given the plane-wave source with take-off angle of α , I use tilted coordinates (x', z') with a tilting angle θ close to its take-off angle α . Usually velocity increases with the depth, and the propagation direction of waves becomes increasingly horizontal, so in practice the tilting angle θ is a little larger than the take-off angle. In 2D, the number of coordinate systems used in migration is the same as the number of

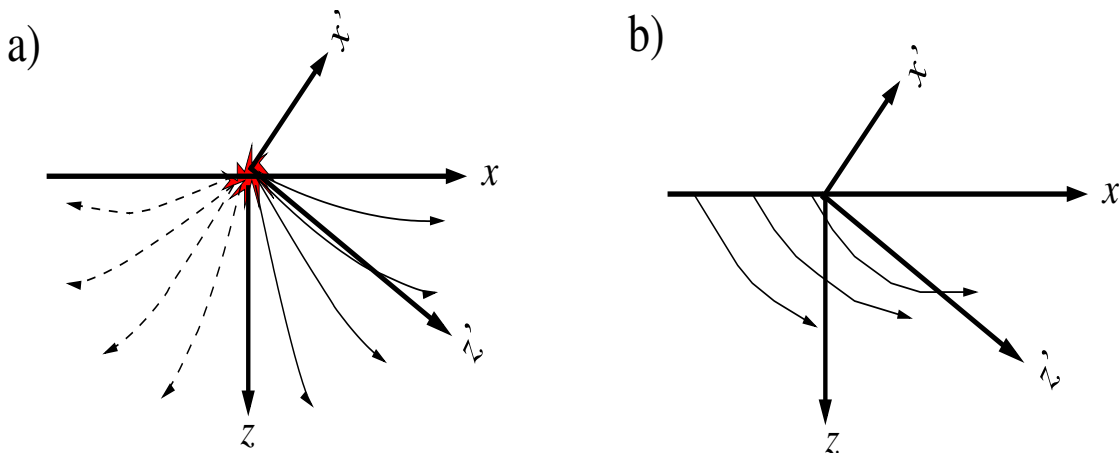
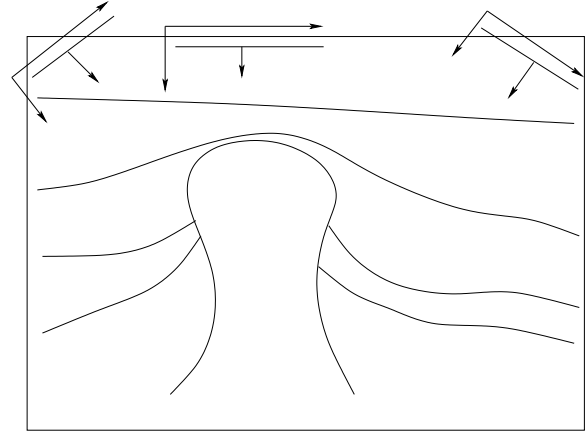


Figure 3.8: Point source (a) and plane-wave sources (b) in tilted coordinates. Waves from a point source propagate radially, and the waves represented by the dash line rays in panel (a) cannot be propagated accurately when we rotate the coordinates counter-clockwise. In contrast, the propagation directions of the plane-wave source are similar at different spacial points along the surface $z = 0$, so generally they can be extrapolated accurately in a tilted coordinate system. plane2d/. pointplane

plane-wave sources. I will show in chapter 4, in 3D the number of coordinate systems used in migration is much smaller than the number of plane-wave sources to save the computational cost.

Figure 3.9 depicts three typical plane-wave sources and their tilted coordinate systems. Plane-wave sources with a small take-off angle mainly illuminate reflectors that are almost horizontal, so I extrapolate wavefields in vertical Cartesian coordinates. In contrast, plane-wave sources with a large take-off angle mainly illuminate steep reflectors, and I use a tilted coordinate system with a large tilting angle. For these waves, it is difficult to model them accurately in vertical Cartesian coordinates, but in tilted coordinates their propagation direction is close to the extrapolation direction, so they can be imaged accurately. Waves that overturn in vertical Cartesian coordinates do not overturn in a proper tilted coordinate system. Therefore, with plane-wave migration in tilted coordinates, each plane-wave source has its own tilted coordinate system such that the extrapolation direction is closer to propagation directions, and steep reflectors and overturned waves can be well imaged.

Figure 3.9: Plane-wave sources and their associated tilted coordinates. The tilting direction for the coordinates corresponding to the plane-wave source depends on its take-off angle. Depicted are three typical plane-wave sources with zero, negative, and positive ray parameter, respectively. For $p_{sx} = 0$, I use conventional Cartesian coordinates. For $p_{sx} > 0$, I rotate coordinates counter-clockwise, and for $p < 0$, I rotate coordinates clockwise. `plane2d/. planetilt`



Marine streamer data are usually recorded for only positive or negative offsets. That is, the acquisition is so-called off-end. Following a conventional approach, however, we simulate split-spread acquisition through use of reciprocity. Merging the original data and the data obtained by reciprocity, we obtain a dataset that would be recorded with a split-spread recording geometry. In plane-wave migration, the aperture for a dataset with split-spread geometry are almost same as that with only single-sided offset; thus the computation cost of plane-wave migration with reciprocity is also the same as that without reciprocity, but split-spread recording geometry improves the robustness of plane-wave gathers and the signal-to-noise ratio in the computed image (Liu et al., 2006).

Plane-wave migration in tilted coordinates can be benefited more than conventional one-way plane-wave migration from the reciprocity. For plane-wave migration in tilted coordinates, a split-spread dataset means designing the coordinates with the propagation direction of both the source and receiver waves at the surface taken into consideration. Figure 3.10 illustrates how reciprocity helps to image steep salt flanks when the source ray does not overturn but the receiver ray does. The source location is s and receiver location is r . Because of the linearity of migration, the resulting image obtained by migrating a dataset with split-spread geometry is equivalent to the stack

of images obtained by migrating the following two datasets: the dataset with only positive offset and the dataset with only negative offset. The positive-offset dataset is the original recorded dataset $R(s_x = s, r_x = r, z = 0, \omega)$, while the negative-offset dataset is the one obtained from reciprocity, $R(s_x = r, r_x = s, z = 0, \omega)$. Without reciprocity, migration is run only on positive-offset dataset $R(s_x = s, r_x = r, z = 0, \omega)$ and the ray parameter for a plane-wave source, p_{s_x} , is p_s , the ray parameter corresponding to s . Given the surface velocity v_{z_0} , the take-off angle for the plane-wave source is $\alpha_s = \arcsin(p_s v_{z_0})$. Both source and receiver wavefields are extrapolated in the coordinates (x_s, z_s) with the z_s -axis α_s from the vertical direction. As a consequence, the overturned receiver wavefield would not be accurately modeled and the overturned event not correctly imaged if we migrate directly the original dataset using plane-wave migration in tilted coordinates. However, this event can be well imaged if we apply plane-wave migration in tilted coordinates on the negative-offset dataset $R(s_x = r, r_x = s, z = 0, \omega)$, which is obtained from the original dataset by reciprocity. When we apply plane-wave migration on the negative-offset dataset, we slant-stack the negative-offset dataset as follows:

$$R(p_{s_x}, r_x, z = 0, \omega) = \int R(s_x = r, r_x = s, z = 0, \omega) e^{i\omega s_x p_{s_x}} ds_x \quad (3.16)$$

$$= \int R(r, s, z = 0, \omega) e^{i\omega r p_r} dr \quad (3.17)$$

Therefore, the ray parameter for a plane-wave source, p_{s_x} is p_r , the ray parameter corresponding to r , and the take-off angle is $\alpha_r = \arcsin(p_r v_{z_0})$. Both source and receiver wavefields are extrapolated in the coordinates (x_r, z_r) with z_r -axis α_r from the vertical direction. In the coordinates (x_r, z_r) , both source and receiver waves are accurately propagated, and the overturned energy can be accurately imaged. Therefore, if we apply plane-wave migration in tilted coordinates to the dataset with split-spread geometry, this event is well imaged, since the resulting image is the stack of the images for positive- and negative-offset datasets.

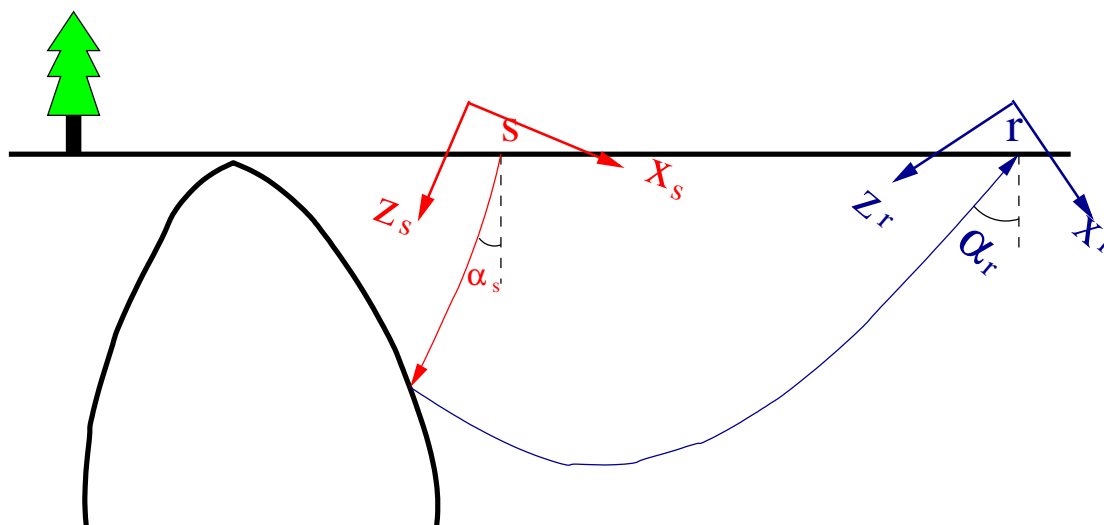


Figure 3.10: Reciprocity improves plane-wave migration in tilted coordinates. The source location is at s , and the receiver location is at r . For this event, the source ray does not overturn, but the receiver ray does. If we were to run plane-wave migration in tilted coordinates only the original one-side offset data, we would use the coordinates (x_s, z_s) for both source and receiver waves. The direction of (x_s, z_s) is determined by the initial source ray direction at the surface. In this coordinate system, the source waves can be handled well but the overturned receiver wave cannot. If we were to run the same migration only for the data generated by reciprocity, we would use the coordinates (x_r, z_r) for both source and receiver wavefield extrapolation. The direction of (x_r, z_r) is determined by the receiver ray direction at the surface. In this coordinate system, both the source and receiver waves can be handled with accuracy.

plane2d/. reciprocity

NUMERICAL EXAMPLES

An exploding-reflector dataset with overturned waves

My first example is a synthetic dataset designed to test of imaging overturned waves (Sava, 2006). Figure 3.5 shows the model with typical overturned rays. The exploding reflector data are modeled from the boundary of the salt and recorded at the surface, using the time-domain two-way wave equation. Figure 3.11 shows the exploding reflector data received at the surface. The overturned events are recorded from $x =$

–20 to $x = 5$ km at $t = 10$ to 25 s.

To make sure that it is overturned events (at “A” in Figure 3.11) that are imaged in the tilted coordinates, I mute the non-overturned events that are received at the surface earlier than 10 s (at “B” in Figure 3.11). I migrate the dataset using a tilted coordinate system with a tilting angle of 70° shown in Figure 3.6. As shown in the previous section, the waves that illuminate the overhanging salt flanks do not overturn in a tilted coordinate system with a tilting angle of 70° (Figure 3.6). For comparison, I also migrate the dataset using reverse-time migration, which is based on two-way wave equation and can accommodate turning waves in a conventional vertical Cartesian coordinate system. Figure 3.12 compares the images obtained by these two methods. Figure 3.12a is the migrated image obtained by plane-wave migration in tilted coordinates, and Figure 3.12b is the image obtained by reverse-time migration. To keep computation cost down, the reverse-time migration result has lower frequency; otherwise both images are comparable. The comparison shows that most of the overturned energy is imaged by the migration in tilted coordinates, and the overhanging salt flanks are imaged correctly.

Impulse responses

The second model has a salt body with steep flanks embedded in a smoothly varying sediment. Figure 3.13 shows the comparison of the impulse responses of the two-way wave equation migration (Figure 3.13a), one-way wave equation migration in vertical Cartesian coordinates (Figure 3.13b), and plane-wave migration in tilted coordinates (Figure 3.13c). I use one hundred plane-wave sources and tilted coordinate systems to generate the impulse response shown in Figure 3.13c. From Figure 3.13a and b, we see that the action of the one-way wave equation mimics that of the two-way wave equation well for energy that propagates with small angle from the vertical, but it has reduced accuracy for energy that propagates nearly horizontally and loses energy that overturns. The wave front of the direct arrival in Figure 3.13c matches that of the two-way wave equation well, even at high angles and for overturned waves,

despite being extrapolated with the one-way wave equation. Figure 3.13c has none of reflections or multiples seen in Figure 3.13a. This is not surprising, since the one-way wave-equation extrapolator allows no such features. This impulse-response comparison shows the potential to image the steep reflectors and overturned waves by plane-wave migration in tilted coordinates.

BP 2004 velocity benchmark dataset

The BP 2004 velocity benchmark dataset is designed to test velocity estimation (Billette and Brandsberg-Dahl, 2005). Figure 5.6 shows the velocity model of the dataset. One of the challenges for velocity analysis of this dataset is the delineation of the two complicated salt bodies. The left salt, modeled after a salt body in the Gulf of Mexico, is complex and multi-valued, with a highly rugose top. Parts of its top and flank as well as the sediments inside the salt are steeply dipping, making it difficult for one-way wave equation migration to image these features in vertical Cartesian coordinates. The right salt body, modeled after a salt feature in west of Africa, is deeply rooted, and its two roots are steep. Overturned and prismatic waves play a key role in imaging these two roots. It is difficult for one-way wave equation migration to image them in conventional vertical Cartesian coordinates. Even with the true velocity, it is still challenging to image the complex salt bodies.

Plane-wave migrations were run in both vertical Cartesian and tilted coordinates for comparison. Two hundred plane-wave sources were generated in total, with the take-off angles at the surface ranging from -45° to 45° . For plane-wave migration in tilted coordinates, vertical Cartesian coordinates are used for small take-off angle plane-wave sources, and 160 coordinate systems are used in total. No attempt is made to run multiple attenuation; thus the images are contaminated by the multiples. The 80° finite-difference one-way extrapolator (Lee and Suh, 1985) was applied for both migrations.

Figure 3.15 shows the velocity model of the left salt body. Figure 3.16 and Figure 3.17 offer a comparison of the images from the two migrations. The annotation A,

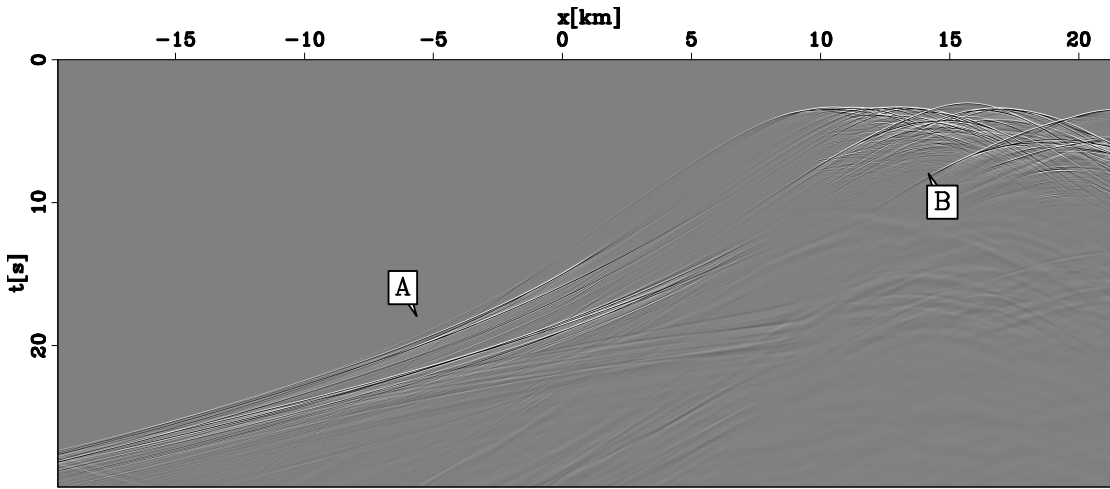


Figure 3.11: The exploding reflector dataset from the revised Sigsbee 2A model. The overturned energy are recorded from -20 to 5 km at $t = 10$ to 25 s. The energy recorded earlier than 10 s is muted before migration to verify the imaging of overturned waves. `plane2d/. zigdata`

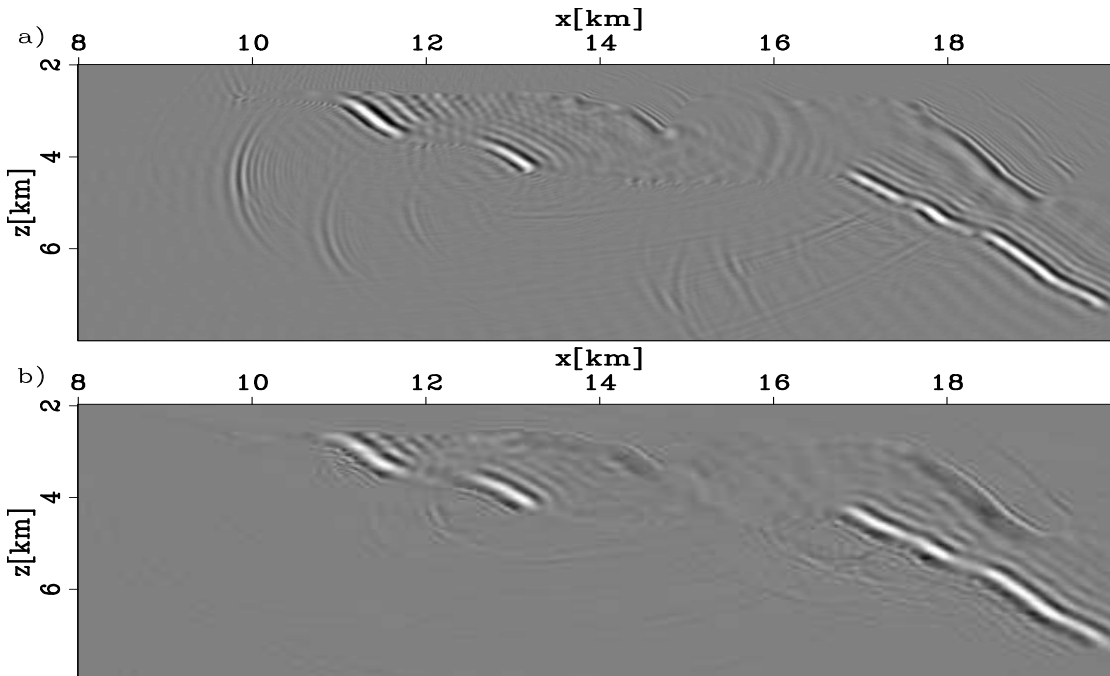


Figure 3.12: Migrated image of the overturned waves: migration in tilted coordinates (a) and reverse-time migration (b). `plane2d/. zigimage`

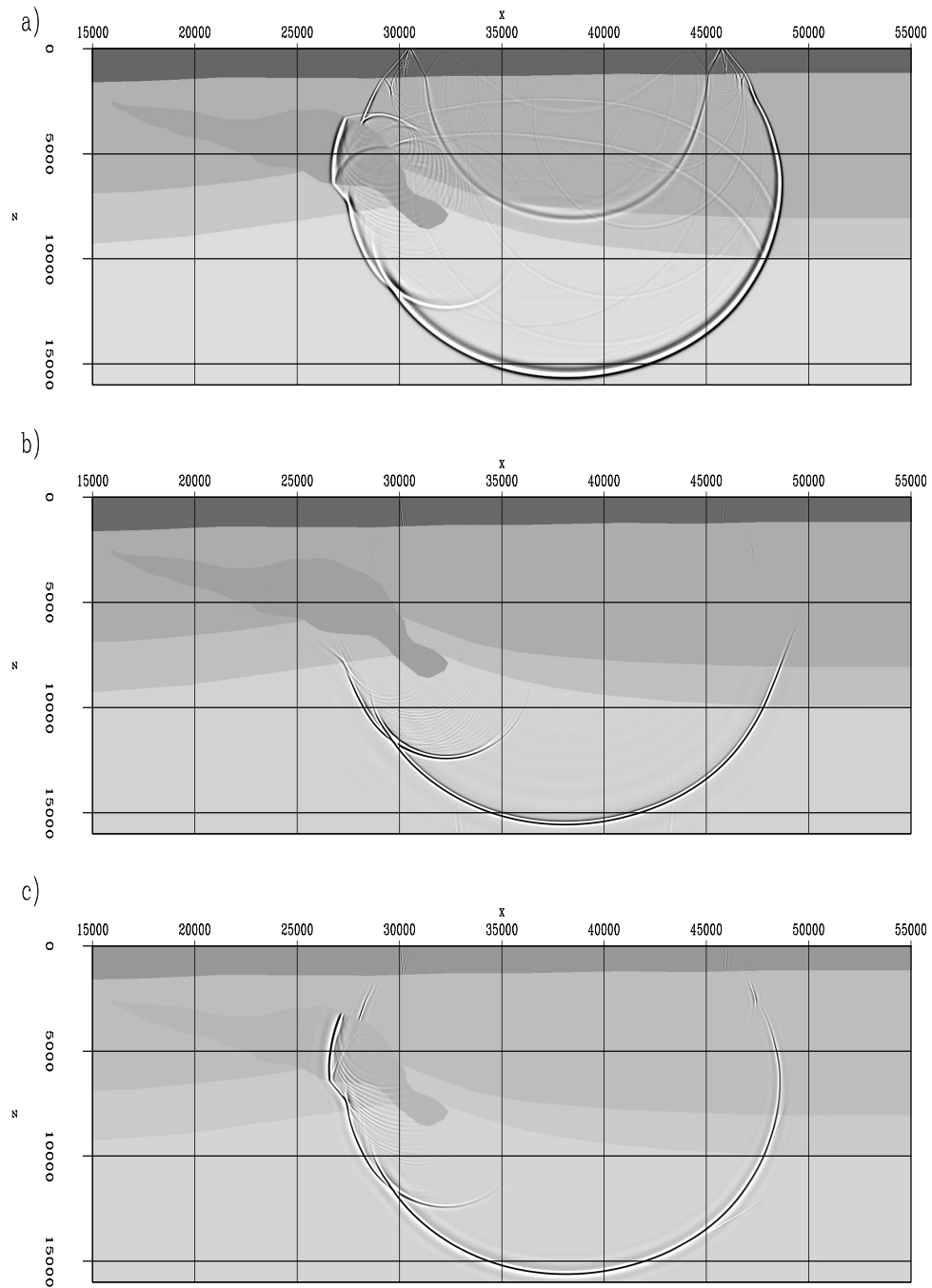


Figure 3.13: Impulse-response comparison among (a) two-way wave equation migration, (b) one-way wave equation migration in vertical Cartesian coordinates, and (c) plane-wave migration in tilted coordinates. `plane2d/. impulse`

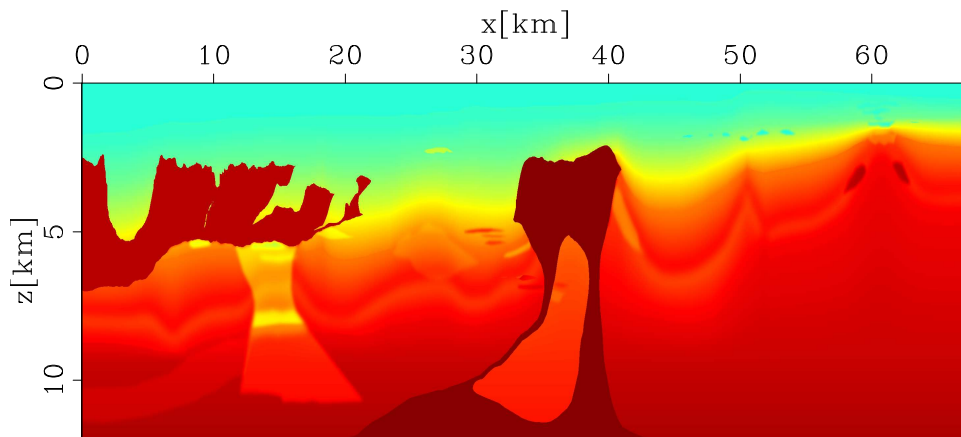


Figure 3.14: The velocity model of BP velocity benchmark. `plane2d/. bpvel`

B, C, D, E, F, G, and H denote the same locations in Figures 3.15, 3.16, and 3.17. Figures 3.16 and 3.17 are the images obtained by plane-wave migration in tilted coordinates, and vertical Cartesian coordinates, respectively. In both figures, the bottom of the large salt canyon is well imaged, but the steep flanks of the canyon at A and B, which are absent in Figure 3.17, are correctly imaged in Figure 3.16. This is also true for the small salt canyon at C. Although the salt canyon flank at D is imaged by plane-wave migration in vertical Cartesian coordinates in Figure 3.17, it is not positioned correctly compared to the model (Figure 3.15) because of the limited accuracy of the extrapolation operator. The rugose top of the salt in Figure 3.16 is more continuous than that in Figure 3.17. The steep salt flanks in the multi-valued part at E, F, and G, and the sediment intrusion below the small salt canyon at H, are greatly improved in Figure 3.16 by plane-wave migration in tilted coordinates, because they are illuminated by overturned or high-angle energy, which cannot be handled by the one-way wave-equation migration in vertical coordinates.

Figure 3.18 shows the velocity model of the right salt body. Figure 3.19 and Figure 3.20 are the comparison of the images from the two migrations. The annotation A, B, C, D, and E in Figure 3.18, 3.19 and Figure 3.20 denote the exact same locations. Figure 3.19 is obtained by plane-wave migration in tilted coordinates, and Figure 3.20 is obtained by plane-wave migration in vertical Cartesian coordinates. The top of salt

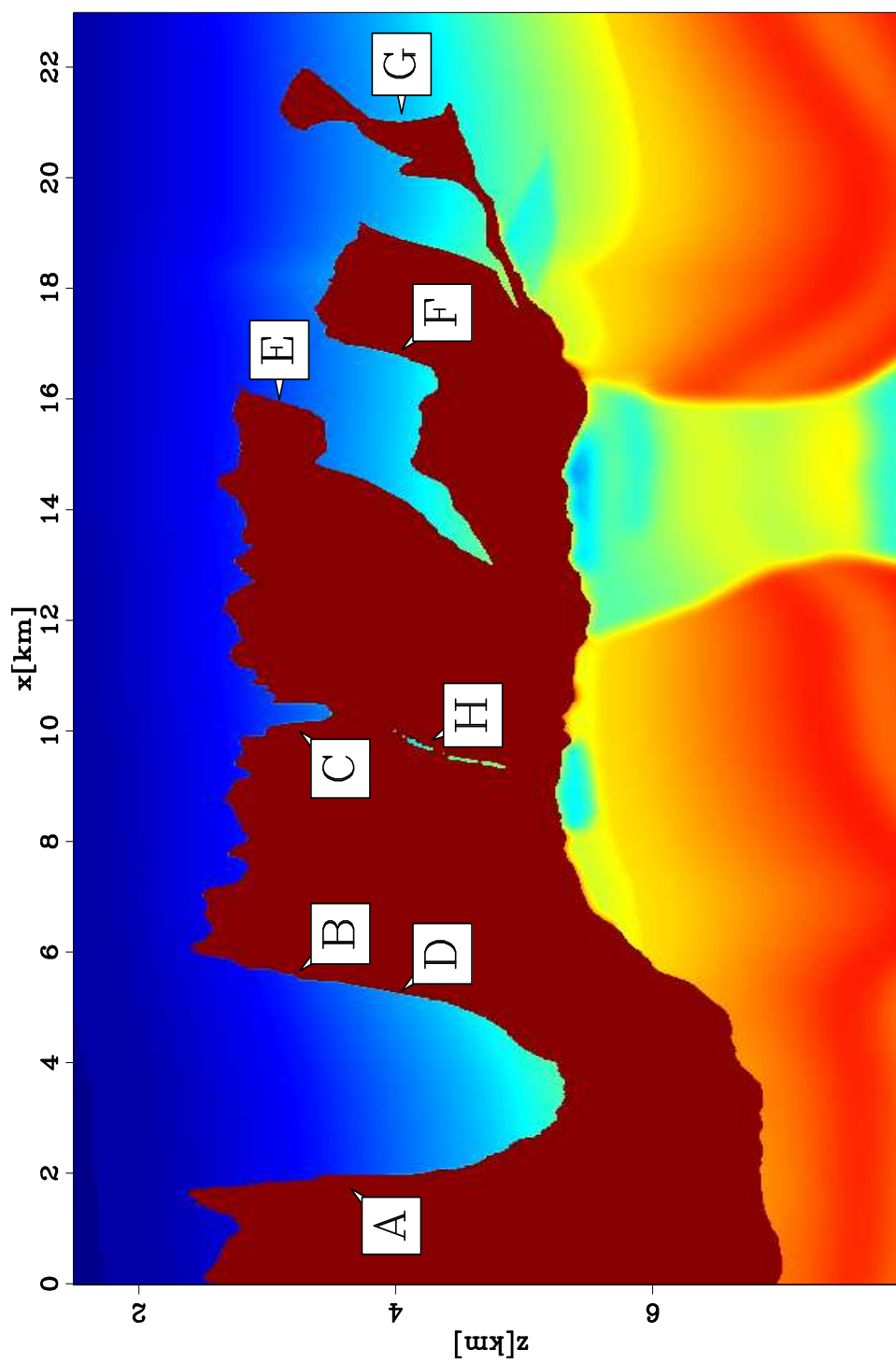


Figure 3.15: Detail of velocity model for the left salt body. `plane2d/. bpleftvel`

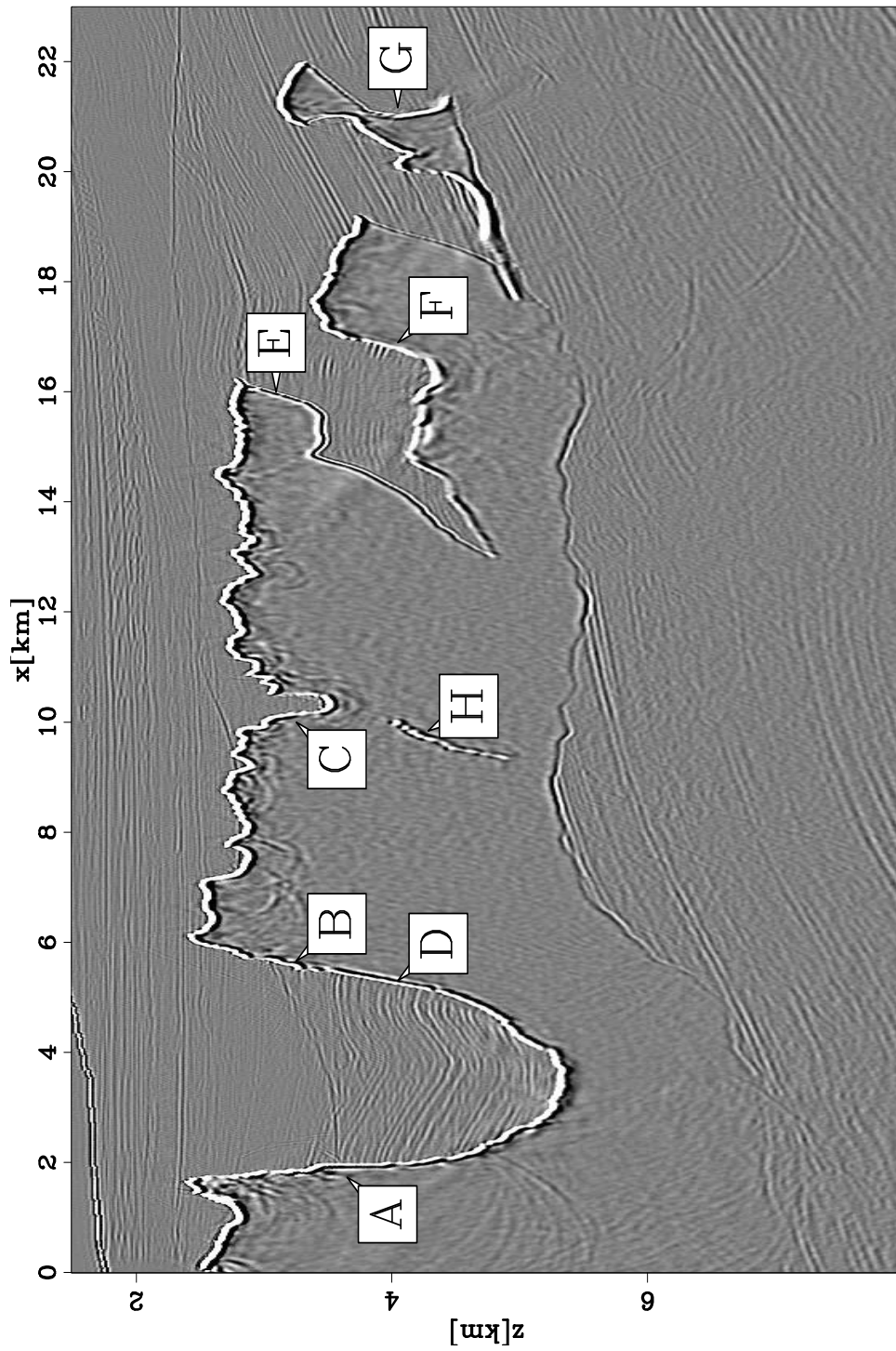


Figure 3.16: Image of the left salt body obtained by plane-wave migration in tilted coordinates. `plane2d/. bpleftsalttilt`

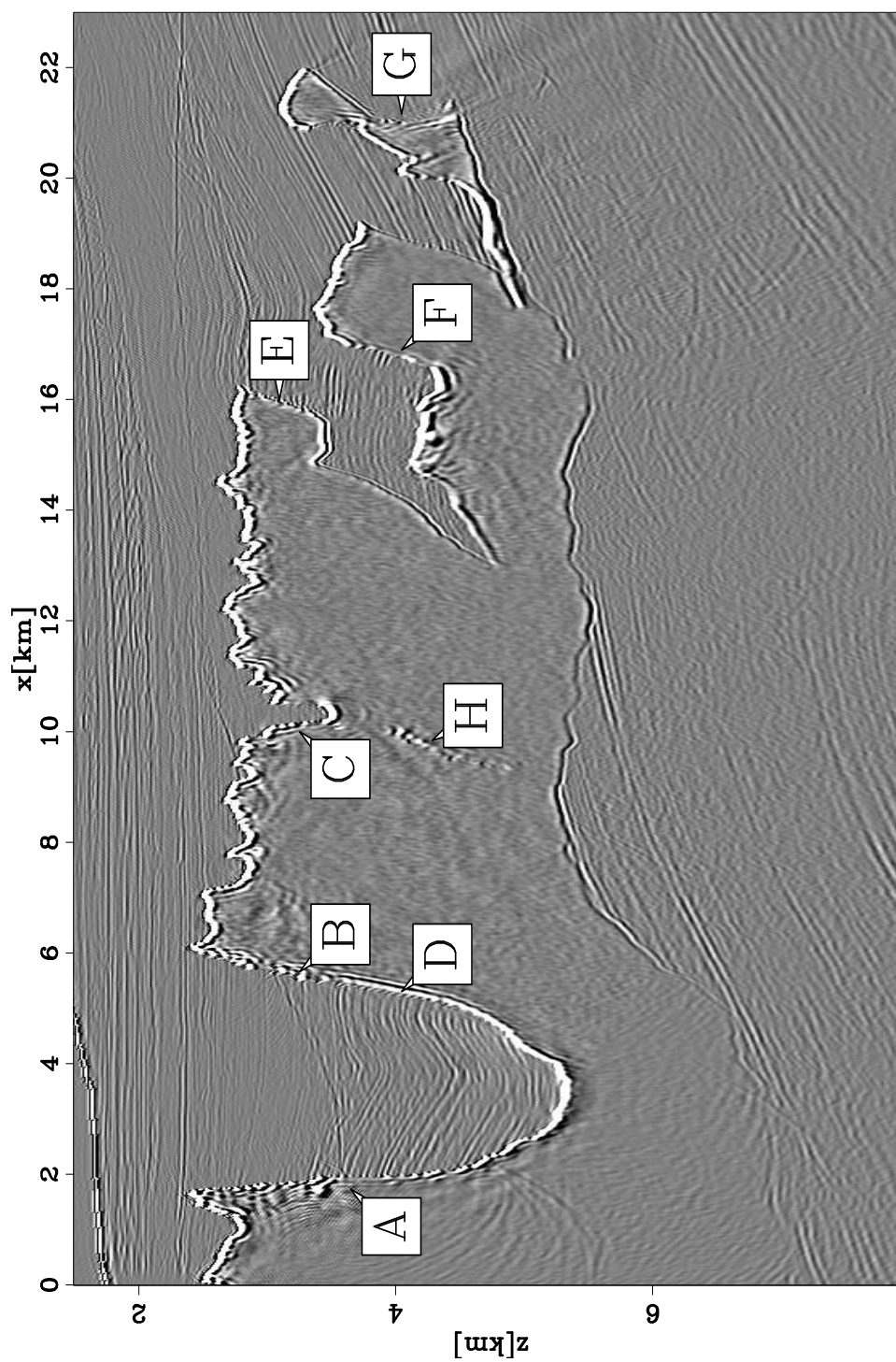


Figure 3.17: Image of the left salt body obtained by plane-wave migration in vertical Cartesian coordinates. `plane2d/. bpleftsaltnotilt`

and sediments inside the salt are well imaged in both panels, but the salt flanks at A, B, and D that should be illuminated by the overturned or high angle energy are absent in Figure 3.20. In contrast, this overturned energy is handled by plane-wave migration in tilted coordinates, producing good image of flanks of the salt. In Figure 3.20, we can see the steep flank at C, but it is incorrectly positioned compared to the model (Figure 3.18) because of the limited accuracy of the extrapolation operator. Note that the salt flank at E is absent in both images. This flank is mainly illuminated by prismatic waves that bounce at the salt flanks below E. The propagation direction of the prismatic waves varies greatly before and after bounce at the salt boundary, making it is difficult to model them accurately in any one Cartesian coordinate system.

Figures 3.16, 3.17 3.19 and 3.20 show that with the same extrapolation operator, plane-wave migration in tilted coordinates can handle overturned and high angle energy, and delineate the complex salt body much better than can one-way wave-equation migration in vertical Cartesian coordinates.

A VTI synthetic dataset

Figure 3.21 shows the parameters of the VTI model for a synthetic dataset. Panel a shows the density model, panel b the vertical qP-wave velocity, and panel c the anisotropy parameter ε . The highest value of ε in the anisotropic layer is 0.3. The value of δ of the model is zero.

The overall structure of the model is simple. It is a salt body surrounded by sedimentary layers, one of which is anisotropic. The salt flank is relative steep, and part of flank is overhanged. Rays in Figure 3.22 show that the flank is mainly illuminated by overturned waves.

Figures 3.23 through 3.25 compare various images of the synthetic dataset. Figure 3.23 is obtained by isotropic plane-wave migration in tilted coordinates, Figure 3.24 is obtained by the anisotropic plane-wave migration in vertical Cartesian coordinates, and Figure 3.25 is obtained by the anisotropic plane-wave migration in tilted coordinates. One hundred plane-waves were generated in total and the take-off angles at

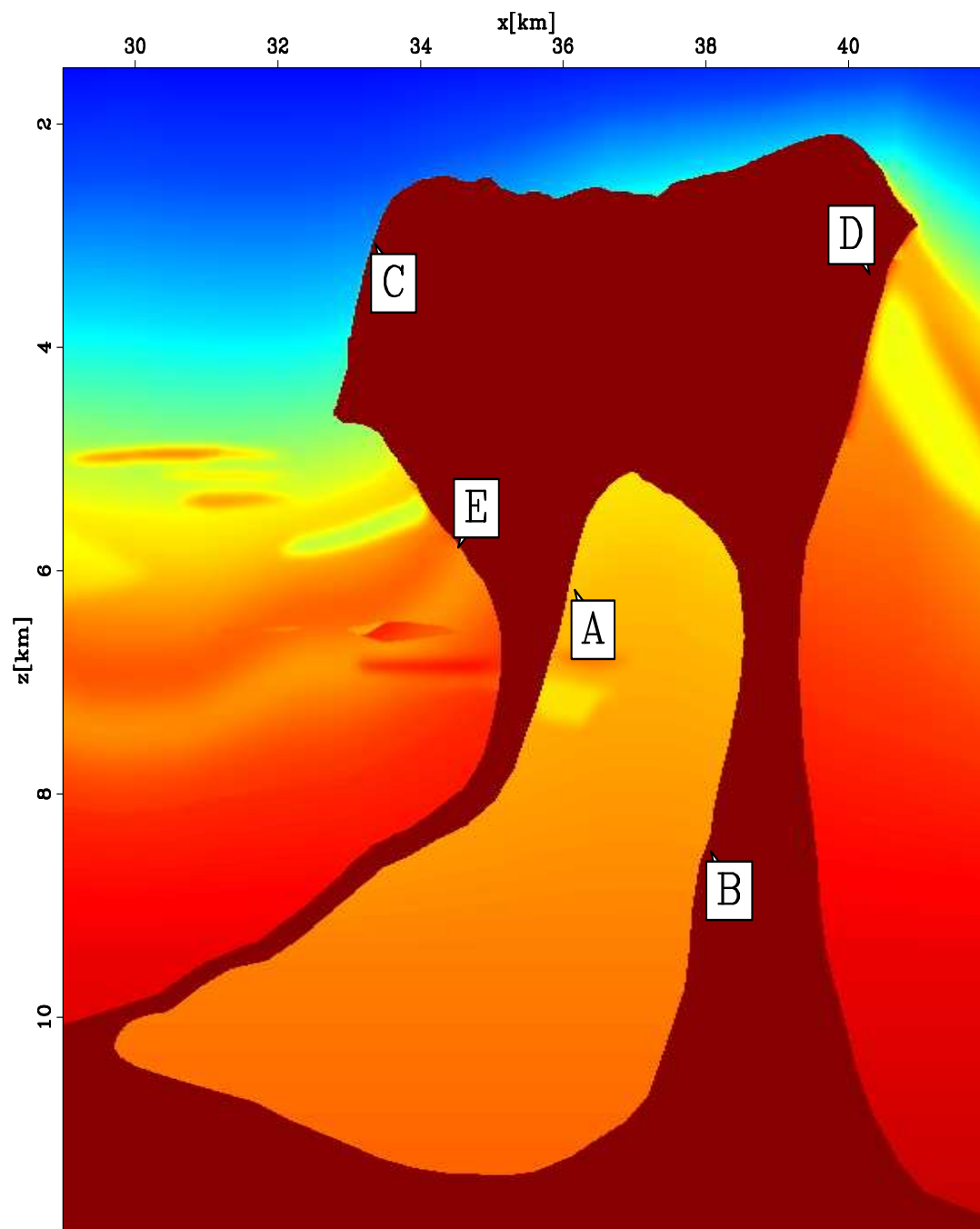


Figure 3.18: Detail of velocity model for the right salt body. `plane2d/. bprightvel`

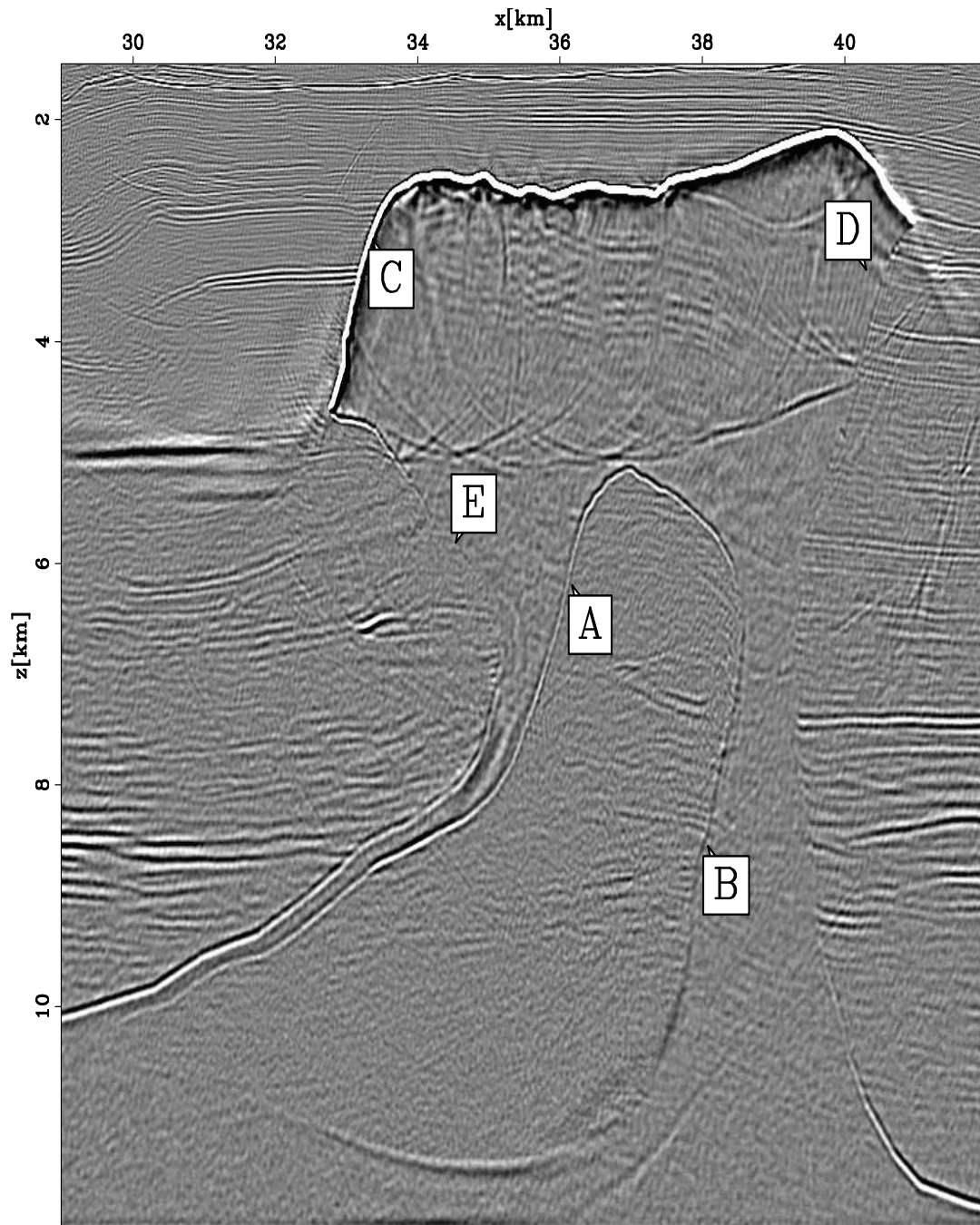


Figure 3.19: Image of the right salt body obtained by plane-wave migration in tilted coordinates. `plane2d/. bprightsalttilt`

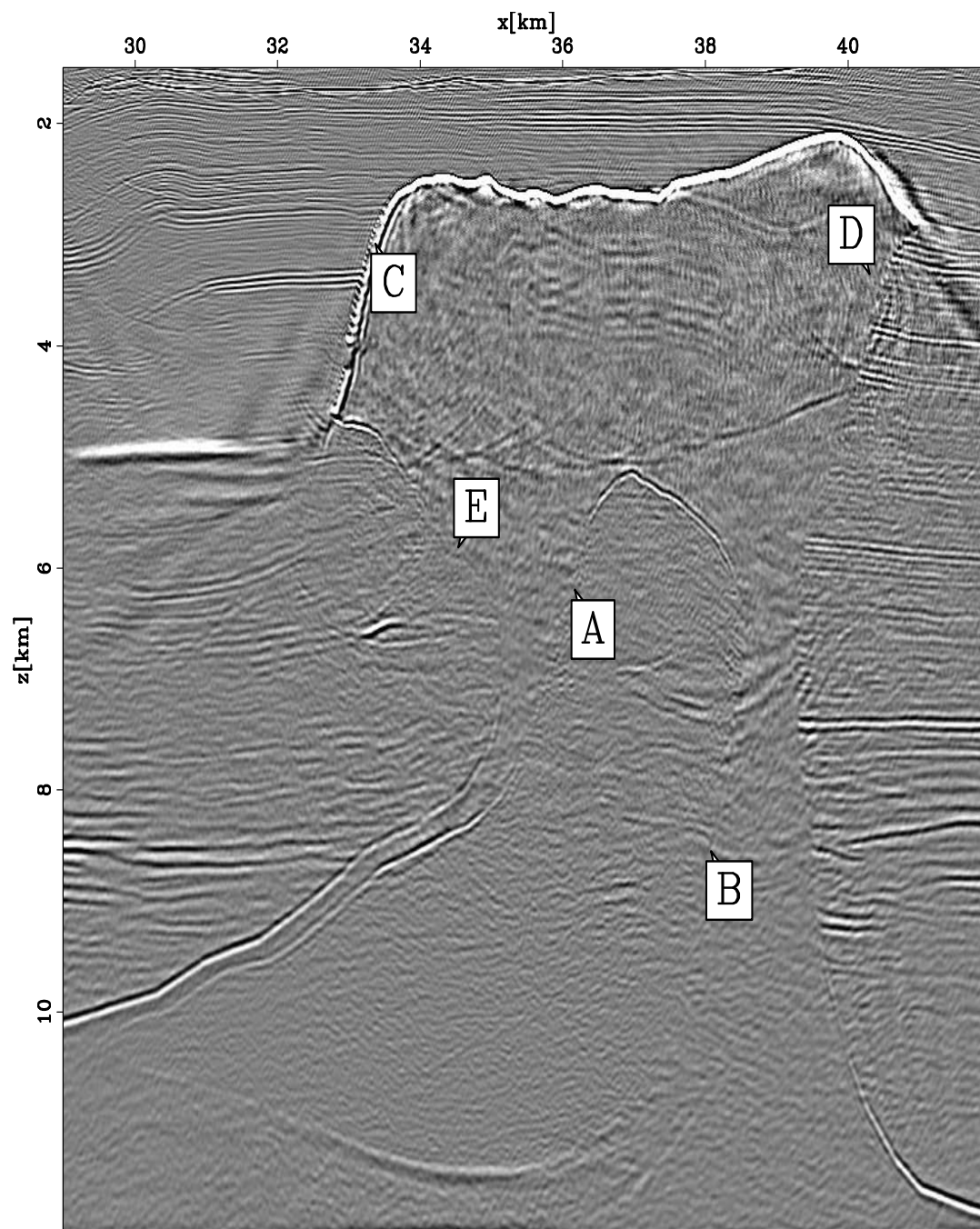


Figure 3.20: Image of the right salt body obtained by plane-wave migration in vertical Cartesian coordinates. `plane2d/. bprightsaltnotilt`

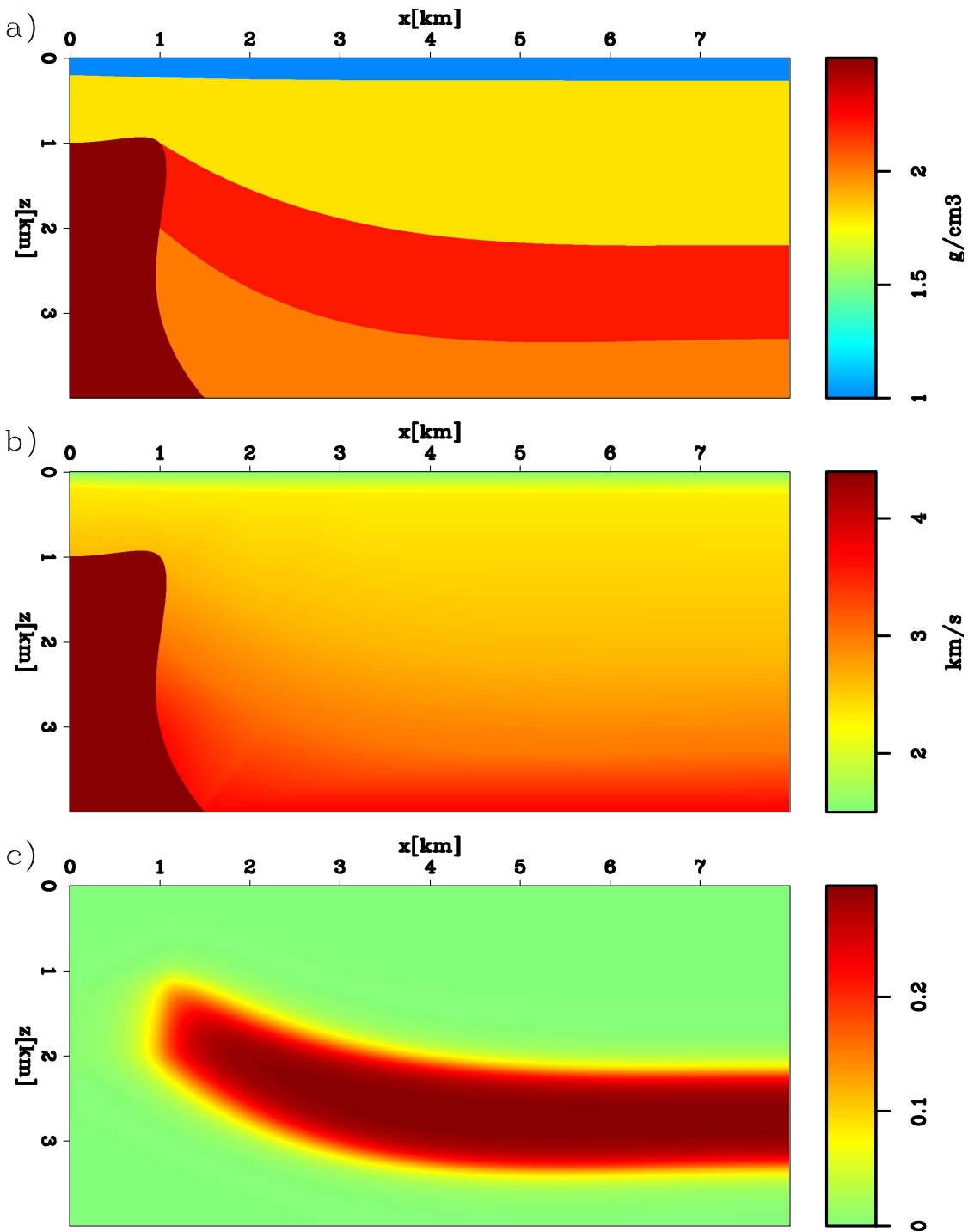


Figure 3.21: The parameters of the VTI model: density (a), qP-wave vertical velocity v_{p_0} (b), and anisotropy parameter ε . The anisotropy parameter δ is zero.

plane2d/. exxonsyn-model

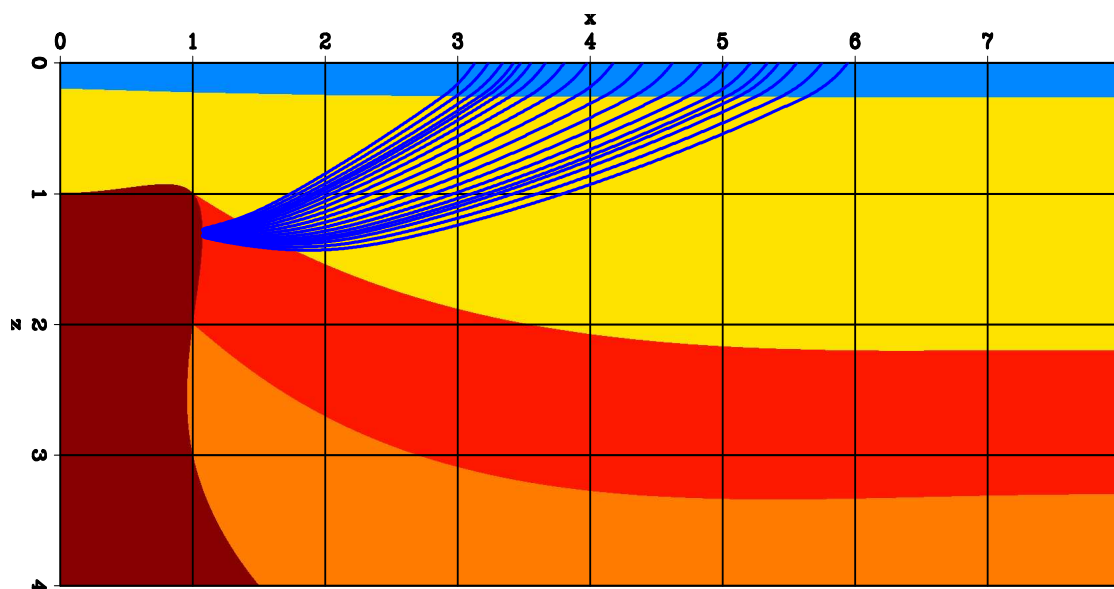


Figure 3.22: Rays show that the steep salt flank is mainly illuminated by overturned energy. `plane2d/. exxon-syn-ray`

the surface range from -45° to 45° . For plane-wave migration in tilted coordinates, vertical Cartesian coordinates were used for plane-wave sources with small take-off angle, and 80 coordinate systems in total are used. I used the 5-point explicit finite-difference scheme (Shan and Biondi, 2005) as the wavefield extrapolation operator for all the three migrations. This scheme is accurate to 45° . In Figure 3.23, the overturned energy is imaged, but at incorrect position because anisotropy was ignored in the migration. The bottom of the anisotropy layer, however, is imaged at nearly the correct position because the reflector is illuminated mainly by waves traveling almost vertically; thus the migration velocity is almost the same as the true propagation velocity, since the value of δ is zero in this model. In Figure 3.24 the bottom half of the salt flank is well imaged after incorporating anisotropy in the migration, but the top half of the salt flank disappears because the overturned energy is filtered out during the one-way wavefield extrapolation. In Figure 3.25, the salt flank is well imaged although the center of the flank is out of the acquisition range. Figure 3.26 shows that the reflectors imaged with anisotropic plane-wave migration in tilted coordinates

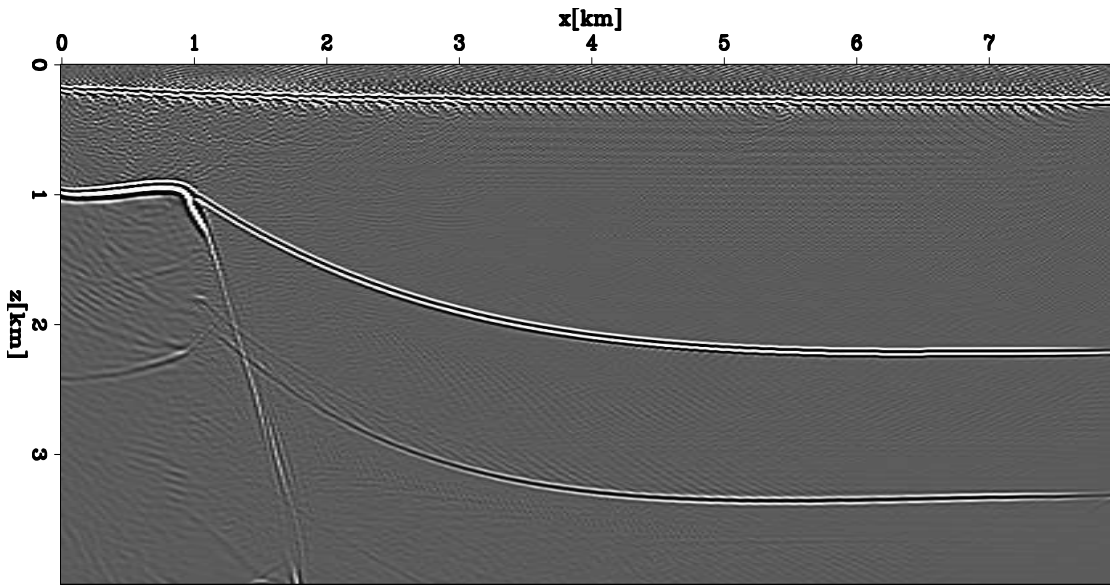


Figure 3.23: The resulting image obtained by isotropic plane-wave migration in tilted coordinates. `plane2d/. exxon-syn-iso-tilt`

are at the correct position.

MIGRATION FOR SPARSELY SAMPLED SHOTS IN TILTED COORDINATES

The theory derived in previous sections requires densely sampled shot gathers. However, in practical application, shots are not always well sampled. Especially, in 3D, shot gathers are usually sparsely sampled in the cross-line direction, even for datasets with wide-azimuth acquisition recorded recently. To apply “plane-wave” migration to a dataset with sparsely sampled shots, we use the discrete version of equation 3.7,

$$S_p(p_{s_x}, r_x, z = 0, \omega) = \sum_{s_x} \delta(r_x - s_x) e^{i\omega s_x p_{s_x}}, \quad (3.18)$$

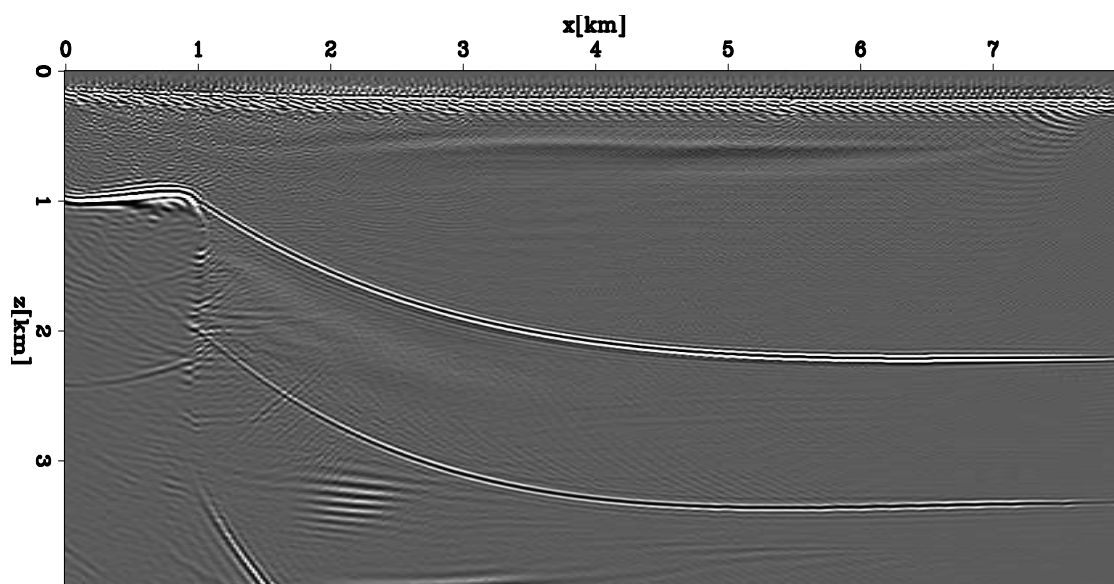


Figure 3.24: The resulting image obtained by anisotropic plane-wave migration in vertical Cartesian coordinates. `plane2d/. exxon-syn-notilt`

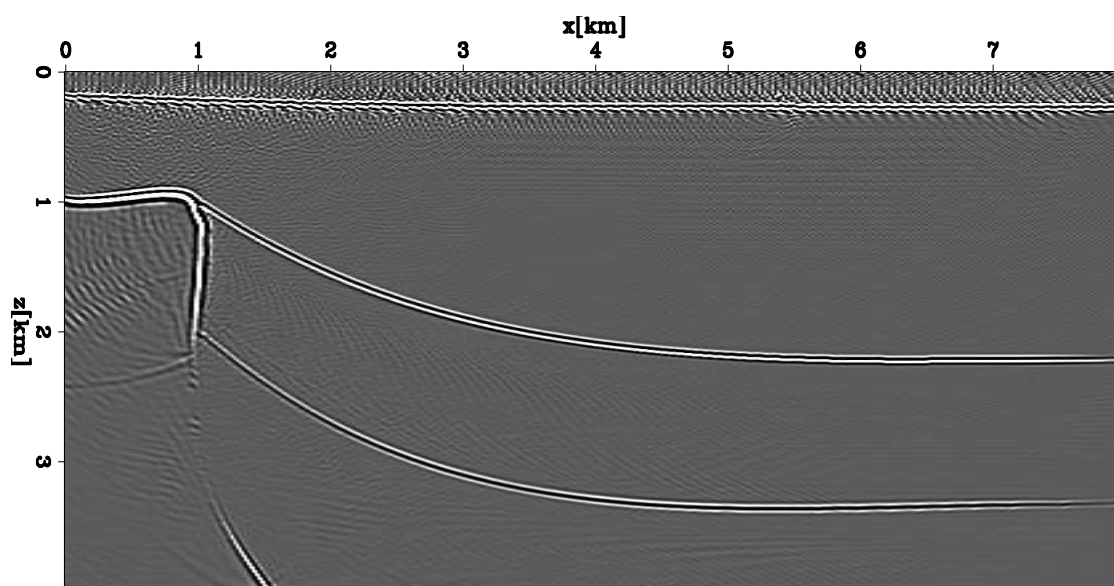


Figure 3.25: The resulting image obtained by anisotropic plane-wave migration in tilted coordinates. `plane2d/. exxon-syn-tilt`

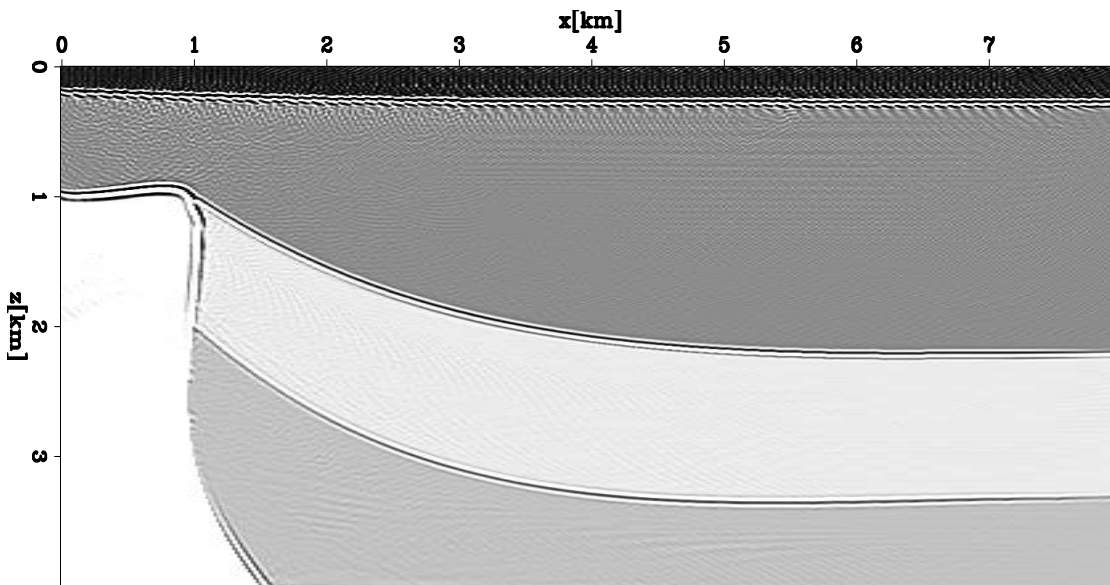


Figure 3.26: The density model overlaid with the image obtained by anisotropic plane-wave migration in tilted coordinates. `plane2d/. Exxon-syn-tiltdn`

to construct the source wavefield at the surface, and use the discrete version of equation 3.6,

$$R_p(p_{s_x}, r_x, z = 0, \omega) = \sum_{s_x} R(s_x, r_x, z = 0, \omega) e^{i\omega s_x p_{s_x}}, \quad (3.19)$$

to construct the receiver wavefield at the surface. For a dataset with densely sampled shot gathers, The source wave generated with equation 3.18 is a plane wave (Figure 3.27(a)) for datasets with densely sampled shot gathers, but not for datasets with sparsely sampled shot gathers (Figure 3.27(b)). Liu et al. (2006) demonstrate that no matter what acquisition geometry is used, “plane-wave” migration is an accurate phase-encoded shot migration (Morton and Ober, 1998; Romero et al., 2000). When shot gathers are sparsely sampled, I call the source wavefield generated with equation a 3.18 *phase-encoded source*, and call the corresponding migration *phased-encoded source migration*.

In this section, I discuss phase-encoded source migration in tilted coordinates for datasets with sparsely sampled shot gathers. I start with comparing real plane-wave

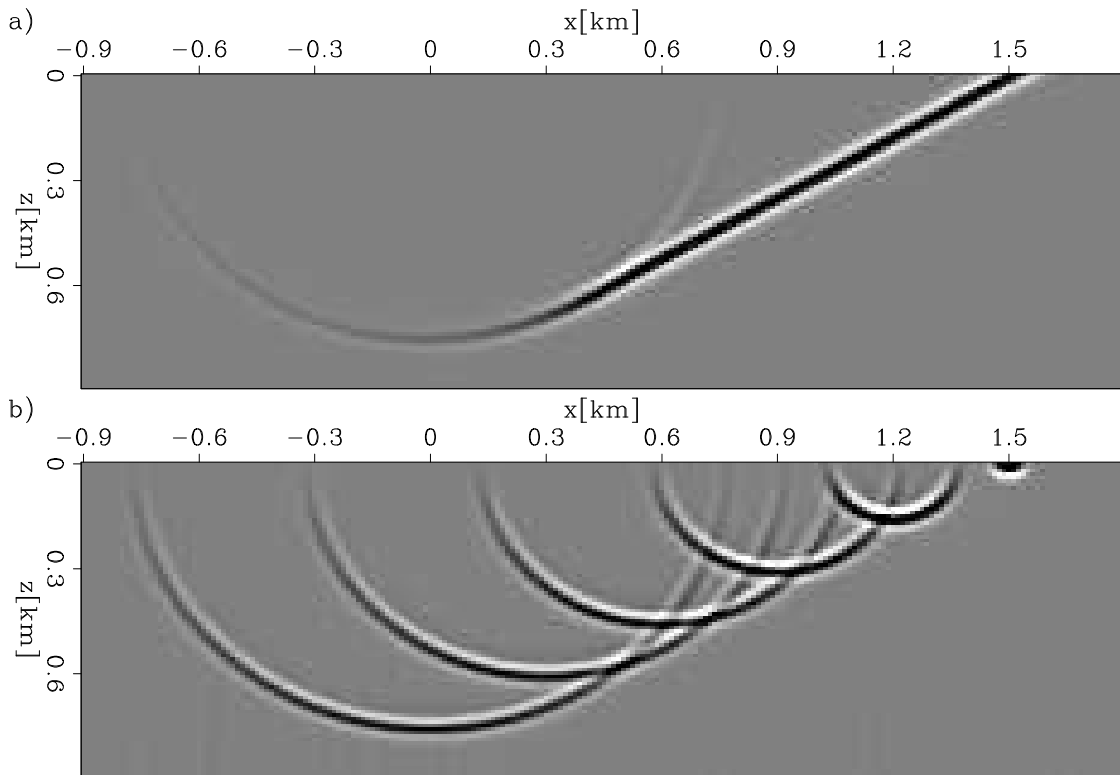


Figure 3.27: A snapshot of the source wavefield generated using equation 3.18: (a) dense shot gathers with a 25 m shot interval and (b) sparse shot gathers with a 300 m shot interval. `plane2d/. sourcecom`

source migration with phase-encoded source migration.

Plane-wave source versus phase-encoded source

Consider a dataset with N_s shots located at $s_{x_j} = j\Delta s_x$, $j = 1, 2, \dots, N_s$, where Δs_x is the interval between adjacent shots. Let $S(s_{x_j}, x, z, \omega)$ and $R(s_{x_j}, x, z, \omega)$ represent source and receiver wavefields, respectively, of a shot located at s_{x_j} in shot-profile migration. In shot-profile migration, the final image is constructed by

$$I_s(x, z) = \sum_{j=1}^{N_s} \sum_{\omega} S^*(s_{x_j}, x, z, \omega) R(s_{x_j}, x, z, \omega), \quad (3.20)$$

where S^* is the complex conjugate of the source wavefield S . In phase-encoded source migration, because of the linearity of the wavefield extrapolation operator, the source wavefield for a phase-encoded source with a ray parameter p_{s_x} is

$$S_p(p_{s_x}, x, z, \omega) = \sum_{j=1}^{N_s} e^{i\omega s_{x_j} p_{s_x}} S(s_{x_j}, x, z, \omega), \quad (3.21)$$

and receiver wavefield is

$$R_p(p_{s_x}, x, z, \omega) = \sum_{j=1}^{N_s} e^{i\omega s_{x_j} p_{s_x}} R(s_{x_j}, x, z, \omega). \quad (3.22)$$

With the cross-correlation imaging condition, the image corresponding to this phase-encoded source is constructed as follows:

$$I_{p_{s_x}}(x, z) = \sum_{\omega} |\omega| S_p^*(p_{s_x}, x, z, \omega) R_p(p_{s_x}, x, z, \omega), \quad (3.23)$$

$$= \sum_{\omega} \sum_{j=1}^{N_s} \sum_{k=1}^{N_s} |\omega| e^{i\omega p_{s_x} (s_{x_k} - s_{x_j})} S^*(s_{x_j}, x, z, \omega) R(s_{x_k}, x, z, \omega), \quad (3.24)$$

where $|\omega|$ is the “rho filter” discussed earlier (Claerbout, 1985).

Assume $2N_p + 1$ phase-encoded sources are used in a migration, and the ray parameters corresponding to these phase-encoded sources are:

$$p_{s_x} = -N_p \Delta p, -(N_p - 1) \Delta p, \dots, \Delta p, 0, \Delta p, \dots, (N_p - 1) \Delta p, N_p \Delta p,$$

where Δp is the interval of the ray parameters. The final image is constructed by stacking images of all phase-encoded sources:

$$I_p(x, z) = \sum_{\omega} \sum_{j=1}^{N_s} \sum_{k=1}^{N_s} S^*(s_{x_j}, x, z, \omega) R(s_{x_k}, x, z, \omega) \left(|\omega| \sum_{m=-N_p}^{N_p} e^{i\omega m \Delta p (s_{x_k} - s_{x_j})} \right). \quad (3.25)$$

Liu et al. (2006) show that I_p is equivalent to I_s , if N_p is large enough and Δp is small

enough, regardless of the acquisition's geometry, because

$$\lim_{N_p \rightarrow \infty} |\omega| \sum_{m=-N_p}^{N_p} e^{i\omega m \Delta p (s_{x_k} - s_{x_j})} = \delta(s_{x_k} - s_{x_j}). \quad (3.26)$$

Therefore, in equation 3.25, because of the non-linearity of the imaging condition, in addition to signal terms ($j = k$), there are crosstalk terms ($j \neq k$). Equation 3.26 shows that when N_p is large enough, the crosstalk terms in equation 3.25 are entirely canceled by each other.

For a dataset with sparse shot gathers, we can also use a real plane-wave source instead of phase-encoded sources. We construct source wavefields at the surface with equation 3.18 as if the shot gathers were densely sampled. For a dataset with sparsely sampled shots, the interval of x used in the migration, Δx , is much smaller than Δs_x . The source wavefield of a plane-wave source with the ray parameter p_{s_x} is:

$$\tilde{S}_p(p_{s_x}, x, z, \omega) = \sum_{j=1}^{\tilde{N}_s} e^{i\omega \tilde{s}_{x_j} p_{s_x}} S(\tilde{s}_{x_j}, x, z, \omega), \quad (3.27)$$

where $\tilde{s}_{x_j} = j\Delta x$, $\tilde{N}_s = \frac{\Delta s_x}{\Delta x} N_s \gg N_s$. Unlike with the source wavefield, I still use equation 3.22 to construct the receiver wavefield. Therefore, for sparsely sampled data, compared to phase-encoded source migration, plane-wave source migration adds a large number of shots with a receiver wavefield of zero value. The image corresponding to the ray parameter p_{s_x} is constructed as follows:

$$I_{p_{s_x}}(x, z) = \sum_{\omega} |\omega| \tilde{S}_p^*(p_{s_x}, x, z, \omega) R_p(p_{s_x}, x, z, \omega), \quad (3.28)$$

$$= \sum_{\omega} \sum_{j=1}^{\tilde{N}_s} \sum_{k=1}^{N_s} |\omega| e^{i\omega p_{s_x} (s_{x_k} - \tilde{s}_{x_j})} S^*(\tilde{s}_{x_j}, x, z, \omega) R(s_{x_k}, x, z, \omega). \quad (3.29)$$

The final image is constructed by stacking the images of all plane-wave sources:

$$\tilde{I}_p(x, z) = \sum_{\omega} \sum_{j=1}^{\tilde{N}_s} \sum_{k=1}^{N_s} S^*(\tilde{s}_{x_j}, x, z, \omega) R(s_{x_k}, x, z, \omega) \sum_{m=-N_p}^{N_p} |\omega| e^{i\omega m \Delta p (s_{x_k} - \tilde{s}_{x_j})}. \quad (3.30)$$

Again, if N_p is large enough,

$$\lim_{N_p \rightarrow \infty} |\omega| \sum_{m=-N_p}^{N_p} e^{i\omega m \Delta p (s_{x_k} - \tilde{s}_{x_j})} = \delta(s_{x_k} - \tilde{s}_{x_j}). \quad (3.31)$$

In equation 3.31, all terms where $s_{x_k} = \tilde{s}_{x_j}$ are signal terms, and all terms where $s_{x_k} \neq \tilde{s}_{x_j}$ are crosstalk noise. Compared to I_p , \tilde{I}_p has the same signal terms but it has many more crosstalk terms. Equation 3.31 shows that if N_p is large enough, all crosstalk terms ($s_{x_k} \neq \tilde{s}_{x_j}$) in equation 3.30 are entirely canceled by each other, and the image \tilde{I}_p is also equivalent to I_s , although \tilde{I}_p has many more crosstalk terms than I_p .

I use impulse responses to compare plane-wave source and phase-encoded source migrations. The input dataset has only three single-trace shots. The shots are located at 0 m, 500 m and 1000 m. The offset for the single trace is 1000 m, and each trace has only three impulses at 1 s, 1.5 s and 2 s. For comparison, I migrate the dataset with shot-profile migration and show the image in Figure 3.28.

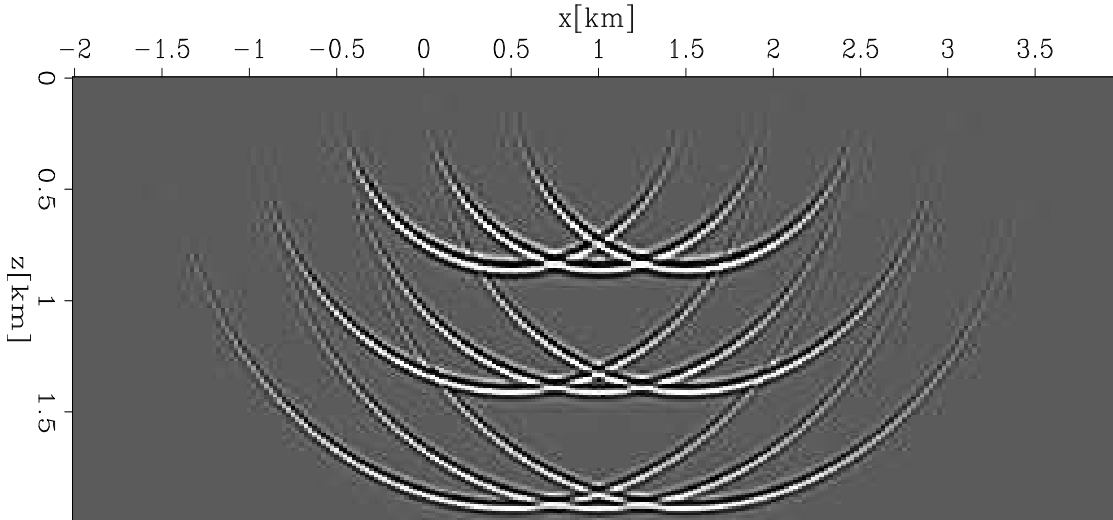


Figure 3.28: Shot-profile migration of the dataset with 3 single-trace shots. `plane2d/. impulse-sp`

Figure 3.29 compares images of a single-ray-parameter section obtained by plane-wave source migration (Figure 3.29(a)) and by phase-encoded source migration (3.29(b)). The ray parameter is zero. The two images are very different. In 3.29(a), we can see a clean plane-wave component of the nine impulse-response smiles. In 3.29(b), although only one ray-parameter section is migrated, we can see all nine impulse-response smiles, but they are contaminated by crosstalk noise.

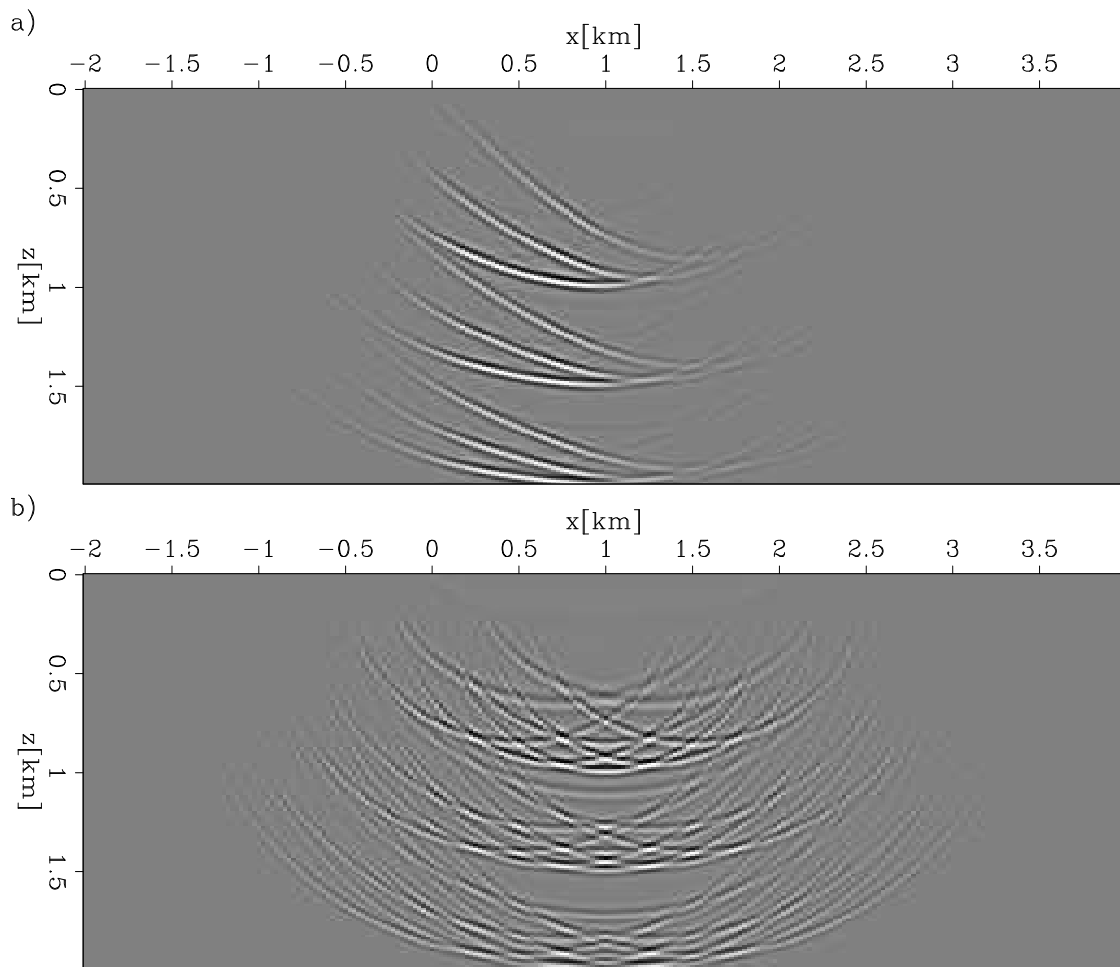


Figure 3.29: Migration of a single ray-parameter section ($p_{s_x} = 0$): (a) phase-encoded source, (b) plane-wave source. `plane2d/. impulse1p`

Figure 3.30 compares the images obtained by stacking the images of 65 ray-parameter sections with $N_p = 32$ and $\Delta p = 0.000015$ s/m. Figure 3.30(a) is obtained

by plane-wave source migration and Figure 3.30(b) is obtained by phase-encoded source migration. Since N_p is large enough, crosstalk noise is well suppressed in both images. Both images are similar to the image obtained by shot-profile migration in Figure 3.28.

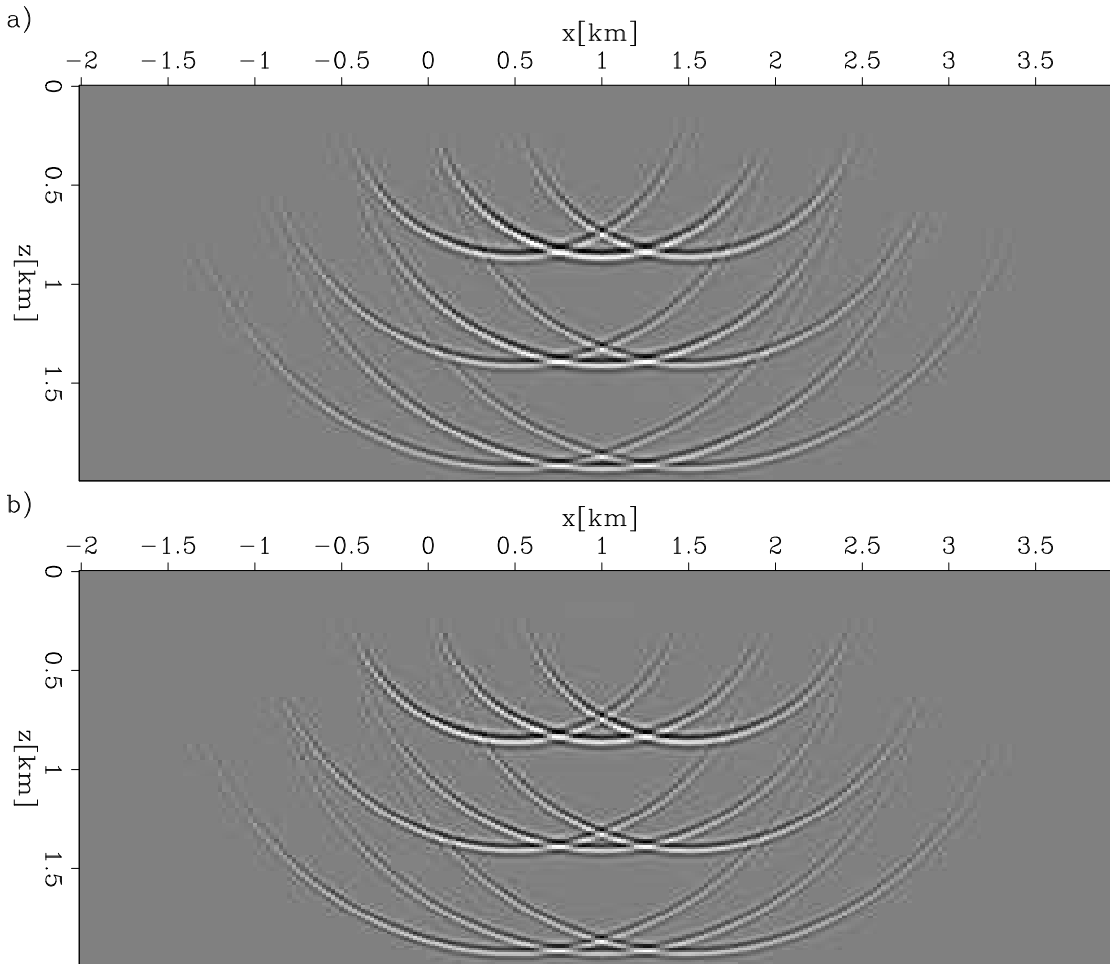


Figure 3.30: Images of 65 ray parameters: (a) plane-wave source, (b) phase-encoded source. `plane2d/. impulse65`

Figure 3.31 compares the images obtained by stacking the images of 13 ray-parameter sections with $N_p = 6$ and $\Delta p = 0.000075$ s/m. Figure 3.31(a) is obtained by plane-wave source migration and Figure 3.31(b) is obtained by phase-encoded source migration. There is crosstalk left in both images, but the crosstalk noise in

Figure 3.31(a) is stronger than that in Figure 3.31(b).

Figures 3.29 to 3.31 show that although for a single ray parameter, plane-wave source migration has a cleaner image than phase-encoded source migration, crosstalk noise is suppressed better in phase-encoded source migration if 13 ray parameters are used and two migration algorithms have similar images if 65 ray parameters are used.

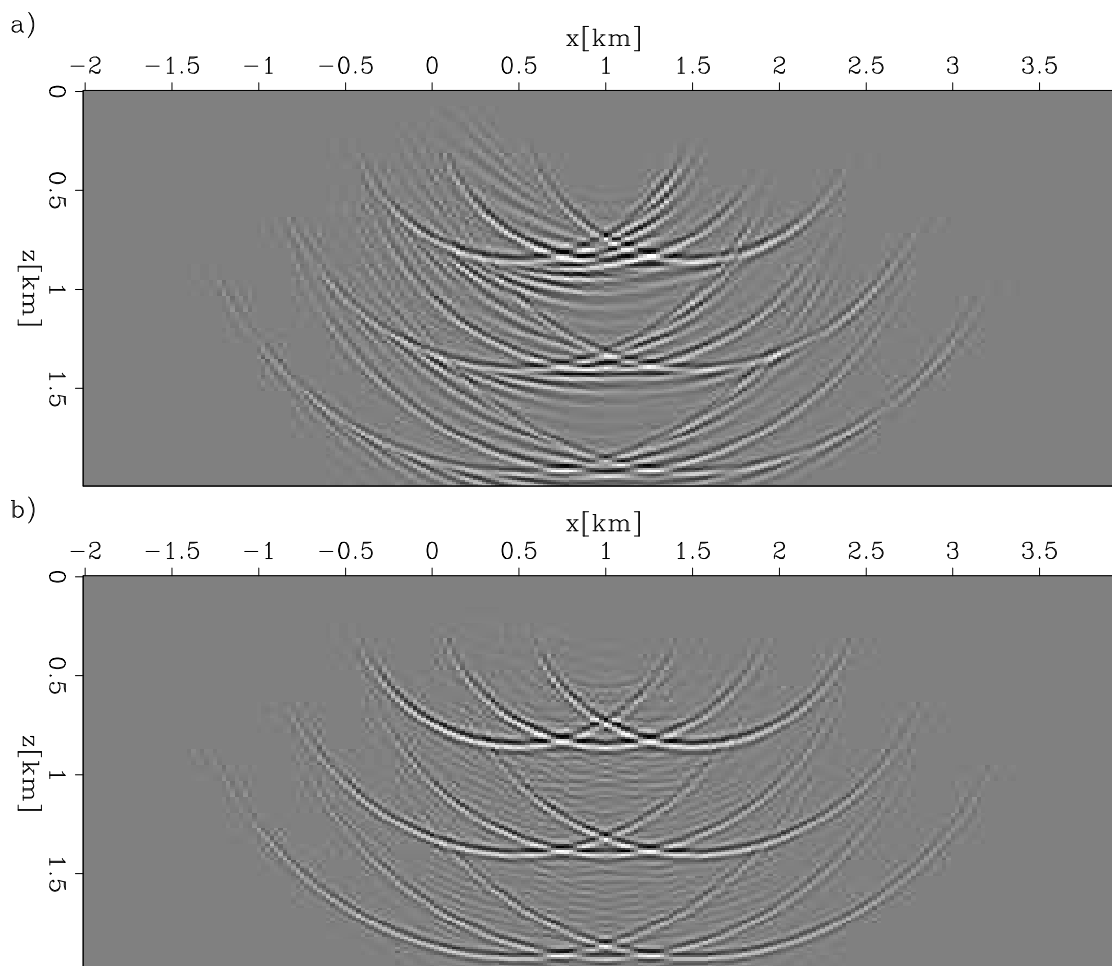


Figure 3.31: Images of 13 ray parameters: (a) plane-wave source, (b) phase-encoded source. `plane2d/. impulse13`

I also use the 2004 BP velocity benchmark to compare plane-wave source migration with phase-encoded source migration. The velocity model is shown in Figure 5.6. I mainly focus on the area from $x = 20$ km to $x = 35$ km. The shot interval in the

original dataset is 50 m. To mimic a dataset with sparsely sampled shots, I decimate the shot sampling, so that the shot interval is 500 m after shot decimation. Figure 3.32 shows the images after stacking 51 ray-parameter sections with $\Delta p = 0.00002s/m$ and $N_p = 25$. Figure 3.32(a) shows the image obtained by plane-wave source migration and Figure 3.32(b) shows the image obtained by phase-encoded source migration. As with the impulse response example, there is more crosstalk noise left in the image obtained by migration using plane-wave sources.

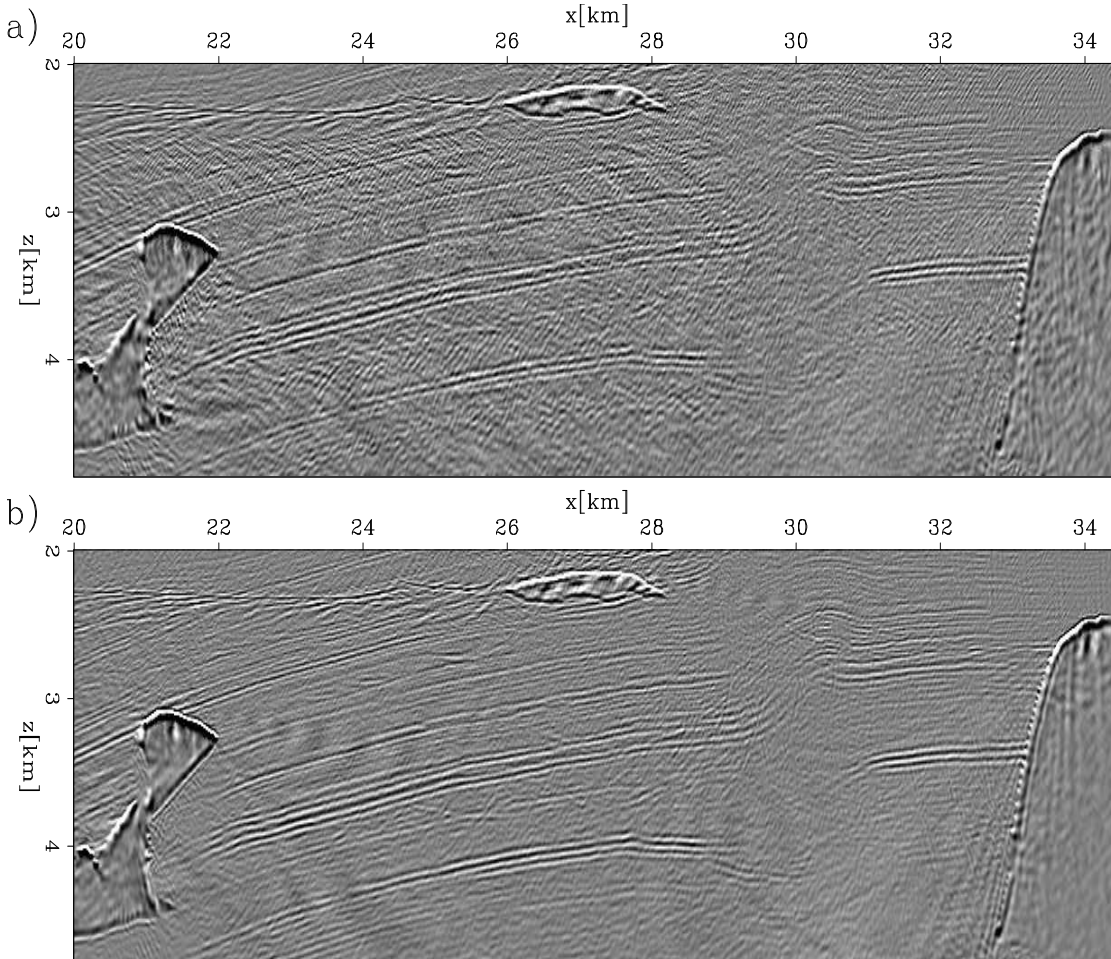


Figure 3.32: Image of the 2004 BP velocity benchmark with a shot interval of 500 m: (a) plane-wave source, (b) phase-encoded source. `plane2d/. bp-en-plane`

Impulse responses and synthetic data examples show that the two migration algorithms have similar images if the ray parameters are well sampled; otherwise, there is more crosstalk noise left in images obtained by plane-wave source migration. Therefore, for a dataset with sparse shot gathers, phase-encoded sources are better than real plane-wave sources for migration.

Phase-encoded source migration in tilted coordinates

As with plane-wave migration in tilted coordinates, to migrate a dataset with sparsely sampled shots using phase-encoded source migration, the source and receiver wavefields can also be extrapolated in tilted coordinates. Given the surface velocity v_{z_0} , we can calculate the “take-off” angle α of a phase-encoded source with a ray parameter p_{s_x} as if it were a plane-wave source:

$$\sin \alpha = p_{s_x} v_{z_0}. \quad (3.32)$$

I extrapolate source and receiver wavefields corresponding to this phase-encoded source in a tilted coordinate system with the tilting angle θ close to the angle α .

Assume $2N_p + 1$ phase-encoded sources are used in the migration, and their ray parameters are $p_m = m\Delta p$, $m = -N_p, -(N_p - 1), \dots, 1, 0, 1, \dots, N_p - 1, N_p$. For the phase-encoded source with the ray parameter p_m , I extrapolate the source and receiver wavefields a tilted coordinate system (x_m, z_m) , whose tilting angle is $\theta_m \approx \arcsin(p_m v_{z_0})$. The image of this phase-encoded source is constructed as follows:

$$I_{p_m}(x, z) = \sum_{\omega} \sum_{j=1}^{N_s} \sum_{k=1}^{N_s} S_{\theta_m}^*(s_{x_j}, x, z, \omega) R_{\theta_m}(s_{x_k}, x, z, \omega) |\omega| e^{i\omega p_m (s_{x_k} - s_{x_j})}, \quad (3.33)$$

where S_{θ_m} and R_{θ_m} are the source and receiver wavefields extrapolated in the tilted coordinate system (x_m, z_m) , and $S_{\theta_m}^*$ is the complex conjugate of S_{θ_m} . The final image

is constructed by stacking the images of all phase-encoded sources as follows:

$$I_p = \sum_{m=-N_p}^{N_p} \sum_{\omega} \sum_{j=1}^{N_s} \sum_{k=1}^{N_s} S_{\theta_m}^*(s_{x_j}, x, z, \omega) R_{\theta_m}(s_{x_k}, x, z, \omega) |\omega| e^{i\omega m \Delta p(s_{x_k} - s_{x_j})}, \quad (3.34)$$

$$= I_{signal} + I_{crosstalk}, \quad (3.35)$$

where

$$I_{signal} = \sum_{j=1}^{N_s} \sum_{m=-N_p}^{N_p} \sum_{\omega} |\omega| S_{\theta_m}^*(s_{x_j}, x, z, \omega) R_{\theta_m}(s_{x_j}, x, z, \omega), \quad (3.36)$$

and

$$I_{crosstalk} = \sum_{j=1}^{N_s} \sum_{k \neq j} \sum_{\omega} \sum_{m=-N_p}^{N_p} S_{\theta_m}^*(s_{x_j}, x, z, \omega) R_{\theta_m}(s_{x_k}, x, z, \omega) |\omega| e^{i\omega m \Delta p(s_{x_k} - s_{x_j})}. \quad (3.37)$$

As with conventional phase-encoded source migration, the final image I_p consists of two parts: the signal part I_{signal} and the crosstalk part $I_{crosstalk}$. Let I_s^m be the image obtained by shot-profile migration in the tilted coordinate system (x_m, z_m) , $m = -N_p, \dots, -1, 0, 1, \dots, N_p$. Approximately, I_{signal} is the stack of $I_s^{-N_p}, \dots, I_s^{-1}, I_s^0, I_s^1, \dots, I_s^{N_p}$. Therefore, as far as the signal part is concerned, phase-encoded source migration in tilted coordinates is the average of the shot-profile migrations in all the $2N_p + 1$ tilted coordinate systems. Shot-profile migration in a tilted coordinate system can handle a range of reflector dip components. For instance, nearly-horizontal dip components of reflectors are well imaged by shot-profile migration in vertical Cartesian coordinates, and steep dip components of reflectors are well imaged by shot-profile migration in tilted coordinates with a large tilting angle. Therefore, all dip components of the signal part are well imaged by phase-encoded source migration in tilted coordinates. In the crosstalk part, because S_{θ_m} and R_{θ_m} depend on the tilting angle θ_m , we can not move S_{θ_m} and R_{θ_m} out of the summation along m in equation 3.37. As a consequence, we can not stack the term $|\omega| e^{i\omega m \Delta p(s_{x_k} - s_{x_j})}$ independently, and the crosstalk terms can not be entirely canceled by each other.

My first example is a dataset with three single-trace shots located at 0 m, 500 m and 1000 m. The offset of the trace for all three shots is 1 km and the trace has only

one impulse at 2 s. Figure 3.33 shows images of single phase-encoded sources. The ray parameters of phase-encoded sources used for Figures 3.33(a), (b) and (c) are -0.0003 , 0 , and 0.0003 , respectively. The tilting angle of tilted coordinate systems used for Figure 3.33(a) and (c) are -35° and 35° , respectively. Vertical Cartesian coordinates are used for Figure 3.33(b). I also show images obtained by migrating each shot independently using shot-profile migration in the same tilted coordinate systems in Figure 3.34. The image of a phase-encoded source is approximately the stack of the image obtained by shot-profile migration in the same coordinate system and the crosstalk noise. Therefore, Figures 3.34(a), (b) and (c) are approximately the signal parts of Figures 3.33(a), (b) and (c), respectively. For each phase-encoded source, a portion of the dip components of the impulse-response smiles are well imaged. For a phase-encoded source with a negative ray parameter, the tilting angle of the coordinate system is -35° , and the high-angle energy of the left side is well imaged (Figure 3.33(a)). For a phase-encoded source with positive ray parameter, the tilting angle of the coordinate system is 35° , and high-angle energy of the right side is well imaged (Figure 3.33(c)). When the ray parameter is almost 0, vertical Cartesian coordinates are used, and low-angle energy is well imaged (Figure 3.33(b)). I show the stack of the images of the three phase-encoded source sections in Figure 3.35(a). Although the image is contaminated by crosstalk noise, all dip components of the signal part are well imaged. After I stack the images of 65 phase-encoded sources, the crosstalk noise is well suppressed (Figure 3.35(b)).

My second example is the 2004 BP velocity benchmark. As in the previous subsection, I mainly focus on the area from $x = 20$ km to $x = 35$ km, and I mimic a dataset with sparsely sampled shots by decimating the shot sampling to yield a shot interval of 500 m.

Figure 3.36 shows images obtained by phase-encoded source migration in vertical Cartesian coordinates (a), phase-encoded source migration in tilted coordinates (b), and reverse-time migration (c). As with the images of the original densely sampled dataset (Figures 3.19 and 3.20), in Figure 3.36(a), the steep reflectors are not well

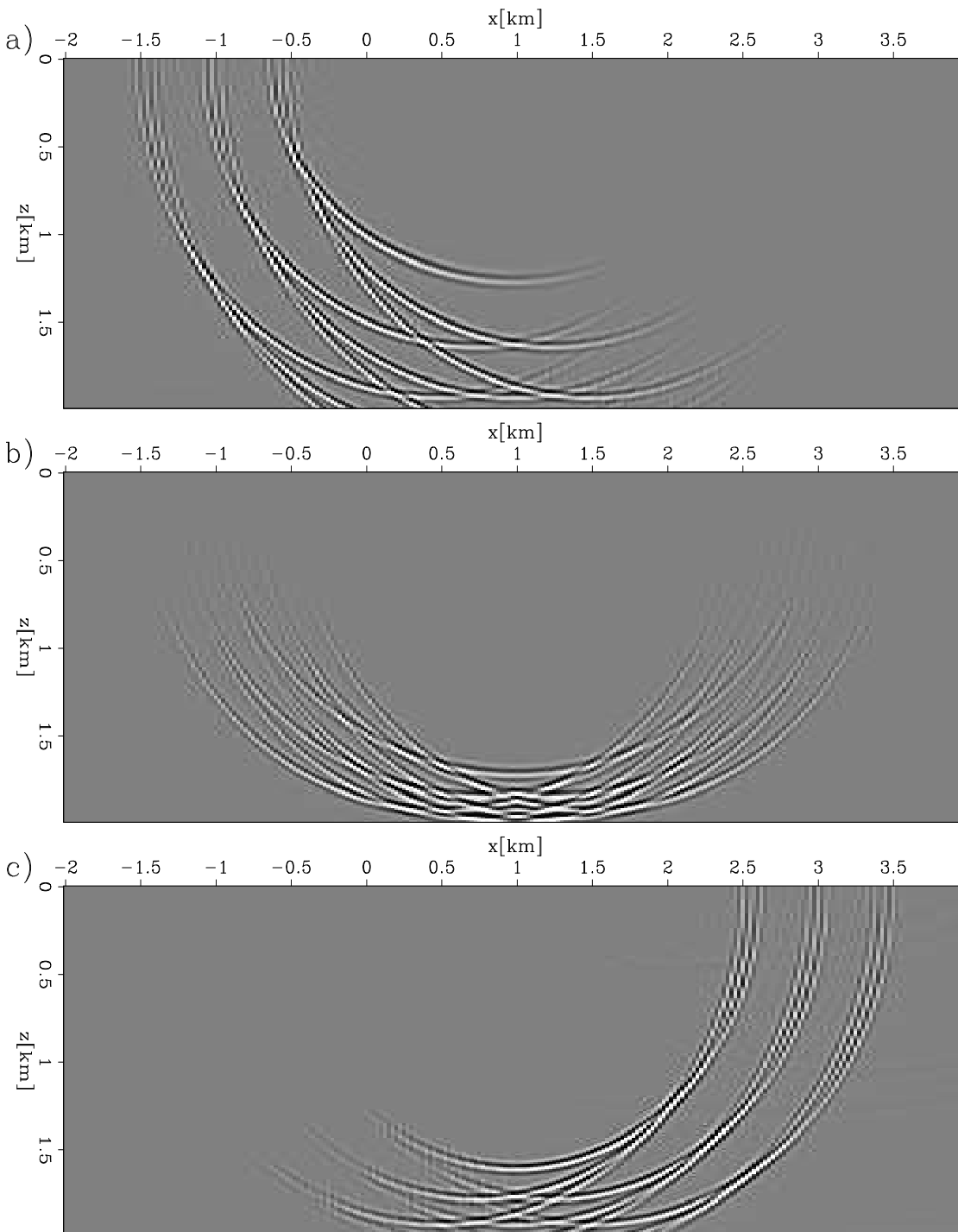


Figure 3.33: Single phase-encoded source image of a dataset with three single trace shots: (a) ray parameter $p_{s_x} = -0.0003$ s/m, tilted coordinates with tilting angle $\theta = -35^\circ$; (b) ray parameter $p_{s_x} = 0$ s/m, vertical Cartesian coordinates; and (c) ray parameter $p_{s_x} = 0.0003$ s/m, tilted coordinates with tilting angle $\theta = 35^\circ$.

plane2d/. impulse-1ptilt

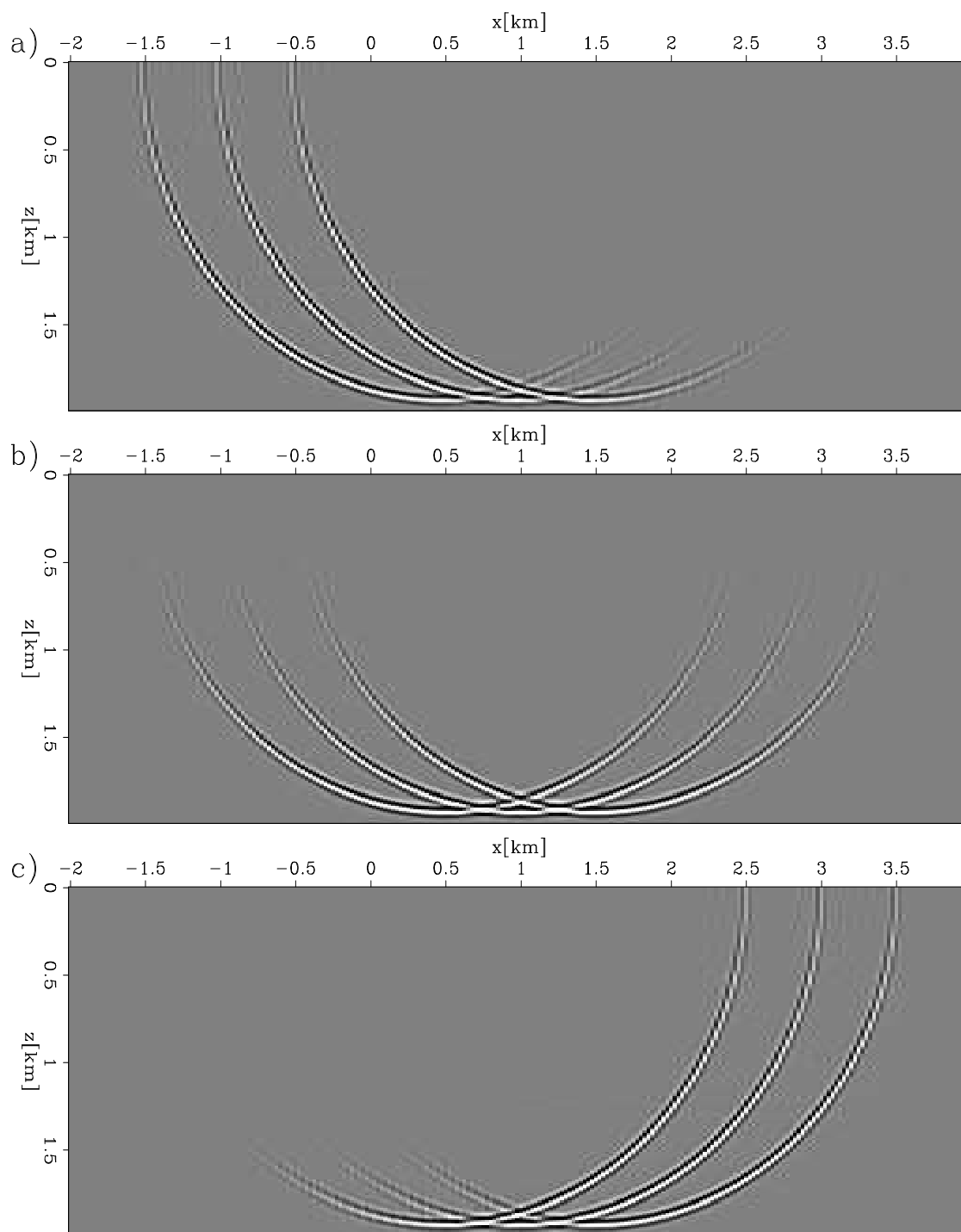


Figure 3.34: Image of a dataset with three single trace shots: (a) shot-profile migration in tilted coordinates with tilting angle $\theta = -35^\circ$; (b) shot-profile migration in vertical Cartesian coordinates; (c) shot-profile migration in tilted coordinates with tilting angle $\theta = -35^\circ$. `plane2d/. impulse-shottilt`

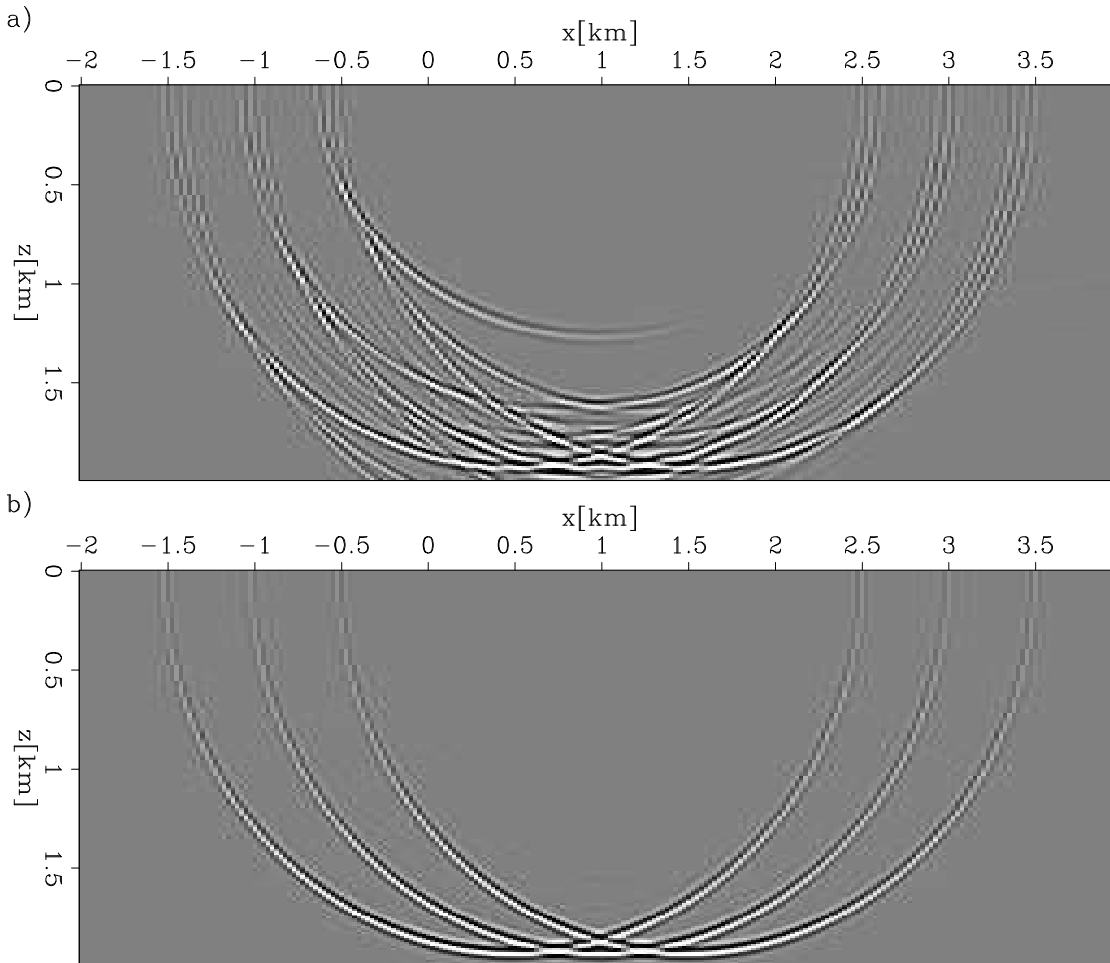


Figure 3.35: Phase-encoded source migration in tilted coordinates for the dataset with 3 single-trace shots: (a) 3 phase-encoded sources with $\Delta p = 0.0003$ s/m and (b) 65 phase-encoded sources with $\Delta p = 0.000015$. `plane2d/. impulse-pe-tilt`

imaged by phase-encoded source migration in vertical Cartesian coordinates. However, steep reflectors are well imaged by both phase-encoded source migration in tilted coordinates and reverse-time migration. The images in Figure 3.36(b) and (c) are comparable, except that they have different phases, because the wavelets used to construct the source wavefields at the surface have different phases in the two migrations

The two synthetic data examples show that for sparsely sampled shot gathers, steep reflectors are well imaged by phase-encoded source migration in tilted coordinates.

CONCLUSION

Plane-wave migration in tilted coordinates makes the extrapolation direction close to the actual propagation direction in the subsurface by assigning a proper tilted coordinate system for each plane-wave source. One-way wave equations in tilted coordinates are exactly the same as those in vertical Cartesian coordinates; therefore we can still use the accurate one-way extrapolator methods developed for vertical Cartesian coordinates in the past two decades to reduce the sensitivity to the coordinates. Plane-wave migration in tilted coordinates is much less computationally intensive than reverse-time migration, but it can still handle waves that illuminate steep reflectors and overhanging flanks, such as high-angle energy and overturned waves. These events are a challenge to image with conventional one-way migration in vertical Cartesian coordinates. Examples show that plane-wave migration in tilted coordinates is a good tool for delineating complex salt bodies. For sparsely sampled data, phase-encoded source migration in tilted coordinates is the average of the shot-profile migrations in all coordinate systems used in the migration, and steep reflectors are well imaged.

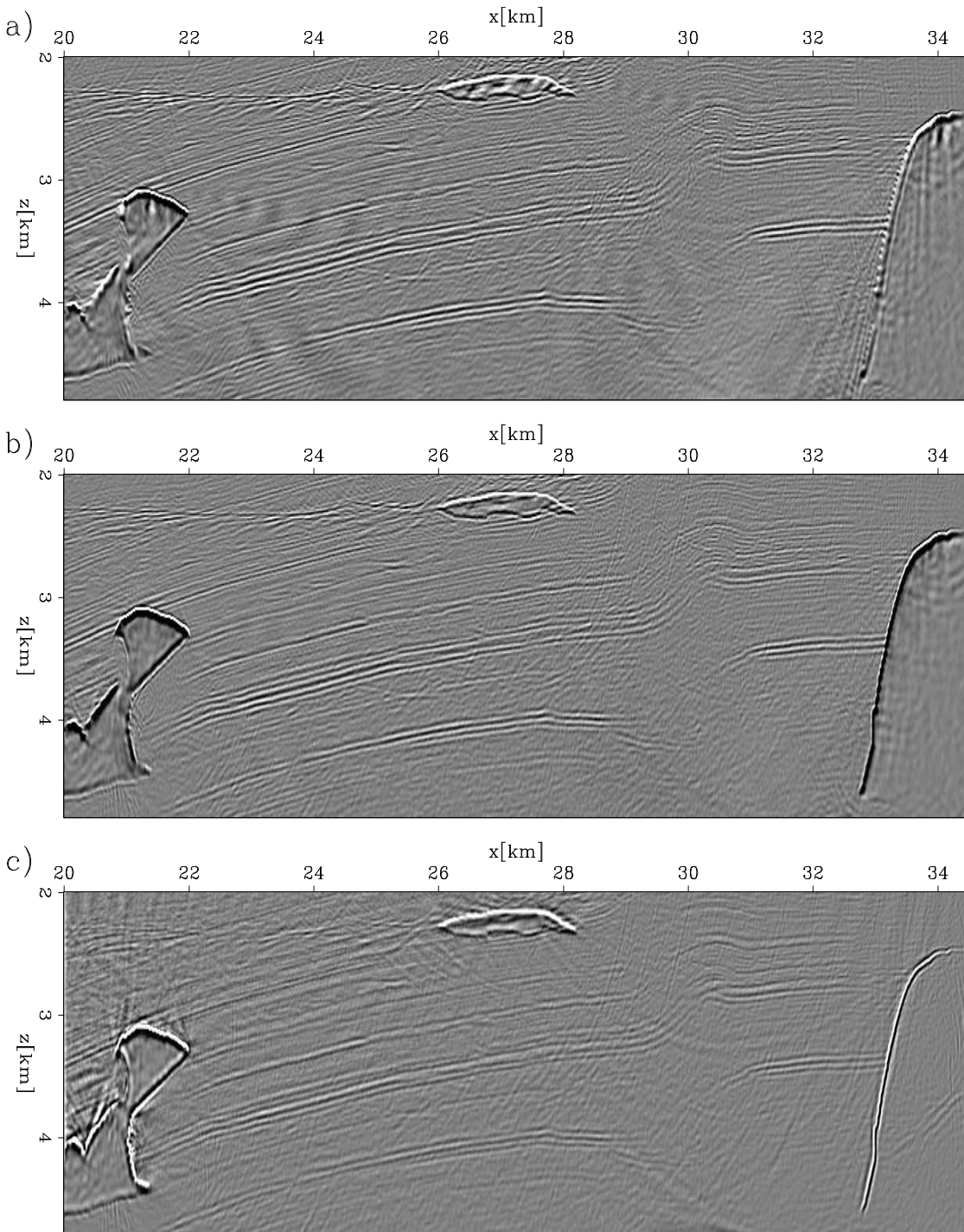


Figure 3.36: Image of BP velocity benchmark with shot interval of 500 m: (a) phase-encoded source migration in vertical Cartesian coordinates, (b) phase-encoded source migration in tilted coordinates, and (c) reverse-time migration.

`plane2d/. bpphaseencode`

ACKNOWLEDGMENTS

I thank Amerada Hess for the velocity model used for impulse response, BP for the BP 2004 velocity benchmark, and Exxonmobil for the VTI synthetic dataset. I also thank Paul Sava of Center for Wave Phenomena, Colorado School of Mines for the exploding reflector dataset.

Chapter 4

Plane-wave migration in tilted coordinates: A 3-D field data example

INTRODUCTION

In chapter 3, I introduced the basic idea of plane-wave migration in tilted coordinates and showed several 2D synthetic data examples. In this chapter, I generalize the technique to 3D, discuss its implementation, and apply it to a 3D field dataset from the Gulf of Mexico. I present two kinds of 3D migration algorithms based on plane-wave decomposition: conical-wave migration and 3D plane-wave migration.

Conical-wave migration, introduced by Whitmore (1995), Rietveld (1995) and Zhang et al. (2005b), synthesizes conical-wave-source datasets by slant-stacking receiver gathers only in the inline direction. For each navigation line, conical-wave-source data are synthesized and migrated independently. The final image is formed by stacking the images for all conical-wave sources of all navigation lines. A conical-wave source is specified by its inline ray parameter and the cross-line location relative to the navigation line. This algorithm is commonly used for marine narrow-azimuth

data. As with 2D plane-wave migration in tilted coordinates, for each conical-wave source I keep the cross-line axis unchanging and tilt the coordinate system only in the inline direction with an angle determined by the ray parameter of the source and the velocity at the surface. Conical-wave-source migration in tilted coordinates can image reflectors that are steep in the inline direction, but it fails to image reflectors with steep dips in the cross-line direction.

We can also synthesize 3D plane-wave datasets and migrate them with plane-wave migration (Liu et al., 2006; Duquet and Lailly, 2006). A 3D plane-wave source dataset is synthesized by slant-stacking receiver gathers in both inline and cross-line directions. A plane-wave source is specified by a ray-parameter pair: the ray parameter in the inline direction and the ray parameter in the cross-line direction. Each plane-wave source dataset is migrated independently, and the final image is formed by stacking all possible plane-wave sources. For most marine data, the shot sampling is relatively sparse in the cross-line direction. Consequently, in the cross-line direction, the synthesized dataset is actually a phase-encoding source dataset instead of a plane-wave source one (Liu et al., 2002). In chapter 3, I showed that steep reflectors are well imaged by phase-encoded source migration in tilted coordinates. In 3D, I design coordinates depending on its ray-parameter pair and the surface velocity, no matter what shot interval is used in the data. I tilt coordinates in both inline and cross-line directions, and therefore can image reflectors with dips in both inline and cross-line directions.

The field dataset used for examples was donated by ExxonMobil. The dataset also comes with vertical-velocity and anisotropy-parameter models. The velocity and anisotropy parameters have been estimated, assuming that the medium is vertically transversely isotropic (VTI) (Bear et al., 2005). As with the 2D case, a VTI medium in a vertical Cartesian coordinate system becomes a tilted TI medium in a tilted coordinate system. The implicit finite-difference wavefield-extrapolation schemes for VTI and tilted TI media developed in chapter 2 are applied in migrations. Since the salt flanks and faults are steep in both inline and cross-line directions, I choose 3D plane-wave migration in tilted coordinates for this dataset.

In this chapter, I begin with a review of 3D plane-wave migration, and then describe how to design coordinates depending on the propagation direction of plane-wave sources at the surface. Finally, I introduce the field dataset and compare images obtained from conventional plane-wave migration and plane-wave migration in tilted coordinates.

3D PLANE-WAVE MIGRATION

Surface seismic data are usually recorded as shot gathers. A typical surface seismic dataset (receiver wavefields at the surface) is a five-dimensional object: $R(s_y, s_x, r_y, r_x, z = 0, t)$, where (s_y, s_x) is the source location, (r_x, r_y) is the receiver location, z is the depth, and t is the travel time. After a Fourier transformation in t , we can obtain the recorded wavefield in the frequency domain, $R(s_y, s_x, r_y, r_x, z = 0, \omega)$, where ω is the circular frequency.

Plane-wave source migration

A surface dataset $R(s_y, s_x, r_y, r_x, z = 0, \omega)$, can be synthesized to a plane-wave source dataset by slant-stacking as follows:

$$R_p(p_{s_x}, p_{s_y}; r_x, r_y, z = 0, \omega) = \int \int R(s_x, s_y; r_x, r_y, z = 0, \omega) e^{i\omega(s_x p_{s_x} + s_y p_{s_y})} ds_x ds_y, \quad (4.1)$$

where p_{s_x} and p_{s_y} are the plane-wave ray parameters in the inline and cross-line directions, respectively. A plane-wave source dataset represents the wavefield that would be received at the surface if a planar source were excited at the surface. Its corresponding plane-wave source wavefield at the surface is

$$S_p(p_{s_x}, p_{s_y}; r_x, r_y, z = 0, \omega) = e^{i\omega(r_x p_{s_x} + r_y p_{s_y})}. \quad (4.2)$$

The original surface dataset can be retrieved from the plane-wave source datasets of all ray parameters by the inverse slant-stacking (Claerbout, 1985) as follows:

$$R(s_x, s_y; r_x, r_y, z = 0, \omega) = \int \int \omega^2 R_p(p_{s_x}, p_{s_y}; r_x, r_y, z = 0, \omega) e^{-i\omega(s_x p_{s_x} + s_y p_{s_y})} dp_{s_x} dp_{s_y}. \quad (4.3)$$

Unlike the inverse Fourier transform, the kernel of the integral in equation 4.3 is weighted by the square of the frequency ω . The inverse transform is also called “rho filter” in Radon-transform literature. Notice, in 2D, the kernel is weighted by the frequency ω (chapter 3).

The synthesized source wavefield S_p and receiver wavefield R_p are extrapolated into the subsurface independently, using the one-way wave equations as follows:

$$\frac{\partial S_p}{\partial z} = +i\frac{\omega}{v} \mathbf{S}_z(\mathbf{S}_x, \mathbf{S}_y) S_p, \quad (4.4)$$

$$\frac{\partial R_p}{\partial z} = -i\frac{\omega}{v} \mathbf{S}_z(\mathbf{S}_x, \mathbf{S}_y) R_p, \quad (4.5)$$

where $\mathbf{S}_x = \frac{v}{\omega} \frac{\partial}{\partial x}$, and $\mathbf{S}_y = \frac{v}{\omega} \frac{\partial}{\partial y}$; \mathbf{S}_z is a pseudo-differential operator, which can be computed from the dispersion relation of the medium. For an isotropic medium, \mathbf{S}_z is

$$\mathbf{S}_z(\mathbf{S}_x, \mathbf{S}_y) = \sqrt{1 + (\mathbf{S}_x^2 + \mathbf{S}_y^2)}. \quad (4.6)$$

For a VTI or tilted TI medium, the dispersion relations derived in chapter 2 are used to compute \mathbf{S}_z .

The image of a plane-wave source with a ray parameter pair (p_{s_x}, p_{s_y}) is formed by cross-correlating the source and receiver wavefields weighted with the square of the frequency as follows:

$$I_{p_{s_x}, p_{s_y}}(x, y, z) = \int \omega^2 S_p(p_{s_x}, p_{s_y}; x, y, z, \omega) R_p(p_{s_x}, p_{s_y}; x, y, z, \omega) d\omega, \quad (4.7)$$

and the final image is generated by stacking the images of all possible plane-wave sources:

$$I_p = \int \int I_{p_{s_x}, p_{s_y}}(x, y, z) dp_{s_x} dp_{s_y}. \quad (4.8)$$

As with 2D plane-wave migration, the resulting image of a plane-wave migration, I_p , is equivalent to the image obtained by a shot-profile migration (Liu et al., 2002; Zhang et al., 2005b; Duquet and Lailly, 2006), because both slant-stacking and migration are linear operators.

Conical-wave source migration

For narrow azimuth data, conical-wave source migration has been demonstrated to be an efficient way to image the subsurface (Whitmore, 1995; Duquet et al., 2001; Zhang et al., 2005b). The conical-wave source data are generated as follows:

$$R_c(p_{s_x}, s_y; r_x, r_y, z = 0, \omega) = \int R(s_x, s_y; r_x, r_y, z = 0, \omega) e^{i\omega(s_x p_{s_x})} ds_x. \quad (4.9)$$

The corresponding conical source at the surface is

$$S_c(p_{s_x}, s_y; r_x, r_y, z = 0, \omega) = e^{i\omega r_x p_{s_x}} \delta(r_y - s_y). \quad (4.10)$$

where $\delta(r_y - s_y)$ means a impulse at s_y . As with the plane-wave-source datasets, the original surface dataset can be retrieved from conical-wave-source datasets of all ray parameters by inverse slant-stacking. The source and receiver wavefields, S_c and R_c , are extrapolated into the subsurface using one-way wave equations 4.4 and 4.5. As in the 3D plane-wave source migration, the image of a conical-wave source is obtained by cross-correlating the source and receiver wavefields weighted this time with the frequency ω :

$$I_{p_{s_x}, s_y}(x, y, z) = \int \omega S_c(p_{s_x}, s_y; x, y, z, \omega) R_c(p_{s_x}, s_y; x, y, z, \omega) d\omega. \quad (4.11)$$

The final image is generated by stacking images of all possible conical-wave sources of all sail lines:

$$I_c = \int \int I_{p_{s_x}, s_y}(x, y, z) dp_{s_x} ds_y. \quad (4.12)$$

As is true for 3D plane-wave migration, the image of conical-wave migration is equivalent to the shot-profile migration (Zhang et al., 2005b).

3D PLANE-WAVE MIGRATION IN TILTED COORDINATES

A 3D plane-wave source is specified by two ray parameters, p_{s_x} and p_{s_y} . Given the velocity at the surface, v_{z_0} , I calculate the propagation direction of the plane-wave source at the surface from the two ray parameters. For each plane-wave source, I rotate the Cartesian coordinates, so that the extrapolation direction of the new coordinates is close to the propagation direction of the plane wave. In 3D, the propagation direction of a plane-wave source is defined by the azimuth, ϕ , and take-off angle, θ . Given the velocity at the surface, v_{z_0} , and a plane-wave source with a ray-parameter pair (p_{s_x} , p_{s_y}), its propagation direction at the surface is defined by the vector $\mathbf{q} = (q_x, q_y, q_z)$, where

$$q_x = p_{s_x} v_{z_0}, \quad (4.13)$$

$$q_y = p_{s_y} v_{z_0}, \quad (4.14)$$

$$q_z = \sqrt{1 - (q_x^2 + q_y^2)}. \quad (4.15)$$

The azimuth angle, ϕ , and take-off angle, θ , of the plane-wave source are calculated from the vector \mathbf{q} as follows:

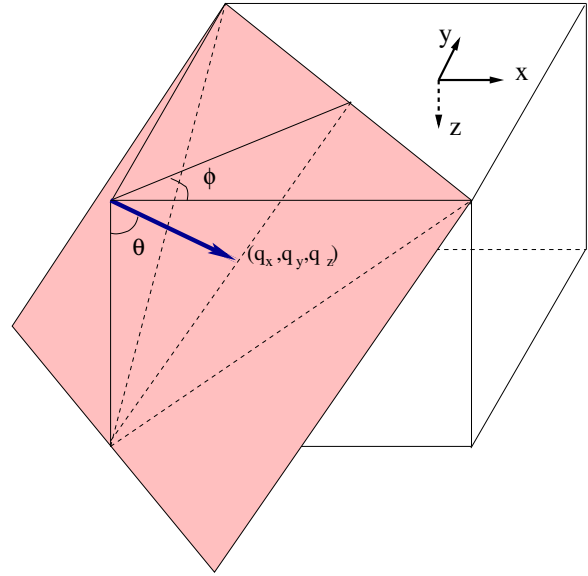
$$\phi = \arctan(q_y/q_x), \quad (4.16)$$

$$\theta = \arccos(q_z). \quad (4.17)$$

Figure 4.1 illustrates a plane-wave source and its propagation-direction vector \mathbf{q} . The angles ϕ and θ in Figure 4.1 are the azimuth and take-off angle of the plane-wave source, respectively.

Rotations in 3D are specified by the axis of rotation and rotation angle. They can

Figure 4.1: A plane-wave source, its azimuth ϕ , take-off angle θ , and propagation-direction vector $\mathbf{q} = (q_x, q_y, q_z)$. `plane3d/. planeang`



be described by a rotation matrix. For example, a rotation about the z -axis by an angle ϕ (Figure 4.2) is

$$\begin{pmatrix} x_1 \\ y_1 \\ z_1 \end{pmatrix} = R_z(\phi) \begin{pmatrix} x \\ y \\ z \end{pmatrix} = \begin{pmatrix} \cos \phi & \sin \phi & 0 \\ -\sin \phi & \cos \phi & 0 \\ 0 & 0 & 1 \end{pmatrix} \begin{pmatrix} x \\ y \\ z \end{pmatrix}. \quad (4.18)$$

To design a coordinate system with an extrapolation direction parallel the propagation-direction vector of the plane-wave source, \mathbf{q} , I obtain the coordinate system from vertical Cartesian coordinates by rotating in two steps. First I rotate about the z -axis by an angle ϕ (equation 4.18), as shown in Figure 4.2. Second I rotate about the y_1 -axis by an angle θ (Figure 4.3) as follows:

$$\begin{pmatrix} x_2 \\ y_2 \\ z_2 \end{pmatrix} = R_{y_1}(\theta) \begin{pmatrix} x_1 \\ y_1 \\ z_1 \end{pmatrix} = \begin{pmatrix} \cos \theta & 0 & \sin \theta \\ 0 & 1 & 0 \\ -\sin \theta & 0 & \cos \theta \end{pmatrix} \begin{pmatrix} x_1 \\ y_1 \\ z_1 \end{pmatrix}. \quad (4.19)$$

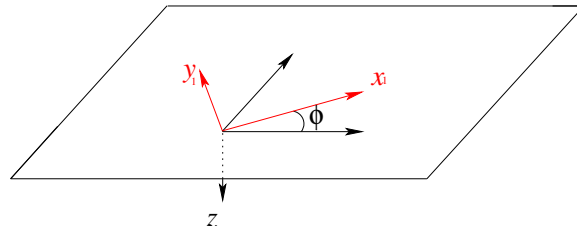
Combining the two rotations, we have the rotation from the original vertical Cartesian

coordinates to the new tilted coordinates as follows,

$$\begin{pmatrix} x_2 \\ y_2 \\ z_2 \end{pmatrix} = \begin{pmatrix} \cos \theta \cos \phi & \cos \theta \sin \phi & \sin \theta \\ -\sin \phi & \cos \phi & 0 \\ -\sin \theta \cos \phi & -\sin \theta \sin \phi & \cos \theta \end{pmatrix} \begin{pmatrix} x \\ y \\ z \end{pmatrix}. \quad (4.20)$$

Figure 4.2: Rotation about the axis z by ϕ .

`plane3d/. rotazimuth`



It is easy to verify that the depth axis of the new coordinates, the z_2 -axis, parallels the propagation-direction vector, \mathbf{q} . In practice, I do not use the direction exactly paralleling the propagation of the plane-wave source at the surface. Considering that the velocity usually increases with the depth, the propagation direction of a plane-wave source becomes increasingly horizontal, so I usually choose a tilting angle θ that is a little larger than $\arccos(q_z)$.

Figure 4.3: Rotation about the axis y_1 by θ .

`plane3d/. rotilt`

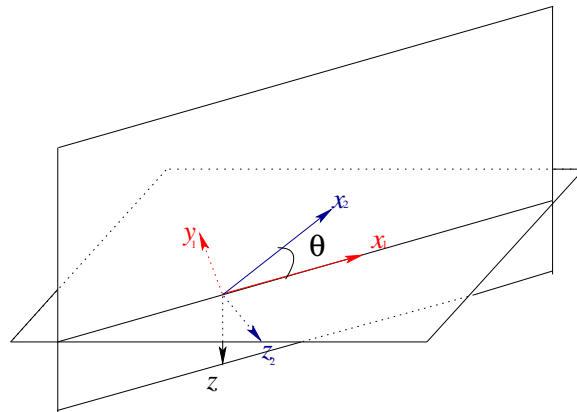


Figure 4.4 shows a typical coordinate system used for a plane-wave source to image a salt dome. The dashed lines with arrows show the propagation directions of the source and receiver waves for the plane-wave source. In the figure, (x, y, z) denotes the

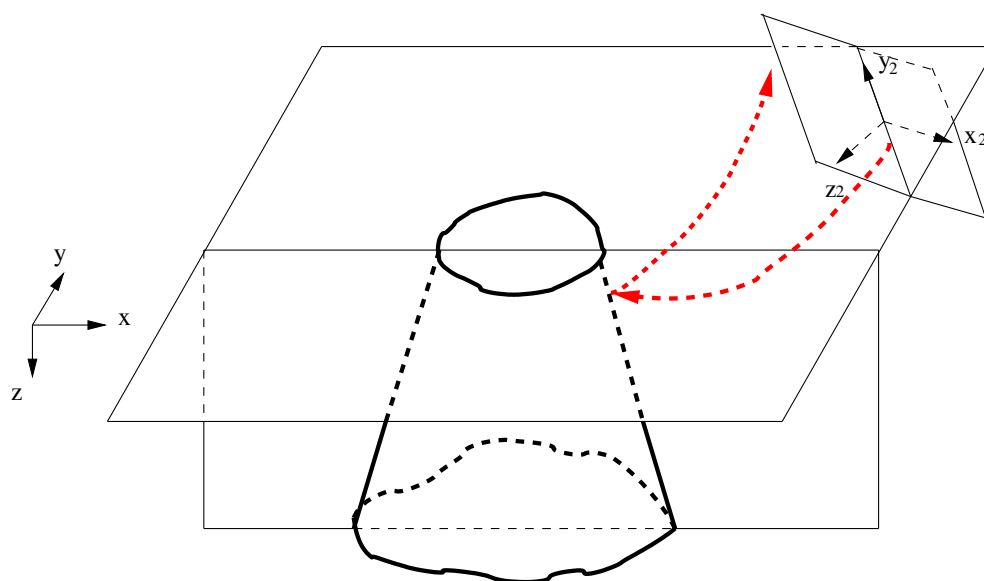


Figure 4.4: A plane-wave source and its coordinates for imaging the salt body. The original vertical Cartesian coordinate system is (x, y, z) , and (x_2, y_2, z_2) is the new tilted coordinate system. The dashed lines with arrows are the source and receiver rays of the plane-wave source. The extrapolation direction, the z_2 axis, in the tilted coordinate system, is close to the propagation direction of the plane-wave source. plane3d/. coordinates

Cartesian coordinate system, and (x_2, y_2, z_2) denotes the tilted coordinate system for the plane-wave source. The extrapolation direction in the tilted coordinate system, which parallels the z_2 -axis, is much closer to the propagation direction of the plane-wave source than is the conventional vertical extrapolation direction.

For conical-wave-source migration, we can similarly design tilted coordinates for each conical source. Unlike the 3D plane-wave-source migration, we apply only the second rotation, without rotating the azimuth of the data. Given the conical-wave source with a ray parameter p_{s_x} and surface velocity, v_{z0} , I rotate the velocity and the surface data around the y -axis by an angle of $\theta = \arcsin(p_{s_x} v_{z0})$, and migrate the data in the new coordinates. This usually works when the inline direction is the predominant dip direction in the subsurface. When there are steep dips in the cross-line direction, it is still difficult to image these dips with conical-wave migration in

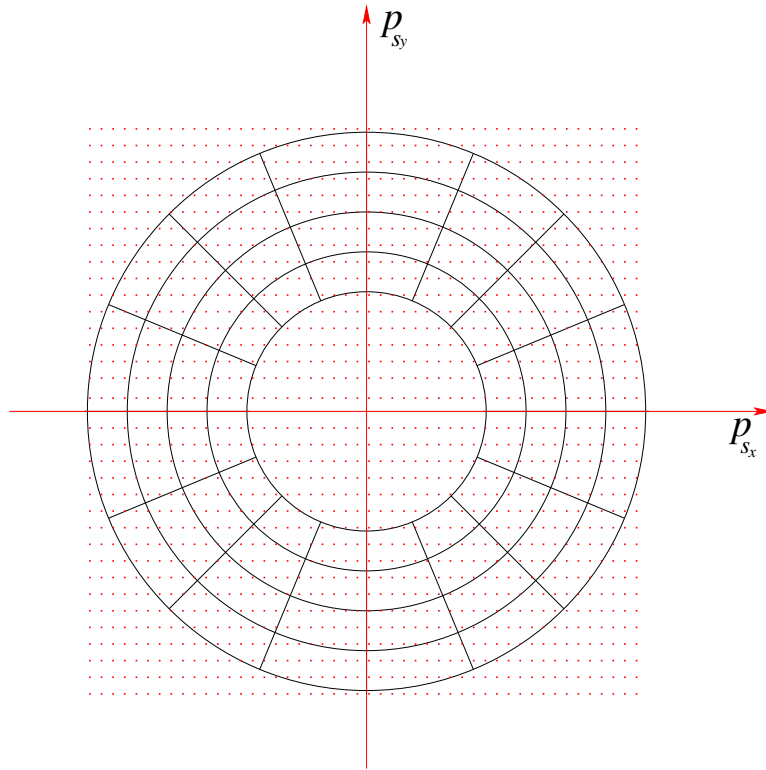


Figure 4.5: The dots represent all possible plane-wave sources. The circles are contours related to their take-off angles; the smallest circle represents plane-wave sources with a take-off angle of 15° . The radial lines show the contours of azimuth angles. All possible plane-wave sources are divided into small cells. The plane-wave sources in any given cell have a similar take-off and azimuth angle and share a coordinate system defined by the central point in the cell. `plane3d/. ppanel`

tilted coordinates. In contrast, 3D plane-wave migration in tilted coordinates rotates the data and model in both inline and cross-line directions to suit the propagation direction, and it can image these cross-line direction dips.

PRACTICAL CONSIDERATIONS

There are three steps in implementing plane-wave migration in tilted coordinates for one plane-wave source. First, the coordinates for the source and receiver wavefields are

rotated. Second, for each frequency, source and receiver wavefields are extrapolated into the subsurface, and the image is generated by cross-correlating the two wavefields in the new coordinates. Third, the image is rotated back to the original Cartesian coordinates after stacking the images of all the frequencies. In the first step, I rotate a 2D dataset for each frequency, at a cost that is trivial compared to the wavefield extrapolation. In the third step, I rotate the 3D image back to Cartesian coordinates after stacking the images for all frequencies.

To further reduce the cost of rotations, plane-wave sources with similar propagation directions share the same tilted coordinate system. This reduces the number of rotations required in the third step. Figure 4.5 illustrates how to sample the ray parameters, p_{s_x} and p_{s_y} , and how to put plane-wave sources together to share a coordinate system. In Figure 4.5 I sample (p_{s_x}, p_{s_y}) in Cartesian coordinates, where p_{s_x}, p_{s_y} are defined as:

$$p_{s_x} = -p_{max}, -p_{max} + dp_{s_x}, \dots, p_{max} - dp_{s_x}, p_{max}, \quad (4.21)$$

$$p_{s_y} = -p_{max}, -p_{max} + dp_{s_y}, \dots, p_{max} - dp_{s_y}, p_{max}, \quad (4.22)$$

where p_{max} is defined by the maximum take-off angle, and dp_{s_x}, dp_{s_y} are the sampling intervals of the ray parameters. In Figure 4.5, each dot represents a plane-wave source with a ray parameter pair (p_{s_x}, p_{s_y}) . Given the surface velocity, I calculate the azimuth angle ϕ and take-off angle θ from (p_{s_x}, p_{s_y}) , and vice versa, using equations 4.16 and 4.17. Therefore, I can divide the whole area into cells using (ϕ, θ) as the coordinate system as shown in Figure 4.5. All the plane-wave sources whose ray-parameter pairs (p_{s_x}, p_{s_y}) fall in a common cell share the same tilted coordinate system. The dots in the smallest circle in Figure 4.5 represent plane-wave sources whose take-off angle θ is smaller than 15° . The take-off angle of the smallest circle is determined by the vertical gradient of the velocity. The larger the gradient, the smaller the angle. For those plane-wave sources, I extrapolate the source and receiver wavefields in vertical Cartesian coordinates, with z -axis the extrapolation direction. For all plane-wave sources whose ray-parameter pair (p_{s_x}, p_{s_y}) share a given cell, I use their average take-off angle and azimuth angle to design the tilted coordinate system for the migration.

Figure 4.5 illustrates that 65 coordinate system in total are used. The largest circle represents the largest take-off angle of the plane-wave sources in migration. I do not migrate the plane-wave-source dataset corresponding to dots beyond the largest circle.

VTI MEDIA IN TILTED COORDINATES

A VTI medium is circularly symmetric in the horizontal plane. Therefore, the medium is still VTI after rotating the azimuth of the model (equation 4.18). In the second rotation step (equation 4.19), a VTI medium in Cartesian coordinates changes to a tilted TI medium with a constant tilting angle θ in the new coordinates. I fix the y_2 -axis in the (x, y) plane during the rotation of the coordinates. This guarantees that the symmetry axis of the new tilted TI media will lie in the plane (x_2, z_2) . The dispersion relation in the new coordinates is symmetric in the cross-line direction but not in the inline direction. The extrapolation operator for this kind of tilted TI media is simpler than in general tilted TI media. I still need a wavefield-extrapolation operator for tilted TI media in order to apply plane-wave migration in tilted coordinates in VTI media. I use the implicit finite-difference schemes developed in chapter 2.

FIELD DATA EXAMPLE FROM THE GULF OF MEXICO

The field dataset with the vertical velocity and anisotropy parameter models is provided by ExxonMobil. Figures 4.6, 4.7 and 4.8 show the vertical velocity and anisotropy parameters ε and δ of the dataset, respectively. By agreement with ExxonMobil, the depths shown in all the figures in this section differ from the true ones. The overall structure is not complex, but the salt flank in both the inline and cross-line directions is relative steep. Under the VTI media assumption, the vertical velocity and anisotropy parameters were estimated by a joint inversion method by Bear et al. (2005), which incorporates the surface seismic data with all other data available. For this dataset, in addition to vertical check shots and a substantial number of sonic logs, an offset check-shot survey serves to constrain the estimation of the velocity and

anisotropy parameters. The maximum value of the anisotropy parameters ε and δ are 0.20 and 0.10, respectively. Figures 4.7 and 4.8 show that waves illuminating the salt flanks travel through anisotropic sediments.

For comparison, I show the results of two migrations: 3D plane-wave migration in vertical Cartesian coordinates and 3D plane-wave migration in tilted coordinates. To eliminate the footprint caused by the salt flanks of the velocity model, I replace the velocity in the salt body with the sediment velocity around it. Figure 4.9 shows the velocity model used for migration. I migrate 2700 plane-waves in total. The sampling of ray parameters in both inline and cross-line directions is 0.000013 s/m. Assuming the surface velocity is 1.5 km, the maximum take-off angle θ is 38° . I use the fourth-order optimized implicit finite-difference wavefield-extrapolation operator developed in chapter 2. For plane-wave migration in tilted coordinates, the sampling intervals for cells used for sharing tilted coordinates in Figure 4.5 are $d\theta = 5^\circ$ and $d\phi = 22.5^\circ$, and 65 coordinate systems are used in total.

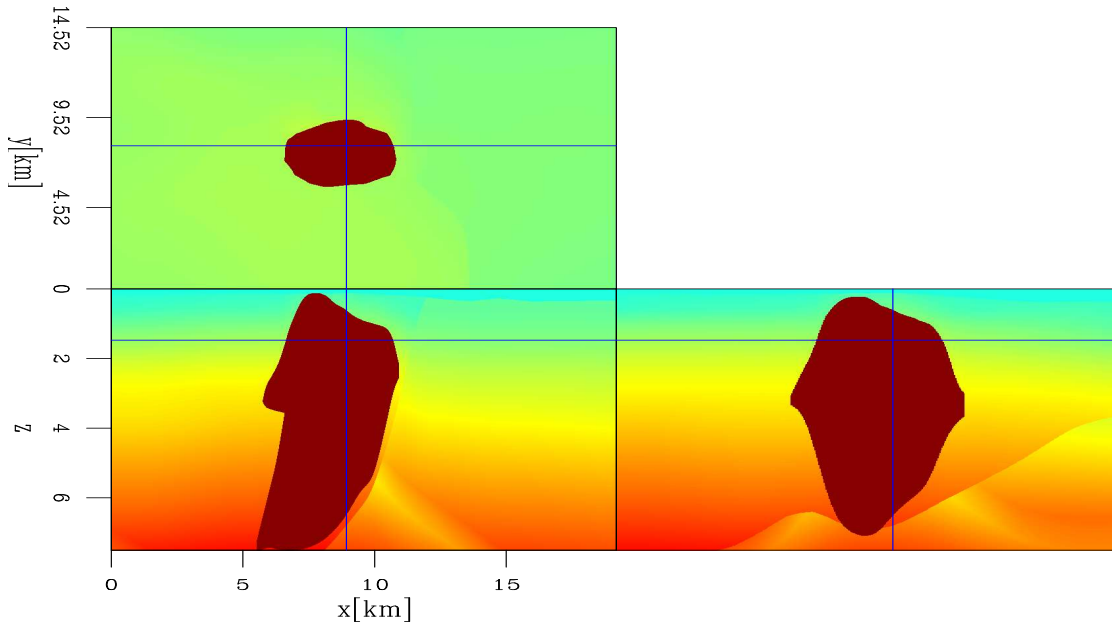


Figure 4.6: Vertical velocity model of the field dataset. The salt body is not complex, but its flanks are steep. `plane3d/. vel`

Figures 4.10 and 4.11 compare the images obtained by the two migrations. The

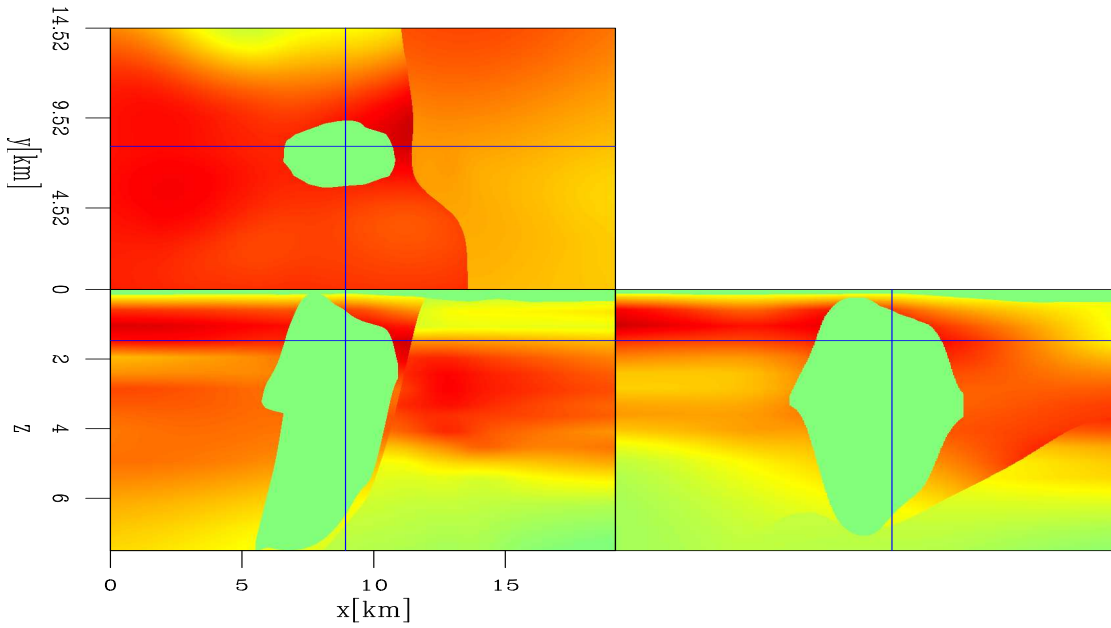


Figure 4.7: The anisotropy parameter ε of the field dataset. The energy illuminating the salt flanks travels through the anisotropic sediments. `plane3d/. eps`

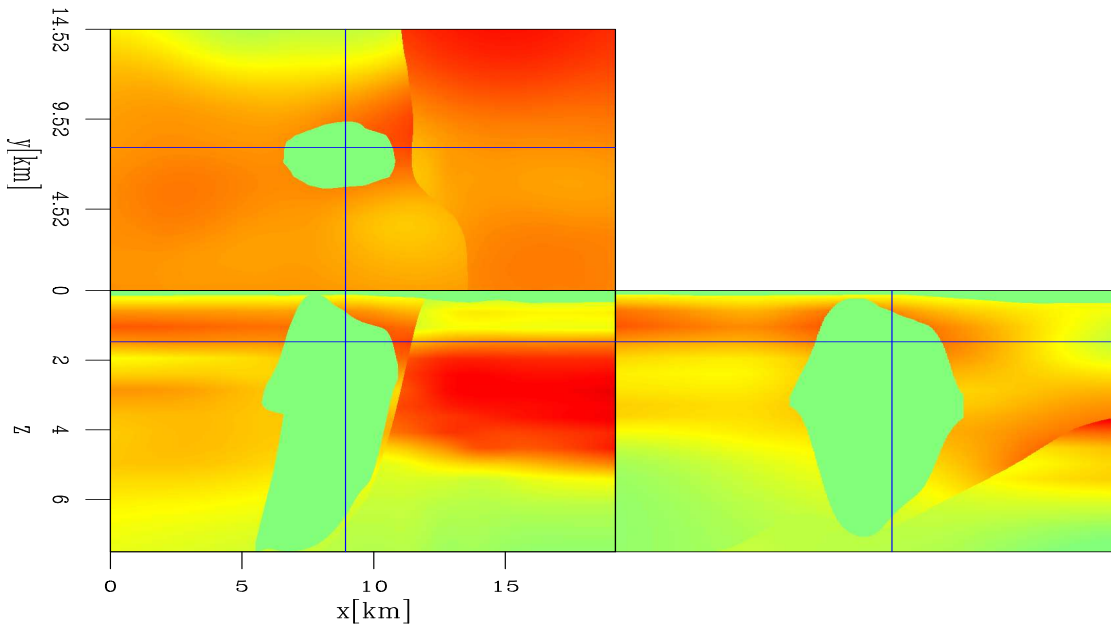


Figure 4.8: The anisotropy parameter δ . `plane3d/. dlt`

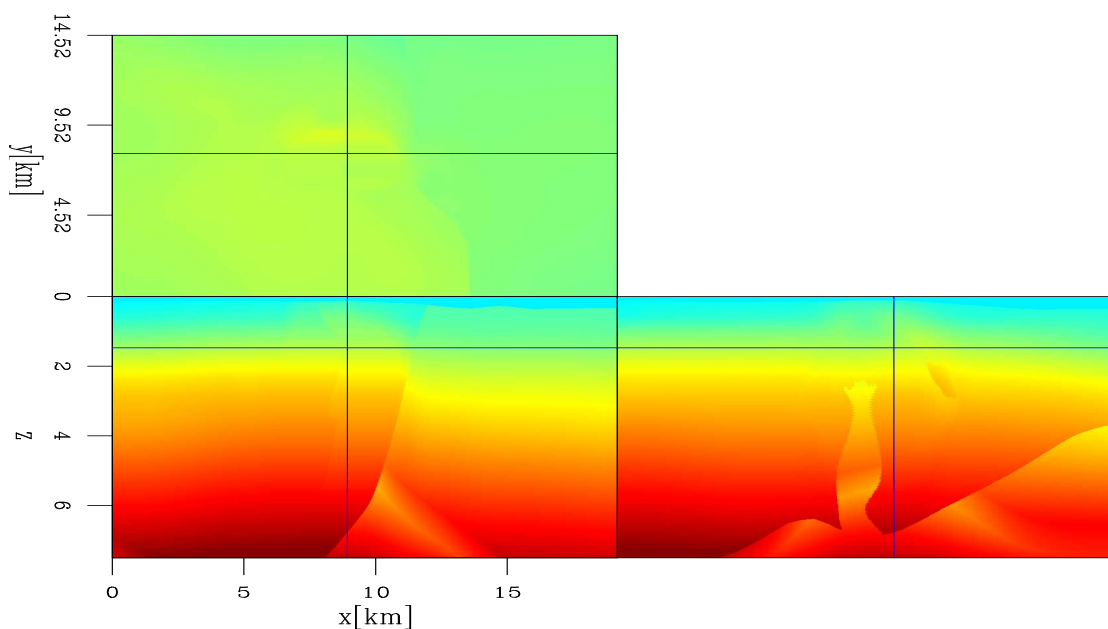


Figure 4.9: The vertical velocity model used for migration. The salt body is filled with the sediment velocity. `plane3d/. velnosalt`

salt flanks are well imaged in Figure 4.10, but absent in Figure 4.11. Notice that in both images the bottom half of the salt flank is not imaged, because the velocity model used for migration is sediment flooded (Figure 4.9). Figures 4.12 through 4.16 compare the images of the two migrations in detail. For these figures, the top panel is obtained by 3D plane-wave migration in tilted coordinates, and the bottom panel is obtained by 3D plane-wave migration in vertical Cartesian coordinates.

Figure 4.12 compares a depth slice of the two images. The boundary between the salt and sediment is well imaged in Figure 4.12(a), while most of the boundary is absent in Figure 4.12(b). At “A” and “B” we can also see small structures immediately around the salt boundary in Figure 4.12(a) that are missing in Figure 4.12(b). At “C” and “D”, the faults are better imaged in Figure 4.12(a) than in Figure 4.12(b).

Figure 4.13 compares the inline section of the two images at $y = 9.16$ km. The salt flank, which is not visible in 4.13(b), becomes clear in Figure 4.13(a). The top of the salt in this section, which is relatively horizontal in the inline direction, is not

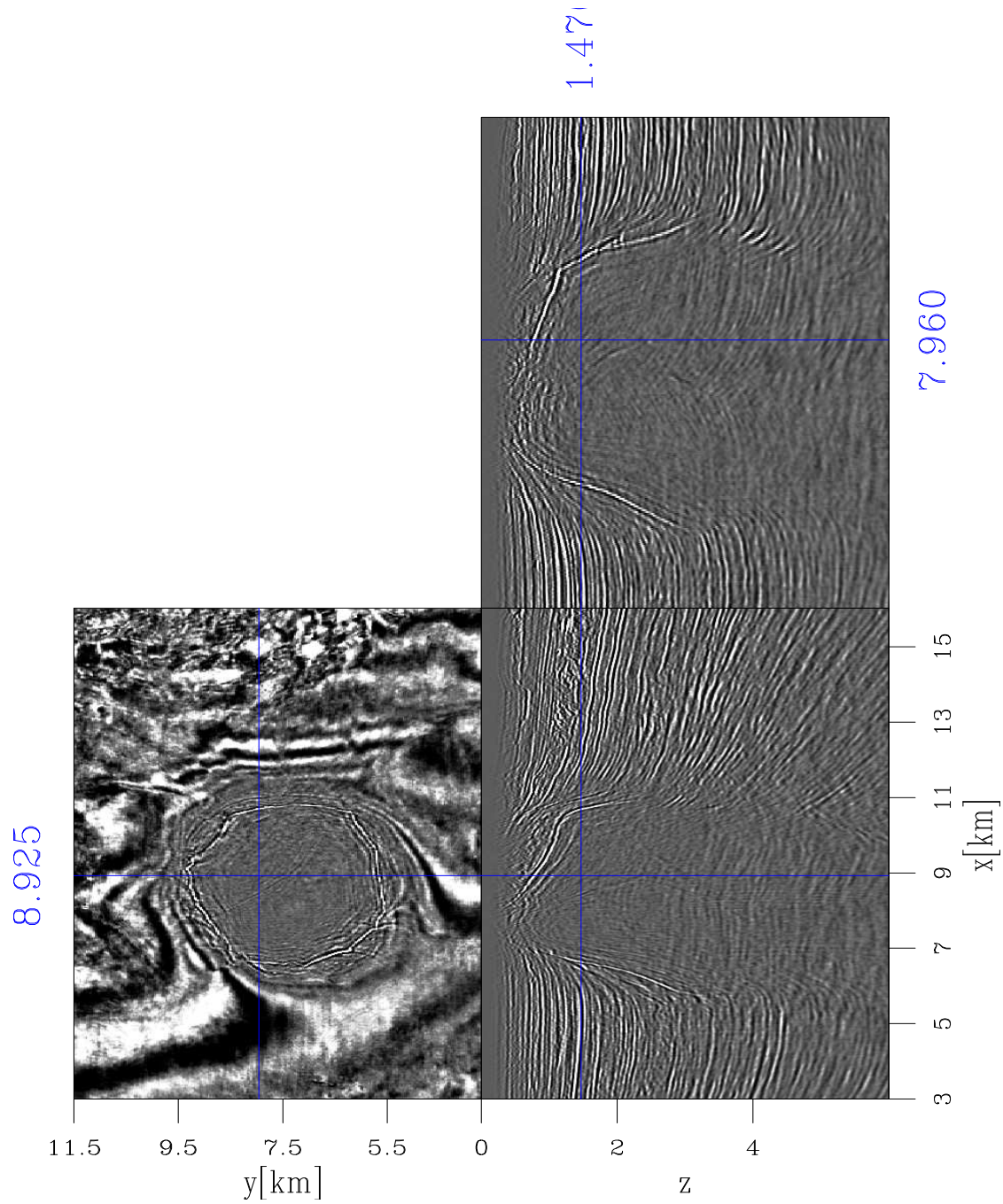


Figure 4.10: The image obtained by 3D plane-wave migration in tilted coordinates using the velocity with sediment flooding. `plane3d/. imagetiltcube`

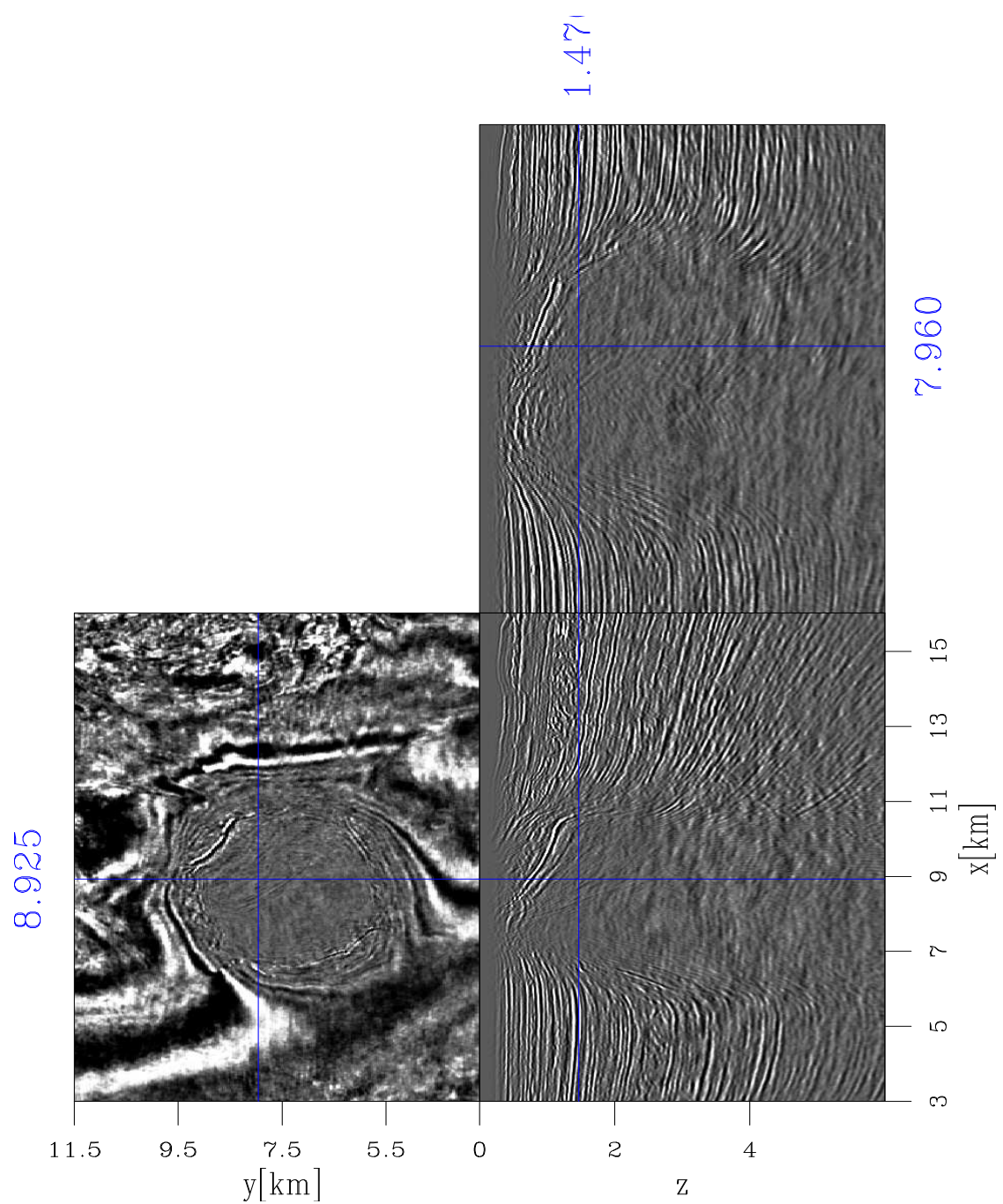


Figure 4.11: The image obtained by 3D plane-wave migration in vertical Cartesian coordinates using the velocity with sediment flooding. `plane3d/. imagenotiltcube`

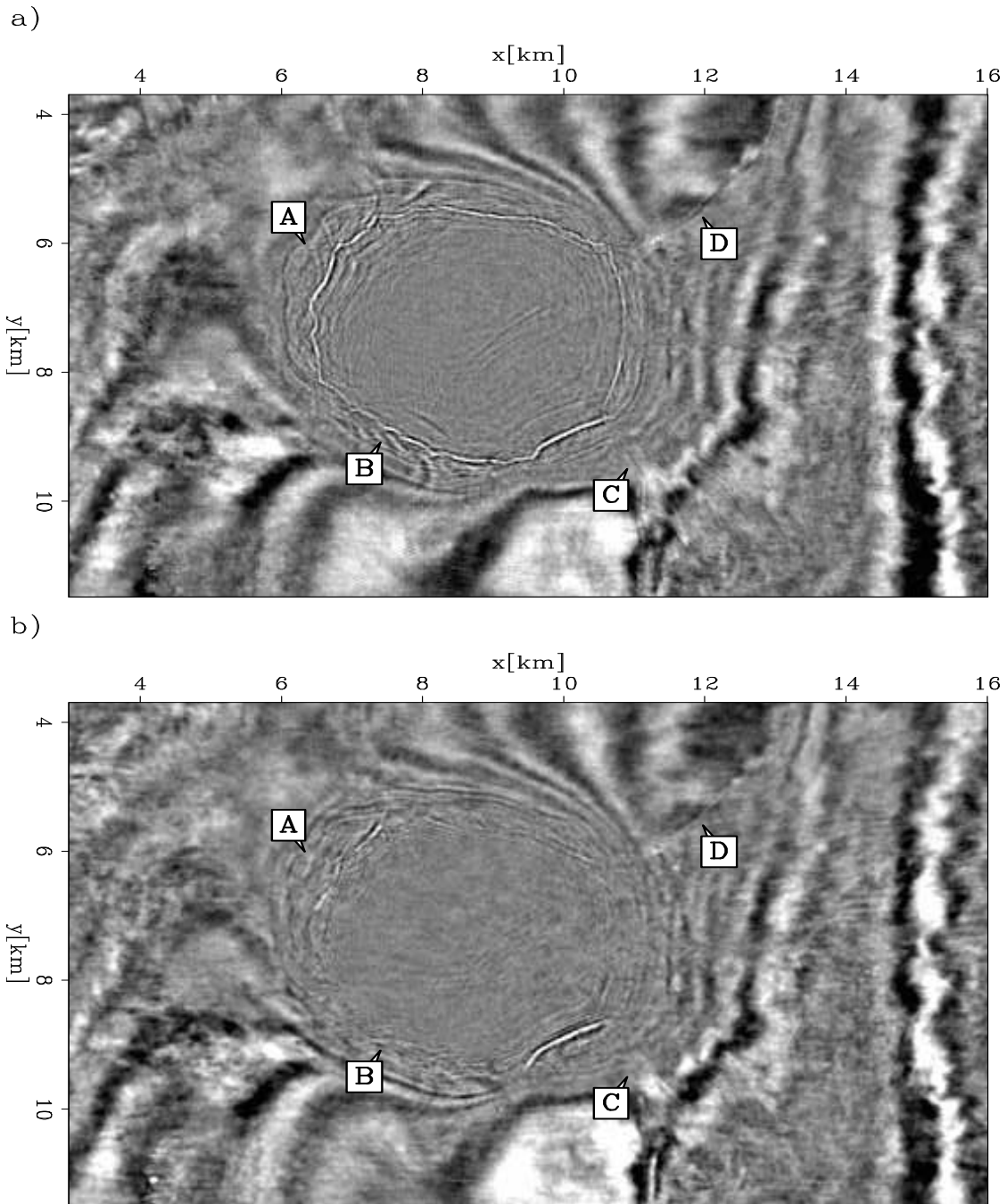


Figure 4.12: A depth slice of the images: (a) 3D plane-wave migration in tilted coordinates; (b) 3D plane-wave migration in vertical Cartesian coordinates.

plane3d/. depth1comparison

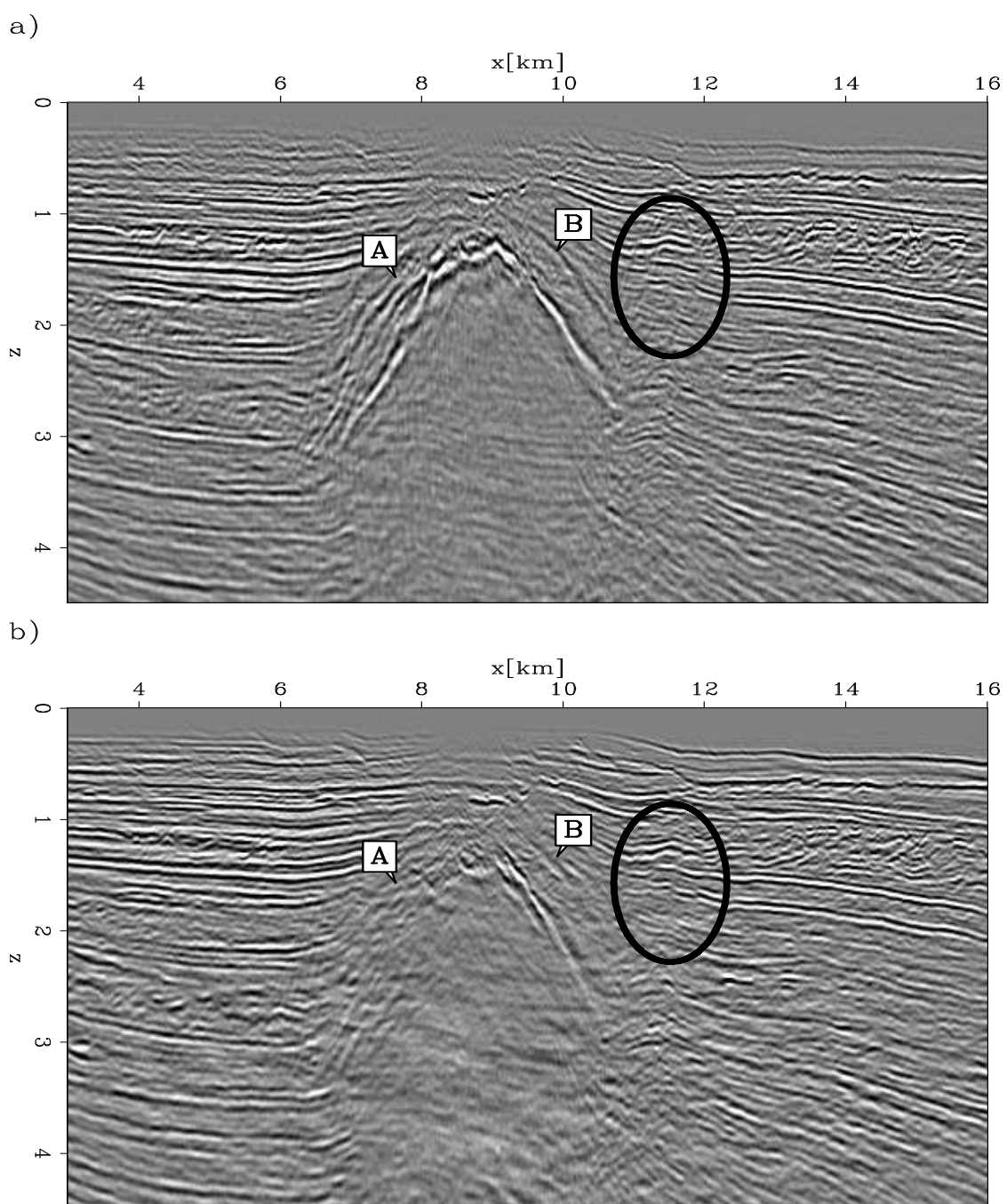


Figure 4.13: An inline section of the images: (a) 3D plane-wave migration in tilted coordinates; (b) 3D plane-wave migration in vertical Cartesian coordinates.

plane3d/. inline1comparison

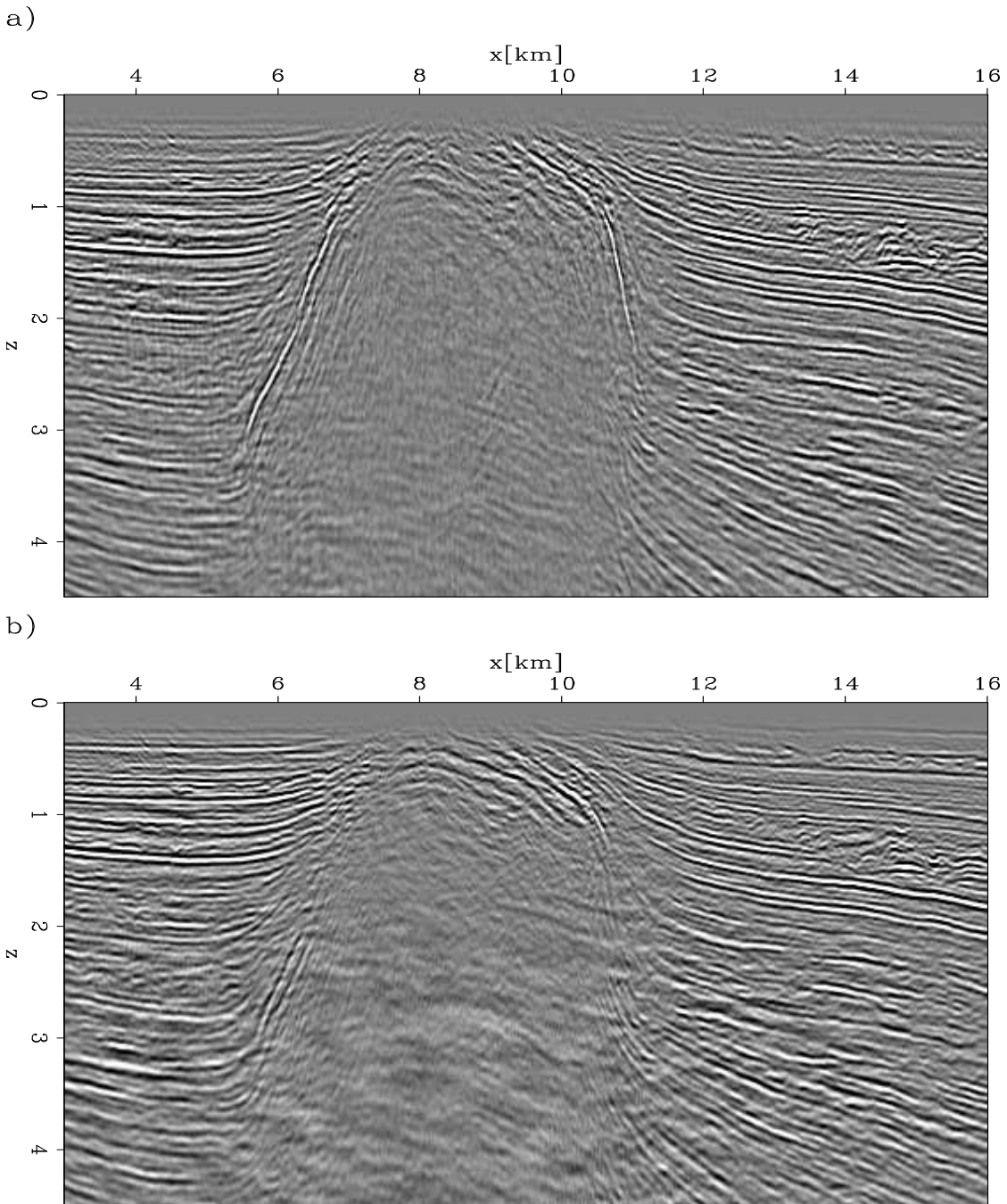


Figure 4.14: An inline section of the images: (a) 3D plane-wave migration in tilted coordinates; (b) 3D plane-wave migration in vertical Cartesian coordinates.

plane3d/. inline2comparison

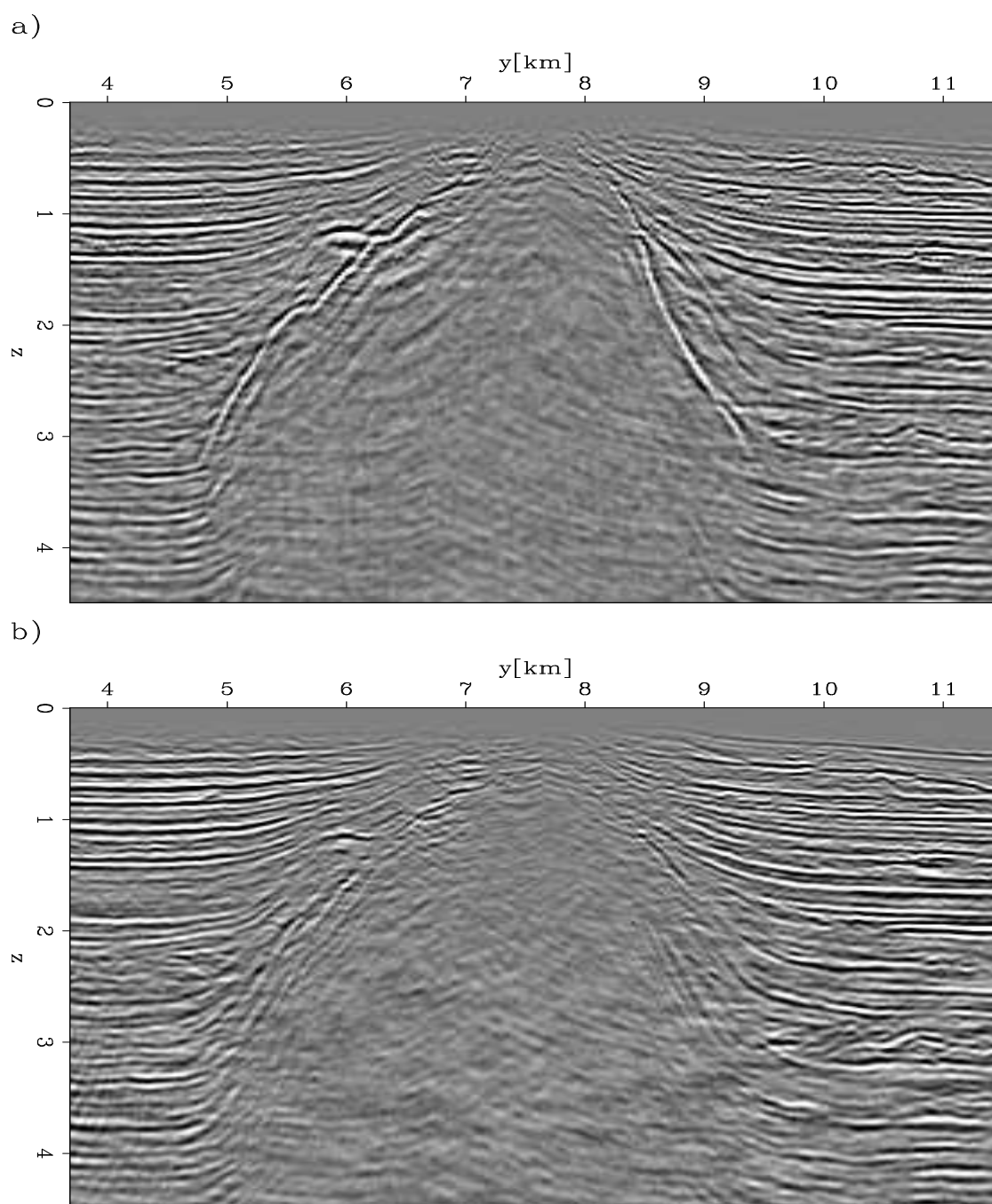


Figure 4.15: A cross-line section of the images: (a) 3D plane-wave migration in tilted coordinates; (b) 3D plane-wave migration in vertical Cartesian coordinates.

plane3d/. cross1comparison

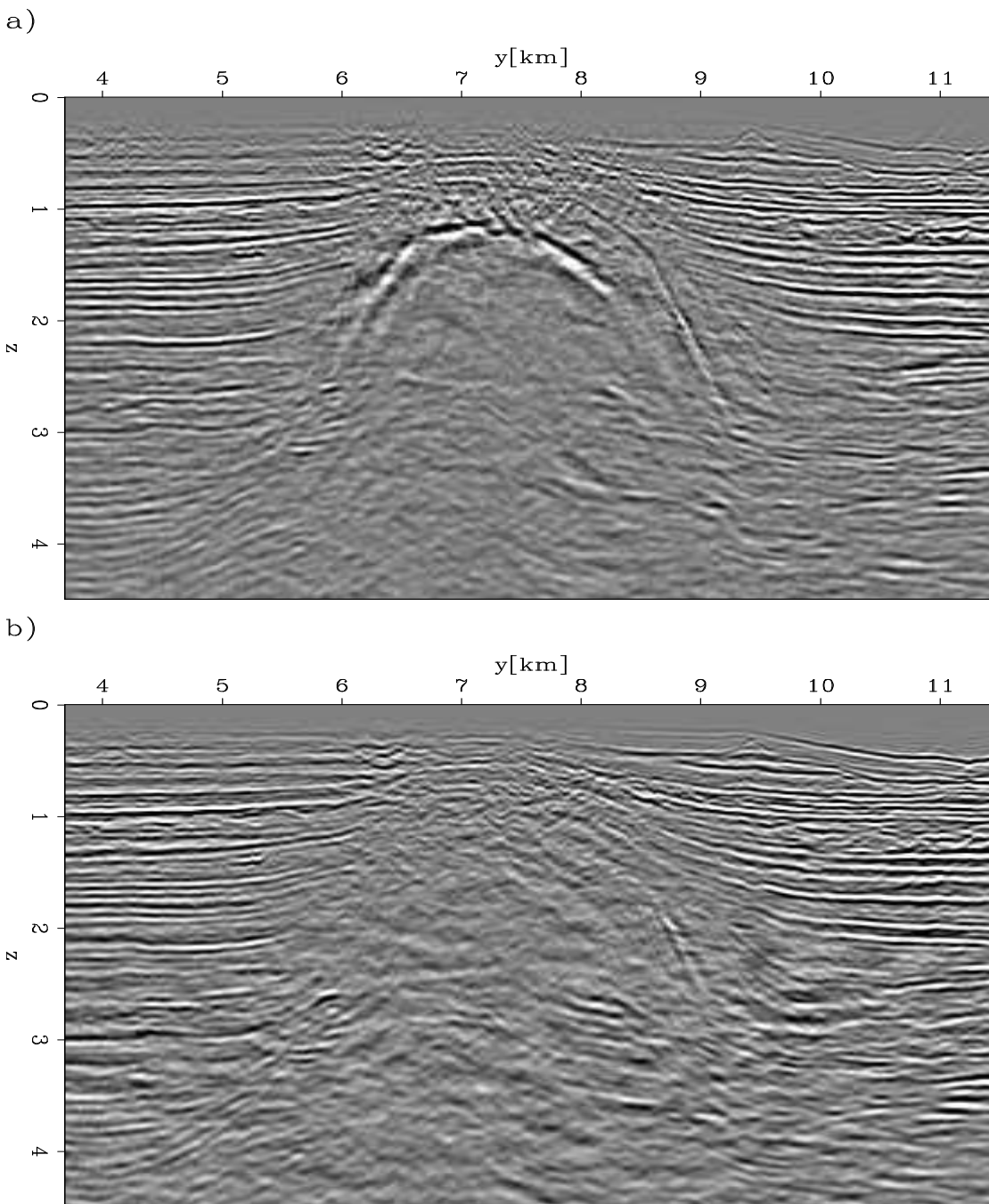


Figure 4.16: A cross-line section of the images: (a) 3D plane-wave migration in tilted coordinates; (b) 3D plane-wave migration in vertical Cartesian coordinates.

plane3d/. cross2comparison

imaged in Figure 4.13(b) because it has large dip in the cross-line direction. In Figure 4.13(a), there are also some dipping reflectors above the salt flank (at “A” and “B”), which disappear in Figure 4.13(b). These events correspond to the structure at ”B” area in Figure 4.12. In Figure 4.13(a), there are a group of faults located to the right of the salt body (in the oval), which are missing in Figure 4.13(b). Figure 4.14 compares the inline section at $y = 6.97$ km of the two images. We see similar improvement of the salt flanks in Figure 4.14(a). Unlike Figure 4.13, the salt flank is missing in Figure 4.14(b) because of the steep dip in the inline direction.

Figure 4.15 compares the cross-line section of the two images at $x = 8.65$ km, where the salt flank is steep in the cross-line direction. The salt flank is well imaged in Figure 4.15(a), while it is missing in Figure 4.15(b). Figure 4.15 compares the cross-line section of the two images at $x = 12.91$ km, where the salt flank is almost flat in the cross-line direction but is steep in the inline direction. We can see similar improvement of the salt flanks in Figure 4.16(a).

These comparisons show that plane-wave migration in tilted coordinates greatly improves the images of the salt-body flanks and steeply dipping faults.

CONCLUSION

In this chapter, I generalized plane-wave migration in tilted coordinates to 3D. As with the 2D case, I decomposed the recorded data into plane-wave source data and migrated them using the one-way wave-equation wavefield-extrapolation operator in tilted coordinates. Plane-wave sources with similar directions share the same tilted coordinate system, whose tilting angle is determined by the propagation direction of plane-wave sources. Examples using field data show that this algorithm effectively images steep reflectors, such as salt flanks and faults, in both inline and cross-line directions.

ACKNOWLEDGMENTS

I thank ExxonMobil for making the dataset available. I also acknowledge the Stanford Center for Computational Earth and Environmental Science for allowing me to use the computational resources to finish the 3D field dataset example.

Chapter 5

Angle-domain common-image gathers for steep reflectors

INTRODUCTION

Velocity estimation plays a key role in seismic imaging. A typical migration velocity analysis method includes three steps: (1) migrations using the background velocity are run to obtain angle-domain common-image gathers (CIGs); (2) curvatures are estimated from angle-domain CIGs by residual moveout (RMO) analysis; (3) curvature information is inverted to update the velocity by back projection.

Most velocity estimation methods make assumptions about the subsurface such as a horizontal stratified earth for normal moveout (NMO), or horizontal reflectors by Toldi (1985). Even recently, for sophisticated tomography, only reflectors with gentle dip are chosen for velocity estimation and are assumed to be horizontal when doing RMO analysis (Clapp, 2000).

Reflections from steep interfaces are important for velocity analysis. Reflections from reflectors with gentle dip are chosen for velocity estimation. Most waves illuminating reflectors with gentle dip travel in a direction that is less than 30° from the vertical. Therefore, seismic reflection tomography is a limited-angle tomography,

an ill-posed problem (Tam and Perez-Mendez, 1981). Since most waves illuminating near-horizontal reflectors travel almost vertically, the vertical resolution in seismic reflection tomography is limited (Clapp, 2000). In contrast, most waves illuminating steep reflectors have a portion of wave-path that is nearly horizontal. Therefore using angle-domain CIGs of steep reflectors improves the angle coverage of rays in tomography, thus reducing the problem of poor conditioning and improving the stability. It also leads to fewer artifacts caused by low angular coverage and better vertical resolution of the estimated velocity. The horizontal portion of the ray path of waves illuminating steep reflectors also provides the sensitivity to anisotropy.

The conventional one-way wave equation has been routinely applied in the industry. It is difficult, however, to obtain reliable angle-domain CIGs of steep reflectors by conventional one-way wave-equation migration (Biondi and Shan, 2002; Biondi and Symes, 2004). One-way wave-equation migration in vertical Cartesian coordinates can model accurately waves traveling almost vertically, but not waves traveling almost horizontally. Waves illuminating steep reflectors usually travel almost horizontally or even overturn before or after they are reflected. Reverse-time migration can image steep reflectors and provide robust angle-domain CIGs by using the vertical subsurface offset in addition to the horizontal one (Biondi and Shan, 2002).

In chapters 3 and 4, I have demonstrated that plane-wave migration in tilted coordinates is an effective tool for imaging steep reflectors. In this chapter, I discuss how to produce reliable angle-domain CIGs using plane-wave migration in tilted coordinates, and how to implement RMO analysis on the CIGs of steep reflectors. I apply reverse-time migration and plane-wave migration in tilted coordinates to the BP velocity benchmark dataset (Billette and Brandsberg-Dahl, 2005), and compare angle-domain CIGs produced by both migrations. Before discussing plane-wave migration in tilted coordinates, I review how to generate angle-domain CIGs by both conventional one-way wave-equation and reverse-time migration.

In this chapter, I limit my discussion in 2D, and I show the derivation for the 3D case in appendix A.

ANGLE-DOMAIN CIGS BY CONVENTIONAL ONE-WAY WAVE-EQUATION MIGRATION

Shot-profile and source-receiver migrations can generate equivalent subsurface-offset-domain CIGs (Shan and Zhang, 2003). In shot-profile migration, the source wavefield $S(s_x, x, z, \omega)$ and receiver wavefield $R(s_x, x, z, \omega)$ are extrapolated into the subsurface, where s_x is source location, x is horizontal location, z is vertical location, and ω is circular frequency. Offset-domain CIGs $I(x, z, h_x)$ are generated by cross-correlating the source and receiver wavefields with a horizontal shift h_x as follows (Rickett and Sava, 2002):

$$I(x, z, h_x) = \int \int S^*(s_x, x - h_x, z, \omega) R(s_x, x + h_x, z, \omega) d\omega ds_x \quad (5.1)$$

where the horizontal shift h_x is called the horizontal subsurface offset, and S^* is the complex conjugate of the source wavefield S . Offset-domain CIGs $I(x, z, h_x)$ are transformed to angle-domain CIGs $I(x, z, \gamma)$ by applying slant-stacking in the space domain or radial-trace transform in the Fourier domain using the following relationship (Sava and Fomel, 2003):

$$\tan \gamma = -\frac{k_{h_x}}{k_z}, \quad (5.2)$$

where k_{h_x} and k_z are wavenumbers corresponding to h_x and z , respectively, and γ is reflection angle.

For nearly horizontal reflectors, angle-domain CIGs obtained by conventional one-way wave-equation migration using equations 5.1 and 5.2 are reliable. However, there are two issues that make it difficult to obtain reliable CIGs for steep reflectors. First, steep reflectors are mainly illuminated by near-horizontal and overturned waves, which cannot be modeled accurately by the one-way wave-equation extrapolator in vertical Cartesian coordinates. Second, we cannot obtain reliable angle-domain CIGs from horizontal-offset-domain CIGs, because given an opening angle, the steeper the

reflector, the larger the horizontal subsurface offset is needed to get a reliable angle-domain CIG (Figure 5.1). However, the length of the subsurface offset is usually limited in shot-profile migration to reduce cost, therefore, limiting the effectiveness of angle-domain CIGs for steep reflectors from horizontal-offset-domain CIGs.

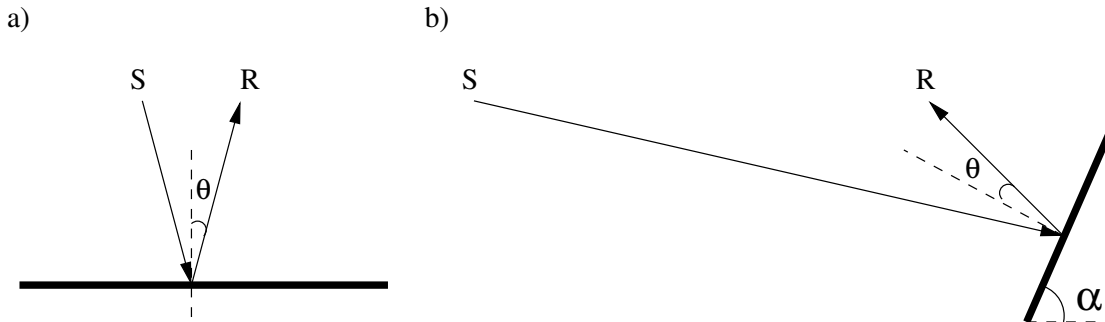


Figure 5.1: Horizontal subsurface offset for a horizontal reflector (a) and steep reflector (b). S and R are end points of source and receiver rays, respectively. Angle θ is the opening angle and α is the dip of the steep reflector. Given an opening angle θ , the steep reflector needs a much larger subsurface offset than the horizontal reflector to construct the angle gather. $\boxed{\text{cigmv}/. \text{horizontaloffset}}$

In the next two sections, I discuss how these two issues in conventional one-way wave-equation migration are solved by reverse-time migration and by plane-wave migration in tilted coordinates.

ANGLE-DOMAIN CIGS BY REVERSE-TIME MIGRATION

Reverse-time migration, based on the two-way wave equation, handles high-angle and overturned waves naturally. In conventional one-way wave-equation migration, source and receiver wavefields are extrapolated along the z -axis (the vertical direction), and the subsurface offset is along the x -axis (the horizontal direction). In contrast, in reverse-time migration the source wavefield $S = S(s_x, x, z, t)$ and the receiver wavefield $R = R(s_x, x, z, t)$ are extrapolated along the time axis, where t is the traveltimes. There is no functional difference between the x - and z -axis for wavefield

extrapolation along the t -axis. Therefore, reverse-time migration can yield general-direction subsurface-offset CIGs, and horizontal and vertical offsets are just two special cases (Biondi and Shan, 2002). As with conventional one-way wave-equation migration, in reverse-time migration, horizontal-offset-domain CIGs are generated by cross-correlating source and receiver wavefields with a horizontal subsurface offset h_x as follows:

$$I_x(x, z, h_x) = \int \int S(s_x, x - h_x, z, t) R(s_x, x + h_x, z, t) dt ds_x. \quad (5.3)$$

Similarly, vertical-offset-domain CIGs are constructed by cross-correlating source and receiver wavefields with a vertical shift h_z , as follows:

$$I_z(x, z, h_z) = \int \int S(s_x, x, z - h_z, t) R(s_x, x, z + h_z, t) dt ds_x, \quad (5.4)$$

with shift h_z the vertical subsurface offset.

As with conventional one-way wave-equation migration, we can apply equation 5.2 to transform the horizontal-offset-domain CIGs $I_x(x, z, h_x)$ to angle-domain CIGs $I_x(x, z, \gamma)$. Similarly, we can also transform the vertical-offset-domain CIGs $I_z(x, z, h_z)$ to angle-domain CIGs $I_z(x, z, \gamma)$ by using the relation,

$$\tan \gamma = -\frac{k_{h_z}}{k_x}, \quad (5.5)$$

where k_{h_z} and k_x are wavenumbers corresponding to h_z and x , respectively.

Neither vertical nor horizontal CIGs are robust for an area with complex geology, where reflectors have a full range of dips. Horizontal CIGs are suitable for nearly-horizontal reflectors, but not reliable for steep reflectors while vertical CIGs are good for steep reflectors, but not reliable for nearly-horizontal reflectors. The subsurface offset along the dip direction of the reflector is called *geologic offset*. CIGs would be robust if we used geologic offset, but it is too expensive to generate geologic offset CIGs directly. Biondi and Symes (2004) demonstrate that the geologic offset h_0 ,

horizontal offset h_x , and vertical offset h_z are linked by the following relationships:

$$h_x = \frac{h_0}{\cos \alpha}, \quad (5.6)$$

$$h_z = \frac{h_0}{\sin \alpha}, \quad (5.7)$$

where α is the dip of the reflector. Equations 5.6 and 5.7 show why we fail to obtain reliable angle-domain CIGs from horizontal-offset CIGs for steep reflectors. The length of horizontal subsurface offsets must be large to obtain reliable angle-domain CIGs for steep reflectors. In the extreme where the reflector is vertical, from equation 5.6, we would need infinite horizontal subsurface offset.

Robust angle-domain CIGs, however, can be constructed by merging horizontal and vertical angle-domain CIGs as follows (Biondi and Symes, 2004):

$$I(x, z, \gamma) = \cos^2 \alpha(x, z) I_x(x, z, \gamma) + \sin^2 \alpha(x, z) I_z(x, z, \gamma), \quad (5.8)$$

where $\alpha(x, z)$ is the dip at location (x, z) . Equation 5.8 is performed in the Fourier domain (k_x, k_z) , with the dip of the reflector calculated using the relation,

$$\tan \alpha = \frac{k_x}{k_z}, \quad (5.9)$$

where k_x and k_z are wavenumbers corresponding to x and z , respectively.

ANGLE GATHERS BY PLANE-WAVE MIGRATION IN TILTED COORDINATES

Reverse-time migration provides reliable CIGs for steep reflectors, but it is expensive to apply reverse-time migration routinely. In this section, I discuss how to generate angle-domain CIGs by plane-wave migration in tilted coordinates, and show that it can produce reliable CIGs for steep reflectors. I start with CIGs in conventional plane-wave migration.

In conventional plane-wave migration, offset-domain CIGs are constructed by cross-correlating source and receiver wavefields, weighted with frequency,

$$I(x, z, h_x) = \int \int \omega S_p^*(p_{s_x}, x - h_x, z, \omega) R_p(p_{s_x}, x + h_x, z, \omega) d\omega dp_{s_x}, \quad (5.10)$$

where h_x is the horizontal subsurface offset, ω is the circular frequency; $S_p(p_{s_x}, x, z, \omega)$ and $R_p(p_{s_x}, x, z, \omega)$ are the plane-wave source and receiver wavefields corresponding to the ray parameter p_{s_x} , respectively. As with the conventional zero-subsurface-offset image, offset-domain CIGs defined in equation 5.10 are equivalent to those obtained by shot-profile migration (Liu et al., 2002; Zhang et al., 2005b). Thus, as in equation 5.2, offset-domain CIGs, $I(x, z, h_x)$, are transformed to angle-domain CIGs, $I(x, z, \gamma)$, by local slant-stacking.

Given a plane-wave source corresponding to ray parameter p_{s_x} , we extrapolate wavefields in the tilted coordinates (x', z') with a tilting angle θ . The subsurface-offset-domain CIGs for this plane-wave source are constructed as follows:

$$I_{p_{s_x}}(x', z', h_{x'}) = \int \omega S_p^*(p_{s_x}, x' - h_{x'}, z', \omega) R_p(p_{s_x}, x' + h_{x'}, z', \omega) d\omega. \quad (5.11)$$

where the subsurface offset $h_{x'}$ is along the x' -axis. The subsurface offset $h_{x'}$ is not necessarily along the geologic dip, but for steep reflectors it is generally closer to the dip direction than is the conventional horizontal offset. As for the conventional plane-wave migration, offset-domain CIGs, $I_{p_{s_x}}(x', z', h_{x'})$, corresponding to the plane-wave source p_{s_x} are transformed to angle-domain CIGs, $I_{p_{s_x}}(x', z', \gamma)$, by applying slant stacking in tilted coordinates,

$$\tan \gamma = -\frac{k_{h_{x'}}}{k_{z'}}, \quad (5.12)$$

where $k_{h_{x'}}$ and $k_{z'}$ are wavenumbers corresponding to $h_{x'}$ and z' , respectively. The angle-domain CIG cube corresponding to the plane-wave source p_{s_x} , $I_{p_{s_x}}(x', z', \gamma)$, is rotated back to vertical Cartesian coordinates. Angle-domain CIGs of all possible plane-wave sources are then stacked in vertical Cartesian coordinates.

We can alternatively transform offset-domain CIGs obtained by plane-wave migration in tilted coordinates, $I_{p_{sx}}(x', z', h_{x'})$, into horizontal- and vertical-offset-domain CIGs, and merge them using equation 5.8 after transforming them into angle-domain CIGs. Again, equations 5.6 and 5.7 are the relationships linking the geologic offset h_0 , horizontal offset h_x , and vertical offset h_z . Figure 5.2 illustrates the relationships linking the geologic offset h_0 and a general-direction offset \bar{h} for a single event. The migration velocity is assumed to be lower than the true velocity. For the geologic offset h_0 , S_0 and R_0 are end points of source and receiver rays, respectively. For a general-direction offset \bar{h} , \bar{S} and \bar{R} are end points of source and receiver rays, respectively. The difference between the direction of offset h_0 and the direction of \bar{h} is the angle ψ . The dip of the event is α and the reflection angle is γ . There is a crucial constraint on the geometric construction of all offsets; that is, the traveltimes along the source and receiver rays is the same for all the offset directions, and it is the recording time of the event. With the assumption that the velocity in a small area around the reflection point is constant, this constraint leads to the following equality:

$$|S_0\bar{S}| = |R_0\bar{R}|, \quad (5.13)$$

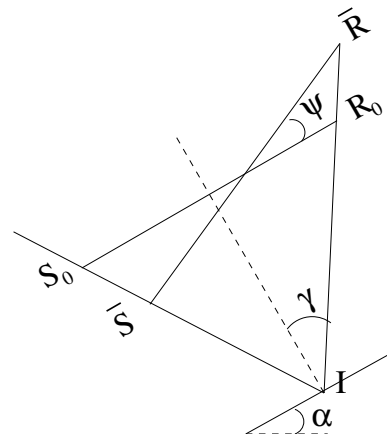
from which we can obtain the relationship linking h_0 and \bar{h} as follows:

$$\bar{h} = \frac{h_0}{\cos \psi}. \quad (5.14)$$

Equation 5.14 shows that the geologic offset is the project of a general offset onto the dip plane of the reflector. The angle ψ in equation 5.14 for horizontal offset $\bar{h} = h_x$ is α , and for vertical offset $\bar{h} = h_z$ is $90^\circ - \alpha$. Equation 5.14 shows that the geologic offset h_0 is the optimal offset for generating angle-domain CIGs; the more the offset direction differs from the dip direction, the larger the subsurface offset needed, for given opening angle.

In the tilted coordinate system (x', z') , the angle between the subsurface offset in the x' -direction and geologic offset is $\theta - \alpha$. Therefore, the subsurface offset $h_{x'}$ and

Figure 5.2: Geometry of geologic offset and a general-direction offset. `cigmv/. offsetgeo`



the geologic offset h_0 are linked by the relationship,

$$h_{x'} = \frac{h_0}{\cos(\theta - \alpha)}. \quad (5.15)$$

From equations 5.15, 5.6, and 5.7, the subsurface offset in the x' -direction, $h_{x'}$, the vertical offset h_z , and the horizontal offset h_x are linked by the relationships,

$$h_x = \frac{h_{x'} \cos(\theta - \alpha)}{\cos \alpha}, \quad (5.16)$$

$$h_z = \frac{h_{x'} \cos(\theta - \alpha)}{\sin \alpha}. \quad (5.17)$$

With equations 5.16 and 5.17, the offset-domain CIGs in tilted coordinates, $I_{x'}(x', z', h_{x'})$, can be transformed to horizontal- and vertical-offset-domain CIGs. Horizontal- as well as vertical-offset-domain CIGs of all possible plane-wave sources are stacked after being rotated back to vertical Cartesian coordinates. After being transformed to angle-domain CIGs, horizontal and vertical CIGs are merged by using equation 5.8, as with reverse-time migration.

DIP-DEPENDENT RMO ANALYSIS

Biondi and Symes (2004) demonstrate that in an angle-domain CIG cube, image

points move on a line normal to the apparent dip of reflectors, passing through the point where the source and receiver rays intersect. Figures 5.3 and 5.4 illustrates angle-domain CIGs of horizontal, vertical, and dipping reflectors. In Figures 5.3 and 5.4, x and z are the horizontal and vertical axes, respectively; γ denotes the reflection or opening angle, α the dip angle, and \mathbf{n} the axis normal to the reflector. Figure 5.3 illustrates angle-domain CIGs migrated with the true velocity. For a point on a reflector, image points for all opening angles lie at the same location. Therefore, the angle-domain CIG for a point on a reflector is a flat line in an angle-domain CIG cube, no matter how steep the reflector. As a result, the direction from which we view the CIG cube does not matter. Figure 5.4 illustrates angle-domain CIGs migrated with a too low velocity. For a point on a reflector, image points of different angles lie at different locations, and they move along the \mathbf{n} -axis. The larger the opening angle, the shallower the image point along the \mathbf{n} -axis. For a point on a horizontal reflector (Figure 5.4a), the angle-domain CIG curves up vertically. For a point on a vertical reflector (Figure 5.4c), the angle-domain CIG curves horizontally. Therefore, for a reflection point on a dipping reflector, if we still view the CIG cube in the vertical direction as usual (view the CIG cube at each constant x section), what we see are the image points belonging to the neighbor of the reflection point for most opening angle in its CIG.

Conventional RMO, however, ignores the dip of reflectors, and moves image points to flatten CIGs only vertically. For a point on a nearly horizontal reflector, conventional RMO approximately estimates the curvature of angle-domain CIGs, but for a point on a steep reflector, it mistakenly flattens the image points belonging to its neighbors, and cannot obtain the correct curvature of the CIGs. In this section, I describe RMO that incorporates the dip information and shifts image points along the direction normal to the apparent dips of reflectors.

For a horizontal reflector, with the straight-ray assumption, Biondi and Symes (2004) demonstrate that the vertical shift of image points, Δz , at the first order in

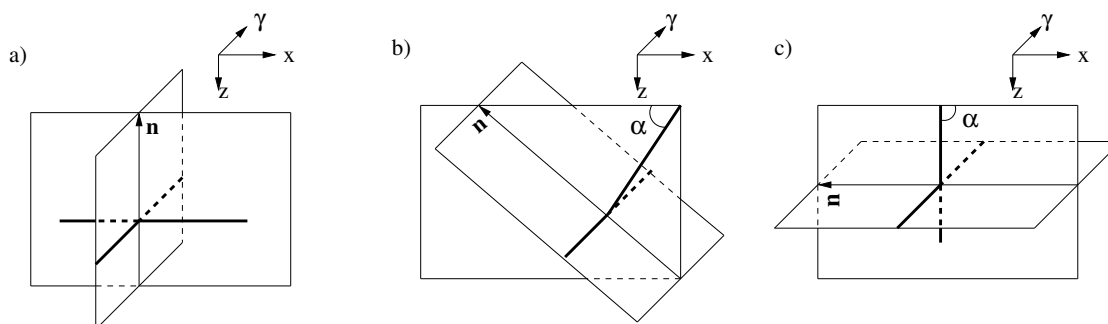


Figure 5.3: Angle-domain CIGs with the true velocity: (a) horizontal reflector; (b) dipping reflector; (c) vertical reflector. `cigmv/. anglecigtrue`

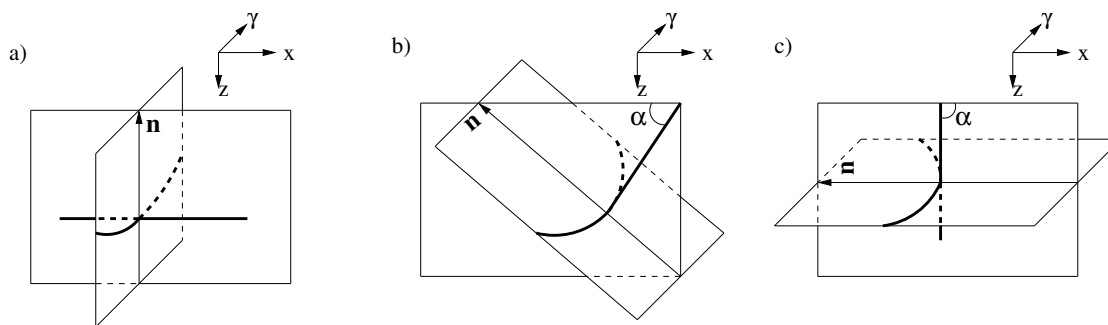


Figure 5.4: Angle-domain CIGs with too low migration velocity: (a) horizontal reflector; (b) dipping reflector; (c) vertical reflector. `cigmv/. anglecigslow`

presence of velocity error, is

$$\Delta z = z_0(1 - \rho) \tan^2 \gamma, \quad (5.18)$$

where ρ is the constant scaling factor of the velocity, γ is the opening angle, and z_0 is the depth at the reflection point. For a steep reflector with the dip α , with the straight-ray assumption, Biondi and Symes (2004) demonstrate that the shift of image points along the normal direction, Δn , at the first order in presence of velocity error, is

$$\Delta n = \frac{1 - \rho}{1 - \rho(1 - \cos \alpha)} \frac{\sin^2 \gamma}{\cos^2 \alpha - \sin^2 \gamma} z_0. \quad (5.19)$$

However, rays usually bend in practical application and equation fails to describe the moveout of an event on a reflector with large dip. In the extreme case that $\alpha = 90^\circ$, equation shows that Δn always equals to $-z_0$, which is not true. Equation 5.18 can be generalized to the case that the reflection point is on a steep reflector and the source and receiver are on a plane paralleling to the dip plane. In this case, the residual moveout along the normal direction of the reflector at the reflection point is

$$\Delta n = n_0(1 - \rho) \tan^2 \gamma, \quad (5.20)$$

where n_0 is the distance between the source-receiver plane and dip plane. For a steep reflector and bended rays, we can integral along the normal ray and use equation 5.20 for each small segment of the normal ray. Therefore, approximately the shift along the normal direction of the reflector at the reflection point, Δn is

$$\Delta n = l_0(1 - \rho) \tan^2 \bar{\gamma}, \quad (5.21)$$

where l_0 is the distance of the normal ray between the surface and the image point, and $\bar{\gamma} = \frac{\gamma + \gamma_{z_0}}{2}$ with γ_{z_0} the opening angle between source and receiver rays at the surface calculated according to Snell's law.

Dip-dependent RMO estimates the curvature of angle-domain CIGs accurately in the Fourier domain, because the dip information can be easily incorporated into

RMO and image points are shift along the normal direction of the reflector. The dip α is calculated in the Fourier domain as follows:

$$\tan \alpha = \frac{k_x}{k_z}. \quad (5.22)$$

Figure 5.5 illustrates the geometric relation linking the normal direction shift, Δn , horizontal shift, Δx , and vertical shift, Δz , for an angle-domain CIG at a reflection point with a dip of α . From the geometric relation, the shift along the normal direction is equivalent to a horizontal shift Δx , followed by a vertical shift Δz , where

$$\Delta x = \Delta n \sin \alpha, \quad (5.23)$$

$$\Delta z = \Delta n \cos \alpha. \quad (5.24)$$

A shift in the space domain is equivalent to a phase shift in the Fourier domain. Let $I(x, z, \gamma)$ be an angle-domain CIG cube in the space domain, and $I(k_x, k_z, \gamma)$ be the CIG in the Fourier domain. Then in the space domain, the shift Δn along the direction normal to the reflector is equivalent to a phase-shift of k_x followed by a phase-shift of k_z in the Fourier domain,

$$I^{RMO}(k_x, k_z, \gamma) = I(k_x, k_z, \gamma) \cdot e^{ik_x \Delta x} \cdot e^{ik_z \Delta z}. \quad (5.25)$$

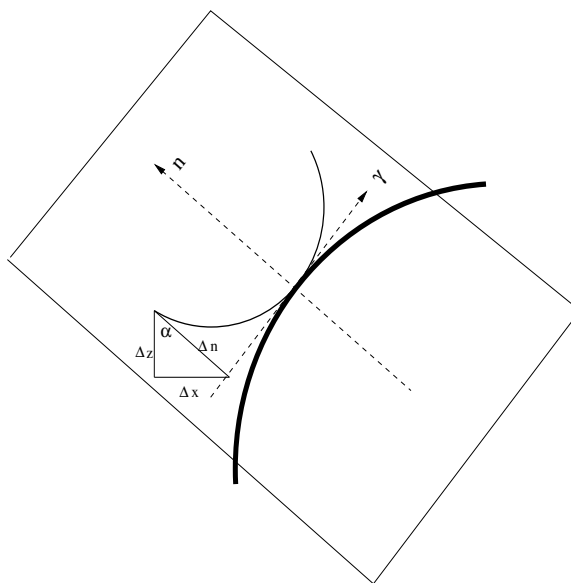
After applying the phase-shift, I transform the cube $I^{RMO}(k_x, k_z, \gamma)$ back to the space domain.

NUMERICAL EXAMPLES

I apply both reverse-time migration and plane-wave migration in tilted coordinates on the BP velocity benchmark dataset (Billette and Brandsberg-Dahl, 2005). Figure 5.6 shows the velocity model of the dataset. The maximum offset for the dataset is 15 km, which is much larger than that in most field surveys case. I mainly focus on the area from $x = 20$ km to $x = 35$ km, where both steep salt flanks and nearly-horizontal sediments are present. Figure 5.7 shows the image of that area obtained

Figure 5.5: Geometric relation linking the shift in normal direction, Δn , the horizontal shift, Δx and the vertical shift, Δz .

cigmv/. geometry



by plane-wave migration in tilted coordinates. I use 100 plane-wave sources and 100 coordinate systems in total in the migration. I run migration with both the true velocity and a too low velocity that is 3 percent slower than the true one. I first show that both horizontal and vertical CIGs obtained by reverse-time migration are not robust where reflectors have a full range of dips. Then I compare angle-domain CIGs obtained by plane-wave migration in tilted coordinates with those obtained by reverse-time migration. Finally, I show dip-dependent RMO analysis for a reflection point on a steep reflector.

Figure 5.8 shows the horizontal-offset-domain CIGs obtained by reverse-time migration with the true velocity. Figure 5.8 (a) shows horizontal-offset-domain CIGs of the nearly horizontal sediments at $x = 23$ km. Energy mostly focuses well at zero subsurface offset for sediments. Notice that multiples (at $z = 2.3$ km and $z = 3.9$ km) do not focus at zero subsurface offset. Figure 5.8 (b) shows horizontal-offset-domain CIGs of the steep salt flank at $x = 33.2$ km. Energy leaks to far subsurface offsets because of the stretch of the horizontal offset at steep reflectors. Figure 5.9 shows vertical-offset-domain CIGs for depth $z = 3.25$ km obtained by reverse-time migration with the true velocity. For the steep salt flank at $x = 33.2$ km, energy focuses well

at zero subsurface offset, while energy leaks to far subsurface offsets for the nearly horizontal sediments at $x = 24.5$ km. Figures 5.8 and 5.9 show that horizontal-offset-domain CIGs are robust for nearly horizontal reflectors, while vertical ones are robust for steep ones.

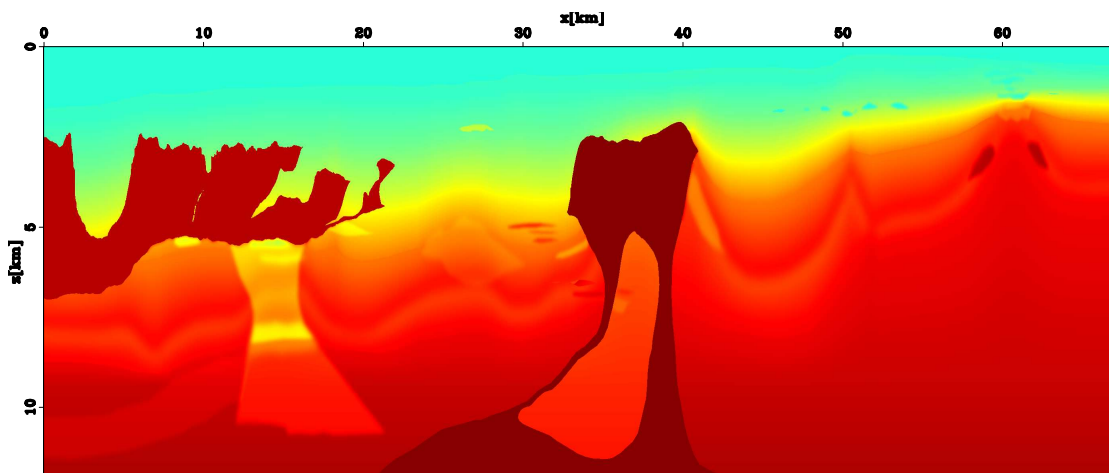


Figure 5.6: Velocity model of the BP velocity Benchmark. `cigmv/. bpvel`

Figures 5.10 and 5.11 show angle-domain CIGs, corresponding to the offset-domain CIGs in Figures 5.8 and 5.9. Figure 5.10 (a) shows horizontal angle-domain CIGs at nearly-horizontal sediments at $x = 23$ km. The gathers for sediments are flat since the true velocity is used in migration. Notice that the gathers of multiples bend downward at $z = 2.3$ km and $z = 3.9$ km. Figure 5.10 (b) shows horizontal angle-domain CIGs at the steep salt flank at $x = 33.2$ km. The angle-domain CIGs transferred from horizontal offset-domain CIGs look smeared at the salt flank because of the offset stretch. In contrast, in Figure 5.11 the angle-domain CIGs transferred from vertical offset-domain CIGs are flat at the steep salt flank (at $x = 33.2$ km), but those of the nearly-horizontal sediments ($x = 24.5$ km) look smeared.

Figures 5.12 and 5.13 show angle-domain CIGs transferred from horizontal and vertical offset-domain CIGs, respectively, both obtained by reverse-time migration with the 3 percent slower velocity. The horizontal locations for CIGs in Figure 5.12 (a) and (b) are at $x = 23$ km and $x = 33.2$ km, respectively. The vertical location for CIGs in Figure 5.13 is at $z = 3.5$ km. Angle-domain CIGs transferred from horizontal

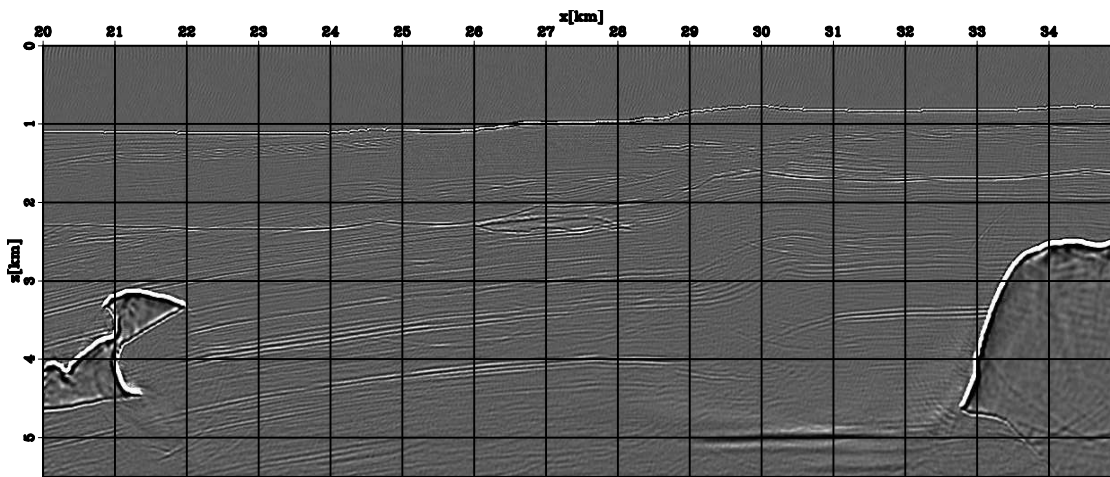


Figure 5.7: Image obtained by plane-wave migration in tilted coordinates. Both a steep salt flank and nearly horizontal sediments are present in this area. `cigmv/. imagetilt`

offset CIGs in Figure 5.12 (a) bend upward, exhibiting moveouts at the sediments, while those at steep salt flank in Figure 5.12 (b) look smeared. The curvature present in CIGs from horizontal offset CIGs is too large at the salt flank, given the 3 percent velocity error. In contrast, in Figure 5.13, the curvature present in angle-domain CIGs transferred from vertical offset CIGs relates to the velocity error at the salt flank (at $x = 33$ km), but CIGs transferred from vertical offset CIGs are smeared at sediments at $x = 30.5$ km.

As predicted by the theoretical analysis, Figures 5.8 through 5.13 demonstrate that in a complex area where there are reflectors with a full range of dips, neither angle-domain CIGs from horizontal offset CIGs nor those from vertical offset CIGs obtained by reverse-time migration are robust. To obtain reliable CIGs, I merge angle-domain CIGs from horizontal and vertical offset CIGs by applying equation 5.8. We can also obtain reliable CIGs by plane-wave migration in tilted coordinates. In the previous section, I discussed two methods to generate angle-domain CIGs by plane-wave migration in tilted coordinates. I choose the former one for the following examples. I transform offset-domain CIGs into angle-domain CIGs in tilted coordinates, and then

rotate the angle-domain CIGs back to vertical Cartesian coordinates. Figures 5.14 through 5.17 compare angle-domain CIGs obtained by reverse-time migration and by plane-wave migration in tilted coordinates. As discussed in the previous section, CIGs should be viewed in the direction normal to the reflector's apparent geologic dip. Otherwise, for reflection points on steep reflectors, most of the observed energy in their CIGs belongs to reflection points in their neighborhood.

Figure 5.8: Horizontal offset-domain CIGs obtained by reverse-time migration with the true velocity. (a) For relatively horizontal sediments, the energy focuses well at zero offset; (b) For steep salt flanks, the energy leaks to far offsets and the frequency is low. `cigmv/. hxgathers`

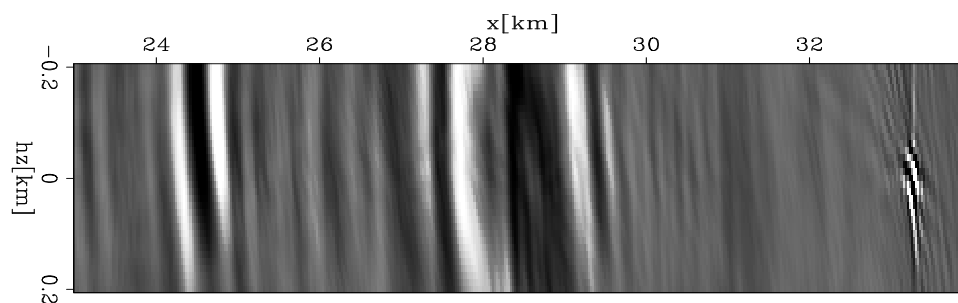
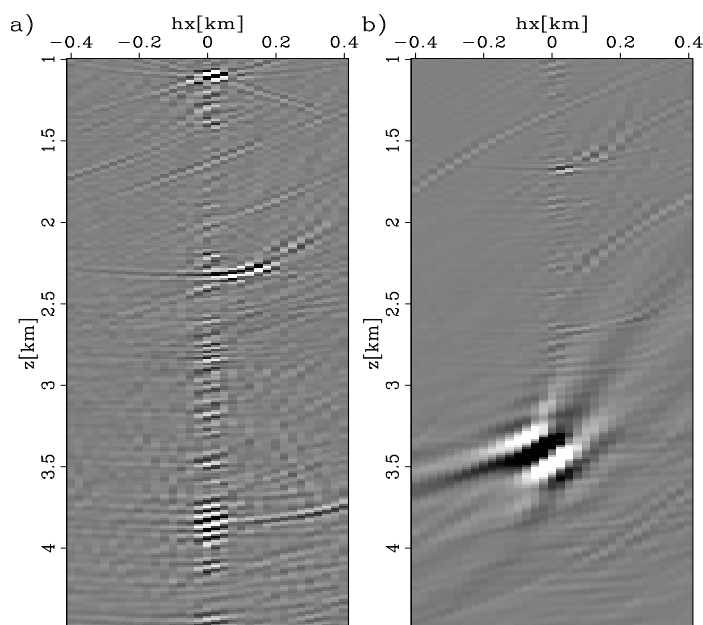


Figure 5.9: Vertical offset-domain CIGs obtained by reverse-time migration with the true velocity. For the steep salt flank at $x = 33.2$ km, the energy focuses well at zero offset. For the nearly horizontal sediments at $x = 24.5$ km, the energy leaks to far offsets. `cigmv/. hzgather`

Figures 5.14 and 5.15, respectively, show the CIG cubes obtained by reverse-time

Figure 5.10: Angle-domain CIGs from horizontal offset CIGs obtained by reverse-time migration with the true velocity. (a) For the nearly horizontal sediments at $x = 23$ km, the gathers are flat except for multiples. (b) For the steep salt flank at 33.2 km, the gathers are smeared because of the horizontal-offset stretch. `cigmv/.axgather`

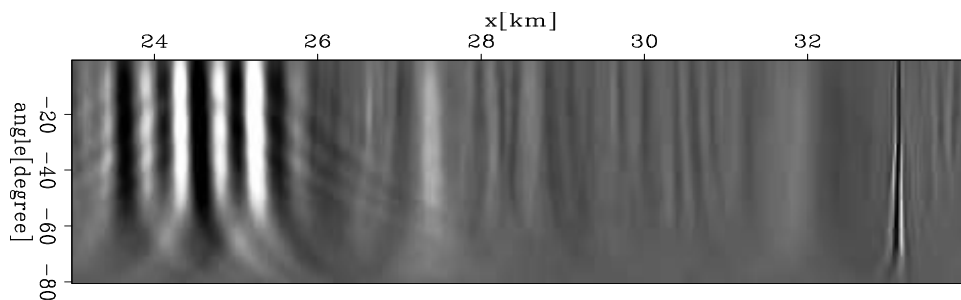
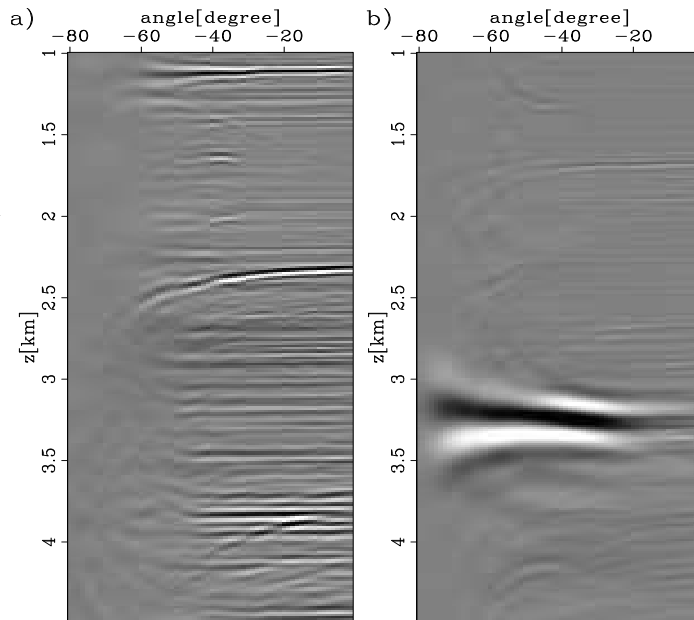


Figure 5.11: Angle-domain CIGs from vertical offset CIGs obtained by reverse-time migration with the true velocity. The CIGs of the sediments at $x = 24.5$ km are smeared, and the CIGs for the salt flank are at the same horizontal location for all angles. `cigmv/.azgather`

Figure 5.12: Angle-domain CIGs from horizontal offset CIGs obtained by reverse-time migration with the velocity underestimated by 3 percent. (a) For the nearly horizontal sediments at $x = 23$ km, the gathers show reasonable curvature. (b) For the steep salt flank at $x = 33.2$ km, the gather is a little smeared. The moveout is not reasonable, given the 3 percent velocity error.

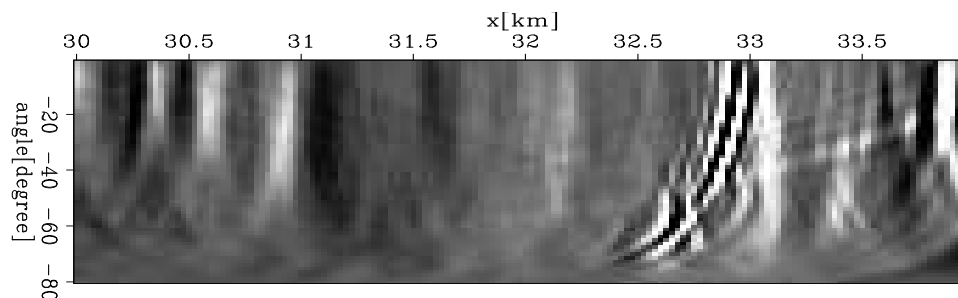
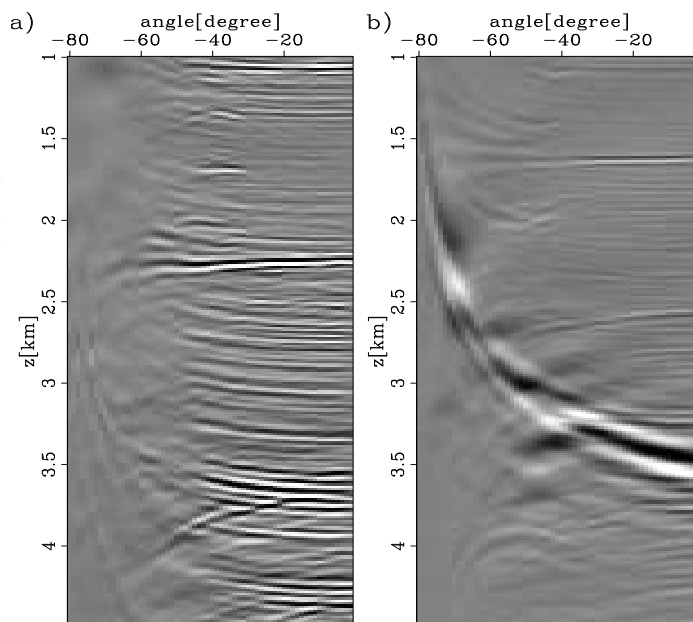


Figure 5.13: Angle-domain CIGs from vertical offset CIGs obtained by reverse-time migration with the velocity underestimated by 3 percent. The gather of the salt flank at $x = 33$ km shows reasonable moveout. The gathers of the sediments at $x = 30.5$ km look smeared.

migration and plane-wave migration in tilted coordinates with the true velocity. The top panel shows the CIGs viewed in the horizontal direction, and the side panel shows the CIGs viewed in the vertical direction. In both figures, CIGs of the steep salt flank look smeared in the side panel, and CIGs of the sediments look smeared in the top panel. This demonstrates that angle-domain CIGs should be viewed in the direction normal to the dip direction. CIGs obtained by reverse-time migration have more wide-angle energy than those obtained by plane-wave migration in tilted coordinates, but otherwise they are comparable. The offset of this dataset is unrealistically large; thus the maximum opening angle is also unrealistically large. In plane-wave migration in tilted coordinates, both source and receiver wavefields are extrapolated in the same coordinates, so when opening angle is very large (more than 60°), the angle difference between source and receiver rays is large; thus one of them cannot be modeled accurately. There is no angle limitation in reverse-time migration, therefore it handles wide-angle energy better than does plane-wave migration in tilted coordinates. Given the realistic offset in real datasets, opening angles are usually smaller than 50° . Therefore, angle-domain CIGs of the two migrations should be more comparable for a real dataset. Figure 5.16 compares the images obtained by stacking angle-domain CIGs along the angle axis. Figure 5.16 (a) is obtained by reverse-time migration, and Figure 5.16 (b) is obtained by plane-wave migration in tilted coordinates. The two images are comparable.

Figure 5.17 shows the comparison of angle-domain CIGs obtained by reverse-time migration and plane-wave migration in tilted coordinates with velocity that is 3 percent too slow. Figures 5.17 (a) and (b) show angle-domain CIGs in the vertical views. Panel (a) is obtained by reverse-time migration and panel (b) plane-wave migration in tilted coordinates. The horizontal location for them is at $x = 32.6$ km, where there are nearly horizontal sediments at the shallow part and steep salt flanks at $z = 4.4$ km. Events bending downward are multiples. Again CIGs obtained by reverse-time migration have better wide-angle energy than those obtained by plane-wave migration in tilted coordinates. In both panels (a) and (b), the curvature present in the CIGs of the sediments is reasonable, since the viewing direction is almost normal to their apparent geologic dip direction. The CIG of the reflection

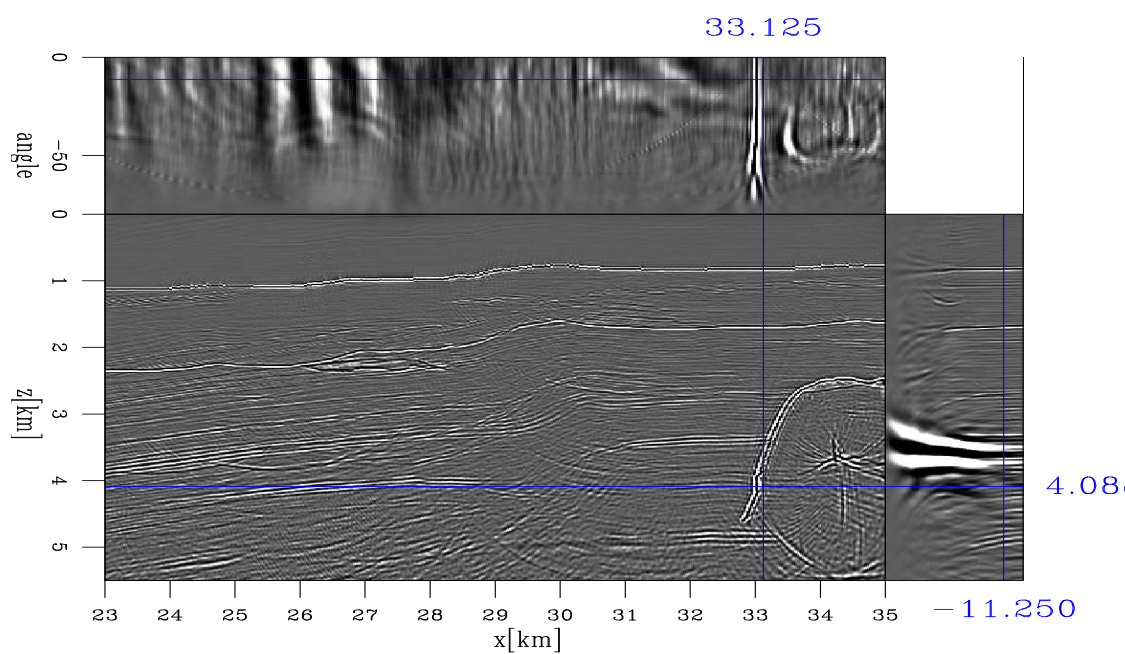


Figure 5.14: Angle-domain CIG cube obtained by reverse-time migration with the true velocity. `cigmv/. cigtruertm`

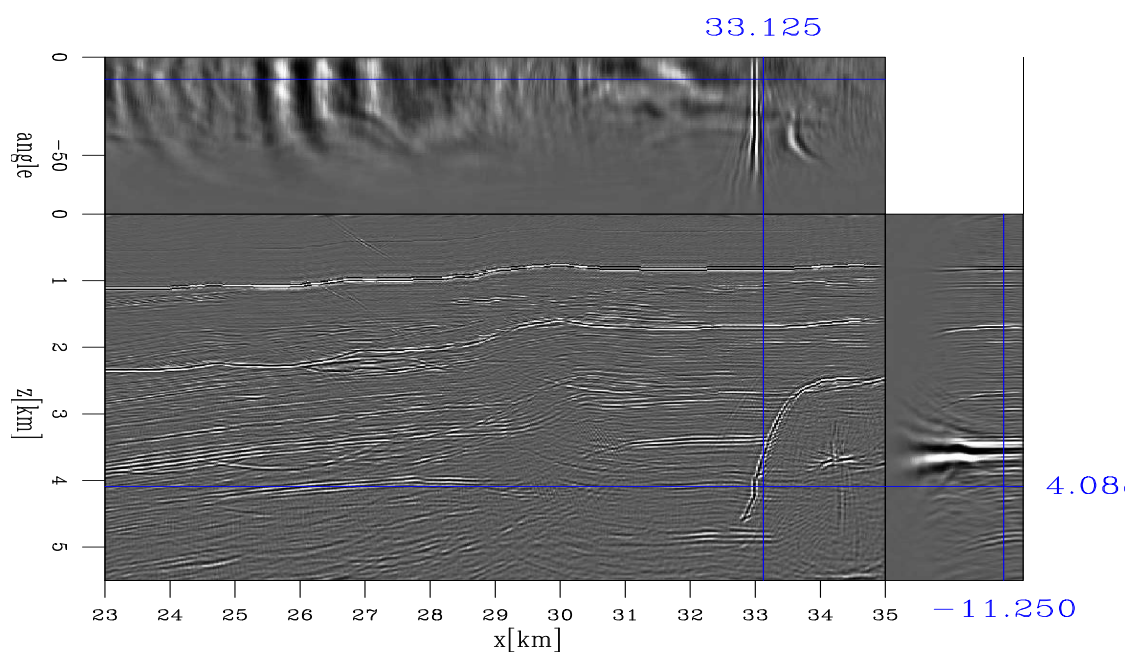


Figure 5.15: Angle-domain CIG cube obtained by plane-wave migration in tilted coordinates with the true velocity. `cigmv/. cigtrueltit`

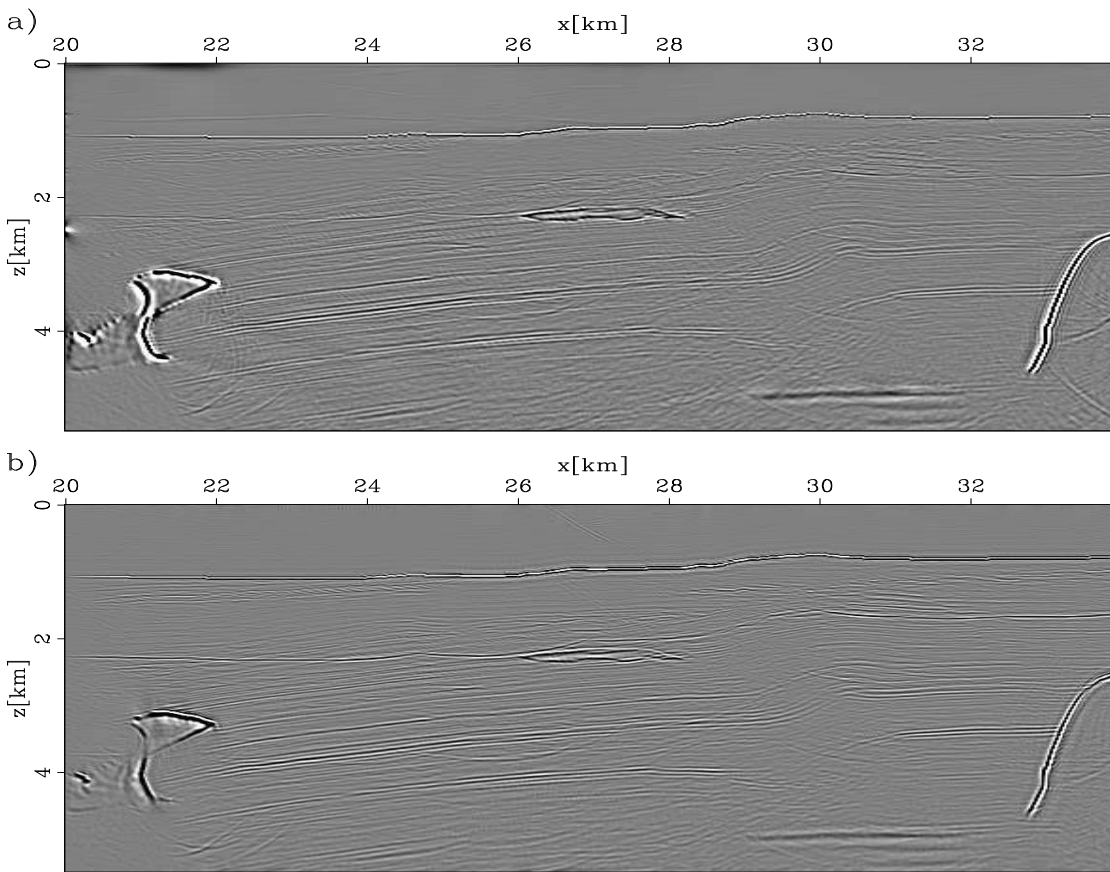


Figure 5.16: Stack images from angle-domain CIGs with the true velocity: (a) reverse-time migration; (b) plane-wave migration in tilted coordinates. `cigmv/. stack`

point on the salt flank (at $z = 4.4$ km), however, looks smeared and forked because the viewing direction almost parallels its dip direction, and most of the wide-angle energy in the CIG belongs to reflection points in the neighborhood of that point. As a result, its curvature is unreasonably large, given the 3 percent velocity error.

Figures 5.17 (c) and (d) show the angle-domain CIG cubes in a normal-direction view. Panel (a) is obtained by reverse-time migration, and panel (b) by plane-wave migration in tilted coordinates. The location of the event is at $x = 32.6$ km, $z = 4.4$ km, where the salt flank is present and the apparent geologic dip at the reflection point is about 70° . The vertical axis in panels (c) and (d) is the direction normal to

the apparent geologic dip of the reflector. Reverse-time migration has better wide-angle energy; otherwise Figures 5.17 (c) and (d) are comparable. Given the 3 percent velocity error, both CIGs show reasonable curvature.

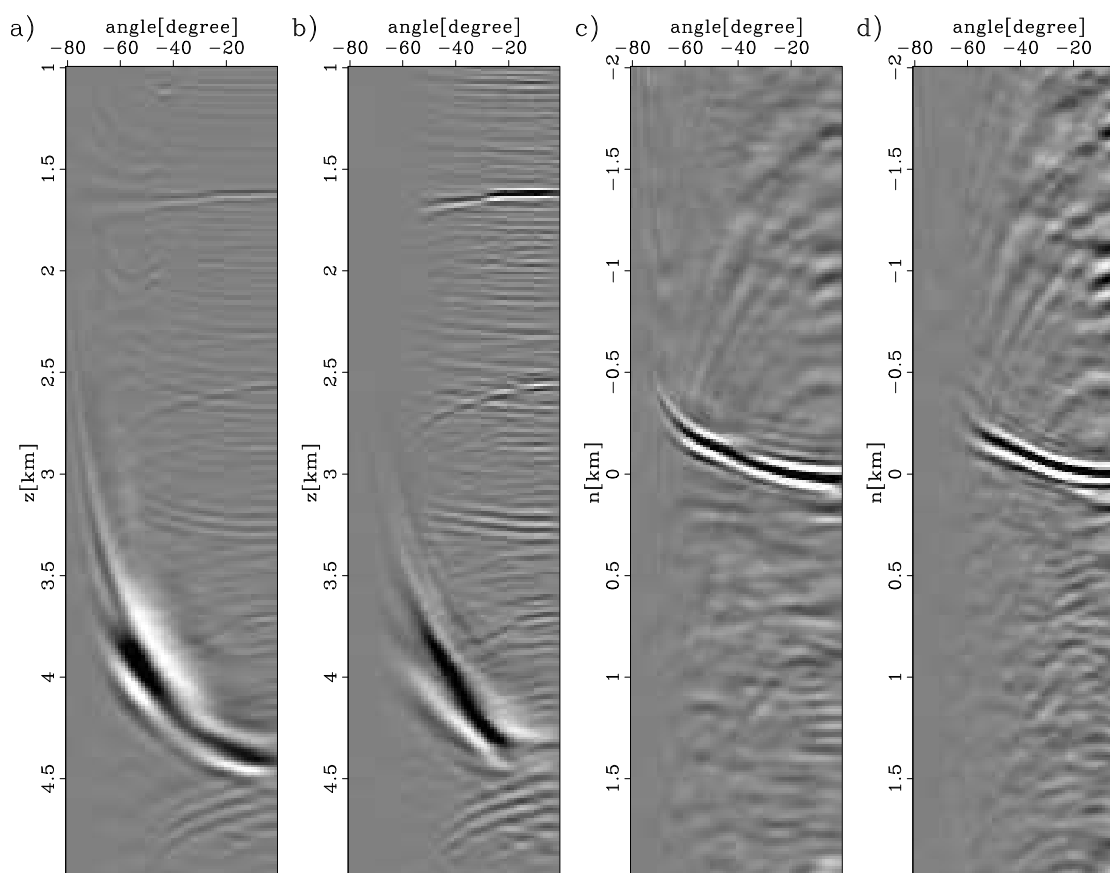


Figure 5.17: Angle-domain CIGs with the velocity underestimated by 3 percent: (a) Vertical view of angle-domain CIGs obtained by reverse-time migration at $x = 32.6$ km. (b) Vertical view of angle-domain CIGs obtained by plane-wave migration in tilted coordinates at $x = 32.6$ km. (c) Normal-direction view of angle-domain CIGs obtained by reverse-time migration at $x = 32.6$ km, $z = 4.4$ km. (d) Normal-direction view of angle-domain CIGs obtained by plane-wave migration in tilted coordinates at $x = 32.6$ km, $z = 4.4$ km. `cigmv/. amerg9770`

Figure 5.18 shows dip-dependent RMO for velocity ratio parameters ρ ranging from 0.93 to 1 for an image point (at $x = 33.5$ km, $z = 2.6$ km) on the salt flank, where the apparent dip is about 70° . For each panel, the vertical axis is the direction

normal to the reflector and the horizontal axis is the opening angle. The migration velocity is 3 percent slower than the true one. The panel with $\rho = 1$ shows the original CIG obtained by plane-wave migration in tilted coordinates. The event on the gather is almost flat for $\rho = 0.97$. Figure 5.19 shows the semblance for the same image point. The estimated velocity scaling ratio from RMO analysis matches the one we use to scale the migration velocity.

CONCLUSIONS

Conventional horizontal CIGs are not reliable for steep reflectors because of the offset stretch. Reverse-time migration provides robust angle-domain CIGs for both steep and near-horizontal reflectors by merging horizontal and vertical CIGs. Plane-wave migration in tilted coordinates can also provide reliable CIGs for both steep and near-horizontal reflectors because the propagation direction is close to the extrapolation direction, and the subsurface offset direction is close to the dip direction in tilted coordinates. Angle-domain CIGs of an image point should be viewed in the direction normal to reflector's dip direction. For the BP velocity benchmark dataset with unrealistically large offsets, comparisons show that reverse-time migration has better wide-angle energy; otherwise the angle-domain CIGs from these two methods are comparable. When the velocity is incorrect, the CIGs from both migration methods provide useful moveout information. Dip-dependent RMO estimates the curvature of angle-domain CIGs of steep reflectors accurately.

ACKNOWLEDGMENTS

I thank BP for making the dataset available.

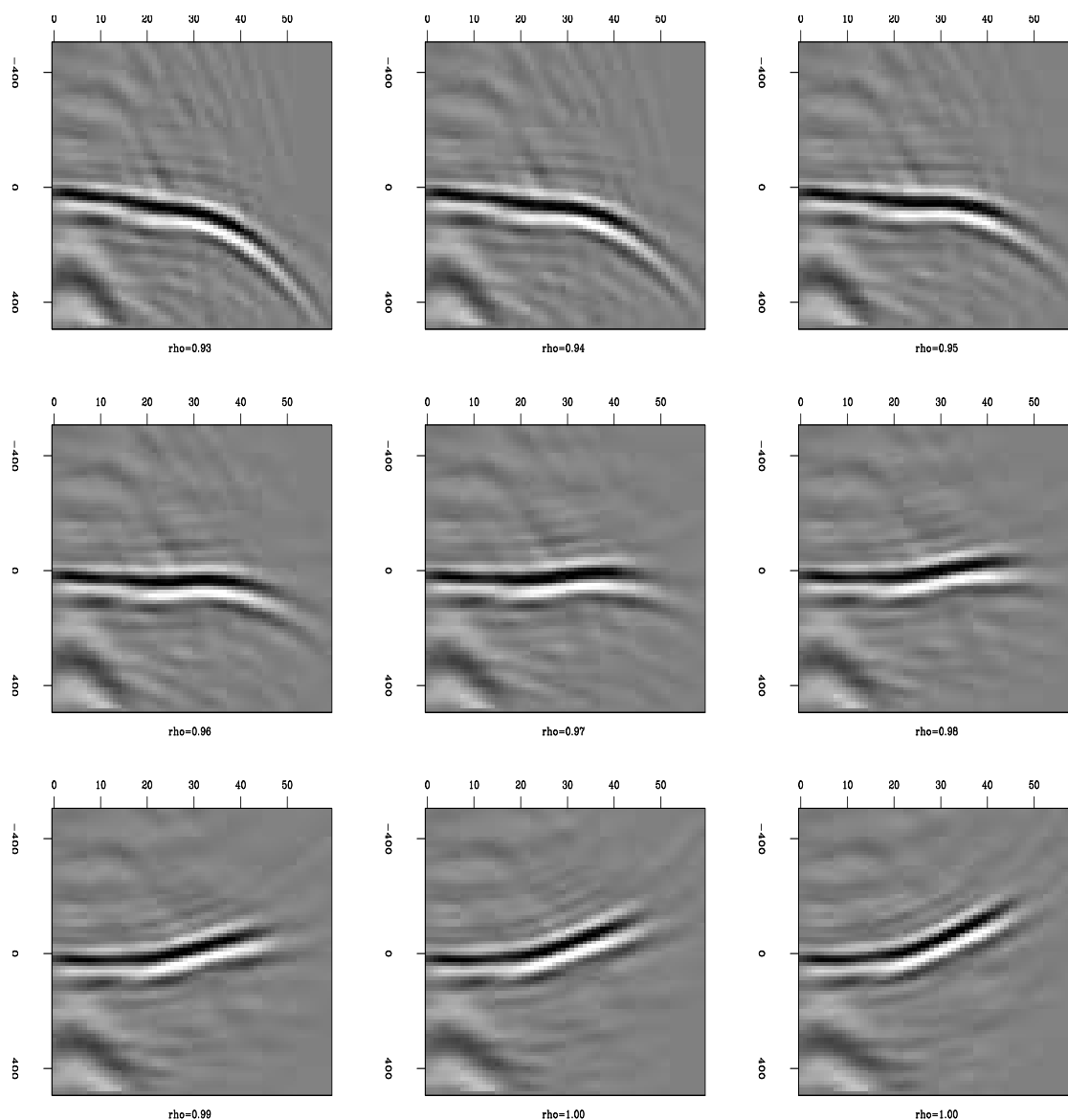


Figure 5.18: Dip-dependent RMO for velocity ratio parameters ρ ranging from 0.93 to 1 for an image point on the salt flank. The vertical axis is the direction normal to the apparent dip, and the horizontal axis is the opening angle. The apparent dip is about 70° . `cigmv/. rmo70`

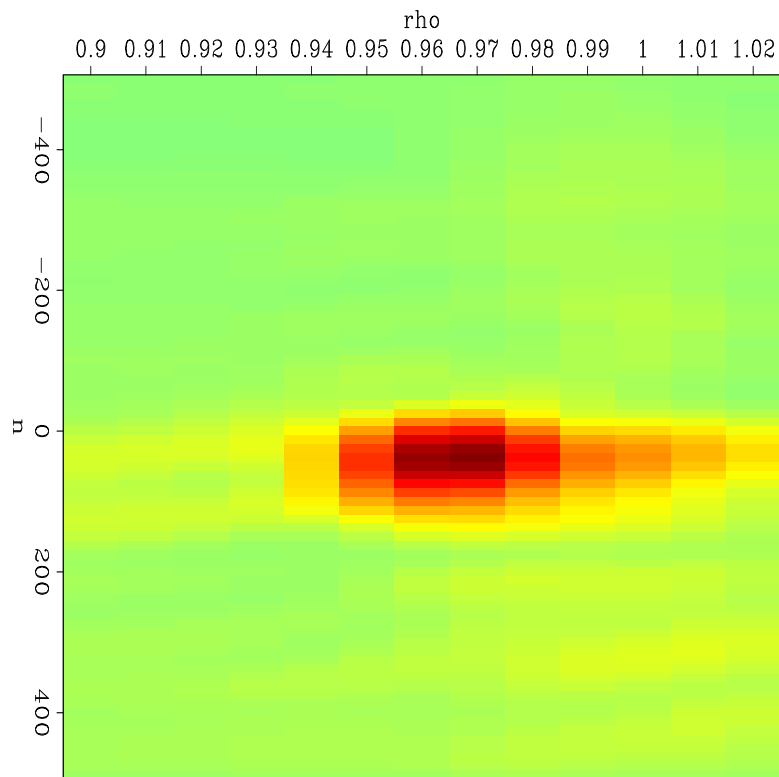


Figure 5.19: Semblance for an image point on a steep reflector with an apparent dip of 70° . `cigmv/. semblance70`

Chapter 6

Conclusion

In this dissertation, I present techniques for imaging steep reflectors in TI media by one-way wavefield extrapolation. In order to achieve the goal, I develop four main novel algorithms for seismic imaging.

First, I develop a new one-way wavefield-extrapolation scheme, optimized finite-difference, for TI media, which allows propagating waves accurately and efficiently in TI media. I designed finite-difference schemes by fitting the dispersion relation with a rational function using weighted least square optimization. The new finite-difference scheme is stable using the bulletproofing theory and it is much more accurate than conventional ones designed by analytical Padé expansion in the same order. The new finite-difference scheme can handle TI media with lateral variation.

Second, I develop a new migration algorithm based on one-way wavefield extrapolation, plane-wave migration in tilted coordinates, which accurately propagate near-horizontal and overturned waves, and image steep reflectors efficiently. Waves in nearly horizontal directions are accurately propagated, because the coordinate system is tilted so that the extrapolation direction is close to their propagation direction. Overturned waves travel only downward or upward in a well chosen tilted coordinate system, so they can be propagated using one-way wavefield extrapolation operators in the new coordinates. I apply plane-wave migration in tilted coordinates to synthetic

and field datasets, and successfully image steep salt flanks and faults.

Third, I develop a new method to produces robust angle-domain common-image gathers for steep reflectors. In plane-wave migration tilted coordinates, the direction of subsurface offset is close to the dip of reflectors. Therefore, angle-domain common-image gathers, transformed from offset-domain common-image gathers obtained by plane-wave migration in tilted coordinates, are robust for reflectors with a wide range of dip.

Fourth, I develop a new residual-moveout method, dip-dependent residual moveout, which accurately estimating the curvature information contained in angle-domain common-image gathers of steep reflectors. Dip-dependent residual moveout incorporates the dip information by moving image points along the normal direction of the reflector. Therefore, it can accurately estimate the curvature information contained in angle-domain common-image gathers. I apply it to synthetic dataset examples show that the curvature estimated by dip-dependent residual moveout matches well the velocity error.

Appendix A

3D common-image gathers in tilted coordinates

In this appendix, I first derive the relationship linking the geologic offset, horizontal and vertical offsets in 3D. Then I derive the relationship linking offset domain common image gathers (CIG) in tilted coordinates and horizontal and vertical offset gathers. Finally I derive formulas for dip-dependent residual moveout in 3D.

HORIZONTAL, VERTICAL AND GEOLOGIC OFFSETS

The axes for vertical Cartesian coordinates are $\mathbf{x} = (1, 0, 0)^T$, $\mathbf{y} = (0, 1, 0)^T$, and $\mathbf{z} = (0, 0, 1)^T$, where “ T ” means transpose. In 3D reverse-time migration, source wavefield is $S(\mathbf{m}, t)$ and receiver wavefield is $R(\mathbf{m}, t)$, where $\mathbf{m} = x\mathbf{x} + y\mathbf{y} + z\mathbf{z}$. In addition to horizontal offset $\mathbf{h}^{\mathbf{xy}} = h_x\mathbf{x} + h_y\mathbf{y}$, I define vertical offsets $\mathbf{h}^{\mathbf{zx}} = h_z\mathbf{z} + h_x\mathbf{x}$ and $\mathbf{h}^{\mathbf{yz}} = h_y\mathbf{y} + h_z\mathbf{z}$. Horizontal- and vertical-offset-domain CIGs are generated by reverse-time migration as follows:

$$I_{xy}(\mathbf{m}, \mathbf{h}^{\mathbf{xy}}) = \int_t S(\mathbf{m} - \mathbf{h}^{\mathbf{xy}}, t) R(\mathbf{m} + \mathbf{h}^{\mathbf{xy}}, t) dt, \quad (\text{A.1})$$

$$I_{zx}(\mathbf{m}, \mathbf{h}^{\mathbf{zx}}) = \int_t S(\mathbf{m} - \mathbf{h}^{\mathbf{zx}}, t) R(\mathbf{m} + \mathbf{h}^{\mathbf{zx}}, t) dt, \quad (\text{A.2})$$

$$I_{xy}(\mathbf{m}, \mathbf{h}^{yz}) = \int_t S(\mathbf{m} - \mathbf{h}^{yz}, t) R(\mathbf{m} + \mathbf{h}^{yz}, t) dt. \quad (\text{A.3})$$

Consider a single event on a reflector with a normal vector $\mathbf{n} = n_x \mathbf{x} + n_y \mathbf{y} + n_z \mathbf{z}$. In the Fourier domain, the normal vector \mathbf{n} and wavenumber vector $\mathbf{k} = (k_x, k_y, k_z)^T$ are linked by the following relationship:

$$n_x = \frac{k_x}{k_r}, \quad (\text{A.4})$$

$$n_y = \frac{k_y}{k_r}, \quad (\text{A.5})$$

$$n_z = \frac{k_z}{k_r}, \quad (\text{A.6})$$

where $k_r = \sqrt{k_x^2 + k_y^2 + k_z^2}$. The dip, α and azimuth angle β of the event are calculated from the normal vector \mathbf{n}

$$\tan \alpha = \frac{\sqrt{n_x^2 + n_y^2}}{n_z}, \quad (\text{A.7})$$

$$\tan \beta = \frac{n_y}{n_x}. \quad (\text{A.8})$$

As with 2D, subsurface offsets that parallel the dip plane of the reflector at the reflection point (or that are normal to \mathbf{n}) are *geologic offsets*. To derive the relationship linking horizontal, vertical and geologic offsets, it is convenient to consider problems in the *geologic coordinate system* with its three axes \mathbf{x}^0 , \mathbf{y}^0 and \mathbf{z}^0 defined as follows:

$$\begin{pmatrix} \mathbf{x}^0 \\ \mathbf{y}^0 \\ \mathbf{z}^0 \end{pmatrix} = \begin{pmatrix} \cos \alpha \cos \beta & \cos \alpha \sin \beta & \sin \alpha \\ -\sin \beta & \cos \beta & 0 \\ -\sin \alpha \cos \beta & -\sin \alpha \sin \beta & \cos \alpha \end{pmatrix} \begin{pmatrix} \mathbf{x} \\ \mathbf{y} \\ \mathbf{z} \end{pmatrix}. \quad (\text{A.9})$$

It is easy to verify that $\mathbf{z}^0 = \mathbf{n}$ and the plane defined by the vectors \mathbf{x}^0 and \mathbf{y}^0 parallel the dip plane. There a geologic offset \mathbf{h}^0 can be written as $\mathbf{h}^0 = h_x^0 \mathbf{x}^0 + h_y^0 \mathbf{y}^0$. As with 2D, the geologic offset is the projection of a general offset onto the geologic dip plane, the plane normal to \mathbf{n} . For example, the geologic offset $\mathbf{h}^0 = h_x^0 \mathbf{x}^0 + h_y^0 \mathbf{y}^0$

corresponding to the horizontal offset $\mathbf{h}^{\mathbf{xy}}$ is

$$\mathbf{h}^0 = (\mathbf{h}^{\mathbf{xy}} \cdot \mathbf{x}^0)\mathbf{x}^0 + (\mathbf{h}^{\mathbf{xy}} \cdot \mathbf{y}^0)\mathbf{y}^0. \quad (\text{A.10})$$

where “ \cdot ” means dot product of two vectors. Therefore, the relationship linking the geologic offset and horizontal offset for a dipping event is

$$\begin{pmatrix} h_x^0 \\ h_y^0 \end{pmatrix} = \begin{pmatrix} \cos \alpha \cos \beta & \cos \alpha \sin \beta \\ -\sin \beta & \cos \beta \end{pmatrix} \begin{pmatrix} h_x \\ h_y \end{pmatrix}. \quad (\text{A.11})$$

As with 2D, equation A.11 becomes singular for $\alpha = 90^\circ$. Similarly, we can obtain the relationship linking \mathbf{h}^0 and $\mathbf{h}^{\mathbf{zx}}$,

$$\begin{pmatrix} h_x^0 \\ h_y^0 \end{pmatrix} = \begin{pmatrix} \cos \alpha \cos \beta & \sin \alpha \\ -\sin \beta & 0 \end{pmatrix} \begin{pmatrix} h_x \\ h_z \end{pmatrix}, \quad (\text{A.12})$$

and the relationship linking \mathbf{h}^0 and $\mathbf{h}^{\mathbf{yz}}$,

$$\begin{pmatrix} h_x^0 \\ h_y^0 \end{pmatrix} = \begin{pmatrix} \cos \alpha \sin \beta & \sin \alpha \\ \cos \beta & 0 \end{pmatrix} \begin{pmatrix} h_y \\ h_z \end{pmatrix}. \quad (\text{A.13})$$

From equations A.11, A.12 and A.13, we can transfer offset-domain CIGs, I_{xy} , I_{zx} and I_{yz} , generated by reverse-time migration, to geologic offset CIGs. Geologic offset CIGs can then be transferred to angle-domain CIGs. An alternative way is to transfer offset-domain CIGs I_{xy} , I_{zx} and I_{yz} to angle domain CIGs independently, and merge them as follow:

$$I = w_{xy}^2 I_{xy} + w_{xz}^2 I_{xz} + w_{yz}^2 I_{yz}, \quad (\text{A.14})$$

where $w_{xy} = \cos \alpha$, $w_{xz} = \sin \alpha \sin \beta$ and $w_{yz} = \sin \alpha \cos \beta$.

SUBSURFACE OFFSET IN TILTED COORDINATES

In this section, I derive the relationship linking $\mathbf{h}^{\mathbf{xy}}$, $\mathbf{h}^{\mathbf{zx}}$, $\mathbf{h}^{\mathbf{yz}}$, and subsurface offset in tilted coordinates.

In chapter 4, I design tilted coordinates by rotating in two steps. First I rotate about \mathbf{z} by an angle ϕ and obtain a new tilted coordinate system with its axes \mathbf{x}^1 , \mathbf{y}^1 and \mathbf{z}^1 . Second I rotate about \mathbf{y}^1 by an angle θ and obtain a tilted coordinate system with its axes, \mathbf{x}^t , \mathbf{y}^t and \mathbf{z}^t ,

$$\begin{pmatrix} \mathbf{x}^t \\ \mathbf{y}^t \\ \mathbf{z}^t \end{pmatrix} = \begin{pmatrix} \cos \theta \cos \phi & \cos \theta \sin \phi & \sin \theta \\ -\sin \phi & \cos \phi & 0 \\ -\sin \theta \cos \phi & -\sin \theta \sin \phi & \cos \theta \end{pmatrix} \begin{pmatrix} \mathbf{x} \\ \mathbf{y} \\ \mathbf{z} \end{pmatrix}. \quad (\text{A.15})$$

The subsurface offset in this coordinate system, $\mathbf{h}^t = h_x^t \mathbf{x}^t + h_y^t \mathbf{y}^t$, is normal to the axis \mathbf{z}^t . For plane-wave migration in tilted coordinates, offset-domain CIGs corresponding to the ray parameter pair p_{s_x}, p_{s_y} are

$$I_t^{p_{s_x} p_{s_y}}(\mathbf{m}^t, \mathbf{h}^t) = \int_{\omega} \omega^2 S(\mathbf{m}^t - \mathbf{h}^t, \omega) R(\mathbf{m}^t + \mathbf{h}^t, \omega) d\omega, \quad (\text{A.16})$$

where S and R are source and receiver wavefield corresponding p_{s_x}, p_{s_y} , and $\mathbf{m}^t = x_t \mathbf{x}^t + y_t \mathbf{y}^t + z_t \mathbf{z}^t$.

As with \mathbf{h}^{xy} , \mathbf{h}^{zx} and \mathbf{h}^{yz} , the geologic offset corresponding to \mathbf{h}^t is the projection of \mathbf{h}^t onto the geologic dip plane of the event. Therefore, offset \mathbf{h}^t and the geologic offset \mathbf{h}^0 are linked by the relationship,

$$\mathbf{h}^0 = (\mathbf{h}^t \cdot \mathbf{x}^0) \mathbf{x}^0 + (\mathbf{h}^t \cdot \mathbf{y}^0) \mathbf{y}^0. \quad (\text{A.17})$$

This leads to the following relationship

$$\begin{pmatrix} h_x^0 \\ h_y^0 \end{pmatrix} = \begin{pmatrix} \cos \alpha \cos \beta & \cos \alpha \sin \beta \\ -\sin \beta & \cos \beta \end{pmatrix} \begin{pmatrix} \cos \theta \cos \phi & -\sin \phi \\ \cos \theta \sin \phi & \cos \phi \end{pmatrix} \begin{pmatrix} h_x^t \\ h_y^t \end{pmatrix} + \begin{pmatrix} \sin \theta \sin \alpha h_x^t \\ 0 \end{pmatrix}. \quad (\text{A.18})$$

From equation A.11, we can obtain the horizontal offset \mathbf{h}^{xy} corresponding to the geologic offset \mathbf{h}^0 ,

$$\begin{pmatrix} h_x \\ h_y \end{pmatrix} = \begin{pmatrix} \cos \beta & -\sin \beta \\ \sin \beta & \cos \beta \end{pmatrix} \begin{pmatrix} h_x^0 \sec \alpha \\ h_y^0 \end{pmatrix}. \quad (\text{A.19})$$

From equations A.18 and A.19, we can obtain the relationship linking \mathbf{h}^t and \mathbf{h}^{xy} . Let $\beta = 0$, $\phi = 0$, from equations A.18 and A.19, we have the relationship

$$h_x = \frac{h_x^t \cos(\theta - \alpha)}{\cos \alpha}, \quad (\text{A.20})$$

which is the same as equation 5.16. Similarly, from equation A.12, we can obtain the vertical offset \mathbf{h}^{zx} corresponding to the geologic offset \mathbf{h}^0 ,

$$\begin{pmatrix} h_y \\ h_z \end{pmatrix} = \begin{pmatrix} 0 & \sec \beta \\ \csc \alpha & -\tan \beta \cot \alpha \end{pmatrix} \begin{pmatrix} h_x^0 \\ h_y^0 \end{pmatrix}. \quad (\text{A.21})$$

From equation A.13, we can obtain the vertical offset \mathbf{h}^{zx} corresponding to the geologic offset \mathbf{h}^0 ,

$$\begin{pmatrix} h_x \\ h_z \end{pmatrix} = \begin{pmatrix} 0 & -\csc \beta \\ \csc \alpha & \cot \alpha \cot \beta \end{pmatrix} \begin{pmatrix} h_x^0 \\ h_y^0 \end{pmatrix}. \quad (\text{A.22})$$

Therefore, from equations A.18 and A.21, we can obtain the relationship linking \mathbf{h}^t and \mathbf{h}^{zx} ; and from equations A.18 and A.22, we can obtain the relationship linking \mathbf{h}^t and \mathbf{h}^{yz} . Let $\beta = 0$ and $\phi = 0$, from equations A.18 and A.21, we have the relationship between h_x^t and h_z ,

$$h_z = \frac{h_x^t \cos(\theta - \alpha)}{\sin \alpha}, \quad (\text{A.23})$$

which is the same as equation 5.17.

DIP DEPENDENT RESIDUAL MOVEOUT

When the migration velocity is not the true velocity, image points move along the normal direction of the reflector, \mathbf{n} . Given opening angle γ , the moveout Δn is calculated using equation 5.21. Therefore, in 3D the moveout $\Delta \mathbf{n}$ is

$$\Delta \mathbf{n} = \Delta n \mathbf{n} = \Delta n (-\sin \alpha \cos \beta \mathbf{x} - \sin \alpha \sin \beta \mathbf{y} + \cos \alpha \mathbf{z}). \quad (\text{A.24})$$

As with 2D case, we can shift image points by applying phase-shift in the Fourier domain as follows:

$$I^{RMO}(\mathbf{k}, \gamma) = I(\mathbf{k}, \gamma)e^{i\mathbf{k} \cdot \Delta \mathbf{n}} = I(\mathbf{k}, \gamma)e^{ik_x \Delta x} e^{ik_y \Delta y} e^{ik_z \Delta z}, \quad (\text{A.25})$$

where $\Delta x = -\Delta n \sin \alpha \cos \beta$, $\Delta y = -\Delta n \sin \alpha \sin \beta$, and $\Delta z = \Delta n \cos \alpha$.

Bibliography

- Abramowitz, M. and I. Stegun, 1972, Solutions of quartic equations: Handbook of Mathematical Functions with Formulas, Graphs, and Mathematical Tables, 17–18, New York: Dover.
- Alkhalifah, T., 1998, Acoustic approximations for processing in transversely isotropic media: *Geophysics*, **63**, 623–631.
- Baumstein, A. and J. Anderson, 2003, Wavefield extrapolation in laterally varying VTI media: 73rd Ann. Internat. Mtg., 945–948, Soc. of Expl. Geophys.
- Baysal, E., D. D. Kosloff, and J. W. C. Sherwood, 1983, Reverse time migration: *Geophysics*, **48**, 1514–1524.
- Bear, L., T. Dickens, J. Krebs, J. Liu, and P. Traynin, 2005, Integrated velocity model estimation for improved positioning with anisotropic PSDM: The Leading Edge, **24**, 622–634.
- Billette, F. and S. Brandsberg-Dahl, 2005, The 2004 BP velocity benchmark: 67th meeting, Expanded Abstracts, B035, Eur. Assn. Geosci. Eng.
- Biondi, B., 2002, Stable wide-angle Fourier finite-difference downward extrapolation of 3-D wavefields: *Geophysics*, **67**, 872–882.
- , 2003, Equivalence of source-receiver migration and shot-profile migration: *Geophysics*, **68**, 1340–1347.
- Biondi, B. and G. Shan, 2002, Prestack imaging of overturned reflections by reverse time migration, *in* Expanded Abstracts, 1284–1287, Soc. of Expl. Geophys., 72nd Ann. Internat. Mtg.
- Biondi, B. and W. Symes, 2004, Angle-domain common-image gathers for migration velocity analysis by wavefield-continuation imaging: *Geophysics*, **69**, 1283–1298.

- Blacquiere, G., H. W. J. Debye, C. P. A. Wapenaar, and A. J. Berkhout, 1989, 3D table-driven migration: *Geophys. Prosp.*, **37**, 925–958.
- Brown, D., 1979, Muir’s rules for matrices: Another look at stability: *SEP-Report*, **20**, 125–142.
- Claerbout, J. F., 1971, Toward a unified theory of reflector mapping: *Geophysics*, **36**, 467–481.
- , 1985, *Imaging the Earth’s interior*: Blackwell Scientific Publications.
- Clapp, R., 2000, *Geologically constrained migration velocity analysis*: PhD thesis, Stanford University.
- de Hoop, M. V., 1996, Generalization of the Bremmer coupling series: *J. Math. Phys.*, 3246–3282.
- Duquet, B. and P. Lailly, 2006, Efficient 3D wave-equation migration using virtual planar sources: *Geophysics*, **71**, S185–S197.
- Duquet, B., P. Lailly, and A. Ehinger, 2001, 3D plane wave migration of streamer data: 71st Ann. Internat. Mtg, Expanded Abstracts, 1033–1036, Soc. of Expl. Geophys.
- Etgen, J., 2002, Waves, beams and dimensions: an illuminating if incoherent view of the future of migration: Presented at the 72nd Ann. Internat. Mtg, Soc. of Expl. Geophys.
- , 2005, How many angles do we really need for delayed-shot migration?: *SEG, Expanded Abstracts, 1985–1988, 74th SEG Ann. Gen. Meeting and Exhibition*.
- Fei, T., J. A. Dellinger, G. E. Murphy, J. L. Hensley, and S. H. Gray, 1998, Anisotropic true-amplitude migration: 68th Ann. Internat. Mtg, Expanded Abstracts, 1677–1679, Soc. of Expl. Geophys.
- Fei, T. and C. Liner, 2006, Hybrid Fourier finite-difference 3D prestack depth migration for VTI media, *in* Expanded Abstracts, 2377–2381, Soc. of Expl. Geophys.
- Ferguson, R. J. and G. F. Margrave, 1998, Depth migration in TI media by non-stationary phase shift: 68th Ann. Internat. Mtg, Expanded Abstracts, 1831–1834, Soc. of Expl. Geophys.
- Gazdag, J., 1978, Wave equation migration with the phase-shift method: *Geophysics*, **43**, 1342–1351.

- Godfrey, R. J., F. Muir, and J. F. Claerbout, 1979, Stable extrapolation: SEP-Report, **16**, 83–87.
- Golub, G. and C. Van Loan, 1996: Presented at the Matrix computation(3rd ed.), Johns Hopkins University Press.
- Hale, D., 1991a, 3-D depth migration via McClellan transformations: *Geophysics*, **56**, 1778–1785. (Erratum in GEO-57-2-370).
- , 1991b, Stable explicit depth extrapolation of seismic wavefields: *Geophysics*, **56**, 1770–1777.
- Helbig, K., 1956, Die ausbreitung elastischer Wellen in anisotropen Medien: *Geophys. Prosp.*, **04**, 70–81.
- Higginbotham, J. H., Y. Shin, and D. V. Sukup, 1985, Directional depth migration (short note): *Geophysics*, **50**, 1784–1796.
- Holberg, O., 1988, Towards optimum one-way wave propagation: *Geophys. Prosp.*, **36**, 99–114.
- Huang, L. Y. and R. S. Wu, 1996, Prestack depth migration with acoustic screen propagators: 66th Ann. Internat. Mtg, Expanded Abstracts, 415–418, Soc. of Expl. Geophys.
- Larner, K. and J. K. Cohen, 1993, Migration error in transversely isotropic media with linear velocity variation in depth: *Geophysics*, **58**, 1454–1467.
- Lee, M. W. and S. Y. Suh, 1985, Optimization of one-way wave-equations (short note): *Geophysics*, **50**, 1634–1637.
- Li, Z., 1991, Compensating finite-difference errors in 3-D migration and modeling: *Geophysics*, **56**, 1650–1660.
- Liu, F., R. Day, D. Hanson, D. Whitmore, C. Mosher, and J. Sinton, 2005, A stable wave equation migration method in 3D VTI media: 67th Ann. Internat. Mtg., Expanded Abstracts, P002, EAGE.
- Liu, F., D. W. Hanson, N. D. Whitmore, and R. S. D. ann Robert H. Stolt, 2006, Toward a unified analysis for source plane-wave migration: *Geophysics*, **71**, S129–S139.
- Liu, F., R. Stolt, D. Hanson, and R. Day, 2002, Plane wave source composition: An accurate phase encoding scheme for prestack migration: 72nd Ann. Internat. Mtg,

- Expanded Abstracts, 1156–1159, Soc. of Expl. Geophys.
- Ma, Z., 1981, Finite-difference migration with higher-order approximation: Presented at the 1981 joint meeting of the China Geophysical Society and Soc. of Expl. Geophys., Beijing China.
- McCollum, B. and F. Snell, 1932, Asymmetry of sound velocity in stratified formations: *Physics (Journal of Applied Physics)*, **2**, 174–185; reprinted in SEG, *Early Geophysical Papers*, 217–227.
- McMechan, G. A., 1983, Migration by extrapolation of time-dependent boundary values: *Geophys. Prosp.*, **31**, 413–420.
- Morton, S. A. and C. C. Ober, 1998, Faster shot-record migrations using phase encoding: 68th Ann. Internat. Mtg, Expanded Abstracts, 1131–1134, Soc. of Expl. Geophys.
- Nichols, D., 1994, Imaging in complex structures using band-limited Green's function: PhD thesis, Stanford University.
- Postma, G. W., 1955, Wave propagation in a stratified medium: *Geophysics*, **20**, 780–806.
- Ren, J., C. Gerrard, J. McClean, and M. Orlovich, 2005, Wave equation prestack depth migration in laterally varying VTI media: 75th Ann. Internat. Mtg., Expanded Abstracts, 104–107, Soc. of Expl. Geophys.
- Rickett, J. E. and P. C. Sava, 2002, Offset and angle-domain common image-point gathers for shot-profile migration: *Geophysics*, **67**, 883–889.
- Rietveld, W. E. A., 1995, Controlled illumination of prestack seismic migration: PhD thesis, Delft University of Technology.
- Ristow, D., 1999, Migration of transversely isotropic media using implicit finite-difference operators: *Journal of Seismic Exploration*, **8**, 39–55.
- Ristow, D. and T. Ruhl, 1994, Fourier finite-difference migration: *Geophysics*, **59**, 1882–1893.
- , 1997, 3-D implicit finite-difference migration by multiway splitting: *Geophysics*, **62**, 554–567.
- Romero, L. A., D. C. Ghiglia, C. C. Ober, and S. A. Morton, 2000, Phase encoding of shot records in prestack migration: *Geophysics*, **65**, 426–436.

- Rousseau, J. H. L., 1997, Depth migration in heterogeneous, transversely isotropic media with the phase-shift-plus-interpolation method: 67th Ann. Internat. Mtg, Expanded Abstracts, 1703–1706, Soc. of Expl. Geophys.
- Sava, P., 2006, Imaging overturning reflections by riemannian wavefield extrapolation: Journal of Seismic Exploration, **15**, 209–223.
- Sava, P. and S. Fomel, 2005, Riemannian wavefield extrapolation: Geophysics, **70**, T45–T56.
- Sava, P. C. and S. Fomel, 2003, Angle-domain common-image gathers by wavefield continuation methods: Geophysics, **68**, 1065–1074.
- Shan, G. and B. Biondi, 2005, 3D wavefield extrapolation in laterally-varying tilted TI media: 75th Ann. Internat. Mtg., Expanded Abstracts, 104–107, Soc. of Expl. Geophys.
- Shan, G. and G. Zhang, 2003, Equivalence between shot-profile and source-receiver migration: SEP-Report, **113**, 121–126.
- Shragge, J., 2006, Non-orthogonal Riemannian wavefield extrapolation: SEG, Expanded Abstracts, 2236–2240, 75th SEG Ann. Gen. Meeting and Exhibition.
- Stoer, J. and R. Bulirsch, 1992, Introduction to numerical analysis (2nd ed.): Springer-Verlag.
- Tam, K. and V. Perez-Mendez, 1981, Tomographical imaging with limited-angle input: J. Opt. Soc. Am., **71**, 582–592.
- Thomsen, L., 1986, Weak elastic anisotropy: Geophysics, **51**, 1954–1966. (Discussion in GEO-53-04-0558-0560 with reply by author).
- Thorbecke, J. W., K. Wapenaar, and G. Swinnen, 2004, Design of one-way wavefield extrapolation operators, using smooth functions in WLSQ optimization: Geophysics, **69**, 1037–1045.
- Toldi, J., 1985, Velocity analysis without picking: PhD thesis, Stanford University.
- Tsvankin, I., 1996, P-wave signatures and notation for transversely isotropic media: An overview: Geophysics, **61**, 467–483.
- Uzcategui, O., 1995, 2-D depth migration in transversely isotropic media using explicit operators: Geophysics, **60**, 1819–1829.
- Whitmore, N. D., 1983, Iterative depth migration by backward time propagation, *in*

- Expanded Abstracts, Session:S10.1, Soc. of Expl. Geophys.
- , 1995, An imaging hierarchy for common angle plane wave seismograms: PhD thesis, University of Tulsa.
- Yevick, D. and D. Thomson, 2000, Complex Padé approximants for wide-angle acoustic propagators: *J. Acoust. Soc. Am.*, **108**, 2748–2790.
- Zhang, G., 1993, System of coupled equations for up-going and down-going waves: *Acta Mathematicae Sinica*, **16**, 251–263.
- Zhang, J. and G. A. McMechan, 1997, Turning wave migration by horizontal extrapolation: *Geophysics*, **62**, 291–297.
- Zhang, J., D. J. Verschuur, and C. P. A. Wapenaar, 2001a, Depth migration of shot records in heterogeneous, transversely isotropic media using optimum explicit operators: *Geophys. Prosp.*, **49**, 287–299.
- Zhang, J., C. Wapenaar, and D. Verschuur, 2001b, 3D depth migration in VTI media with explicit extrapolation operators: 75th Ann. Internat. Mtg., Expanded Abstracts, 1085–1088, Soc. of Expl. Geophys.
- Zhang, L., B. Hua, and H. Calandra, 2005a, 3D Fourier finite difference anisotropic depth migration, *in* Expanded Abstracts, 1914–1917, Soc. of Expl. Geophys.
- Zhang, Y., J. Sun, C. Notfors, S. Gray, L. Chernis, and J. Young, 2005b, Delayed-shot 3D depth migration: *Geophysics*, **70**, E21–E28.